Femtosecond time-resolved soft X-ray spectroscopy for an element-specific analysis of complex materials

Der Fakultät für Physik der Universität Duisburg-Essen
zur Erlangung des akademischen Grades eines Doktors der
Naturwissenschaften (Dr. rer. nat.)

vorgelegte Dissertation von

Nico Rothenbach

aus Miltenberg

Tag der Disputation: 12. Oktober 2020
1. Gutachter: Prof. Dr. Heiko Wende
2. Gutachter: Prof. Dr. Hans Jakob Wörner
3. Gutachter: Prof. Dr. Michael Farle

Abstract

In this thesis, I report on femtosecond time-resolved soft X-ray absorption spectroscopy (XAS) measurements performed on an Fe/MgO multilayer sample acting as a model system for metal-insulator heterostructures. The element-, and therefore constituent-specific character of X-ray absorption spectroscopy makes it an optimal measurement technique to analyze the ultrafast dynamics induced in both constituents of the heterostructure, after a localized optical excitation of only the metal constituent. XAS, which is sensitive to both the electronic and the lattice excitations, has been complemented with ultrafast electron diffraction (UED) experiments, independently analyzing the Fe constituent's lattice dynamics. Together with *ab initio* calculations, this yields a comprehensive insight into the microscopic origin of the induced dynamics, i.e., local relaxation processes within a single constituent and non-local energy transfer processes between the two constituents. The investigation of the pump-induced ultrafast dynamics taking place in the heterostructure revealed that ultrafast energy transfer across the Fe-MgO interface is, independently of the pump photon energy, not mediated by a direct electronic charge transfer. Instead, it is driven by high-frequency interface vibrational modes, which get excited by the hot electrons in Fe, and then couple to vibrations in MgO in a mode-selective, non-thermal manner. Consequently, this demonstrates the importance of a hot phonon population for the ultrafast interfacial non-equilibrium energy transfer dynamics.
Furthermore, I present a systematic fluence-dependent study of the distinct time-dependent and constituent-specific spectral changes in transient XAS for the transition metal Fe L_3-edge and the O K-edge of the insulator. Introducing two simple modeling and fitting procedures for the individual absorption edges allows me to identify the pump-induced spectral changes. While the Fe absorption edge exhibits a clear energy red-shift of the spectrum upon laser excitation, the oxygen absorption edge features a uniform intensity decrease of its fine structures. I explicitly demonstrate the sensitivity of time-resolved XAS to phonons, showing the possibility of quantifying temperature changes in complex materials.
Lastly, the study of the Fe/MgO system is dedicated to the ultrafast magnetization dynamics of the thin Fe constituents in the heterostructure, which are embedded between the insulating MgO constituents. Thus, suppressing all contributions of spin transport processes to the ultrafast demagnetization dynamics. Comparing all

the individual transients, i.e., the demagnetization dynamic and the energy transfer dynamics, shows that the local demagnetization process of the Fe constituent is determined by a phonon-mediated process. Hence, in the absence of spin transport processes, a significant degree of demagnetization requires the excitation of phonons, which eventually leads to a heating of the sample as a consequence of incoherent lattice excitations an unavoidable side-effect accompanying the ultrafast laser-induced demagnetization.

To illustrate the great opportunities of conducting X-ray absorption measurements at a free-electron laser, I present in this thesis first results of two open community proposals, including the very-first user experiment, conducted at the Spectroscopy and Coherent Scattering instrument of the European XFEL. In contrast to the study of the Fe/MgO system, both community proposals are focused on a X-ray absorption study of Ni and NiO films. I demonstrate and highlight the possibilities of performing high-quality static, as well as femtosecond time-resolved XAS measurements at the XFEL facility, i.e., being able to identify time-resolved, pump-induced dynamics of several spectral signatures, and investigating a series of pump-induced spectral changes at various time delays. This clearly emphasizes that the fast acquisition time for high-quality femtosecond time-resolved XAS measurements present a promising addition to synchrotron-based femtoslicing sources, allowing a variety of systematic measurements, which would not be possible at the latter.

Kurzfassung

Diese Arbeit widmet sich Femtosekunden-zeitaufgelösten Röntgenabsorptionsmessungen (kurz XAS) an einer, als allgemeines Modellsystem für Metall-Isolator-Heterostrukturen dienenden, Fe/MgO-Mehrschichtprobe. XAS bietet hierbei, aufgrund des elementspezifischen Charakters, die optimale Messtechnik zur Analyse der ultraschnellen Dynamik, die nach lokaler optischer Anregung der Fe-Schicht in beiden Bestandteilen der Heterostruktur stattfindet, an. Da XAS auf Anregung sowohl der Elektronen sowie des Gitters empfindlich ist, wurden die Messungen mit unabhängigen Experimenten der ultraschnellen Elektronenbeugung (UED) ergänzt, welche einzig die Gitterdynamik der Fe-Konstituente analysieren. Zusammen mit *ab initio*-Berechnungen ermöglicht dies einen umfassenden Einblick in den mikroskopischen Ursprung der induzierten Dynamik, d.h. sowohl in die lokalen Relaxationsprozesse innerhalb einer einzelnen Komponente der Heterostruktur, als auch in Prozesse des Energietransfers zwischen den beiden Komponenten. Die Untersuchung der laserinduzierten ultraschnellen Dynamik zeigt, dass der ultraschnelle Energietransfer über die Fe-MgO-Grenzfläche unabhängig von der Photonenenergie der Laseranregung ist und nicht durch einen direkten elektronischen Ladungstransfer vermittelt wird. Stattdessen treiben hochfrequente Grenzflächen-Schwingungsmoden, die durch die heißen Elektronen in Fe angeregt werden und dann modenselektiv, nicht-thermisch, an Schwingungen in MgO koppeln, den Energietransfer. Die Messungen verdeutlichen die Bedeutung einer Nichtgleichgewichts-Phononenbesetzung für die ultraschnelle Energietransferdynamik der Fe/MgO-Mehrschichtprobe.

Die fluenzabhängige Untersuchung der zeitabhängigen, elementspezifischen spektralen Änderungen der Eisen L_3- und der Sauerstoff K-Absorptionskante ermöglicht es, mit Hilfe der Einführung von zwei einfachen Modellierungsverfahren, die individuellen laserinduzierten spektralen Änderungen der einzelnen Absorptionskanten zu identifizieren. Es zeigt sich, dass die Laseranregung eine energetische Rotverschiebung des Eisen-Spektrums verursacht, während die Sauerstoffabsorptionskante eine gleichmäßige Intensitätsabnahme der Feinstrukturen zeigt. Die Messungen demonstrieren explizit die Empfindlichkeit der zeitaufgelösten XAS auf Phononen und präsentieren damit die Möglichkeit XAS als ein leistungsfähiges Werkzeug zur Quantifizierung von Temperaturänderungen in komplexen Materialien einzusetzen.

Abschließend wird die ultraschnellen Magnetisierungsdynamik der Fe-Schicht untersucht und in das umfassende Verständnis der Gesamtdynamik des Fe/MgO-Systems integriert. Dabei ist vorallem entscheidend, dass die dünnen Fe-Schichten zwischen den isolierenden MgO-Schichten eingebettet sind, was jegliche Beiträge durch Spin-Transportprozesse zur ultraschnellen Entmagnetisierungsdynamik unterdrückt. Der Vergleich der einzelnen zeitaufgelösten Prozesse zeigt, dass die lokale Entmagnetisierungsdynamik eindeutig durch einen phononenvermittelten Prozess bestimmt ist. Dies macht ein Erwärmen der Probe aufgrund inkohärenter Gitteranregungen zu einem unvermeidlichen Nebeneffekt, der ultraschnellen laserinduzierten Entmagnetisierung.

Darüber hinaus zeigt diese Arbeit erste Ergebnisse von Röntgenabsorptionsmessungen an Ni und NiO aus zwei Gemeinschaftsanträgen (engl. *open community proposals*), die am *Spectroscopy and Coherent Scattering* Instrument des European XFEL durchgeführt wurden. Darunter zeige ich insbesondere auch Ergebnisse des allerersten Nutzerexperiments. In diesem Kapitel demonstriere ich vor allem die umfangreichen Möglichkeiten des Freien-Elektronen-Laser, sowohl statische als auch zeitaufgelöste XAS-Messungen von hoher Qualität durchzuführen. Insbesondere die schnelle Akquisitionszeit qualitativ hochwertiger Femtosekundenzeitaufgelöster XAS-Messungen macht den Freien-Elektronen-Laser eine vielversprechende Ergänzung zu synchrotronbasierten Femtoslicing-Quellen, da er eine Vielzahl systematischer Messungen, wie z.B. der Dynamiken von verschiedenen spektralen Signaturen oder der Entwicklung von laserinduzierten spektralen Änderungen bei verschiedenen Zeitpunkten, ermöglicht, die an letzteren nur bedingt möglich wären.

Contents

1 Introduction

1.1 Ultrafast processes and their timescales in nature and technology

> *How long did it take you to read this sentence? Just recognizing the first letter took only milliseconds. Around 0.05 millisecond, or 50 microseconds, passes each time chemicals diffuse across a synapse, carrying a signal from one neuron to another in your brain. Are you holding [this thesis] at a comfortable reading distance? It takes light one or two nanoseconds to travel from the page to your eye and about 20 picoseconds to pass through the lens in your eye. And yet these brief natural events are epically long compared with the shortest man-made events, which proceed 1,000-fold more swiftly: pulses of laser light that last for only a few femtoseconds.*
>
> **— J. M. Hopkins and W. Sibbett** [1]

Our modern day technology and the understanding of ultrafast processes in solids are strongly connected with each other. Standard electronic circuits, e.g., in computers, operate at clock speeds in the GHz range, corresponding to the *nanosecond* timescale. The clock speed is hereby basically limited by the waste heat generated by the device itself, and not by the intrinsic switching time of its transistors, since electrons need only *hundred femtoseconds* to pass through modern day state of the art transistors, with only 10 nm length [2]. Small and specialized electronic devices, e.g., used for high speed optical telecommunication, can operate on even faster timescales of the order of *ten picoseconds* [2]. The magnetic recording speed in computer hard disks, based on the magnetization reversal by damping, is currently limited to a few *hundred picoseconds* [2]. Today, some of the fastest technologies, e.g., used for surgery applications [3–5], are based on *femtosecond* laser sources [1]. On this timescale, of only *hundred femtosecond* and less, some of the most fundamental processes in nature take place, i.e., electrons moving between atoms, or the breaking and formation of molecular bonds [1].

Since the late 1980s, femtosecond laser sources were quickly adopted by biologists, chemists, and physicists, and provide till today the foundation of time-resolved pump-probe experiments, which are inevitable in a very large range of fields of today's solid state research [6]. Throughout the years, the technological progression of those pump-probe experiments lead to their permanently advancing time resolu-

tion, enabling the ability to capture events at increasingly shorter time intervals. For instance, a striking achievement was made in 1999 in the so-called field of femtochemistry, resulting in the Nobel Prize in chemistry for studying the transition states of chemical reactions using femtosecond spectroscopy [7]. But also in other fields, ultrafast spectroscopic techniques are continuously enhancing our basic understanding of fundamental processes, and allowing us to gain more and more insight into the non-equilibrium properties of condensed matter, which might be highly relevant for all sorts of technological applications. In particular, while initially the timescale for magnetization reversal was believed to be limited to hundred picoseconds, given by the timescale of magnetic precession, the first demonstration of sub-picosecond demagnetization by a femtosecond laser [8] started a new, fascinating research topic in modern magnetism with a potentially high impact for future data storage and manipulation [9]. First and foremost, the development of a profound microscopic understanding of the elementary non-equilibrium interaction processes among electrons, phonons, and spins, and of their collective relaxation mechanisms is of great fundamental interest [10]. Thus, ultimately aiming towards the manipulation and control of material properties upon external excitation, which could optimistically impact a wide range of applications for future technologies. In that sense, the aim of this work is assigned to advance the development of the fundamental understanding, especially being dedicated to the investigation of these microscopic non-equilibrium interaction and relaxation processes in complex materials.

1.2 Scope of this thesis

After this short general introduction into the research area of ultrafast dynamics, I will give in chap. 2.1 a basic overview of the theoretical background of laser-induced ultrafast dynamics in condensed matter. I start with a phenomenological description of the non-equilibrium situation and derive a basic timeline of the most prominent microscopic processes after ultrafast laser excitation. Then I introduce the energy flow dynamics of a metal-insulator heterostructure system after laser-induced excitation, which builds the focal point of the analysis of my thesis. Lastly, I will outline the fundamentals and open questions of the investigation of ultrafast magnetization dynamics. In the second part of my theory chapter, chap. 2.2, I introduce my main investigation technique, namely soft X-ray absorption spectroscopy, since it is acting as the constituent-specific probe of the heterostructure system due to its element-specific character.

In chap. 3, I show the technological progression of how to conduct ultrafast time-resolved X-ray absorption measurements at large scale research facilities. Starting in chap. 3.1.1 from the general question, how does a synchrotron work, ranging from the emission of synchrotron radiation from bending magnets to insertion devices, I will come in chap. 3.1.2 to synchrotron-based femtoslicing sources to produce sub-ps short X-ray pulses, at the example of the synchrotron BESSY II. After that, chap. 3.2 introduces X-ray free electron lasers, which are based on the self-amplified spontaneous emission process. Finally, in chap. 3.2.2, the European XFEL facility, and its specifications are highlighted.

Chap. 4 represents the focal point of my thesis. This chapter is dedicated to the investigation of the pump-induced dynamics in a Fe/MgO heterostructure model system, whose sample preparation is shown in chap. 4.1. The results of this chapter are divided into three main parts: Chap. 4.2 reports on the microscopic non-equilibrium energy transfer dynamics after localized optical excitation of the metal constituent in the Fe/MgO heterostructure. I show complementary time-resolved X-ray absorption spectroscopy and ultrafast electron diffraction experiments, combined with *ab initio* density-functional theory calculations, to analyze and disentangle the electronic and phononic contributions to the ultrafast dynamical processes. Second, in chap. 4.3, I concentrate on the understanding of the spectral pump-induced changes of the spectroscopic fine structures in soft X-ray absorption spectroscopy. I introduce two distinct modeling and fitting procedures for the fundamentally different absorption edges, namely the transition metal L-edge and the oxygen K-edge. Furthermore, I demonstrate the sensitivity of transient X-ray absorption spectroscopy to phonons and show that it can be used as a powerful tool to quantify

temperature changes in complex materials. Chap. 4.4 is focused on the investigation of the ultrafast magnetization dynamics of the Fe constituent in the heterostructure, while contributions of spin transport processes are suppressed. By comparing the various transient behaviors reported throughout chap. 4, I can identify how the local demagnetization process is mediated.

During the time of my Ph.D. thesis, I participated in the very-first user experiment at the Spectroscopy and Coherent Scattering instrument of the European XFEL in December 2018, followed by a second beamtime in November 2019, both dedicated to an entirely different sample system, namely nickel and nickel oxide. However, since the investigation of the Fe/MgO sample system represents the focal point of my thesis, I will not report on a profound analysis of those data but show first results of both experiments. Therefore, chap. 5 represents a kind of "outlook" of this thesis, both reporting on the conducted measurements, as well as highlighting the possibilities of the European XFEL facility. Starting with the description of the working principle of the specially designed transmission zone plate setup preparation in chap. 5.1, the preparation of the investigated Ni and NiO samples is shown in chap. 5.2. Thereafter, static, and time-resolved X-ray absorption spectroscopy data are shown in chap. 5.3, and chap. 5.4. Finally, I will shortly report in chap. 5.5 on the possibility of conducting non-linear X-ray spectroscopy data at the European XFEL, at the example on the Ni L-edge.

To close this work, I will recapitulate and summarize in chap. 6 the main experimental results presented in my thesis.

Theoretical background

2

2.1 Laser-induced ultrafast dynamics in condensed matter

Optical excitation of condensed matter with an ultrashort femtosecond laser pulse induces ultrafast dynamics involving elementary scattering processes between electrons, phonons, and other degrees of freedom on the femtosecond timescale. To better understand the non-equilibrium situation, and get a feeling of the issues in the field, I will start in the following to introduce a widely used and convenient phenomenological description of the ultrafast dynamics, and derive from this a basic timeline of the most prominent microscopic processes happening after femtosecond laser excitation.

2.1.1 Phenomenological description of ultrafast dynamics

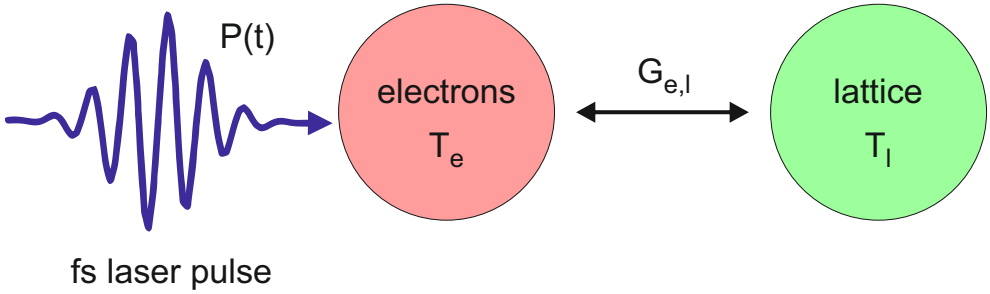

Fig. 2.1.: Schematic representation of the phenomenological description of the energy redistribution between the electron and phonon subsystem after optical laser excitation within the so-called two-temperature-model. The optical excitation initially excites the electron subsystem exclusively. The two subsystems are pictured as heat baths/reservoirs with their own temperature T_i, and contribution to the overall specific heat c_i. The energy transfer from the electrons to the lattice is described by a single (electron-phonon) coupling parameter $G_{e,l}$.

Already in 1974, Anisimov et al. introduced the so-called two-temperature model (2TM), to empirically describe the energy transfer from optically excited electrons in metals to the lattice [11, 12]. Fig. 2.1 schematically depicts the basic concept of the 2TM: Within the 2TM, the electrons and the lattice are treated as individual

subsystems, which are pictured as heat baths/reservoirs. Both subsystems have been assigned their own temperature, namely the temperature of the electron subsystem T_e, and the phonon subsystem T_l; and their contribution to the overall specific heat c_e, and c_l, respectively. The energy transfer between the electron and the phonon subsystem is given by a single electron-phonon coupling parameter $G_{e,l}$.
Later, the basic concept of the 2TM was adopted and extended by Vaterlaus et al. [13, 14], by introducing not two but three distinct reservoirs, namely the electron, the phonon, and the spin subsystem, which was then incorporated by Beaurepaire et al. in 1996 [8] to explicitly describe the very first experiment on sub-ps ultrafast demagnetization after femtosecond laser excitation (cf. chap. 2.1.3). Within this now so-called three-temperature-model (3TM), also the spin subsystem has assigned its own temperature T_s and contribution to the specific heat c_s. Similarly to the description of the 2TM, the now three reservoirs are coupled with each other via a corresponding coupling constant $G_{i,j}$, and therefore can exchange energy among each other. However, it should be noted that it is up to now still frequently questioned whether the introduction of a spin temperature T_s is truly justified on the femtosecond timescale, and what is the scientific meaning behind this temperature. That is why the description of laser-induced ultrafast dynamics is often restricted to the electrons and the lattice dynamics within the 2TM, providing that the magnetization dynamics are not the main focus of the respective investigation. That being said, in the framework of both the 2TM and the 3TM, it is assumed that an optical excitation $P(t)$ initially excites the electron subsystem exclusively. The exchange of energy between the three reservoirs can be described via the following rate equation model:

$$\begin{aligned} c_e\left(T_e\right)\frac{dT_e}{dt} &= -G_{e,l}\left(T_e - T_l\right) - G_{e,s}\left(T_e - T_s\right) + P(t), \\ c_s\left(T_s\right)\frac{dT_s}{dt} &= -G_{e,s}\left(T_s - T_e\right) - G_{s,l}\left(T_s - T_l\right), \\ c_l\left(T_l\right)\frac{dT_l}{dt} &= -G_{e,l}\left(T_l - T_e\right) - G_{s,l}\left(T_l - T_s\right). \end{aligned} \tag{2.1}$$

Without any external excitation, the three subsystems are in thermal equilibrium, and the corresponding three temperatures are equal. However, after optical excitation, the electron subsystem is assumed to be instantly heated to an elevated thermalized electron temperature T_e. Hence, the model neglects entirely the process of electron thermalization (described below), happening within the first tens of fs [15]. Furthermore, in both the 2TM or 3TM, the non-equilibrium phonon distributions are assumed to be thermalized. However, it is highly questionable [16, 17] whether either phenomenological description can, under this assumption, really provide a realistic description for the actual non-equilibrium state after ultrafast laser excitation. This is because, in reality, the energy transfer between the electron and phonon subsystem may drive the relaxation dynamics in a non-thermal regime

[18, 19], and on the other hand a rather weak, anharmonic coupling between phonons [20, 21] may hinder the phonon thermalization. Up to now, all experimental observations indicate that a universal answer to the importance of non-thermal phonon populations to the energy redistribution after optical laser excitation does not exist. That is why, one central aspect of this thesis will be addressed to identify the *role of non-thermal phonons in the energy transfer dynamics* in a suitable model system, which I discuss in more detail below (cf. chap. 2.1.2).

It should be noted that the general concept of using quasiparticles and their mutual interactions has proven itself to be very successful in describing *equilibrium* properties of condensed matter. To name just one example: the electron-phonon interaction turned out to be the critical point in the understanding of conventional superconductivity [10]. Consequently, it was, and still is, of great fundamental interest to gain a conclusive insight in the underlying microscopic interaction mechanisms between the different kinds of quasiparticles, and in the respective relaxation mechanisms in condensed matter. However, up to now, a complete and profound understanding of the laser-induced *dynamics* of the collective excitation of the electrons, phonons, and spins does not exist and is therefore still a highly interesting topic in the current solid state research [10]. In the following, I try to construct, in the framework of the 3TM (and beyond), a basic timeline of the most prominent microscopic processes happening after femtosecond laser excitation of condensed matter.

When a femtosecond laser interacts with condensed matter, the ultrashort light pulse will induce an electronic polarization in the material, which leads to the absorption of the laser light pulse by exclusively the electronic subsystem [10, 23]. Before time zero the occupation of the electronic state is described by a Fermi-Dirac distribution $f(T_0, E)$ at the temperature T_0 (Fig. 2.2, left):

$$f(T_0, E) = \left(\exp\left(\frac{E - E_F}{k_B \cdot T_0} \right) + 1 \right)^{-1}, \tag{2.2}$$

with E_F being the Fermi-level, and k_B the Boltzmann constant. At time zero, the absorption of the laser pulse induces a highly non-equilibrium situation in the electron system. First, these (hot) non-thermal electrons will redistribute the excess energy by electron-electron scattering, and excitation of secondary electrons among their own subsystem (Fig. 2.2, middle), which leads to internal electron thermalization within the electron thermalization time t_{th}. Consequently, before t_{th}, since the electron subsystem is not longer described by a Fermi-Dirac distribution, but by a strongly non-thermal distribution function f_{nt}, the reservoir cannot be described by an electron temperature T_e. However, after the electron thermalization time, the electron subsystem is again represented by a Fermi-Dirac distribution function

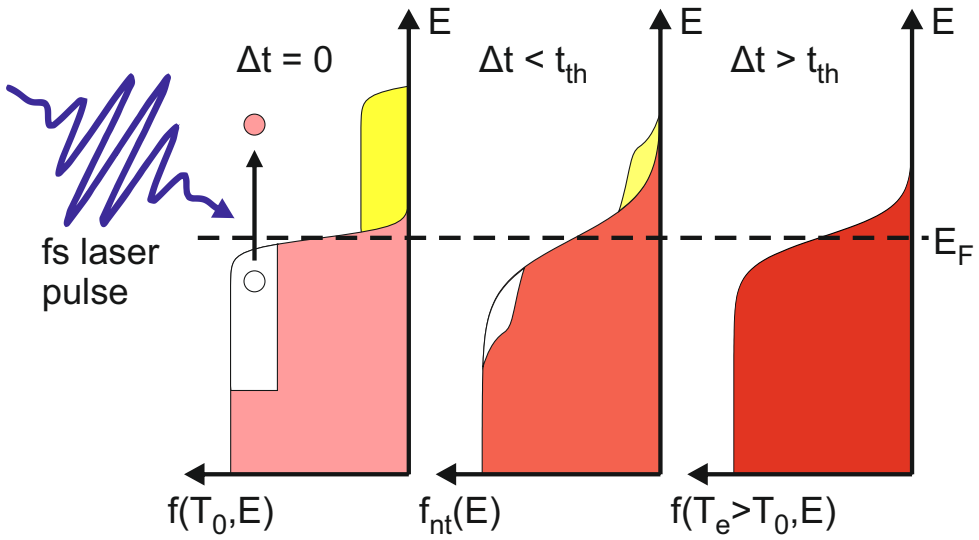

Fig. 2.2.: Schematic representation of the relaxation process of the electronic subsystem in a metal after optical excitation with a fs laser pulse. Left, time zero: The occupation of the electronic state is described by a Fermi-Dirac distribution $f(T_0, E)$. The laser pump pulse induces a highly non-equilibrium situation in the electronic system. Middle, before thermalization time t_{th}: Internal thermalization within the thermalization time t_{th}, accompanied by a strongly non-thermal distribution function f_{nt}. Right, after t_{th}: The electron subsystem is again represented by a Fermi-Dirac distribution function, but at an elevated temperature T_e. The figure is redrawn based on [10, 22].

(eq. 2.2), but at an elevated temperature T_e (Fig. 2.2, right) [22]. Typically, the electron thermalization time t_{th} is of the order of 100 fs for laser fluences of about ~ 1 mJ/cm^2 [10]. The thermalization time t_{th} decreases with increasing absorbed laser fluence and can in the experiment be drastically modified due to effects of ballistic electron transport [10, 24].

Directly after electron thermalization, the elevated electron temperature T_e is different from the temperature T_l of the lattice (phonon) subsystem. At subsequent time delays after the laser excitation, the electron subsystem will, according to the 3TM (eq. 2.1), redistribute its excess energy to the other subsystems like, e.g., the phonon subsystem by electron-phonon coupling. Or, in magnetically ordered systems, e.g., by spin-lattice-coupling to the spin subsystem. This redistribution of excess energy will lead to the cooling of the hot electron system, but on the other side inducing non-equilibrium situations in the others, which will, in turn, induce redistribution and thermalization of their given excess energy.

Typical timescales of the processes within and between the three subsystems are the following: As mentioned above, a typical electron thermalization time is of the order of 100 fs, and below [10, 15]. The timescale for electron-phonon coupling is around 0.1 ps to 1 ps for metals [9, 25], followed by phonon thermalization of several 10 ps [20]. Because the heat capacity of the electrons is typically one to two orders of magnitudes smaller than the one of the phonons, the electron temperature

T_e typically can reach several thousand Kelvin within the first hundred femtoseconds after laser excitation. In contrast, the lattice temperature T_l remains relatively cold [10, 26]. Furthermore, in magnetic systems, the interaction of these two subsystems with the spin subsystem may have to be considered to understand the overall dynamics. The typical timescale for the spin-lattice coupling is stated around 100's of ps [27]. However, the observed demagnetization times for itinerant ferromagnets upon fs laser excitation have been reported to be considerably faster, namely within the first few 100's of fs [8] (c.f. Fig. 2.5, below). The ultrafast demagnetization process will be addressed in more detail in chap. 2.1.3.

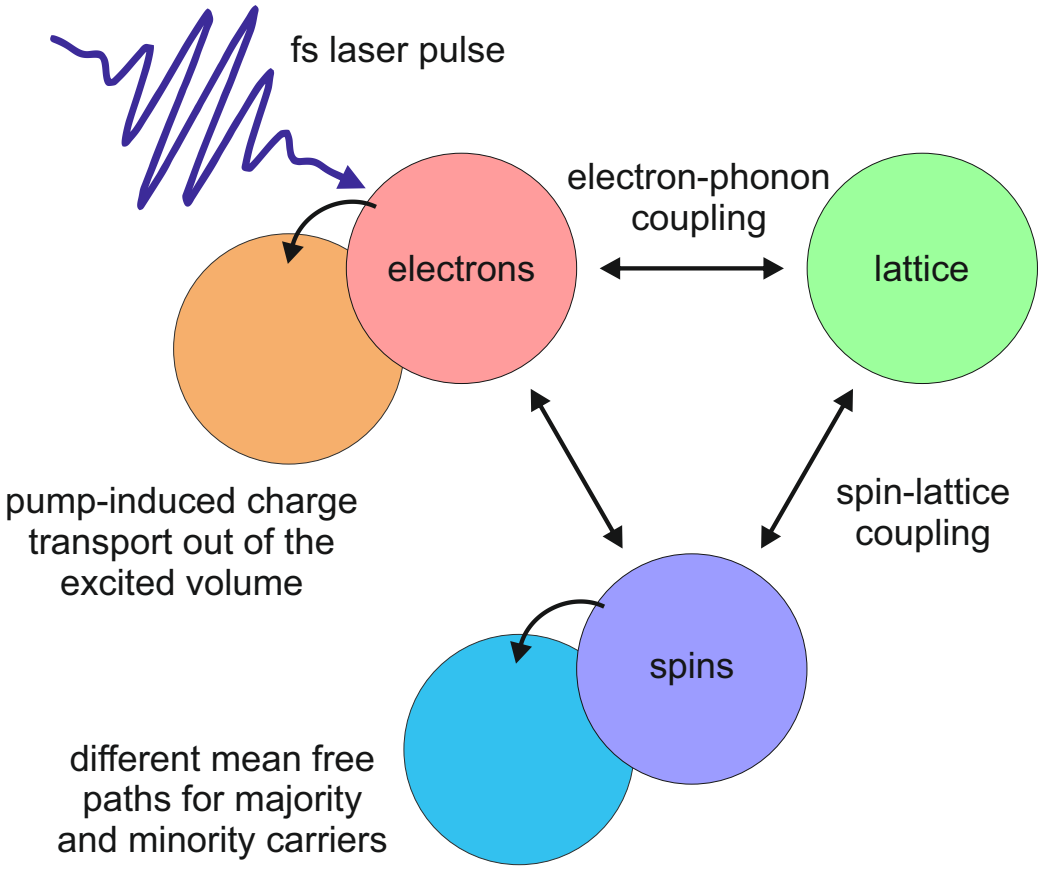

Fig. 2.3.: Schematic representation of the extended energy redistribution processes after optical laser excitation. Next to the processes described in the 2TM (cf. Fig. 2.1), the interaction with the spin subsystem is considered. Furthermore, especially for a spatially inhomogeneous excitation of a bulk sample, additional transport processes can play an important role for the observed pump-induced dynamics. The figure redrawn based on [28].

Even though the 3TM is a very simplified picture to describe the dynamics after laser excitation, it has extensively been proven to be successfully applied to explain various experiments (after electron thermalization is completed) [22, 25, 29], it is for other situations also often too much simplified, and has to be adjusted according to the experimental conditions [30–34].

Fig. 2.3 shows one extended representation of the possible energy redistribution processes among the electron, phonon, and spin subsystem after optical laser excitation schematically. I stress that the respective thermalization and cooling times of all subsystems highly depend on the investigated material system, the absorbed laser fluence, and the optical penetration depth of the laser pulse. As indicated in Fig. 2.3, for a spatially inhomogeneous excitation of a bulk sample, also transport processes can play an important role in the observed pump-induced dynamics [10, 22, 24, 35]. In particular, especially for surface sensitive experiments, i.e., 2PPE measurements, both ballistic and diffusive transport of excited hot electrons out of the investigated volume can lower the observed redistribution of excess energy density near the surface [10]. The typical timescale for the ballistic electron motion is approximately 1 fs per 1 nm [36]. Hence, depending on the experiment, the excited hot charge carriers may be transported out of the excited and investigated volume. Due to different mean free paths for the excited majority and minority carriers [37–40], this can lead to the observation of demagnetization processes, i.e., for inhomogeneous excitations of bulk samples, or for samples with/on an adjacent conducting layer/substrate, which can act as a sink for the transported charge carriers. Furthermore, next to transport processes, depending on the excitation conditions and the investigated sample system, a vast number of other adjustments to the 3TM may be necessary to describe the dynamics. To name just one example: It was reported that an unequal coupling to different phonon modes had to be taken into account to describe the experimental data [31]. However, for some experiments the 3TM have also proven to be, even with adjustments, not anymore sufficient to provide a microscopic, quantitative description of the true non-equilibrium situation. In this cases, other models may be more suitable to describe the dynamics, e.g., the superdiffusive spin transport model (see below) [36].

2.1.2 Laser-induced dynamics in a heterostructure sample

The development of a profound understanding of the non-equilibrium properties of condensed matter, and the underlying microscopic processes responsible for the induced ultrafast dynamics after excitation with a fs laser pulse, represents a highly interesting but challenging task in the current solid state research [41]. Even though, with the development of permanently advancing sub-picosecond lasers since the late 1980s, and the corresponding technological progression of pump-probe experiments, which allow us to gain more and more insight in the non-equilibrium situation our understanding is, unfortunately, mostly still on the stage of fundamental research [9]. Nonetheless, in recent years a significant effort was made to understand the el-

ementary non-equilibrium interaction processes on the femtosecond and picosecond timescale, aiming towards the manipulation and controlling of material properties upon, and depending on the external excitation [42].

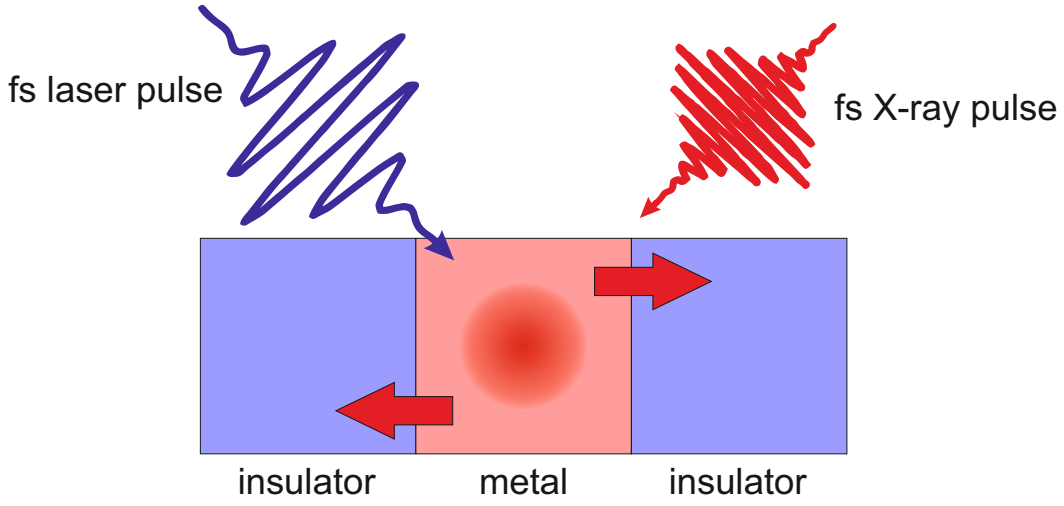

Fig. 2.4.: Schematic representation of the energy flow between single constituents in a metal-insulator heterostructure system after localized optical excitation of the metallic system. Using element-specific fs X-ray absorption spectroscopy as a constituent-specific probe technique, allows to investigate the non-equilibrium processes happening within the constituents of the heterostructure. For more details see text.

Despite the already difficult problem to fully understand the non-equilibrium dynamics in a single component condensed matter system, the focal point of this thesis will be dedicated to the investigation of the laser-induced dynamics in a metal-insulator heterostructure system, as indicated in Fig. 2.4. The multi-component character of a heterostructure introduces new complexity to the non-equilibrium situation, namely the factor of interface vs. bulk effects as well as local vs. non-local dynamics, i.e., the energy transfer between the different constituents [42]. Even though it first seems like that the investigation of the non-equilibrium situation in such a heterostructure might be, at the current state of research, not the most profitable, the analysis of the electron and lattice dynamics in such a material is actually highly welcome, especially if such a study is specific to the constituents itself, and their interfaces. Consequently, using element-specific fs X-ray absorption spectroscopy (cf. chap. 2.2) as a local probe technique is one key feature for the presented experiments of this thesis.

Both aspects alone, the understanding of the energy redistribution within one constituent, as well as the energy transfer across the interfaces, are challenging themselves. That is why, a localized optical excitation of exclusively the electronic subsystem of the metal constituent, is another crucial point of the presented experiments of this thesis, to limit the possible pathways of the energy redistribution (cf. chap. 4.2 for more details of the actual excitation scheme) in the heterostructure.

As I depicted above, the local energy transfer from the optically excited electrons in the metal to the phonon subsystem of the metal can (with certain limitations) be described in the framework of the 2TM (cf. Fig. 2.1). The non-local energy transfer to the insulator on the other hand requires either a purely electronic-mediated process, i.e., a direct charge transfer from the hot electronic system of the metal to the conduction band of the insulator; or a phononic-mediated process, e.g., either the direct coupling of hot, thermalized electrons in the metal to phonons in the insulator, or a coupling of these hot electrons to bulk phonons in the metal, which subsequently couple to phonon modes in the insulator. The non-local electron-phonon energy transfer process can be classified into an extended version of the 2TM, including the coupling between the electronic and lattice sub-systems, phonon-phonon coupling contributions, and even cross-interfacial coupling between hot electrons in the metal to interface vibrational modes [43, 44], which has been reported to be crucial as long as the electron and phonon subsystem are not in equilibrium with each other [45–47]. However, as I stated above, the quantitative analysis within the 2TM requires the assumption of a thermal phonon distributions in both constituents. Since, this assumption is already highly questionable for an accurate description of the ultrafast dynamics in a single constituent [20, 21, 31, 48], it will be presumably not suitable for a true quantitative analysis of a sub-ps non-local energy transfer. On the other hand, the phonon-phonon transfer mechanism from the metal to the insulator constituent is distinctively different from the electron to phonon redistribution process of the 2TM, and can be assigned best to the diffuse mismatch model (DMM) [49]. In the DMM, the energy transfer across the interface is driven by a temperature gradient, which can be described in terms of thermal boundary conductance, or Kapitza resistance [50]. The DMM can be extended to include also optical phonos [51], inelastic scattering [43, 52], and interface roughness [53]. It was found that the especially strength of interface bonding as well as phonon dispersion and population are crucial for the energy transfer across the interface [49]. The typical timescale of the energy transfer mechanism associated with the DMM is in the range of 10 ps, and longer [54]. Furthermore, I want to note that the description of the DMM requires the thermalization of the lattice excitation by phonon-phonon coupling, which takes place on similar timescales [20]. Moreover, in the case of a metal-insulator interface, an additional electronic contribution to the Kapitza conductance may become important [55], which can lead to a considerable increase in the energy transfer due to the scattering of electrons with interface vibrational modes [43, 56]. However, the interpretation using the thermal boundary Kapitza conductance implies that the excitations in both layers can be described by thermal distribution functions. Consequently, I want to stress that it is so far not established how the energy transfer across the interface evolves under non-equilibrium conditions, as the description using the DMM or Kapitza conductance depend, similar to the 2TM, on the possibility to associate a temperature to the

respective phonon subsystems. Therefore, as stated above, in this thesis I investigate and clarify the *importance of non-thermal phonons in the energy transfer dynamics* in a metal-insulator heterostructure.

2.1.3 Ultrafast magnetization dynamics

In the research area dedicated to the laser-induced ultrafast dynamics in condensed matter, the segment focused on the ultrafast magnetization dynamics has developed into its own fascinating research topic in both, the magnetism and the ultrafast community. Starting with the very first discovery of sub-picosecond demagnetization in 1996 by Beaurepaire et al. [8], the manipulation of magnetically ordered materials by a fs laser pulse became a fundamentally challenging topic with a potentially high impact on future applications in various areas, e.g., spintronics or data storage [9].

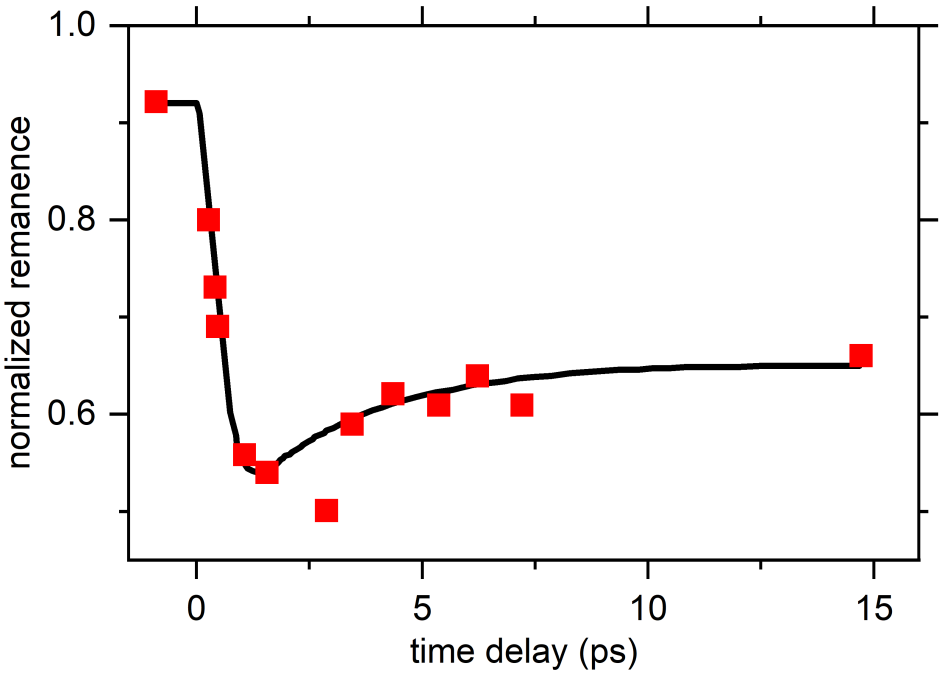

Fig. 2.5.: Pioneering experimental data from Beaurepaire et al. reporting on the very first sub-ps ultrafast loss of magnetic order for a ferromagnetic material, namely a 22 nm Ni film, after excitation with a 60 fs laser pulse. The figure is digitized and redrawn based on [8].

Fig. 2.5 shows the pioneering experimental data from Beaurepaire et al. [8] reporting on the very first sub-ps ultrafast loss of magnetic order for a ferromagnetic material, namely a 22 nm Ni film, after excitation with a 60 fs laser pulse. This experiment started a vast majority of subsequent experiments ranging from confirming these first findings of the ultrafast magnetization dynamics using various experimental techniques [25, 57–62], up to demonstrating further possibilities, i.e., the

magnetization reversal by a single fs laser pulse, the so-called all-optical switching [63–67]. Even though sub-ps demagnetization was found experimentally, next to the first experiments in metal systems, in various kinds of material systems, e.g., semiconductors [68–70], half metals [71–73], heusler systems [72, 74], and dielectrics [75, 76], a complete theoretical understanding of the underlying mechanisms is not fully existing yet [9]. A profound understanding of the ultrafast demagnetization process requires not only the understanding of the interaction of the laser pulse with magnetically ordered matter, and the subsequent redistribution of excess energy within the electron, lattice, and spin subsystems, but also the angular momentum transfer between the latter, which needs to accompany the loss of magnetization. However, in the phenomenological descriptions of the ultrafast dynamics after laser excitation, e.g., the 3TM (cf. eq. 2.1), the transfer of angular momentum is not explicitly included. Furthermore, the 3TM does not directly include any mechanism leading to spin-flips, which are responsible (next to transport mechanisms out of the excited volume, cf. Fig. 2.3) for the observed demagnetization process itself [77]. Moreover, the interpretation and role of fundamental interactions, namely spin-orbit, spin-lattice, and electron-lattice to the ultrafast magnetization dynamics is still subject to debates, which I do not attempt to fully review within the framework of this thesis thoroughly, but can be found elsewhere, i.e., see [9].
Here, I want to point out only one crucial aspect in this debate: The vast majority of experiments reporting on laser-induced ultrafast dynamics in condensed matter, specifically those focused on the entailed ultrafast magnetization dynamics, include a spin-dependent electronic excitations, followed by a lattice excitations. However, the actual role of lattice excitations in the ultrafast demagnetization process remains unclear. There exist three main microscopic models, to describe the underlying microscopic origin of the ultrafast demagnetization, which all explicitly take the transfer of spin angular momentum during the loss of magnetization into account. It is distinguished between, first, the so-called microscopic three-temperature model (M3TM), based on *phonon-mediated* Elliot-Yafet-like electron-phonon spin-flip scattering events [62, 78, 79]. Second, the competing model of (superdiffusive) spin-dependent charge transport [36, 60, 80–82], which describes the demagnetization process being driven by (superdiffusive) spin-dependent charge transport out of the excited volume, and therefore does not need a channel for the transfer of angular momentum, since spin-flip processes are not required in this model. And third, a model also based on spin-flip mechanisms, which do not require the excitation of phonons but are mediated by spin-orbit coupling on the < 100 fs timescale [83–85]. Moreover, it has been reported that coherent lattice excitations, namely transverse strain waves, can result from the angular momentum change during the ultrafast demagnetization process [86]. Therefore, one big key question remains: Are incoherent lattice excitations, which will ultimately lead to a heating of the sample on longer timescales, required to achieve a significant degree of ultrafast loss of mag-

netization? To address this question, one has first to disentangle the laser-induced dynamics of each individual subsystem, to establish a clear relation between the dynamics of the phonon subsystem, especially of the corresponding lattice heating, and the magnetization dynamics. Second, one has to suppress any contributions to the ultrafast demagnetization due to spin currents, which can be achieved by using a heterostructure system (cf. chap. 2.1.2), consisting of thin ferromagnetic constituents embedded between insulating constituents. In summary, conducting a *systematic investigation of the various local and non-local dynamics induced in the metal-insulator heterostructure* system after fs laser excitation, as it will be presented in this thesis in chap. 4.4, *will give insight into the microscopic origin of the fs demagnetization process*. In particular, if one can achieve a significant degree of demagnetization of the ferromagnetic material on the electronic timescale, and therefore identifying the role of phonon excitation to it.

2.2 X-ray absorption spectroscopy

X-ray absorption spectroscopy (XAS) is a versatile tool to analyze the local electronic structure, the magnetic properties, or the chemical environment of condensed matter in an element-specific and orbital-sensitive way [87]. For this thesis, especially the element-specific character of XAS is crucial for a profound investigation of the dynamics happening in the heterostructure system after laser excitation, since a constituent-specific probe technique is mandatory to truly disentangle the possible local and non-local relaxation mechanisms (cf. chap. 2.1.2).
Generally, XAS can be divided in the X-ray absorption near-edge structure (XANES), tens of eV around the X-ray absorption edge, and the extended X-ray absorption fine structure (EXAFS) techniques, up to several hundreds of eV above the edge. Both techniques are based on the energy-dependent absorption of X-ray photons. Therefore, I start in the following with the basic understanding of the interaction of X-ray photons with condensed matter, and the element-specific characteristic of XAS in general.

2.2.1 Interaction of X-rays and matter

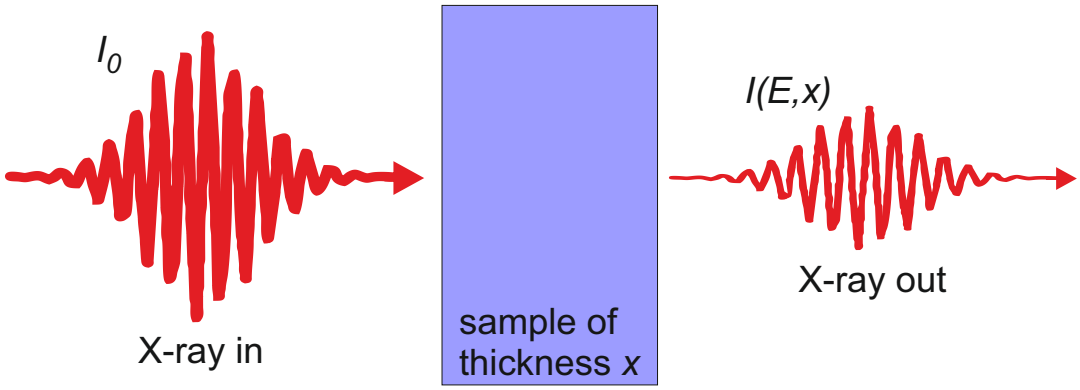

Fig. 2.6.: Schematic representation of the Beer-Lambert law, describing the attenuation of the initial X-ray intensity upon transmission through a sample of the thickness x, and attenuation coefficient $\tilde{\mu}(E)$.

When X-ray radiation traverse matter, the initial X-ray intensity I_0 is attenuated in the material. The X-ray intensity upon transmission through a sample of the thickness x with an attenuation coefficient $\tilde{\mu}(E)$ is described by the Beer-Lambert law:

$$I(E,x) = I_0 \cdot \mathrm{e}^{\tilde{\mu}(E)\cdot x}, \tag{2.3}$$

resulting in an exponential decay of the initial X-ray intensity [88, 89]. The attenuation coefficient $\tilde{\mu}(E)$ is energy-dependent and is made up of contributions of absorption, as well as elastic Rayleigh and inelastic Compton scattering (and

pair production if the photon energy is $1.022\,\mathrm{MeV}$ or higher). However, for soft X-ray energies, which are exclusively used within this thesis, the elastic and inelastic scatter contributions are negligible. Hence, the attenuation coefficient $\tilde{\mu}(E)$ can be replaced solely by the absorption coefficient $\mu(E)$. The effective cross section of the absorption process $\sigma(E)$, which is defined as the number of photons absorbed per atom divided by the number of incident photons per unit area, is connected with the absorption coefficient over the atomic number density n: $\sigma(E) = \mu(E)/n$ [87].
In the simplest picture to describe the X-ray absorption process, the X-ray photon transfers its energy to a core electron which becomes excited into an unoccupied electronic state. In more detail, a X-ray photon of energy E can be absorbed by exciting an electron from an initial state $|i\rangle$ with the energy E_i, into a continuum of empty final states $\langle f|$ with the energy E_f and state density $\rho_f(E_f)$. The cross section of the absorption process $\sigma(E)$ is given by the transition probability $\Gamma_{i\to f}$ between the initial and final state, and the photon flux F_{ph}:

$$\sigma(E) \propto \mu(E) = \frac{\Gamma_{i\to f}}{F_{ph}}.$$

This description assumes that the excited electron is in an effective potential of the other electrons and atomic cores (so-called one-electron approximation) and that the transition happens quickly enough (so-called sudden approximation), that the other electrons cannot rearrange themselves and the effective potential remains the same during the transition [87].
The transition probability per unit time $\Gamma_{i\to f}$ for the excitation of an electron between the initial and final state is given by Fermi's golden rule:

$$\Gamma_{i\to f} = \frac{2\pi}{\hbar} \left| \left\langle f \left| \hat{H}_{int} \right| i \right\rangle \right|^2 \delta\left(E_i - E_f + E\right) \rho_f(E_f), \tag{2.4}$$

where $\hat{H}_{int}$ is the interaction Hamiltonian which describes the time dependent perturbation of the electron through the incident electromagnetic wave [90, 91]. For the X-ray absorption process this Hamiltonian is given by the product of the momentum operator $\vec{p} = i\hbar\vec{\nabla}$ of the electron and the vector potential $\vec{A}(\vec{r},t) = A_0\,\vec{\epsilon}\,\mathrm{e}^{\mathrm{i}\vec{k}\cdot\vec{r}}$ of the incident electromagnetic wave with the unit photon polarization vector $\vec{\epsilon}$ and the photon wave vector $\vec{k}$.
Furthermore, for photon energies in the soft X-ray regime the dipole approximation can be applied, which assumes that the electric field, which drives the electronic transition, is constant over the atomic volume of the absorbing atom. Effectively, this results in the simplification $\mathrm{e}^{\mathrm{i}\vec{k}\cdot\vec{r}} \cong 1$. According to eq. 2.4 the transition between the initial and final state is, within this approximations, given by the polarization-dependent transition matrix element

$$\mathcal{M} = \left\langle f \left| \hat{H}_{int} \right| i \right\rangle \propto \langle f \left| \vec{r}\cdot\vec{\epsilon} \right| i \rangle . \tag{2.5}$$

In the one-electron picture, the initial state $|i\rangle$ is given by the core electron wavefunction, while the final state $\langle f|$ consists of the valence electron wavefunctions. Hence both states of the electron can be described with the respective principal, orbital and spin quantum numbers in the form $|n, l, m_l, s, m_s\rangle$. Finally, eq. 2.5 results to the so called dipole selection rules, which determine all the allowed optical transitions of the electron between the initial state into the final state with the form $|n, l, m_l, s, m_s\rangle$:

$$\begin{aligned} \Delta l &= \pm 1, \\ \Delta m_l &= 0, \pm 1, \\ \Delta s &= 0, \\ \text{and} \quad \Delta m_s &= 0, \end{aligned} \tag{2.6}$$

with the angular momentum of the incident X-ray photon being $q\hbar$ and $q = 0, \pm 1$ its polarization [87].

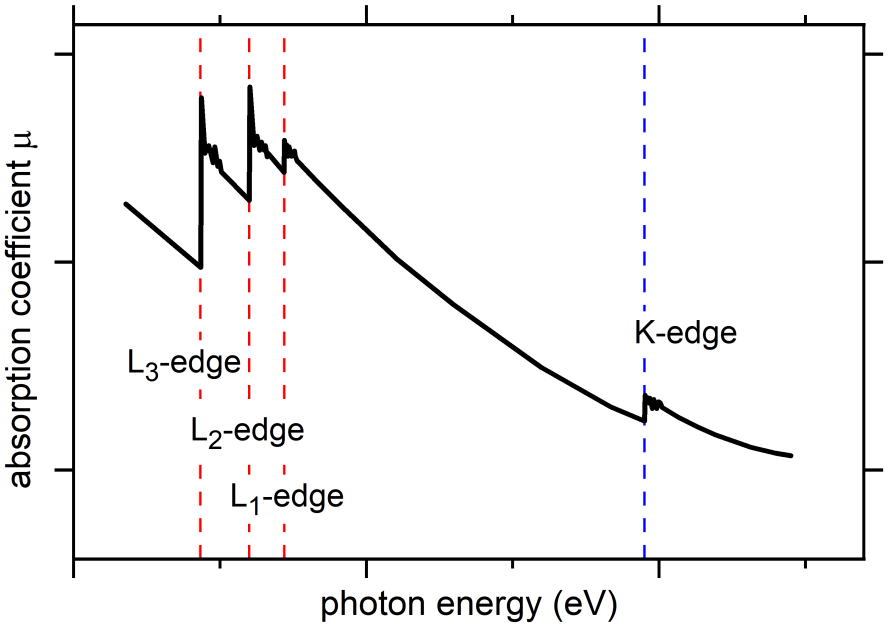

Fig. 2.7.: Schematic exemplary representation of the energy dependence of the absorption coefficient $\mu(E)$ in the region of the L- (red vertical lines) and K- (blue vertical line) absorption edges. For more details see text. The figure is redrawn based on [92].

Fig. 2.7 shows exemplary the energy dependence of the absorption coefficient $\mu(E)$. With increasing X-ray photon energy, the absorption coefficient, or in other words, the absorption cross section, decreases continuously. However, if the photon energy matches the binding energy of a core electron of the absorbent material, the absorption increases drastically. These abrupt changes in $\mu(E)$ are the so-called

absorption edges. Here the photon energy is sufficient to excite the electron in an empty final state $\langle f|$. Depending on the principal and orbital quantum number of the initial state $|i\rangle = |n, l\rangle$ = 1s, 2s, $2p_{1/2}$, $2p_{3/2}$, ... the absorption edges are referred to as K-, L_1-, L_2-, L_3-, ... edge, respectively. Since the binding energy of a core electron is specific for each absorbing atom (and the corresponding subshell), X-ray absorption spectroscopy is a powerful element-specific and orbital-sensitive method. Furthermore, according to the dipole selection rules (see eq. 2.6), from each initial state, only transitions in specific empty final states are allowed, making X-ray absorption spectroscopy a probe-technique specifically sensitive for the electronic state of the probed unoccupied final states. Consequently, XAS can provide element-specific information on the local electronic and geometric structure, chemical surrounding, and the local magnetic properties of the absorbing atom.

2.2.2 X-ray magnetic circular dichroism

X-ray magnetic circular dichroism (XMCD) is one specification of XAS measurements, describing the magnetization-dependent absorption of circularly polarized X-ray photons, which allows to conclude on the magnetic properties of the absorbing atom. The XMCD-effect is a relatively young measurement technique, firstly theoretically proposed 1975 by Erskine and Stern [93], and experimentally verified 1987 by Schütz et al. [94]. However, since its discovery, the XMCD-effect developed to one of the most powerful experimental tools to measure the element-specific magnetic properties of condensed matter. Hereby, especially the applicability of the so-called sum rules [95–99], which allow to disentangle the contributions of the spin and orbital magnetic moments, display one main advantage to other magneto-optic measurement methods.

The origin of the XMCD-effect can be described illustratively in a simple two-step model for the $L_{3,2}$-edges of a 3d-transition metal, i.e., Fe as shown in Fig. 2.8. In the first step, the X-ray absorption step, an incident circularly polarized X-ray photon is absorbed by an electron in the 2p core state, which is spin-orbit split into the $2p_{1/2}$ and $2p_{3/2}$ level. Upon absorption of the right (or left) circularly polarized photon, it transfers its angular momentum $+\hbar$ ($-\hbar$) to the excited electron. The probability if the excited electron from one of the two core levels has either spin up or spin down direction results from a detailed evaluation of the transition matrix element (see eq. 2.5). It turns out that right circularly polarized photons ($+\hbar$) preferentially excite electrons with spin up direction from the $2p_{3/2}$ level (L_3-edge in Fig. 2.8) and electrons with spin down direction from the $2p_{1/2}$ level (L_2-edge). In contrast, left circularly polarized photons ($-\hbar$) preferentially excite electrons

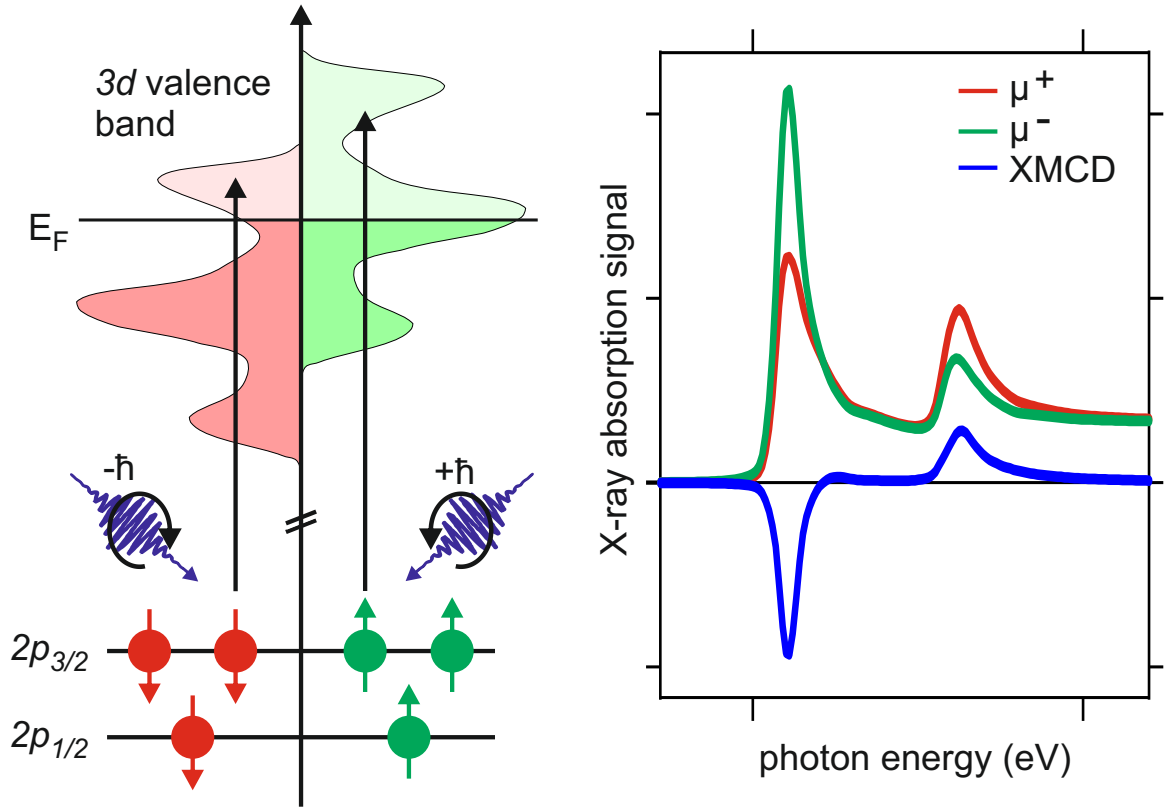

Fig. 2.8.: Left: Schematic illustration of the XMCD-effect in a two-step model for the $L_{3,2}$-edges of a 3d-transition metal. For more detail see text. The figure is redrawn based on [87]. Exemplary absorption spectra of the Fe $L_{3,2}$-edge using right (red) and left (green) circularly polarized X-ray photons, and the corresponding difference spectrum (blue) representing the XMCD-signal. The figure is digitized and redrawn based on [97].

with the opposite spin direction at the two respective edges [87]. In summary, the spin-orbit splitting of the initial state leads to spin-polarized photoelectrons, with opposite spin polarization for the different helicity of the incident X-ray photon as well as with opposite spin polarization for the different spin-orbit coupling ($l+s$ and l-s, respectively) of the two spin-orbit split states $2p_{3/2}$ and $2p_{1/2}$ [100].
In the second step, the photoelectron detection step, the unoccupied 3d final states, which are determined from the 2p initial states by the dipole selection rules (see eq. 2.6), act as a detector for the spin polarization of the excited photoelectrons. According to the dipole selection rule $\Delta s = 0$, the excited photoelectrons cannot change their spin state during the transition. Hence, spin up or spin down electrons can only populate empty 3d spin up or spin down valence states, respectively. However, due to the exchange interaction and the Pauli exclusion principle, the spin up and spin down states are shifted against each other and therefore not equivalently occupied. Consequently, according to Fermi's golden rule (see eq. 2.4) the absorption coefficient $\mu(E)$ is proportional to the density of free states $\rho_f(E_f)$ and therefore different for the different spin polarization at the two edges for the two opposite

helicities, see Fig. 2.8.
The XMCD signal is defined as the difference spectrum of the X-ray absorption spectra for right and left circularly polarized light

$$\Delta\mu(E) = \mu^{+}(E) - \mu^{-}(E), \tag{2.7}$$

and is a direct result of the exchange splitting of the valence band and reflects the resulting imbalance of the nonequivalently filled valence states. The intensity of the XMCD signal I_{XMCD} is not only depending on the pure size of the magnetic moment $|\vec{m}|$, which is reflected directly by the size of the imbalance in the valence states. The XMCD intensity further depends on the angle θ between the directions of the photon angular momentum and the magnetic moment and the degree of circular photon polarization P_{circ}. Hence, the XMCD signal probes only the projection of the magnetic moment direction on the photon spin quantization axis:

$$I_{\text{XMCD}} \propto P_{\text{circ}} \cdot |\vec{m}| \cdot \cos(\theta)$$

Finally, it should be noted that the two major advantages of the XMCD spectroscopy over other magneto-optical methods is its element-specific character as well as the existence of the so-called sum rules for the measured X-ray absorption spectra with the two different helicities. The evaluation of the sum rules [95, 96] allows a quantitative analysis of the spectra to evaluate the contributions of both the spin magnetic moment μ_s per atom and the orbital magnetic moment μ_l per atom to the magnetization. It has been shown that the validity of the sum rules also applies for the highly non-equilibrium states [60, 101]. I want to note that even though I will report on magnetic measurements within the framework of this thesis using the described XMCD-effect (cf. chap. 4.4), I will dispense on any kind of quantitative sum rule analysis, since I am primarily interested in the time-dependent dynamic of the XMCD-signal of the transition metal L_3-edge of the investigated heterostructure. However, since it has been shown that the spin as well as the orbital moment are both decreasing on the relevant timescales of > 100 fs investigated in this thesis [61, 102], the analysis of the L_3-edge dynamic is sufficient to represent full transient demagnetization behavior of the transition metal constituent.

3 Methods: Ultrafast measurements at large scale research facilities

As indicated in chap. 2, Fig. 2.4, the key investigation technique used within this thesis is element-specific femtosecond time-resolved X-ray absorption spectroscopy, to analyze the constituent-specific dynamics of a metal-insulator heterostructure system after localized laser excitation. In particular, I will concentrate on the investigation of the transition metal absorption L-edges and the oxygen K-edge, which are located in the photon energy range between ~ 500 eV and ~ 1000 eV. One crucial aspect to be able to conduct such X-ray spectroscopy measurements is a tunable X-ray source, which provides femtosecond short X-ray pulses, with high (enough) intensity in this photon energy range, which is up to now only given at large scale research facilities, i.e., at synchrotron-based femtoslicing sources [103–111], or at X-ray free-electron lasers (XFEL) [112–119].
To understand the characteristics and peculiarities of the generation of sub-ps short X-ray pulses, necessary to conduct ultrafast time-resolved X-ray absorption measurements, I will show in the following the technological progression of those large scale research facilities, starting from the general questions, what is synchrotron radiation and how does a synchrotron work.

3.1 Synchrotron radiation facilities

3.1.1 What is a synchrotron radiation facility?

The electromagnetic radiation emitted by accelerated relativistic charged particles is called synchrotron radiation (SR). Synchrotron radiation can be naturally emitted by cosmic sources, e.g., in solar flares by stars [120] or supernova remnants like the crab nebula [121], [122]. Artificially, this radiation is produced in electron or positron particle accelerators i.e., circular storage rings. Fig. 3.1 shows a simplified, schematic picture of a synchrotron radiation facility. The charged particles, more specifically electrons, are first accelerated by a linear accelerator (LINAC) until they reach energies on the order of MeV and are then transferred to a booster ring that increases their energy up to GeV. The GeV electrons are injected into the final circular accelerator, the storage ring, where they remain for several hours in a

quasi-stationary situation. The storage ring consists of an array of bending magnets to force the electrons on their circular path, linear sections with radio frequency (RF) cavities to (re-)accelerate the electrons and additional quadrupole magnets to focus and de-focus the electrons. Whenever the electrons are subjected to the magnetic fields of the bending magnets, they lose part of their energy and emit the desired synchrotron radiation. The lost energy is then fully compensated throughout a turn when they pass through the respective RF cavities. Additional insertion devices like wigglers or undulators (described in more detail below), placed in the straight sections of the storage ring, offer further ways to produce synchrotron radiation with improved spectral brightness compared to one produced in the bending magnets. [122, 123]

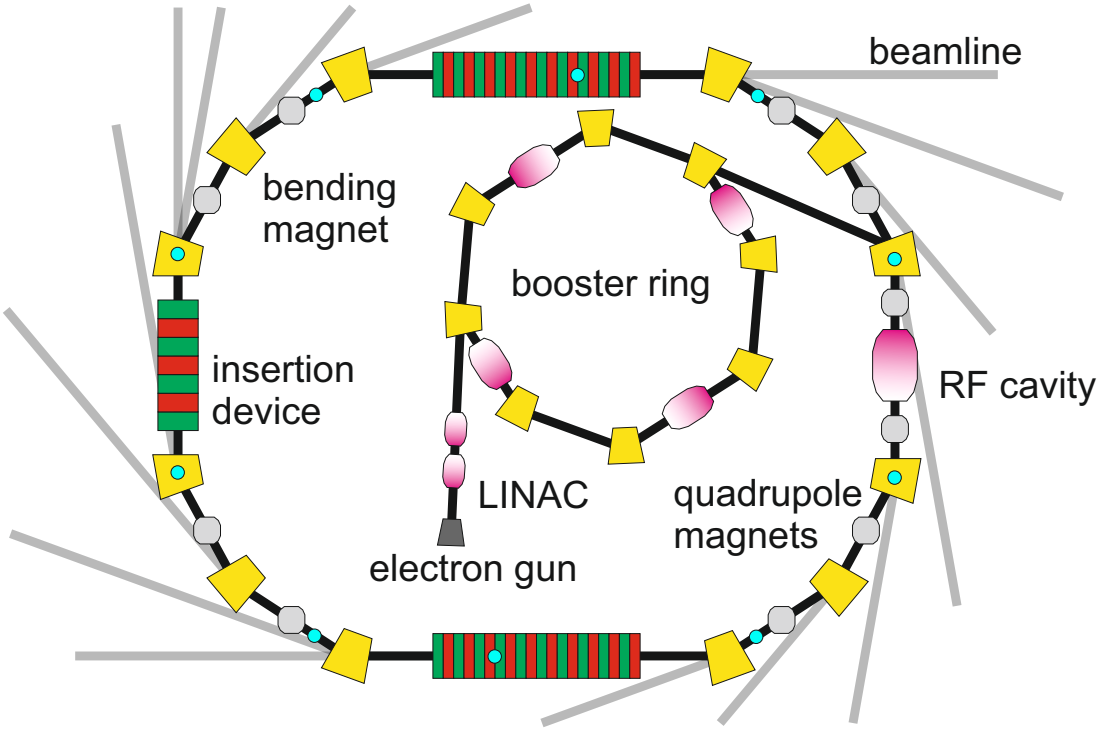

Fig. 3.1.: Schematic, simplified picture of a synchrotron radiation facility consisting of three main parts, the linear accelerator (LINAC), the booster ring and the final storage ring. Furthermore, some of the main elements like bending magnets (yellow), radio frequency (RF) cavities (pink), quadrupole magnets (light grey), additional insertion devices (green-red) and the beamlines are illustrated. The figure is inspired by [122].

Emission pattern of a relativistic moving charged particle

In order to understand the fundamental properties, advantages, and differences of the emitted synchrotron radiation originating from the different sources, namely bending magnets or insertion devices, one has to start from the basic emission patter of a moving charged particle, e.g., an electron. For relativistic effects, which have to be considered for the GeV electrons in the storage ring, the moving speed v of the

electron is close (e.g., $> 99.999\%$ for BESSY II [124]) to the speed of light c, and the electron has an energy of

$$E = \gamma E_0,$$

with $E_0 = m_0 c^2 = 0.511\,\text{MeV}$ being the electron energy at rest, m_0 the electron rest mass, and $\gamma = 1/\sqrt{1 - v^2/c^2}$ the relativistic Lorentz factor. According to the laws of electrodynamics, the charged particle sends out electromagnetic radiation whenever it becomes accelerated. In the inertial system of the electron, the resulting emission pattern is similar to the one of an oscillating dipole, with the maximum intensity of the emitted radiation pointing in the direction perpendicular to the acceleration (see Fig. 3.2, left side). However, in the experiment, the observer receives this emitted radiation in a cone of an opening angle $\pm 1/\gamma$, due to the relativistic Lorentz transformation of the angles from the moving frame of the electron to the laboratory frame of the observer (see Fig. 3.2, right side). According to the transformation, the higher the energy of the electron, the smaller becomes the collimation angle, and therefore the higher is the respective flux of the emitted synchrotron radiation. Consequently, SR is highly collimated, however depending on the actual source inducing the acceleration, some specific parts of this natural collimation can be lost for the observer. In the following, I will discuss in more detail the different types and properties of SR sources, namely bending magnets and insertion devices. [122, 123]

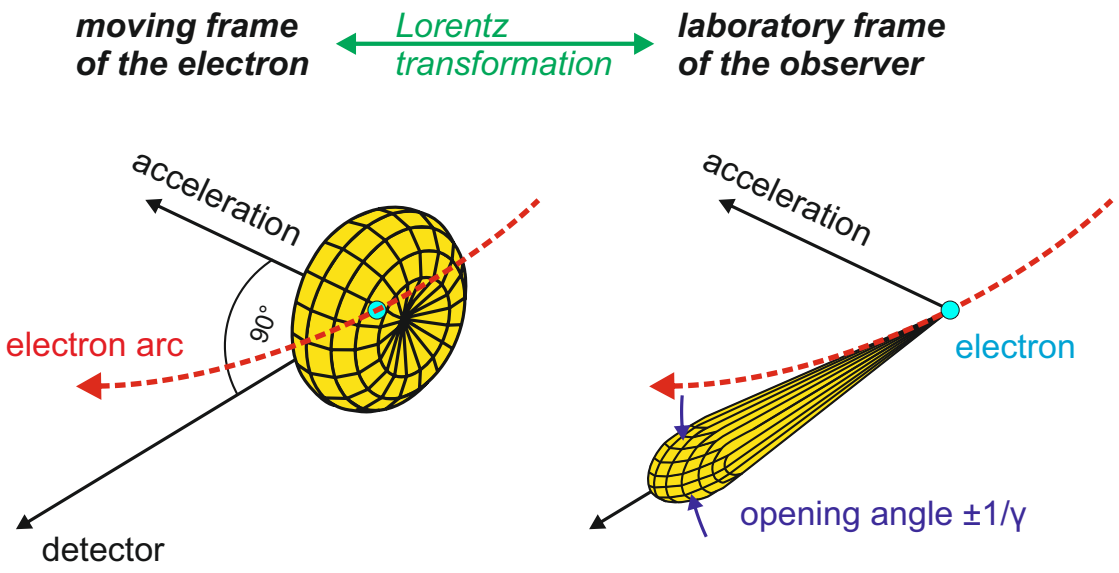

Fig. 3.2.: Qualitative emission patterns of a charged particle, e.g., an electron, moving in a circular orbit. Left side: Seen from the inertial system of the moving electron, the resulting emission pattern is similar to the one of an oscillating dipole. Right side: In contrast, in the laboratory frame of the observer the emitted radiation is distorted into a narrow cone of an opening angle $\pm 1/\gamma$ due to the relativistic Lorentz transformation. The figure is redrawn based on [122, 125].

Synchrotron radiation from bending magnets

Historically, the first available sources for synchrotron radiation have been bending magnets, since they are in any case needed to enable the closed, circular path motion in the storage ring. Concerning its fundamental properties, the SR originating from a bending magnet has a continuous energy spectrum, ranging from the X-rays to the far-infrared region, with a peak wavelength depending on the electron energy and the magnetic dipole field of the corresponding bending magnet. However, the SR from a bending magnet has lost its natural horizontal collimation.

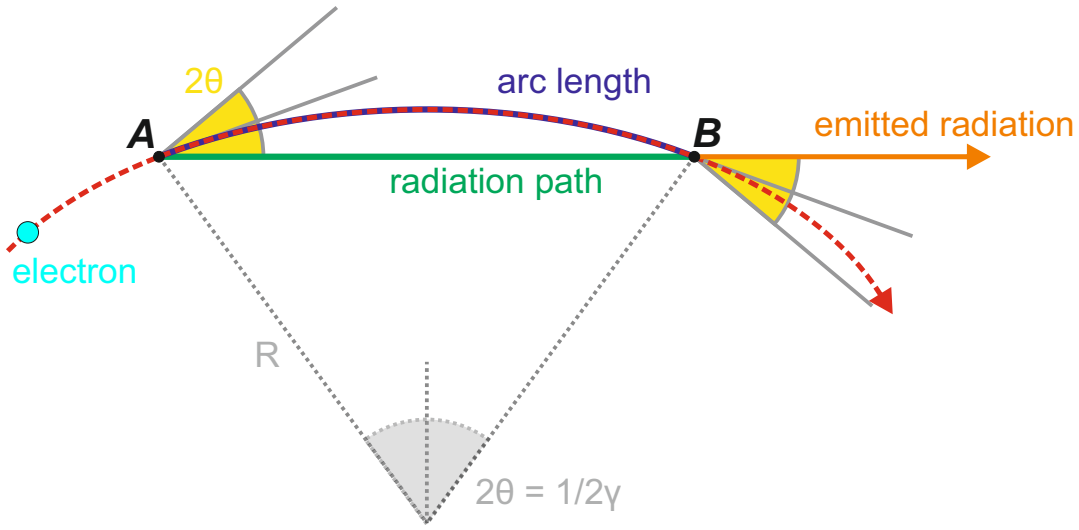

Fig. 3.3.: Visualization of the so-called lighthouse effect, explaining schematically the origin of the lost horizontal collimation, the broad energy distribution and the pulse length of the SR originating from a bending magnet, for more details see text. The point-like observer collects all the SR emitted by the electron along the path of the arc $\Delta\Theta \gg 1/\gamma$ from point A to B. The figure is redrawn based on [122].

The origin of the lost horizontal collimation and the broad energy distribution of a bending magnet can be easily understood by the so-called lighthouse effect [122], visualized in Fig. 3.3. For this let us consider a single electron moving in the storage ring, and a point detector as an observer, who looks tangentially at a specific point of the orbit: When the charged particle, of charge e, is submitted to the magnetic field $\vec{B}$ of the dipole for the time interval τ its movement is described by the Lorentz equation

$$\gamma\, m_0\, \frac{d\vec{v}}{d\tau} = e\, \vec{v} \times \vec{B}.$$

In a uniform magnetic field the trajectory of the electron will then form an arc of a circle with radius

$$R = \frac{m_0\, \gamma\, v}{e\, B}.$$

In the experiment, the point detector like observer, placed on-axis, collects all the radiation emitted by the electron along the path of the arc $\Delta\Theta \gg 1/\gamma$ from point

A to B (see Fig. 3.3). The radiation is summed incoherently, and the horizontal collimation is lost, while the natural collimation in vertical direction is preserved.

The pulse duration Δt_{SR} of the observed synchrotron radiation originating from a bending magnet is given by the difference of the time t_e the electron needs to travel trough the orbital arc $\Delta\Theta$ and the time t_{ph} the emitted radiation from the starting point of the arc needs to travel along the chord subtended by the arc (see Fig. 3.3):

$$\Delta t_{SR} = \frac{\text{arc length}}{v} - \frac{\text{radiation path}}{c} = \frac{2\,R\,\Theta}{v} - \frac{2\,R\,\sin(\Theta)}{c} \approx \frac{4\,R}{3\,c\,\gamma^3}$$

Hence, the SR coming from the bending magnet results in a short signal pulse duration, which is in the order of $50\,\text{ps}$ for BESSY II. This in turn corresponds, according to the Fourier-theorem, to a broadband frequency spectrum, given by the so-called typical frequency

$$\omega_{typ} = \frac{2\,\pi}{\Delta t_{SR}} = \frac{3\,\pi\,c\,\gamma^3}{2\,R}.$$

Further, one defines the so-called critical frequency

$$\omega_c = \frac{\omega_{typ}}{\pi} = \frac{3\,c\,\gamma^3}{2\,R},$$

from which derives the critical wavelength or critical energy

$$\lambda_c = \frac{2\,\pi}{\omega_c} = \frac{4\,\pi\,R}{3\,\gamma^3},$$
$$E_c = \hbar\,\omega_c = \frac{3\,\hbar\,c\,\gamma^3}{2\,R},$$

of the storage ring. The critical energy divides the energy spectrum of the emitted synchrotron radiation into two parts of equal power, meaning that 50 % of the total power is radiated at energies smaller than E_c and 50 % at energies higher than E_c. Since E_c only depends on the machine parameters of the synchrotron, namely the magnetic field of the bending magnet (typically in the order of $1\,\text{T}$ and similar for all storage rings) and the energy of the circulating electrons, storage rings are characterized by the energy of the circulating electrons. The higher the energy of the electrons, the higher the peak photon energy of the ring. For modern rings, typical electron energies range from 2 to $8\,\text{GeV}$, resulting in peak photon energies ranging from a few keV to $50\,\text{keV}$ and more [126].

Another widely used concept to define and compare different synchrotron light sources is the so-called brilliance, which acts as the figure of merit for many experi-

ments. The brilliance of the source is defined as the number of emitted photons per second in a narrow energy bandwidth (usually $0.1\,\%$ BW) per unit solid angle

$$\text{brilliance} = \text{number of photons} \,/\, \text{s} \,/\, \text{mrad}^2 \,/\, \text{mm}^2 \,/\, 0.1\,\%\ \text{BW}. \tag{3.1}$$

In contrast to the flux, which measures the total intensity of the radiation, integrated over the total accepted solid angle, the brilliance takes the collimation of the emitted radiation into account. Although bending magnets can be sources of synchrotron radiation with very high flux, in terms of brilliance, one can archive several orders of magnitude higher values by using insertion devices, particularly undulators. [127]

Synchrotron radiation from insertion devices

Synchrotrons of the so-called third-generation use, next to bending magnets as described above, insertion devices like wigglers and undulators, which are placed in the straight section of the storage ring to produce the SR used in the experiment. Both wigglers and undulators consist of a periodic structure of dipole magnets with alternating polarity, generating an alternating static magnetic field. Electrons passing through such a magnetic field perform an oscillating motion around the straight path and therefore emit radiation during each wiggle (see Fig. 3.4). One defines the wiggler- or undulator parameter

$$K = \frac{\lambda_u \, e \, B}{2 \, \pi \, m_0 \, c},$$

where λ_u represents the period of the magnetic field, and derives from this the wiggling-angle of the trajectory

$$\Theta_w = \frac{K}{\gamma},$$

which is used to classify between the wiggler and the undulator regime.
In the wiggler regime $K > 1$ (see Fig. 3.4, top half), the wiggling-angle Θ_w is large with respect to the natural emission angle $1/\gamma$. The emission cones of each wiggle do not overlap and superpose incoherently. Therefore, the emitted synchrotron radiation of a wiggler can be treated as the sum of a series of bending magnets, which enhances the overall intensity simply by summing the contributions of the individual poles. Hence, also a wiggler emits synchrotron radiation over a wide spectral range, like a bending magnet, but with higher intensity. More precisely, the intensity in a wiggler increases with $2\,N$ compared to a simple bending magnet, with N being the number of period lengths λ_u. Moreover, the critical energy of the wiggler radiation is compared to the bending magnet shifted to higher values due to the higher magnetic fields. The horizontal collimation, similar to the case of the bending magnet, remains lost. [122, 123]

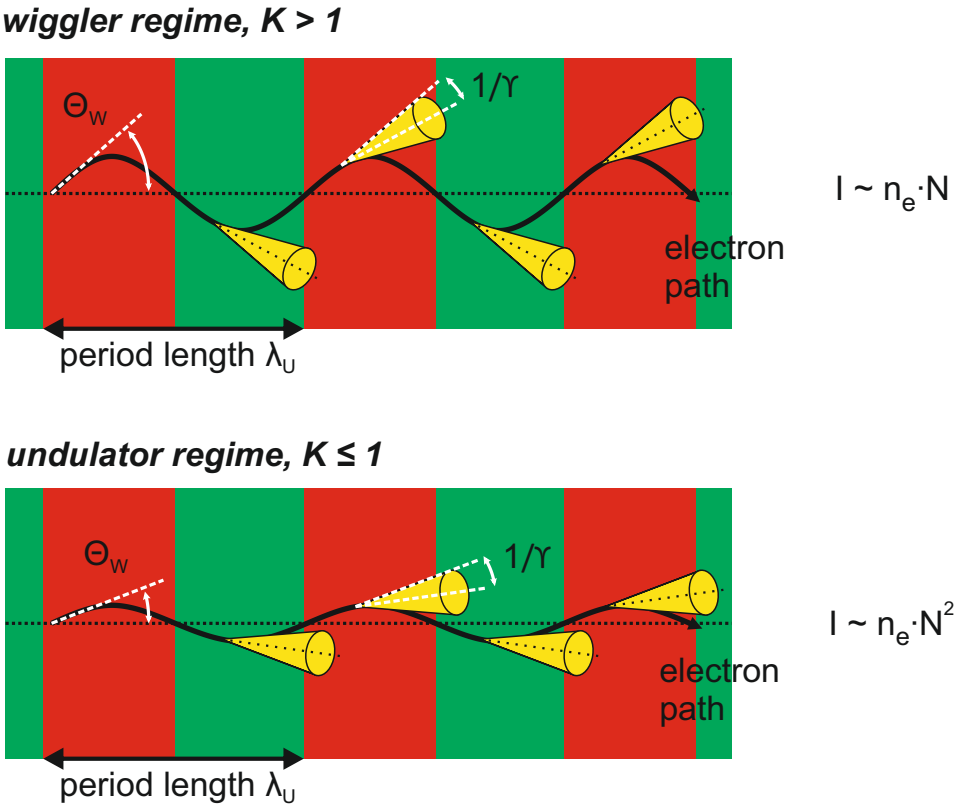

Fig. 3.4.: Schematic representation of insertion devices, i.e., wigglers and undulators, consisting of a periodic structure of dipole magnets with alternating polarity, generating an alternating static magnetic field. Top half: In the wiggler regime the wiggling-angle Θ_w is large with respect to the natural emission angle $1/\gamma$. Bottom half: In the undulator regime the wiggling-angle is smaller than the natural emission angle and the emission cones from the different poles are overlapping. The dependence of the total intensity I of the emitted radiation on the number N of period lengths λ_u and on the number of electrons n_e for both regimes is indicated. The figure is redrawn based on [122].

In the undulator regime $K \leq 1$ (see Fig. 3.4, bottom half), the wiggling-angle Θ_w is smaller than the natural emission angle $1/\gamma$. The emission cones from the different poles overlap. Hence, the radiation emitted by the electrons at different points of the path superpose coherently, and interference occurs. By considering the phase differences between the photons emitted at the different points of the trajectory, one observes constructive interference at wavelengths λ_{SR} in the direction of an angle θ with respect to the axis of the undulator when the undulator condition is fulfilled [128]:

$$\lambda_{SR} = \frac{\lambda_U}{2\,\gamma^2}\left(1 + \frac{K^2}{2} + \gamma^2\,\theta^2\right). \tag{3.2}$$

In addition to this fundamental wavelength λ_{SR}, higher harmonics with a shorter wavelength of $\lambda_{SR,n} = \lambda_{SR}/n$ are emitted. I want to note that on the undulator axis ($\theta = 0$), only odd harmonics are emitted. Due to the dependence of λ on $K^2 \sim B^2$, one can easily tune the photon energy by changing the gap between the upper and

lower arrays of dipole magnets mechanically. Due to the coherent superposition of the radiation emitted by each period of dipole magnets, the intensity of the synchrotron radiation in an undulator increases with N^2. [122]
The opening angle σ of the emission cone of the n-th harmonic is for horizontal and vertical direction approximately

$$\sigma \approx \frac{1}{\gamma}\frac{1}{\sqrt{n\,N}},$$

and therefore, always smaller than the natural emission angle $1/\gamma$ [122].
Recapitulating, the constructive interference of the different emission cones leads to a very small collimation of the emitted synchrotron radiation which, combined with the strong dependency of the intensity with N^2, leads to several orders of magnitude higher spectral brightness of the undulator radiation compared to radiation from a bending magnet or wiggler.

Moreover, I note that the synchrotron radiation produced by bending magnets is solely linearly polarized in its horizontal plane. Only by observing the radiation at finite vertical angles above or below the horizontal plane, the radiation is partially right or left elliptically polarized. In contrast, with both insertion devices, namely the wiggler and undulator, it is possible to generate on-axis elliptically polarized synchrotron radiation by forcing the electrons to wiggle not only in the horizontal plane but also in the vertical plane. Hence, by suitable tuning the mechanical properties of the insertion device, one can switch during the experiment between vertical and horizontal linear polarized radiation, and left and right elliptical (or circular) polarization. This ability of generating a high degree of left and right circular polarization with a single insertion device is especially of interest when measuring magnetic properties of the sample, i.e., by the X-ray magnetic circular dichroism (cf. chap. 2.2.2).

3.1.2 Synchrotron-based femtoslicing sources

As described above, the electrons circulating in the storage ring emit synchrotron radiation whenever they move through a bending magnet or pass through an insertion device. Consequently, the electrons lose a part of their kinetic energy gradually. However, to keep the electrons for every turn at constant energy and thus for several hours inside of the storage ring, with each turn, one has to restore the kinetic energy, which is lost by the emission of radiation. For this, the electrons pass through radio frequency (RF) cavities, where a longitudinal electrical field accelerates the electrons and reestablish their energy. Electrons arriving too early or too late, with respect to the RF period, in the cavity will be lost. Hence, given the period of the

radiofrequency cavities, in the normal operation of a synchrotron, the electrons can not be continuously distributed inside the storage ring, but are divided into electron bunches. The minimum possible separation time of two electron bunches is equal to the radio frequency period, which is typically in the order of ns. Furthermore, due to the coulomb interaction of the electrons with each other, electrons in a single bunch can not be compressed infinitely, but have a certain spacial expansion of typically $1\,\mathrm{cm}$. As a consequence, the electron bunches in the storage ring emit X-ray pulses with a certain pulse length on the order of $\sim 50\,\mathrm{ps}$ (for the synchrotron BESSY II [104]). Hence, a synchrotron is not a continuous but a pulsed X-ray source with picosecond long X-ray pulses separated by nanoseconds [122].

In 1996, Zholents and Zolotorev [103] first proposed the idea of the so-called femtoslicing, to produce at a synchrotron X-ray pulses with a pulse length of only a hundred femtoseconds. The proposed method was the following: An intense femtosecond laser pulse co-propagates with one selected electron bunch in the storage ring. By interaction of the electric field generated by the laser pulse with a small part of the electrons in the bunch, the femtosecond laser pulse modulates their energy. As a consequence, the energy modulated electrons can be spatially separated from the main bunch and subsequently generate the short X-ray pulses, with a pulse length approximately given by the pulse length of the laser pulse itself. Hence, it can be said that the femtosecond laser pulse cuts out a fs-slice of the electron bunch, from which originates the name femtoslicing. The idea of femtoslicing was first realized at the advanced light source (ALS) synchrotron in Berkeley, USA, utilizing a bending magnet to produce $300\,\mathrm{fs}$ short X-ray pulses [111]. In 2004, the first undulator based source to produce sub-ps soft X-ray pulses with tunable polarization was commissioned at the synchrotron BESSY II in Berlin, Germany [105, 106, 108]. Shortly after, in 2006, the first hard X-ray undulator source at the synchrotron SLS in Villigen, Switzerland, followed [129]. [130]
In the following, the working mechanism of the soft X-ray femtoslicing source at BESSY II will be described in detail, since all the time-resolved X-ray absorption data shown throughout chap. 4 have been measured at this specific source.

The femtoslicing source at the synchrotron BESSY II

At the synchrotron BESSY II, the femtoslicing setup is implemented at the UE56/1-PGM and -ZPM beamlines. The femtoslicing scheme is localized at only one specific arrangement of two insertion devices of the storage ring. It runs without disturbing the generation of X-ray pulses at other insertion devices of the synchrotron. Fig. 3.5 shows the femtoslicing source schematically, which is described in the following: The femtoslicing setup consists of three main parts. First, the planar undulator U139

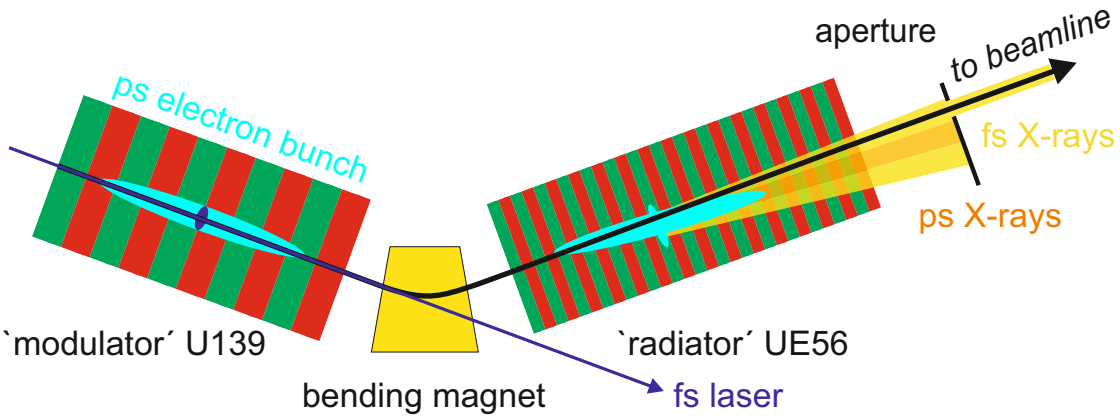

Fig. 3.5.: Schematic representation of the femtoslicing setup implemented at the UE56/1 beamline of the synchrotron BESSY II: An intense femtosecond laser pulse co-propagates with an electron bunch in the planar undulator U139 ("modulator") and modulates the energy of a small slice of the electrons. The subsequent bending magnet spatially separates the energy modulated electrons from the main bunch, followed by generation of the fs X-ray pulses in the undulator UE56 ("radiator"). The aperture dumps the residual ps radiation to use solely the fs radiation in the experiment. The figure is redrawn, based on [104, 130].

here called the modulator, where the energy modulation takes place. Second a bending magnet, and third the elliptical undulator UE56/1, here called the radiator, where the fs X-ray pulses used in the experiment are generated. In the modulator, the femtosecond laser pulse co-propagates with the electron bunch and modulates the energy of a small slice of the electrons. For the energy modulation the laser pulse and the electron beam have to be in spatial and temporal overlap, as well as fulfill a certain resonance condition, namely that the laser wavelength λ_L is equal to the undulator condition for constructive interference (see eq. 3.2, for $\theta = 0$):

$$\lambda_L = \lambda_{SR} = \frac{\lambda_U}{2\,\gamma^2}\left(1 + \frac{K^2}{2}\right). \tag{3.3}$$

Due to the modulated energy, the sliced electrons will take a slightly different path through the bending magnet than the main electron bunch and arrive, therefore, also spatially separated in the subsequent radiator. As a consequence, also the X-ray pulses radiated by the energy modulated electrons are slightly spatially separated from the X-ray pulses emitted by the main electron bunch. With an aperture placed behind the radiator, it is now possible to dump away the X-rays originating from the main bunch and use in the experiment only the short X-ray pulses from the sliced electrons (which only works really effectively when the fs pulses are on the radiator axis, see below). The pulse length of the X-rays is mainly given by the pulse length of the fs laser pulse. Taking additionally slippage of the electrons with respect to the laser field, path length differences of the electrons between modulator and

radiator, and temporal broadening due to the monochromator grating into account, the X-ray pulses usable in the experiment have a resulting pulse length of down to 100 fs. [130]

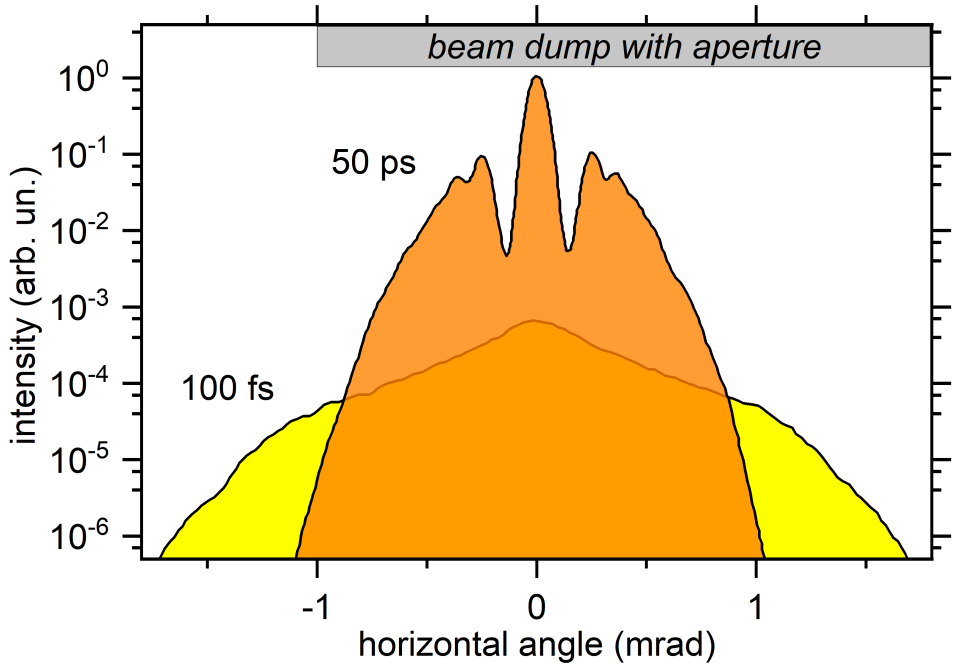

Fig. 3.6.: Quantitative comparison of the intensity of the off-axis 100 fs X-ray pulse originating from the sliced electrons and the on-axis $\sim$ 50 ps X-ray pulse originating from the main electron bunch: The intensity of the fs X-rays is several magnitudes smaller than for the ones from the main bunch, which are dumped by the aperture in order to use in the experiment only the fs short X-ray pulses. The figure is digitized and redrawn, based on [104].

Only a small part of the electrons from the electron bunch generate the fs X-ray pulse. Since the intensity of the emitted radiation is proportional to the number of electrons, the short pulse duration comes with a substantial loss of intensity compared to the ps X-ray pulse produced by the whole electron bunch. Fig. 3.6 shows an exemplary comparison of the intensity of the off-axis 100 fs X-ray pulse and the on-axis $\sim$ 50 ps X-ray pulse. It is directly visible that the intensity of the radiation generated by the femtoslicing technique is several magnitudes smaller than the one originating from the main bunch. Consequently, the separation of background radiation is crucial for the fs time-resolved experiments. Moreover, and most likely one of the biggest disadvantage of the femtoslicing scheme, is the time necessary for data acquisition with a reasonable signal to noise ratio. While the latter will be addressed, especially in chap. 3.2, and in chap. 5, the issue with the background radiation will be shortly discussed in the following.

The main contributions to the background radiation consist of two parts, namely the so-called halo and the residual ps radiation. Firstly, the residual ps radiation is generated by the bending magnet located between the modulator and radiator and by the radiator itself. However, by suitable positioning of the beamline, one

can ensure that the ps radiation is not radiating into the endstation and hence not affecting the experiment. Furthermore, by a local adjustment of the electron orbit in the storage ring, the so-called femtobump, one can push the sliced electrons onto the radiator axis. With the femtobump activated, the fs X-rays are now generated on-axis while the main bunch ps X-rays are pushed off-axis and can be blocked more effectively by the aperture. Thereby, the fs X-rays with femtobump "on" will take the same path as the ps X-rays with femtobump "off", which allows to easily switch between normal operation mode and slicing mode at the beamline without any changes of the beamline or monochromator settings. This makes it much easier to deal with the issue of the residual background radiation when changing between the different operation modes of the beamline.
Secondly, the so-called halo is caused when the sliced, off-axis electrons relax on-axis, which is accompanied by increased emittance of radiation. The relaxation of the energy modulated electrons lasts typically about 1 ms. Since one has to synchronize the fs laser pulse via a master clock with the electron bunches, primarily always the same electron bunch in the storage ring was used for the femtoslicing process. But this turned out to be problematic when increasing the repetition rate, because the halo contribution to the background radiation increases with the repetition rate of the fs laser. In order to counteract this, the so-called sequence femtoslicing mode was introduced. Here, the synchronization of the fs laser with the master clock is modulated in such a way, that the fs X-ray pulses are not generated from the same electron bunch in the storage ring, but generated alternating from three electron bunches, separated by 12 ns, which effectively gives the electrons in one bunch more time to relax and subsequently keeps the halo contribution on an acceptable level [110].

The laser pump X-ray probe setup

The femtoslicing scheme enables, with its source of fs short X-ray pulses, to measure non-equilibrium dynamics by using a laser pump X-ray probe setup, which is schematically shown in Fig. 3.7. The whole laser pump X-ray probe setup consists of the femtoslicing source described above (cf. Fig. 3.5), and two laser hutches for the amplifier lasers generating the fs X-ray pulses and to induce the pump-induced dynamics in the sample, respectively. The femtoslicing setup is implemented at the undulator UE56, enabling two beamlines, namely UE56/1-PGM and UE56/1-ZPM, at the synchrotron BESSY II to exploit the emitted SR of the respective insertion device. At both beamlines, the fs X-ray pulses, as well as the ps X-ray pulses from the main bunch, can be used for the experiment. However, the -PGM beamline with its plane grating monochromator (PGM) and the -ZPM with its zone plate monochromator (ZPM) are not equally suited for all time and energy resolutions. While the ZPM is specially designed for femtosecond time-resolved measurements,

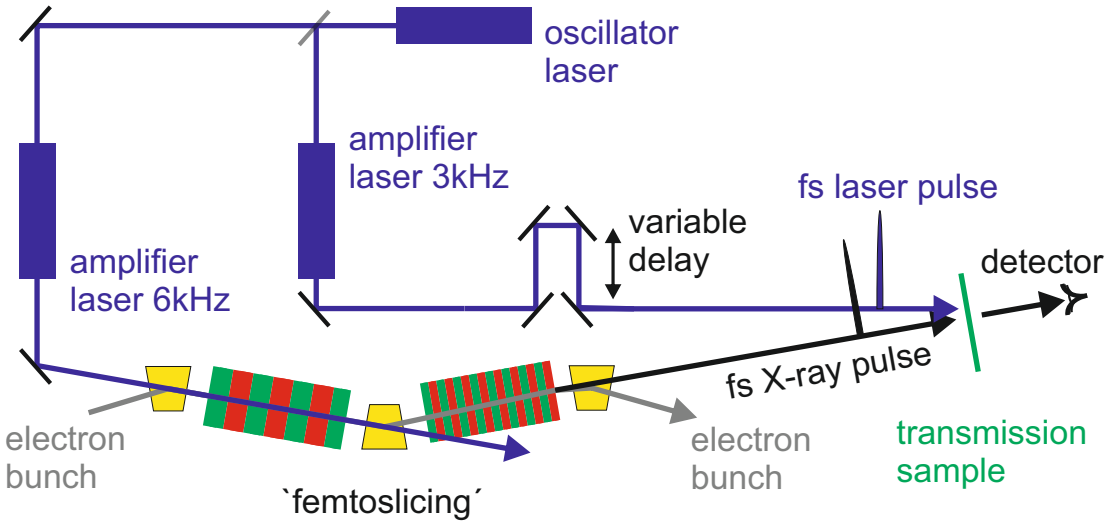

Fig. 3.7.: Schematic representation of the laser pump and X-ray probe setup used to measure non-equilibrium fs time-resolved dynamics at the UE56/1 beamline of the synchrotron BESSY II. The setup consists of the femtoslicing source (cf. Fig. 3.5) and an oscillator laser which drives both, the amplifier lasers to generate the fs X-ray pulses and to induce the pump-induced dynamics in the sample. By using the same oscillator laser in order to seed both amplifier lasers, one enables a intrinsic jitter-free synchronization between the fs laser pump and the fs X-ray probe pulses. The figure is redrawn, based on [104, 109, 130].

keeping the total X-ray pulse length at 100 fs after the monochromator, the design leads to a reduced energy resolution and a larger focus size compared to the PGM. On the other hand, the PGM design is optimized for high(-er) energy resolution, but not perfectly suitable for femtoslicing mode, since the X-ray flux becomes even further reduced due to reflection losses at the optical elements. Additionally, when using fs X-ray pulses at the PGM beamline, the standard 1200 lines/mm grating used for static spectroscopy, would cause substantial, unwanted pulse lengthening. Hence, at the ZPM, designed for fs X-ray pulses, a grating with only 150 lines/mm is used, which unfortunately decreases the possible energy resolution of the beamline. Concluding, the ZPM is used for measurements where the focus lies on the optimal time resolution if the moderate energy resolution of $E/\Delta E = 500$ is sufficient enough for the experiment. In contrast, the PGM is used especially when the focus lies on the energy resolution. [130]

All the time-resolved XAS measurements shown in chap. 4 are done at the -ZPM beamline. In the following, I will focus exclusively on the parameters of this specific beamline if not noted otherwise. Tab. 3.1 summarizes the most important properties of UE56/1-ZPM used for the measurements presented in chap. 4. The possible energy range of the X-rays covered by the monochromator is 410-1330 eV with an energy resolution $E/\Delta E$ of 500 for both, fs and ps X-ray pulses. In detail,

Energy range	[eV]	410-1330	
Energy resolution	[E/ΔE]	500	
Polarisation	-	linear vertical or circular	
Laser photon energy	[nm]	266	800
Laser pulse length	[fs]	70	50
Laser spot size	[μm^2]	160×300	310×440
Laser pump fluence	[,mJ/cm^2]	8 to 25	20
X-ray pulse length	[fs]	100	
X-ray spot size	[μm^2]	50×100	

Tab. 3.1.: Parameters for the time-resolved XAS measurements shown in chap. 4.

the presented measurements have been conducted in the vicinity of the O K-edge (≈ 540 eV) an the Fe L_3-edge (≈ 710 eV), resulting in $\Delta E \approx 1.1$ eV and ≈ 1.4 eV, respectively. The polarization of the X-rays is variable between linear vertical and circular polarization. The X-ray flux is on the order of 10^6 photons / s / 0.1 % BW when femtoslicing mode is active.

For laser pump X-ray probe experiments, a stable temporal and spatial overlap of the pump and probe pulses is indispensable. As indicated in Fig. 3.7, the pump laser and the laser for generating the X-ray pulses are both driven by the same oscillator laser source. This ensures an intrinsic, jitter-free synchronization between the two pulses. To archive optimal sensitivity to the pump-induced effects after exciting the sample, the pump-probe signal is measured alternating with the unpumped signal without the laser pumping. Hence the X-ray repetition rate is the double, namely 6 kHz of the repetition rate of the pump laser, namely 3 kHz. For the measurements in chap. 4 two different laser pump photon energies will be presented, namely the 800 nm fundamental wavelength of the Ti:sapphire amplifier laser, and 266 nm wavelength generated by frequency tripling of this fundamental. The individual laser pump length can be verified by auto-correlation measurements and was reported to be 70 fs, and 50 fs for the two laser photon energies, respectively. The laser spot size was adjusted by a telescope made of two pairs of cylindrical lenses and determined with a CCD camera from a reference path with the same path length as the distance between telescope and sample position. The pump laser spot size was ranging from $\sim 140 \times 140\ \mu m^2$ (measurements with ps time resolution) to $\sim 160 \times 300\ \mu m^2$ (measurements with fs time resolution) for the 266 nm wavelength, and $\sim 310 \times 440\ \mu m^2$ for the 800 nm wavelength. The laser spot was always bigger than the typical X-ray spot size of the experiments of $\sim 50 \times 100\ \mu m^2$, to ensure a homogeneous excitation of the sample over the whole probed area.

To adjust the spatial overlap of the pump and probe pulse, the X-ray beam was guided through a pinhole mounted on the sample holder, while the pump spot position relative to the pinhole is checked and adjusted with the help of a CCD camera. The temporal overlap of the pump and probe pulse can not be determined

independently of the experiment since no cross-correlation measurement is possible at the beamline. Hence, with every new experiment, the time zero of the pump-probe delay had to be narrowed down step-wise, starting with the normal ps X-ray pulses for the first rough estimation, and subsequently determining the precise overlap with the fs X-ray pulses.
From the laser spot size, the repetition rate of the laser, and the measured laser output power the actual pump fluence ρ can be calculated, using the formula [130]:

$$\rho = \frac{4E_P}{\pi \cdot d^2}, \tag{3.4}$$

with E_P being the measured pump power per pulse, and d the pump-spot diameter. Exemplarily, this results for the fs, $266\,\mathrm{nm}$ measurements in chap. 4, with an output pump power of $25\,\mathrm{mW}$, and a repetition rate of $3\,\mathrm{kHz}$ to a pump power per pulse of $E_P = =8.3\,\mu\mathrm{J}$. This corresponds, with an averaged laser spot diameter of $230\,\mu\mathrm{m}^2$, to a pump fluence of $20\,\mathrm{mJ/cm}^2$. In total pump fluence ranging from $8\,\mathrm{mJ/cm}^2$ to $25\,\mathrm{mJ/cm}^2$ for the $266\,\mathrm{nm}$ measurements and $20\,\mathrm{mJ/cm}^2$ for the $800\,\mathrm{nm}$ measurements have been used. It should be noted that the presented time-resolved X-ray absorption measurements in chap. 4 have been conducted within three independent beamtimes. Even though the laser spot profiles have been inspected individually on all beamtimes, a direct quantitative comparison of just the pump fluence is difficult, since the spot profiles (e.g., due to the existence of hot spots) can vary drastically. Consequently, I will only attempt true quantitative comparisons between measurements conducted within the same beamtime, and restrict myself otherwise to qualitative comparisons, which will be noted in more detail on the respective text passages throughout chap. 4.

3.2 X-ray absorption measurements at the European XFEL

As described above, an important figure of merit of light sources is the brilliance of the source (cf. eq. 3.1). Modern synchrotron light sources of the so-called third-generation reach a peak brilliance of up to 10^{24} photons / s / mrad^2 / mm^2 / 0.1 % BW, which can be achieved due to a small horizontal and vertical emittance of the electron bunch and the use of undulator sources, which concentrate the broadband radiated power of the typical bending magnet radiation in a spectrum of narrow lines [127]. However, the third-generation light sources have two main fundamental limitations. First, in order to increase the brilliance further, a substantial reduction of the emittance has to be accomplished. This is hardly possible in a storage ring because as the electron bunch travels during every turn through all the bending magnets and insertion devices of the ring, the accompanying radiation emission affects the electron bunch and limits its vertical emittance. Moreover, as described the first paragraph of chap. 3.1.2 dedicated to the RF cavities, there is a natural limitation of the horizontal emittance as well. Second, when it comes to time-resolved measurements, storage rings have the significant disadvantage that femtosecond X-rays can only be achieved at the expense of a dramatic loss of photon flux (cf. Fig. 3.6). While there is the approach of diffraction-limited synchrotron radiation (DLSR) light sources, which ideally compress the electron bunch in horizontal and vertical direction until the diffraction limit (see for example [131–133] for more detail), I will discuss in the following the approach of X-ray free-electron laser (XFEL) sources. These sources, based on linear accelerators, allow fs X-ray pulses with a peak brilliance up to 10^{33}.

3.2.1 The self-amplified spontaneous emission process

In an undulator, there is a phase relation between the synchrotron radiation emitted by one electron at the different points of its trajectory. The emitted radiation can constructively interfere for wavelengths fulfilling the undulator condition (see eq. 3.2). Since the electrons are randomly distributed inside the bunch, there is no definite phase relation between different electrons in the electron bunch. Hence, all interference of radiation emitted by different electrons is averaged out. However, if one achieves that the electrons in the bunch are spatially ordered, the radiation of different electrons can be coherently superposed. For simplicity, let us assume two electrons in the undulator. If the second electron lags behind the first one, on

the projection on the undulator axis by an integer multiple of the wavelength, the emitted synchrotron radiation will superpose coherently after the two electrons have run through an integer number of undulator periods. The overall intensity of the radiation will be four times ($\sim n_e^2$) the one of one single electron and not, like in the case of randomly distributed electrons only two times larger ($\sim n_e$). Consequently, coherence effects between different electrons can occur, when the electron density of the electron bunch shows a modulation equal to the radiation wavelength. The total intensity of the emitted radiation is proportional to the square of the number of electrons involved in the modulation and the square of the number of undulator periods, $I \sim n_e^2 \cdot N^2$. [127]

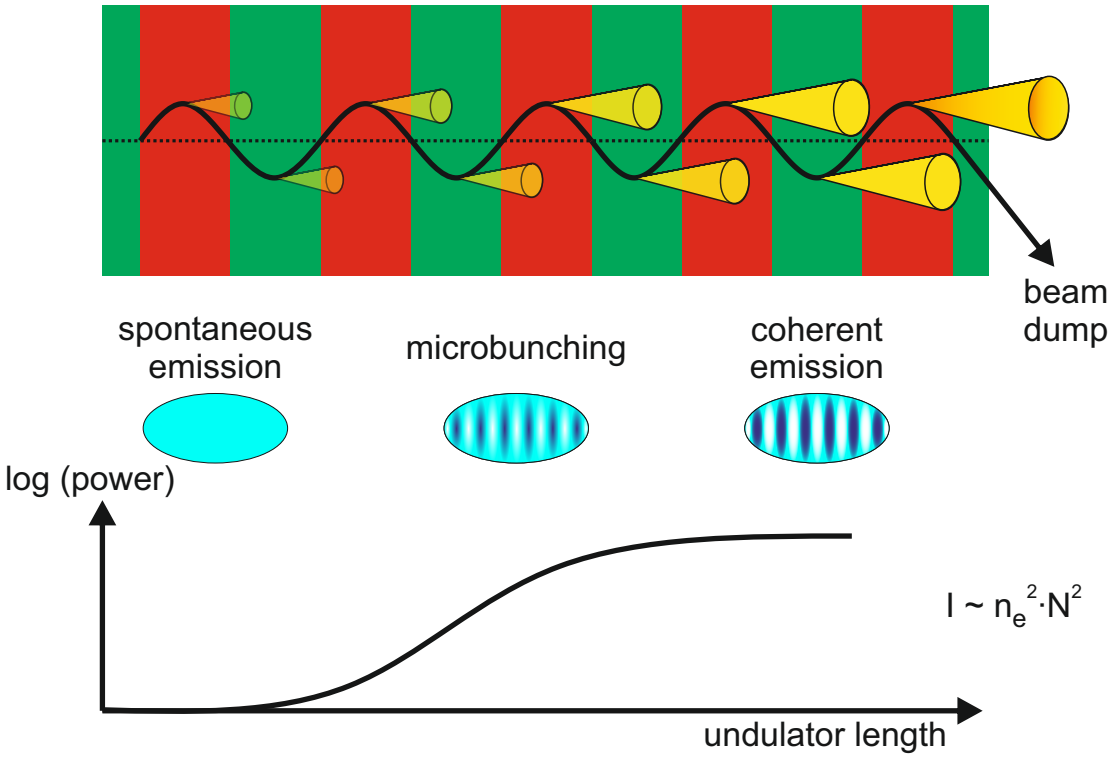

Fig. 3.8.: Schematic illustration of the self-amplified spontaneous emission (SASE) process in a sufficiently long undulator. The SASE process is only indicated until the point of saturation. Starting with a noise fluctuation in the electron bunch, the electrons in the bunch get more and more spatially ordered with increasing undulator length due to the effect of microbunching. This results in increasingly coherent emission of the emitted radiation and therefore in increasing radiation intensity. Due to the SASE process the total intensity of the emitted radiation is proportional to the square of the number of electrons involved in the modulation and the square of the number of undulator periods, $I \sim n_e^2 \cdot N^2$.

At first sight, it seems nearly impossible to precisely control the electron density to ensure coherence effects of all electrons in the bunch. Luckily, in a sufficiently long undulator, the emitted radiation can provide it by itself. This phenomenon is called

microbunching and can be explained as following: The electric field of the radiation has a small component parallel (or anti-parallel) to the electron velocity and accelerates (or decelerates) the electrons which are positioned half a wavelength behind (or ahead), resulting in bunching of the electrons on the scale of the wavelength of the radiation [127]. Starting with a noise fluctuation in the electron bunch, the coherence effect between some electrons increases their radiation intensity. This stronger radiation field leads, due to the microbunching, to a strengthening of the initial density fluctuation, which again increases their radiation intensity further and so on. Consequently, in a long enough undulator, this leads to an exponential amplification until saturation of the effect. Saturation starts, when the radiation is so intense, that further acceleration and deceleration leads to a degradation of the quality of the electron bunch density. The overall process of the microbunching and the subsequent coherent emission of radiation is called the self-amplified spontaneous emission (SASE) process. Fig. 3.8 illustrates the SASE process schematically until the point of saturation in a sufficiently large undulator, indicating the increased power of the emitted radiation and the increasing microbunching effect with growing undulator length. [127]

One of the requirements to effectively trigger the SASE process is that the electron bunch has a small horizontal and vertical emittance and a high peak current. Together with the sufficiently long undulator, it becomes clear that a linear accelerator geometry, not a storage ring geometry, is essential for the X-ray free-electron laser sources. Consequently, in contrast to synchrotrons, the electron bunch is not kept for several hours in the storage ring to emit with each turn the radiation, but fully dumped after running through the long undulator.

In the SASE process, the generation of coherent light emission is initiated by an arbitrary noise fluctuation in the electron bunch. This random fluctuation gives the synchrotron radiation emitted by the SASE process an intrinsic random character. Consequently, successive pulses are not identical and not reproducible. Hence it is necessary to either develop an experiment that does not need a reproducibility, e.g., a single shot experiment (which is, however, for a pump-probe experiment as reported in chap. 5 not suitable) or to ensure the possibility to monitor within each shot its properties to reference the measured data. The latter will be discussed below (cf. chap. 5.1) by introducing the special zone plate setup used at the European XFEL facility. Alternatively, if one replaces the random trigger of the SASE process with a controllable, reproducible trigger, like a laser pulse, one can imprint a controllable density modulation on the electron bunch. Schemes that follow this idea at large scale facilities are called seeded free-electron lasers [127, 134].

Moreover, I want to note that also table-top X-ray sources, based on a high harmonic generation scheme, may represent future alternatives for the large scale research facilities, allowing ultrafast X-ray measurements in the laboratory [135, 136].

3.2.2 The European XFEL facility

The European XFEL is currently the largest facility of the existing next-generation light sources [137]. It consists of three different undulators, called SASE 1, SASE 2, and SASE 3 that generate light for in total seven different endstations. Each endstation is optimized for a particular purpose and requires light with specific properties. Fig. 3.9 shows an overview of the floorplan of the European XFEL facility. In this thesis, I want to focus on the Spectroscopy and Coherent Scattering instrument (SCS), located at the undulator SASE 3, where I participated, among other things, at the very first user experiment in December 2018 (cf. chap. 5).

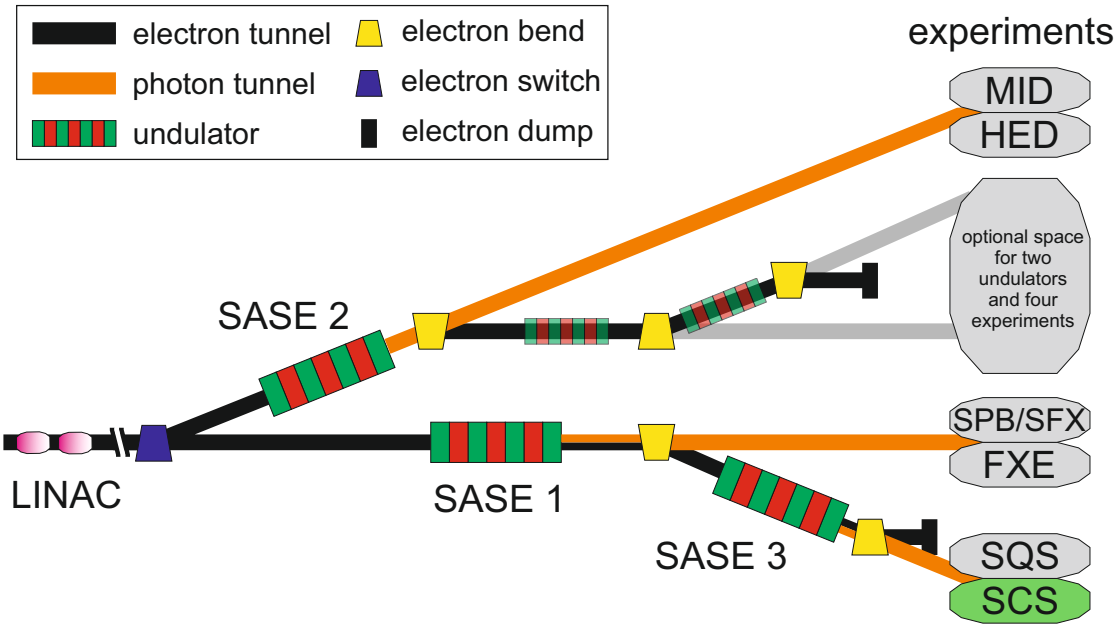

Fig. 3.9.: Schematic floorplan of the European XFEL facility, illustrating the arrangement of the (currently) three different undulators SASE 1, SASE 2 and SASE 3 and the corresponding electron and photon tunnels connecting them to the respective experimental endstations, named by the abbreviations. The measurements presented in chap. 5 have been carried out at the Spectroscopy and Coherent Scattering instrument (SCS) endstation, marked in light green. The figure is redrawn, based on [127, 138].

Fig. 3.9 shows a schematic of the floorplan of the European XFEL facility. First, the linear accelerator (LINAC) is located entirely in an underground tunnel and measures 1700 m, with currently 768 RF cavities. The accelerator can provide electrons with up to 17.5 GeV of energy, which can be fed into two different tunnels. The first tunnel contains the undulator SASE 2 for tunable hard X-rays in the 3 to 25 keV range. Furthermore, the first tunnel offers a place for two more undulators and four additional endstations. The second tunnel includes the undulator SASE 1 for

coherent hard X-ray photons in the 3 to 25 keV range, and the undulator SASE 3, dedicated for the generation of tunable soft X-rays in the 0.26 to 3 keV range. In order to ensure the SASE process, the length of the periodic magnetic structure of the three undulators has to be sufficiently great. The length of the magnetic periodic structure measures 175, 175 and 105 m, respectively [138].

Spectroscopy and Coherent Scattering instrument

The measurements presented in chap. 5 of this thesis have been carried out at the Spectroscopy and Coherent Scattering instrument (SCS), which is located at the undulator SASE 3 of the European XFEL facility (cf. floorplan, Fig. 3.9). The SCS instrument offers (in full user operation) X-ray photon energies from 0.25 to 3.0 keV, with a pulse energy of up to pulse energy up to 5 mJ per pulse [139]. The presented measurements have been carried out during two different experiments. The repetition rate of the XFEL used to measure the presented data was set to only 10 Hz, for the first experiment, and 70000 Hz for the second experiment.
The pulse duration of the X-rays is very short, with only < 25 fs, which makes the instrument ideal for time-resolved measurements (second experiment), using a laser pump X-ray probe setup. However, in contrast to the jitter-free femtoslicing scheme with the intrinsic synchronization between laser and X-ray pulse, the SCS instrument experiences possible drifts and a jitter. Consequently, even though the laser pulse duration was only 35 fs in the presented time-resolved experiments, the total effective time resolution has been 110 fs as determined during the experiments, taking possible drifts and the jitter between the laser and the < 25 fs short X-ray pulse into account. For the measurements a pump laser system with 800 nm central wavelength, 440 µm (FWHM) laser spot size, and a laser fluence of 15 mJ/cm^2 was used. The most essential parameters of the SCS endstation used in the experiments are summarized in Tab. 3.2.

Energy range	[eV]	250 - 3000
X-ray pulse energy	[mJ]	up to 5
X-ray pulse length	[fs]	< 25
FEL repetition rate	[Hz]	10 (first exp.), 70000 (second exp.)
Laser wavelength	[nm]	800
Laser pulse length	[fs]	15 - 100
Laser fluence	[mJ/cm^2]	15
Effective time resolution	[fs]	110

Tab. 3.2.: Key parameters of the Spectroscopy and Coherent Scattering instrument (SCS) endstation used for the presented measurements in chap. 5 of this thesis.

As I will show in chap. 5.1, we introduced during the very-first user experiment successfully a special zone plate setup to be able to reference the measured data with each shot and therefore solve the shot-to-shot-reproducibility issue of the generated X-ray pulses of the SASE process.
I want to note that we did not exploit the full potential of the European XFEL facility [139] during the presented very early user experiments, but rather carefully approached and tested its possibilities.

4 Pump-induced dynamics in a Fe/MgO heterostructure

This Ph.D. thesis was done in the framework of the first funding period of the collaborative research centre CRC 1242, within the project A05. Hence, as the name suggests, the presented work of chap. 4 was done in a joint effort of several researchers, who I want to acknowledge here. The second chap. 4.2 is mostly based on our publication [42]. The third chap. 4.3 is mostly based on our arXiv-preprint [140]. Among the other in the publications listed co-authors, I want to especially emphasize the following contributions of various researchers, namely U. Bovensiepen, A. Eschenlohr, M. E. Gruner, K. Ollefs, R. Pentcheva, S. Salamon, K. Sokolowski-Tinten, and H. Wende from the University Duisburg-Essen, and C. Schmitz-Antoniak from the Forschungszentrum Jülich: All the samples prepared for the various X-ray absorption spectroscopy (XAS) and ultrafast electron diffraction (UED) measurements have been prepared by myself. However, the two test samples for the conversion electron Mössbauer spectroscopy (CEMS) pre-characterization measurement, the CEMS measurement itself, and the analysis have been done by S. Salamon. The UED measurements on the samples prepared by myself, have been carried out and analyzed by K. Sokolowski-Tinten. All presented ab initio density functional theory (DFT) calculations have been done by M. E. Gruner. The two high-resolution XAS measurements have been performed by A. Eschenlohr, and C. Schmitz-Antoniak. All the time-resolved XAS measurements have been done by me personally under the supervision of A. Eschenlohr and with the help of K. Ollefs and C. Schmitz-Antoniak. The analysis of the corresponding data was my work. U. Bovensiepen and H. Wende guided, with the help of A. Eschenlohr, K. Ollefs, and R. Pentcheva the discussion and efforts to finalize the publication and the preprint. During chap. 4, whenever a contribution of one of the co-authors is shown, their effort is mentioned again at the respective text passages.

The focal point of this thesis is the investigation of a $[Fe/MgO]_n$ heterostructure system, which acts as a model system for other simple heterostructure samples. As I outlined in chap. 2.1, by using the multi-component structure of a heterostructure, I aim to achieve insight into interface vs. bulk effects as well as local vs. non-local dynamics, i.e., the transfer of excitations and energy between the different constituents. The general approach of chap. 4 is, therefore, combining a fs local pump excitation of one constituent, with a constituent-specific local probe technique with fs and ps time-resolution. In detail, using, among other things, element-specific and time-resolved X-ray absorption spectroscopy (XAS) at the O K-edge and the Fe L_3-edge allows to specifically analyze the non-equilibrium dynamics in the two constituents of the heterostructure, Fe and MgO.

After a short introduction of the Fe/MgO sample system in chap. 4.1, I will focus in chap. 4.2 explicitly on the understanding of the pump-induced ultrafast microscopic energy transfer dynamics, which take place in the heterostructure after the localized excitation. Therefore, I complement the fs time-resolved XAS measurements

by ultrafast electron diffraction measurements, and *ab initio* DFT calculations to analyze and disentangle the electronic and phononic contributions to the dynamical processes induced on the ultrafast timescales after the localized optical excitation. This yield an overall comprehensive insight into the local and non-local microscopic processes happening in the photo-excited metal/insulator heterostructure. Chap. 4.2 represents the centerpiece of this thesis.
After the understanding of pump-induced *dynamics*, I will dedicate chap. 4.3 to the understanding of the *spectroscopic* differences of the pump-induced spectral changes of the two different absorption edges. To achieve this understanding, I will introduce two distinct modeling and fitting procedures to analyze the measured pump-induced changes in soft X-ray absorption spectroscopy. Moreover, the sensitivity of transient XAS to phonons and its utility for quantifying temperature changes in complex materials will explicitly be demonstrated.
Finally, chap. 4.4 is focused on the investigation of the ultrafast local *demagnetization* behavior of the Fe constituent in the heterostructure. By comparing the various measured transients throughout chap. 4, I can then identify what mediates this local demagnetization process and integrate the dynamics of the Fe spin-system to the understanding of the overall dynamics.

4.1 Sample preparation and characterization

The main focus of this thesis is the investigation of the time-resolved dynamics in a $[\mathrm{Fe/MgO}]_n$ heterostructure. The samples were grown ex situ by molecular beam epitaxy in our laboratory, which allows due to the small growth rates of only $0.05\,\text{Å/s}$ a precise control of the individual layer thicknesses. As indicated in Fig. 4.1a, the used MBE-chamber offers the possibility of subsequently evaporating different materials onto the substrate by using different Knudsen effusion cells, which can be opened/closed by a shutter. Consequently, the complete $[\mathrm{Fe/MgO}]_n$ heterostructure can be grown on the substrate without exposing the unfinished sample to air and ensuring the same experimental conditions for all individual layers. Moreover, the substrate can be heated before and during growth to eliminate any possible pre-existing water on the substrate, and to enhance the quality of the layer growth, respectively.

Within this thesis, I investigated $[\mathrm{Fe/MgO}]_n$ heterostructures on two different $\mathrm{Si_3N_4}$ substrates, depending on whether they were used for the X-ray absorption or the ultrafast electron diffraction measurements. Independent of the substrate, all the sample preparation was carried out at a sample temperature of $400\,\text{K}$ in a background pressure of 10^{-10} mbar, ensuring no contamination of the individual deposited layers

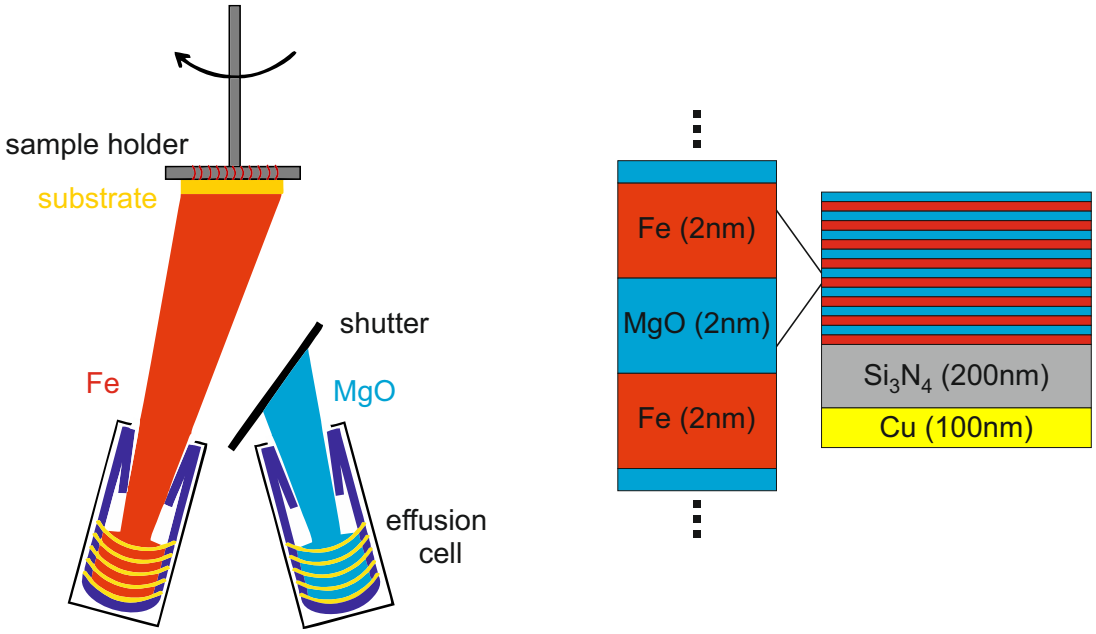

Fig. 4.1.: Left side: Schematic of the MBE-chamber used to grow the $[Fe/MgO]_n$ heterostructure samples. Right side: Schematic of a $[Fe/MgO]_n$ sample on a $200\,nm$ thick Si_3N_4 substrate with a $100\,nm$ thick Cu heatsink on the backside. The nominal thickness of the individual layers of the heterostructure is $2\,nm$.

or oxidation of the Fe layers. Furthermore, to eliminate any possible pre-existing water on the Si_3N_4 substrate, it was heated before growth in situ for $10\,min$ to $600\,K$. The individual Fe and MgO layer thickness was monitored during growth by a quartz crystal microbalance and subsequently determined by X-ray diffraction (XRD) measurements. All Fe/MgO heterostructure samples and reference samples have been prepared using a growth rate of $0.05\,Å/s$.

The $[Fe/MgO]_n$ heterostructure used for the X-ray absorption measurements is exemplarily sketched in Fig. 4.1b for $n=8$. The substrate consists of a $200\,nm$ thick Si_3N_4 membrane, which carries a $100\,nm$ thick Cu heatsink on its backside to dissipate the excess energy deposited by the laser pump beam. The individual Fe and MgO layers are $2\,nm$ thick. Moreover, I prepared two kinds of reference samples on the same substrate, one consisting of only $16\,nm$ MgO, the other consisting of only $20\,nm$ Fe with a $2\,nm$ thick MgO capping layer to prevent subsequent oxidation.

For the ultrafast electron diffraction measurements, the substrate consists of a thinner, only $20\,nm$ thick Si_3N_4 membrane without a Cu heatsink on its backside to ensure that the diffracted electrons can transmit through the sample. I stress that the different substrates for the different measurement techniques do not influence the signal of the multilayer sample itself, but had to be exchanged in order to match the experimental conditions. The number of layers and the individual Fe and MgO layers thicknesses used for electron diffraction vary greatly. Roughly, the samples can be classified in bilayer samples, with only one Fe-MgO interface, and

multilayer samples with several Fe-MgO interfaces. Moreover, I divide into samples with the same or different Fe and MgO individual layer thicknesses. The exact sample composition will be stated explicitly for each measurement shown.

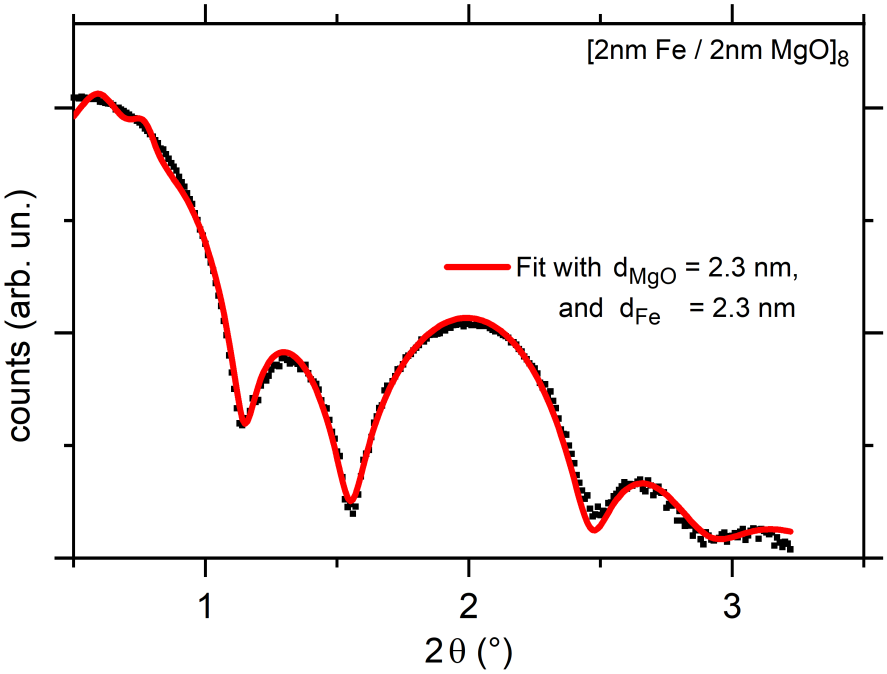

Fig. 4.2.: Small angle X-ray diffraction measurement of a $[Fe/MgO]_n$ multilayer with $n=8$ layer stacks with a nominal thickness of 2 nm of the individual layers.

Although the growth of Fe on MgO(001), as well as the growth of MgO on Fe(001), can proceed epitaxially due to a rather good lattice match [141–144], the use of the Si_3N_4 membrane as a substrate leads to polycrystalline layer stacks. However, the use of Si_3N_4 membranes is inevitable due to the experimental transmission measurement geometry. Fig. 4.2 shows an exemplary small-angle X-ray diffractogram of a $[Fe/MgO]_n$ multilayer with $n=8$ layer stacks with a nominal thickness of 2 nm of the individual layers. I want to note that, due to the polycrystallinity of the [Fe/MgO] layers, the XRD measurement only exhibits the periodicity of the multilayer and no crystallinity within the individual layers itself. Hence, the measured diffractogram displays oscillations caused only by the interference between the X-rays reflected from the surface and all the single interfaces, the so-called Kiessing fringes [145]. The observed Kiessing fringes were fitted (Fig. 4.2, red curve) with the *pi.exe* program package by U. von Hörsten [146] using layer thicknesses of 2.30 ± 0.01 nm, 2.30 ± 0.01 nm and 200.00 nm for Fe, MgO and Si_3N_4, respectively, confirming the thicknesses given by the quartz-crystal microbalance.

To determine the quality of the Fe-MgO interfaces, two test samples were fabricated, were one of the Fe layers of 2 nm nominal thickness was replaced by a layer com-

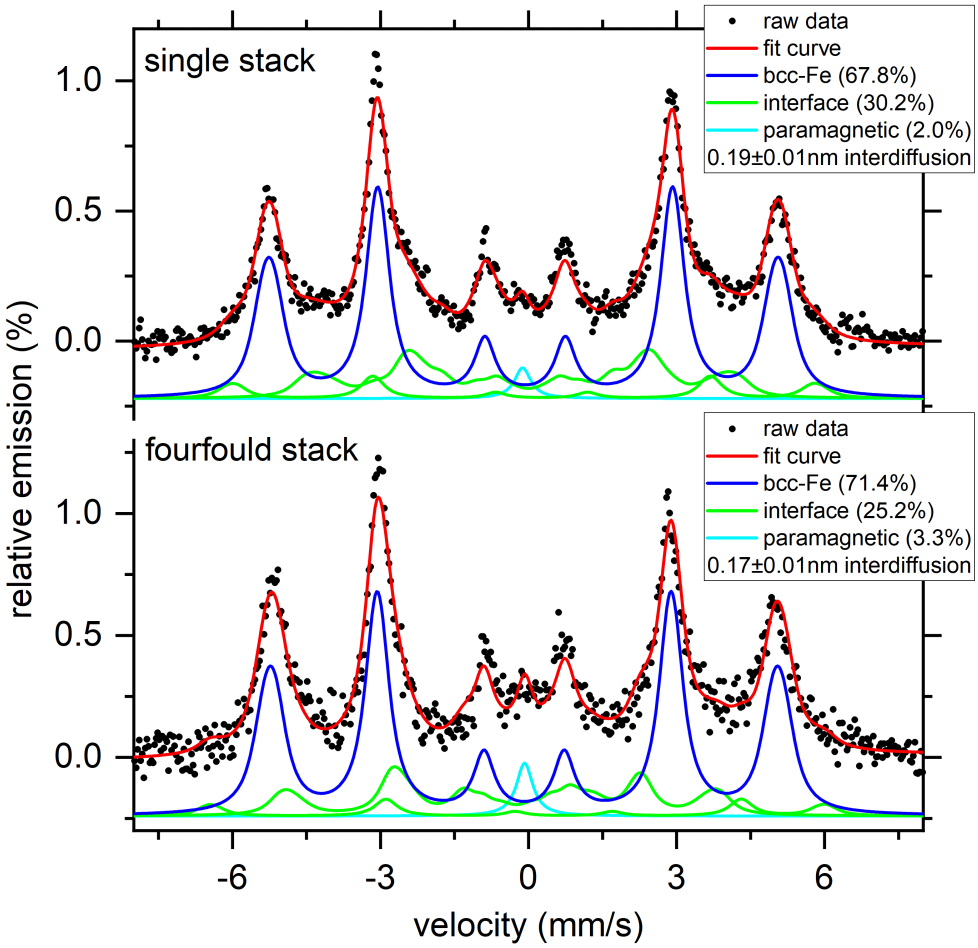

Fig. 4.3.: Conversion electron Mössbauer spectroscopy (CEMS) measurements on two test samples at room temperature, in order to determine the quality of the Fe-MgO interfaces. The CEMS measurements show that a potential intermixing of the Fe and MgO constituents is limited to a maximum of one monolayer at the interfaces. For more details see text.

posed of 1.4 nm natural Fe and 0.6 nm of pure ^{57}Fe referred to as tracer layer. The first sample consisted of only one Fe-MgO layer pair, with the tracer layer located at the interface between the two layers. The second sample had the tracer layer located at the topmost interface in a fourfold stack of Fe-MgO layer pairs. This was done in order to rule out any effects such as increased roughness of the interface after a multitude of layers, compared to only one layer pair. In the following, I will refer to the two samples as single stack and fourfold stack, respectively. The two test samples, the CEMS measurements, and the respective analysis have been done with the help of S. Salamon of the University Duisburg-Essen.

Fig. 4.3 shows ^{57}Fe-sensitive conversion electron Mössbauer spectroscopy (CEMS) measurements carried out on the two samples at room temperature. It is reasonable to assume that almost the entire signal observed in these spectra is being caused by the tracer layer, due to the comparatively low occurrence of ^{57}Fe in natural Fe, which is only ca. $2\,\%$ [147]. To determine the amount of signal being generated by ^{57}Fe atoms that diffused into the MgO layer, the following procedure was used: The

main spectral sextet contribution (dark blue curve) stems from ^{57}Fe atoms that are exclusively surrounded by other Fe atoms. The entire rest of the spectrum can be assumed to originate from ^{57}Fe atoms that have different nearest neighbors, as is the case for interdiffusion into the MgO layer. The main contribution was fitted with a distribution of equidistant sextet sub-spectra, using typical magnetic hyperfine parameters for bcc-Fe. The ^{57}Fe atoms with a nearest neighbor other than Fe lead to a spectral contribution with different magnetic hyperfine fields. To consider this, a free distribution of hyperfine fields (green curve) was utilized to account for the entirety of the spectral area not covered by the bcc-Fe sextet. Furthermore, a very small percentage of ^{57}Fe atoms shows paramagnetic behavior, leading to a miniscule singlet (cyan curve) at the center of the spectrum. Hence, one can assume this contribution to stem from a small number of atoms that lack a relevant number of Fe nearest neighbors, thus not showing any magnetic ordering. Assuming this to be a worst-case approximation, one can use the relative spectral area stemming from the interdiffused atoms to determine the thickness of this interdiffusion zone relative to the nominal thickness of the tracer layer. This provides an estimate of the interdiffusion zone of 0.19 ± 0.01 nm for the single Fe-MgO layer pair and 0.16 ± 0.01 nm for the fourfold layer pairs, clearly showing that even with the worst-case approximation, the higher number of stacked layers does not have a negative effect on the quality of the interface. It has to be stressed that this is an absolute worst-case assumption. Even in case of a theoretically perfect interface, the ^{57}Fe atoms that are at the edge of the Fe layer will produce deviating hyperfine magnetic fields due to MgO as their nearest neighbor to one side. The shown approximation thus also includes these atoms into the spectral area of the interface, even if no real interdiffusion has taken place. The quality of the interface can, therefore, only be higher than what this estimation provides. From the obtained results, I can, therefore, concluded that even in the worst-case assumption, a potential intermixing of the constituents is limited to a maximum of one monolayer at the Fe-MgO interfaces. The Fe-MgO interfaces in the heterostructure are therefore considered to be atomically sharp.

4.2 Microscopic non-equilibrium energy transfer dynamics in a photo-excited metal/insulator heterostructure

4.2.1 Excitation scheme at Fe/MgO interfaces

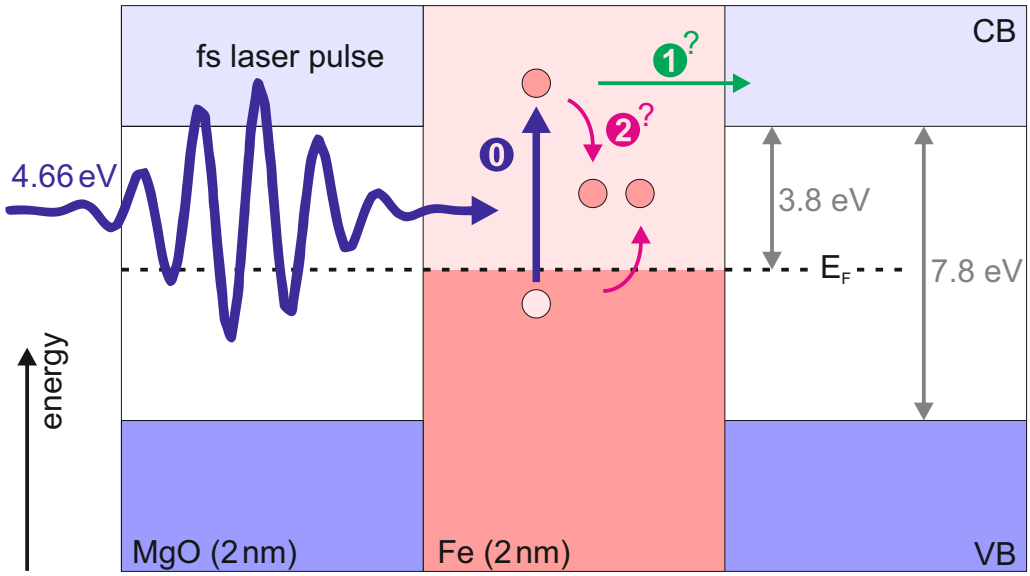

Fig. 4.4.: Schematic of the band alignment of the investigated Fe/MgO heterostructure system and the excitation scheme at the Fe/MgO interfaces. VB and CB indicate the MgO valence and conduction band, respectively. The Fermi-level E_F of Fe is located close to the midgap position of the bandgap of MgO, resulting in an effective charge transfer gap of $\Delta = 3.8\,\text{eV}$ [148]. The excitation photon energy $h\nu = 4.66\,\text{eV}$, indicated by the vertical blue arrow, is generated by frequency tripling of the Ti:sapphire fundamental at $1.55\,\text{eV}$. Relaxation processes due to electron-electron (e-e) scattering in Fe (process 2) followed by subsequent electron-phonon (e-ph) scattering across the interface compete with potential charge injection from hot electrons in Fe into the CB of MgO (process 1).

To understand the microscopic non-equilibrium energy transfer dynamics, which can occur in a photo-excited metal/insulator heterostructure, one has to contemplate the excitation scheme of the corresponding system. Fig. 4.4 shows schematically the band alignment of the investigated Fe/MgO heterostructure system [148]. The insulating constituent, MgO, shows a bandgap of $7.8\,\text{eV}$, dividing the valence band (VB) and conduction band (CB). The Fermi-level E_F of the metallic constituent, Fe, is located close to the midgap position of the bandgap of MgO. This results in an effective charge transfer gap of $\Delta = 3.8\,\text{eV}$.

Due to this specific band alignment, a laser excitation with a pump photon energy smaller than $7.8\,\text{eV}$ provides a local pumping of exclusively the Fe electronic system. This local pumping can be divided into two different possible scenarios: On the one

hand, using an infrared (IR) laser pulse with excitation energy of $h\nu < \Delta$, provided for example by the fundamental of a Ti:sapphire laser at 1.55 eV, limits the excess energy of the photoexcited electrons within the charge transfer gap. Hence, a direct charge transfer from hot electrons in Fe into the conduction band of MgO is energetically impossible. A localized relaxation processes due to electron-electron scattering in Fe (process 2 in Fig. 4.4) and a subsequent electron-phonon scattering across the interface have to take place. This localized relaxation is expected to be very efficient due to the large density of unoccupied $3d$ and $4s$ electronic states in Fe below the conduction band minimum of MgO.
On the other hand, using an ultraviolet (UV) laser pulse with excitation energy of $h\nu = 4.66\,\text{eV} > \Delta$, generated for example by frequency tripling of the Ti:sapphire fundamental, allows to overcome the charge-transfer gap Δ. Now, it is energetically possible that this excess energy induces a direct charge transfer of the hot electrons in Fe into the conduction band of MgO (process 1 in Fig. 4.4). However, this process of direct charge transfer competes with the same localized relaxation processes due to electron-electron scattering in Fe (process 2 in Fig. 4.4), followed by a subsequent electron-phonon scattering across the interface, as for the IR excitation.
It should be noted that the premise of both scenarios is the localized excitation of exclusively the Fe electronic system. This is ensured by using pump photon energies smaller than the bandgap of MgO. However, any two- or multi-photon absorption process of the pump pulse could induce a direct excitation from the valence band into the conduction band of MgO, making the discussion inconsequential. Consequently, it is important to point out that the used pump fluences of the presented experiments do not lead to multi-photon absorption processes (see Fig. 4.6, below) and therefore guarantee the initial localized excitation of Fe.

4.2.2 Ultrafast soft X-ray spectroscopy

The main tool of this thesis to address the pump-induced ultrafast microscopic energy transfer dynamics in the heterostructure after localized excitation, are constituent-specific femtosecond time-resolved X-ray absorption spectroscopy measurements. Considering the excitation scheme of the investigated Fe/MgO heterostructure system (cf. Fig. 4.4), I will report in the following on both pump scenarios: I start with the pump-induced changes in XAS after UV excitation, to identify whether or not a direct charge transfer to the MgO constituent can be observed. This findings will be corroborated afterwards by the changes in XAS after IR excitation.

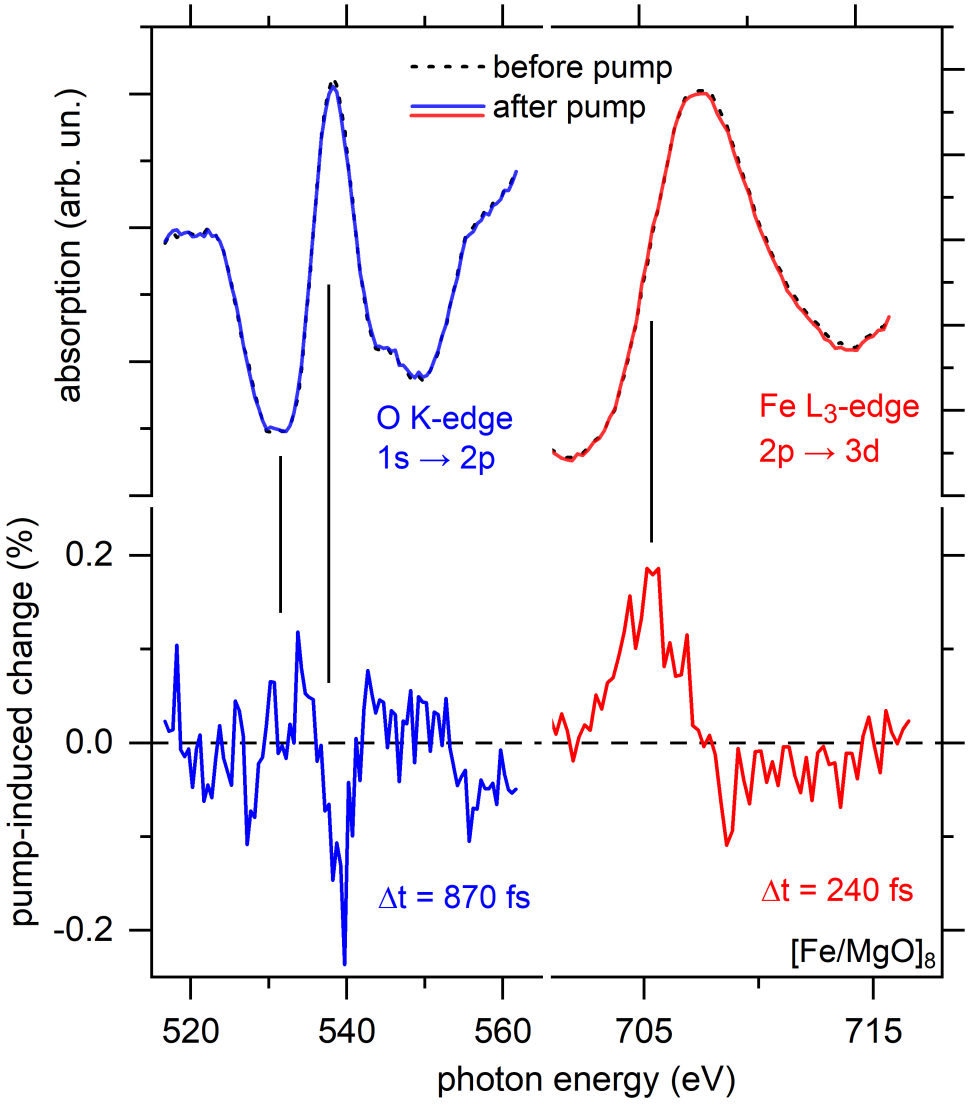

Fig. 4.5.: Top panel: Soft X-ray absorption spectra as a function of photon energy for the O K-edge (left, blue) and the Fe L_3-edge (right, red) before and after UV laser pumping. Bottom panel: Pump-induced changes of the corresponding absorption spectra as a function of soft X-ray photon energy at the indicated fixed pump-probe delays t of the maximum observed change. The incident laser fluence was set to $20\,\mathrm{mJ/cm^2}$. The vertical lines indicate photon energies at which the time-dependent measurements (cf. Fig. 4.6) were conducted.

Fig. 4.5 shows in the top half the X-ray absorption spectra of a $[Fe/MgO]_8$ heterostructure at the O K-edge (left) and the Fe L_3-edge (right) before and after UV laser pumping ($h\nu = 4.66\,\mathrm{eV}$), measured with $\approx 150\,\mathrm{fs}$ time resolution. The incident laser fluence was set to $20\,\mathrm{mJ/cm^2}$. The temporal overlap of the fs UV laser pump and fs X-ray probe pulses was determined by a preceding independent experiment using a $20\,\mathrm{nm}$ thick Fe film with a $2\,\mathrm{nm}$ thick MgO capping layer, which also serves as a Fe reference sample later on. The bottom half of Fig. 4.5 presents the pump-induced changes of the corresponding absorption spectra measured at

fixed pump-probe delays t when the maximum pump-induced changes have been observed. The maximum pump-induced changes at the two different absorption edges are similar in the strength of up to $0.2\,\%$, but occur at different time delays. At the O K-edge, the maximum change occurs at $870\,\text{fs}$, while at the Fe L_3-edge, it occurs already much earlier at $240\,\text{fs}$. These different time delays suggest that different physical processes are responsible for the changes in the different constituents, on which I will focus in the following.
Furthermore, I want to point out the different spectral shapes of the pump-induced changes at the two absorption edges. The maximum change at the Fe L_3-edge occurs at the rising edge of the absorption spectra, i.e., $2\,\text{eV}$ below the maximum absorption. Hence, the pump-induced change at the Fe L_3-edge shows a first derivative-like spectral signature, which indicates a shift of the absorption edge due to the laser pump pulse. In contrast, the maximum pump-induced change at the O K-edge is observed in the vicinity of the maximum of the absorption spectra. Hence, the pump-induced change of the O K-edge exhibits a different spectral signature, dominated by an intensity change at the maximum absorption. While I will address in more detail the understanding of this spectroscopic differences of the pump-induced changes in chap. 4.3, I at first focus on the understanding of pump-induced dynamics which take place in the heterostructure.
For the analysis of the pump-induced dynamics in the heterostructure, I measured the pump-induced changes as a function of the pump-probe delay at a fixed soft X-ray photon energy. The selected fixed energy values are indicated by vertical lines in Fig. 4.5 and namely: (i) at the Fe L_3-edge at the energy of maximum change, (ii) at the O K-edge at the maximum of the absorption spectra, where also the maximum pump-induced change is observed, and (iii) at the O K pre-edge region.

Fig. 4.6 shows the results of the pump-induced changes at the three selected fixed energies measured as a function of pump-probe delay. The transients at the different energies exhibit a very different behavior, which is highlighted at the $0.5\,\text{ps}$ mark, indicated by the vertical dashed line. At this time delay, the pump-induced change at the Fe L_3-edge (Fig. 4.6, bottom panel) has already gone through its maximum and has started to recover. In contrast, the change at the O K-edge (Fig. 4.6, top panel) has just reached its maximum. The change observed in the O K pre-edge region (Fig. 4.6, middle panel) is even slower than the one at the corresponding edge itself and is still slowly building up.
In more detail, the Fe L_3-edge shows a fast increase of the change in absorption, which reaches its maximum at $240\,\text{fs}$, and then relaxes almost back to zero change until $1.2\,\text{ps}$. At longer time delays, a second increase in change appears, however, with a slower time constant. The time-dependent intensity at the Fe L_3-edge can be fitted by taking three distinct time constants into account: One representing the build-up of the change with a time constant τ_1, a second for the exponential

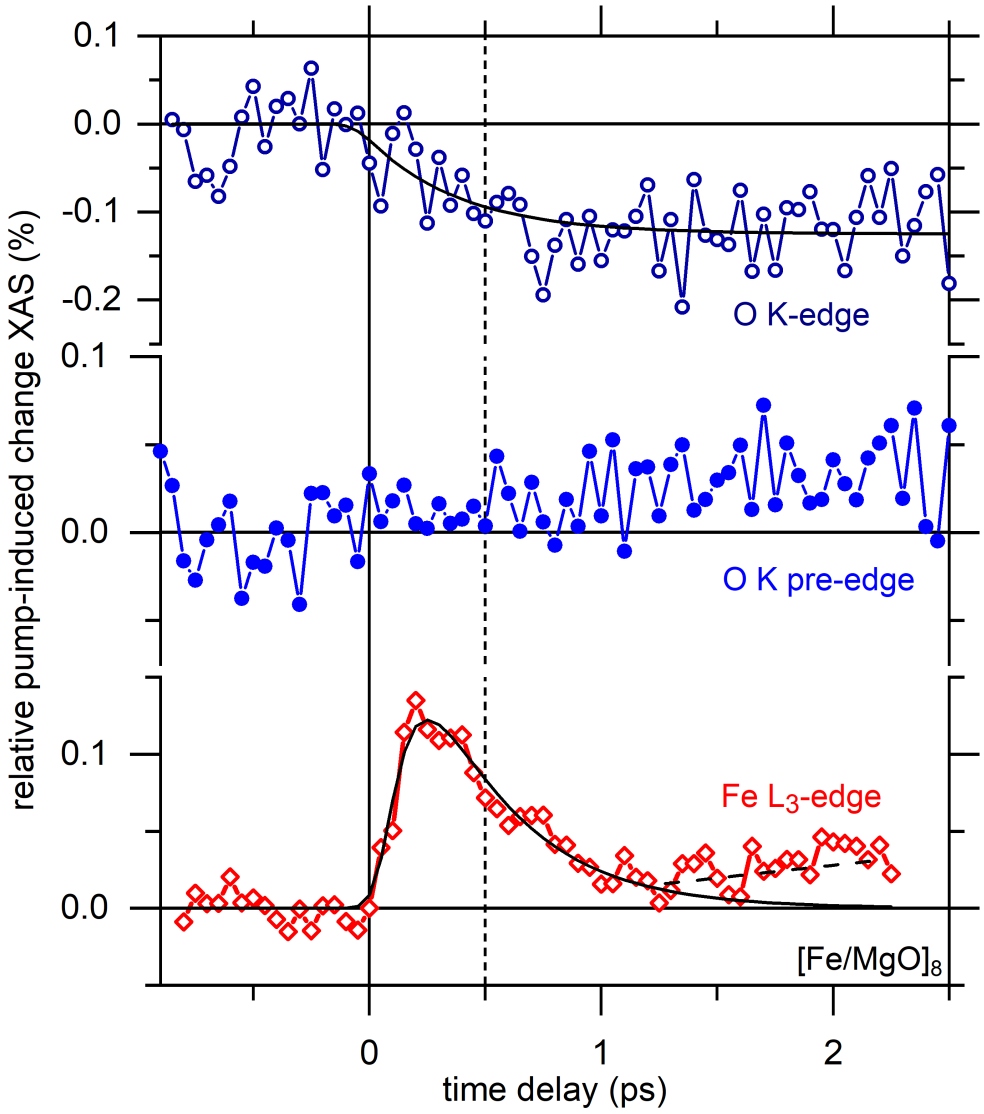

Fig. 4.6.: Pump-induced changes with $4.66\,\text{eV}$ pump photon energy observed for the $[\text{Fe/MgO}]_8$ heterostructure at three selected fixed soft X-ray photon energies as a function of pump-probe delay. Top panel: Maximum absorption of the O K-edge. Middle panel: O K-edge pre-edge region at the Fe-MgO interface state (cf. Fig. 4.20 below). Bottom panel: Rising edge of the Fe L_3-edge. The incident laser fluence was set to $20\,\text{mJ/cm}^2$. The black lines are fits to the data as specified in the text. The transients at the different energies exhibit a very different behavior, which is highlighted at the vertical dashed line at $0.5\,\text{ps}$.

relaxation with a time constant τ_2 and third, the time shift t_0 with respect to the experimentally determined time zero, which is defined as the onset of the transient change:

$$\Delta I_{\text{FeL}_3}(t) \propto \left[\Theta(t,t_0)\cdot\exp-\frac{t-t_0}{\tau_2}\right]\otimes\exp-\frac{(t-t_0)^2}{\tau_1^2}, \tag{4.1}$$

with Θ being the Heaviside function. The fit, done for $t < 1.2\,\text{ps}$, describes the data well with $t_0 = 0.04\pm0.01\,\text{ps}$, $\tau_1 = 0.11\pm0.01\,\text{ps}$ and $\tau_2 = 0.38\pm0.02\,\text{ps}$. At later delay times, the fit, which can be extrapolated to reach the zero level at $2.5\,\text{ps}$, does no longer describe the data. At these delay times, the second absorption increase can be

described by a linear increase, highlighted by the dashed line. This second increase is only observed for the heterostructure, but not for a single 20 nm polycrystalline Fe reference film (see more details in Fig. 4.6).
At the O K-edge, a decrease of the change in absorption, which builds up within 0.5 ps, and then stays constant up to 3 ps is observed. Hence, the time-dependent intensity at the O K-edge can be fitted by considering only the two time constants for the build-up τ_1 and the time shift t_0:

$$\Delta I_{\mathrm{OK}}(t) \propto \Theta(t, t_0) \otimes \exp -\frac{(t - t_0)^2}{\tau_1^2}. \tag{4.2}$$

The fit to describe the data yield $t_0 = -0.06 \pm 0.10$ ps and $\tau_1 = 0.40 \pm 0.14$ ps.
At the O K pre-edge, a slow increase of the change in absorption, which continues to increase within the investigated time delay is observed. This slow change can be described by the same linear increase as for the second increase at later time delays at Fe L_3-edge.
I want to note that the shown fit functions were chosen for the minimum number of free parameters needed to describe the data, and without assuming a particular physical model. Nevertheless, or even more precisely because of that, the resulting time constants are a good measure to compare the dynamics happening in the different constituents of the heterostructure. While I will discuss the dynamics at the O K pre-edge as well as the second increase at the Fe L_3-edge further below, I focus now on the different time-dependent X-ray absorption dynamic at the Fe L_3-edge and O K-edge itself. I start with the observations at the Fe L_3-edge probing the dynamics of the Fe constituent, which is primarily excited by the pump pulse. The time-dependent X-ray absorption at the rising flank of the Fe L_3 edge is characterized by an absorption increase, which reaches its maximum at 240 fs, see Fig. 4.6, resulting from a red-shift of the Fe L_3 absorption edge. This observation is in qualitative agreement with literature results for metal films [60, 101, 149], and the understanding of the effect of the pump-induced changes to the spectroscopic fine structures are addressed in more detail further below in chap. 4.3. The absorption of the UV laser pulse in Fe occurs within the 70 fs pump pulse. The maximum of the X-ray absorption increase is reached at 240 fs, well after the pump pulse duration. This can be explained through inelastic electron-electron (e-e) and hole-hole scattering, which is leading to the relaxation of the primarily excited, non-equilibrium electron distribution and redistribution of electrons and holes towards E_{F} in Fe [11, 22]. Such redistribution is characteristic for a metal system where the chemical potential is positioned within an electron band and therefore expected for the initial step in the Fe L_3-edge dynamics.
Interestingly, the observed timescale of the time-resolved X-ray absorption dynamics at the O K-edge shows a significantly slower response than the initial step of the Fe L_3-edge dynamics. However, a direct charge transfer from the hot electrons in

Fe into the conduction band of MgO (see again process 1 in Fig. 4.4) would have to show a similar fast, direct response in the X-ray absorption dynamics at the O K-edge as at the Fe L_3-edge [150]. Due to the fact that the measurements do not report this fast response, but a significantly slower one, I derive that the transfer of the excitations from the metallic constituent to the insulating constituent has to involve phonons.
Furthermore, also the Fe L_3-edge relaxation dynamics after the absorption increase maximum at 240 fs is assigned to a dissipation of the excess energy from the electronic subsystem to the phononic subsystem, mediated by electron-phonon (e-ph) coupling [18]. It becomes obvious that *phononic processes* are crucial for the overall microscopic non-equilibrium energy transfer dynamics in the Fe/MgO heterostructure. That is why I will report further below on ultrafast electron diffraction measurements as a complementary ultrafast method to analyze the resulting lattice dynamics of the heterostructure exclusively, see chap. 4.2.3. By combining the time-dependent results of X-ray absorption dynamics and electron diffraction experiments I can thus derive a comprehensive insight into the microscopic non-equilibrium dynamics of the heterostructure.

Moreover, it is crucial to turn the attention to the X-ray absorption dynamics observed in a Fe reference sample as well as in a MgO reference sample. As stated in chap. 4.1, the two reference samples are grown on the same corresponding substrates. The hereinafter called MgO reference consists of a pure 16 nm MgO film, the Fe reference of a pure 20 nm Fe film with a 2 nm thick MgO capping layer on top, to prevent subsequent oxidation. Fig. 4.7 shows a comparison of the dynamics observed in the heterostructure (cf. Fig. 4.6) with the dynamics happening in the reference samples after the same initial laser excitation. I first want to point out that the dynamics at the O K-edge occur exclusively in the heterostructure. In the single MgO reference layer, no transient changes are observed at the O K-edge after laser pumping. This proves the premise of the localized excitation of exclusively the Fe electronic system. Consequently, the dynamics of the heterostructure observed at the O K-edge are indeed mediated by a transfer of excitations from the Fe constituent.
Comparing the pump-induced response at the Fe L_3-edge of the $[Fe/MgO]_8$ heterostructure to the Fe reference sample shows that both samples exhibit the same time constant of the initial absorption increase with the maximum at 240 fs. I want to note that the value of the maximum of the pump-induced change of the reference sample is scaled to the one of the heterostructure due to presumably small differences in the actual laser fluences. This does not influence the time constant of the initial rise. However, qualitative differences in the pump-induced changes observed in these samples for the subsequent relaxation dynamics can be identified. The heterostructure exhibits the initial ultrafast increase followed by a

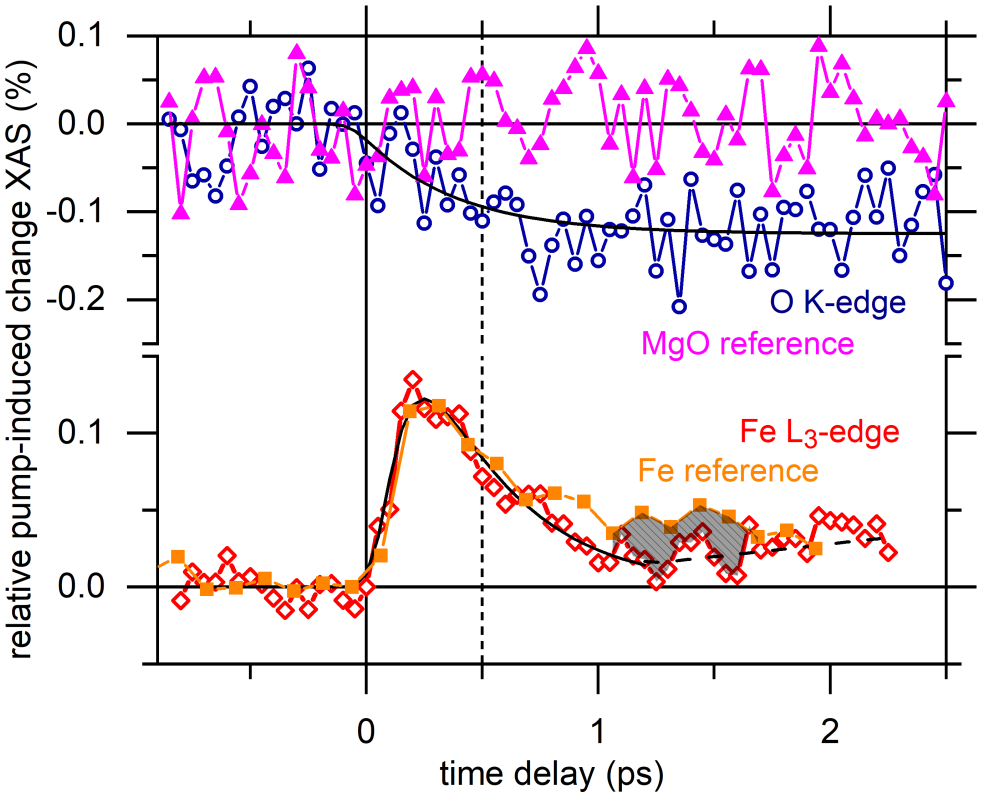

Fig. 4.7.: Comparison of the pump-induced dynamics after 4.66 eV excitation at two selected fixed soft X-ray photon energies observed in the $[Fe/MgO]_8$ heterostructure (cf. Fig. 4.6) with the dynamics happening in two respective reference samples, namely a pure 16 nm MgO film and a pure 20 nm Fe film with a 2 nm MgO capping layer on top. Top panel: Maximum absorption of the O K-edge. Bottom panel: Rising edge of the Fe L_3-edge. The incident laser fluence was set to 20 mJ/cm^2.

decay and a subsequent second slower increase, which results in a local minimum of the pump-induced change at about 1.2 ps. The reference sample exhibits a simpler dynamic with only the initial increase and the decay. I assign this second, slower intensity increase of the heterostructure therefore to the presence of the Fe/MgO interfaces. Furthermore, while the time constant of the initial rise is the same for both samples, the decay dynamic of the reference sample is slightly slower. Hence, the presence of the Fe/MgO interfaces also accelerates the dissipation of the excess energy out of the Fe electronic subsystem.

Pump-induced changes in XAS after IR excitation

Looking back to the band alignment (cf. Fig. 4.4) of the investigated system, I proposed two different possible scenarios happening in the system upon laser excitation. I divided those scenarios according to the pump photon energy: roughly summarized to UV laser excitation (e.g., $h\nu = 4.66\,\text{eV} > \Delta$) and IR laser excitation (e.g., $h\nu = 1.55\,\text{eV} < \Delta$). However, I reported for the UV laser excitation (cf. Fig. 4.6),

that a direct charge transfer to the MgO constituent was not observed. Consequently, I can deduce that whether the heterostructure is excited with a UV or an IR pump laser, the transient behavior of the respective X-ray absorption spectra should behave the same for both kinds of laser excitation, on which I will focus in the following.

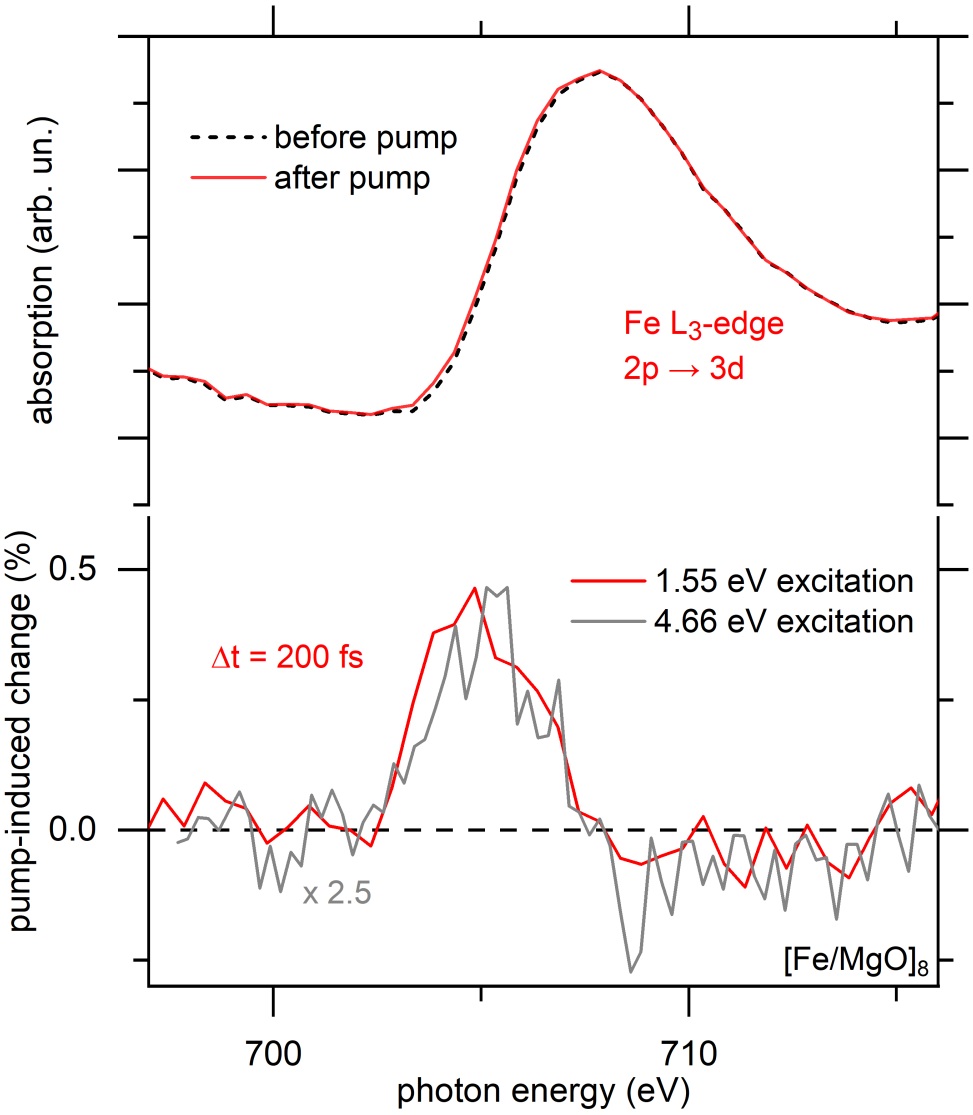

Fig. 4.8.: Top panel: Soft X-ray absorption spectra of the $[Fe/MgO]_8$ heterostructure at the Fe L_3-edge before and after IR laser pumping ($h\nu = 1.55$ eV). Bottom panel: Pump-induced change of the corresponding absorption spectrum as a function of soft X-ray photon energy at the indicated fixed pump-probe delay for the IR 1.55 eV excitation (red curve). The incident laser fluence was set to $20\,\mathrm{mJ/cm^2}$. Additionally, I compare the pump-induced change for the IR excitation with the UV excitation (cf. Fig. 4.5), which was measured at a similar time delay of 240 fs, and is scaled for better visualization by a factor of 2.5 (grey curve).

Fig. 4.8 shows in the top half the X-ray absorption spectra of the Fe/MgO heterostructure at the Fe L_3-edge before and after IR laser pumping ($h\nu = 1.55$ eV). The spectra are measured with 150 fs time resolution, and the incident laser fluence was set to $20\,\mathrm{mJ/cm^2}$, just like for the UV excitation. The corresponding pump-induced change of the absorption spectrum measured at fixed pump-probe delays t of 200 fs, when

the maximum pump-induced change has been observed, is shown in the bottom half of Fig. 4.8. Additionally, I display the pump-induced change induced by the UV laser excitation (cf. Fig. 4.5, red curve) measured at a similar time delay of 240 fs. For better visualization, the UV change was multiplied by a factor of 2.5, to match the maximum strength of the IR change. I note that I will not attempt to quantify the different strength of the pump-induced changes since both measurements have been conducted within different beamtimes. Hence, even though the incident laser fluence was set nominally to the same value, deviating spot profiles, and energy-dependent laser absorption efficiency make it difficult to make both measurements quantifiable. Therefore, I restrict myself in the following solely in a qualitative comparison of the transient behavior and the spectroscopic similarities of the different laser excitation.

For both laser pump photon energies, the maximum pump-induced change occurs on a similar time delay. The maximum changes for the different laser excitation arise both at the rising edge of the respective absorption spectra, i.e., 2 eV below the point of maximum absorption. Furthermore, the two pump-induced changes exhibit an identical derivative-like spectral signature. This implies a shift of the absorption edge due to the laser pump pulse for both excitation photon energies, as addressed in more detail in chap. 4.3, below. Since the Fe L_3-edge exhibits the same pump-induced changes of the spectroscopic fine structure for the different laser excitation, I also expect matching pump-induced dynamics in the heterostructure, measured as a function of the pump-probe delay at a fixed soft X-ray photon energy, for the two pump photon energies. Complementary to Fig. 4.6, I selected the fixed energy values at the Fe L_3-edge at the energy of maximum change and at the maximum of the O K-edge absorption spectrum, where the maximum pump-induced change was observed for the UV excitation. I want to note that (in contrast to Fig. 4.5 above) due to time reasons on the corresponding beamtime, a pump-induced O K-edge *spectrum* could not be measured. Therefore, the X-ray photon energy was fixed according to the UV beamtime on the maximum of the unpumped O K-edge absorption spectrum.

Fig. 4.9 shows the transient of the normalized pump-induced changes at the two selected fixed photon energies. I compare the normalized time-dependent change for the UV 4.66 eV laser excitation (cf. Fig. 4.6, top and bottom panel) and the IR 1.55 eV laser excitation. The vertical dashed line at the 0.5 ps mark highlights the different behavior of the transients at the different photon energies. Consistent with the findings for the UV excitation, the pump-induced change at the Fe L_3-edge (Fig. 4.9, bottom panel) exhibits a much faster response which already has started to recover by the 0.5 ps mark, than the observed change at the O K-edge.

In more detail, both pump-induced changes at the Fe L_3-edge (Fig. 4.9, bottom panel) show the same fast increase in change in absorption with a maximum at

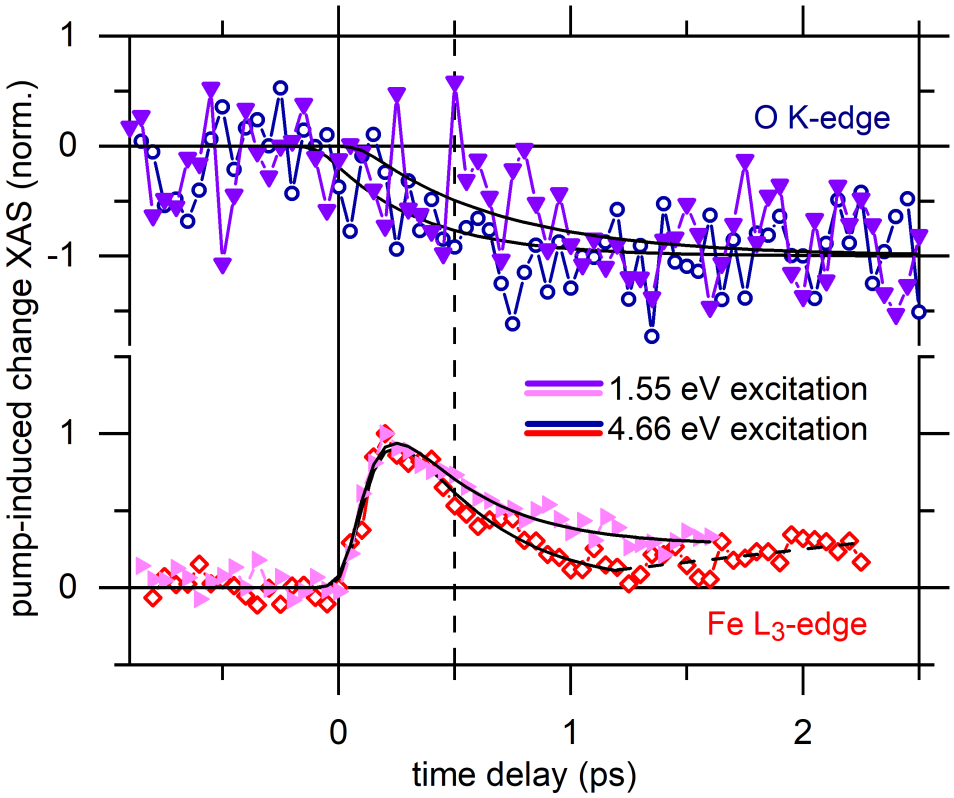

Fig. 4.9.: Comparison of the normalized pump-induced changes of the $[Fe/MgO]_8$ heterostructure at two selected fixed X-ray photon energies as a function of pump-probe delay for the UV $4.66\,eV$ laser excitation (cf. Fig. 4.6) and the IR $1.55\,eV$ laser excitation. Top panel: Maximum absorption of the O K-edge. Bottom panel: Rising edge of the Fe L_3-edge. The incident laser fluence was set to $20\,mJ/cm^2$. The black lines are fits to the data as specified in the text. The vertical dashed line at $0.5\,ps$ highlights the different behavior of the transients at the different energies.

$240\,fs$. For the subsequent relaxation process, qualitative differences for both laser excitation energies can be identified. The heterostructure exhibits for the UV laser excitation the reported initial ultrafast increase followed by a decay and a subsequent second slower increase for longer time delays. This results in a local minimum of the pump-induced change at about $1.2\,ps$. For the IR laser excitation, a simpler dynamics with only the initial fast increase and the subsequent decay is observed. The time-dependent intensity at the Fe L_3-edge for the IR excitation can be fitted using the same fit function as for the UV excitation for $t < 1.2\,ps$ (cf. eq. 4.1). The fit to describe the data yield a time zero shift $t_0 = 0.03 \pm 0.01\,ps$, a time constant $\tau_1 = 0.10 \pm 0.01\,ps$ representing the fast increase of the change, and the exponential relaxation with the time constant $\tau_2 = 0.37 \pm 0.02\,ps$. While the time constant of the initial rise and the decay are the same for both excitation energies, the decay dynamic initiated by the IR laser pulse appears to be slightly slower/weaker, since it does not relax back to nearly zero level. Hence, the transient at the Fe L_3-edge for the IR excitation conforms better to the UV dynamics of the Fe reference sample

(cf. Fig. 4.7, orange curve). For the 4.66 eV laser excitation, I will ascribed below the qualitative differences in the relaxation dynamics of the heterostructure and reference sample to the presence of the Fe/MgO interfaces, which accelerates the dissipation of the excess energy out of the initially excited Fe electronic subsystem. Consequently, it seems like the Fe/MgO heterostructure exhibits a less effective coupling to the interface hybrid phonon modes for the IR 1.55 eV laser excitation than for the UV 4.66 eV laser excitation. Whether this finding is affected by the factor of 2.5 stronger maximum change of the IR excitation remains currently unclear and requires further investigations which go beyond the framework of this thesis. However, it should be noted that the ultrafast electron diffraction measurements shown below (e.g., Fig. 4.13), conducted with different laser photon energies, will report no dependency on the laser photon energies and clearly state the importance of the interfaces.

At the O K-edge (Fig. 4.9, top panel), for both laser excitation energies a decrease of the change in absorption is observed, which builds up significantly slower than the respective change at the Fe L_3-edge and stays then constant up to 3 ps. Both transients exhibit qualitatively the same time-dependent behavior. Hence, the time-dependent intensity at the O K-edge for the IR excitation can be fitted using the same fit function as for the UV excitation (cf. eq. 4.2). The fit to describe the data yield a time zero shift $t_0 = 0.13 \pm 0.17$ ps, and a time constant $\tau_1 = 0.60 \pm 0.25$ ps representing the build-up of the change. Comparing the transients for the two laser excitation energies, it appears that the IR 1.55 eV laser excitation results in a slightly slower dynamic at the O K-edge than the UV 4.66 eV laser excitation, hinting once more a less effective coupling to the interface hybrid phonon modes for the IR XAS measurements. However, I want to note that data quality (signal to noise ratio) of the IR O K-edge data is (due to time reasons on the corresponding beamtime) noticeably smaller than for the UV data. Therefore I do not attempt here to quantify the differences in the pump-induced changes.

Besides the slight differences in the transient behavior of the change in absorption for the two different laser photon energies, both the UV 4.66 eV laser excitation as well as the IR 1.55 eV laser excitation clearly lead to the same overall microscopic non-equilibrium energy transfer dynamics in the photo-excited Fe/MgO heterostructure. I showed that *independently of the two different possible laser pump scenarios*, namely excitation below or above the charge transfer gap Δ (cf. Fig. 4.4), *the experiments do not report a direct charge transfer between the two constituents*.

4.2.3 Ultrafast electron diffraction

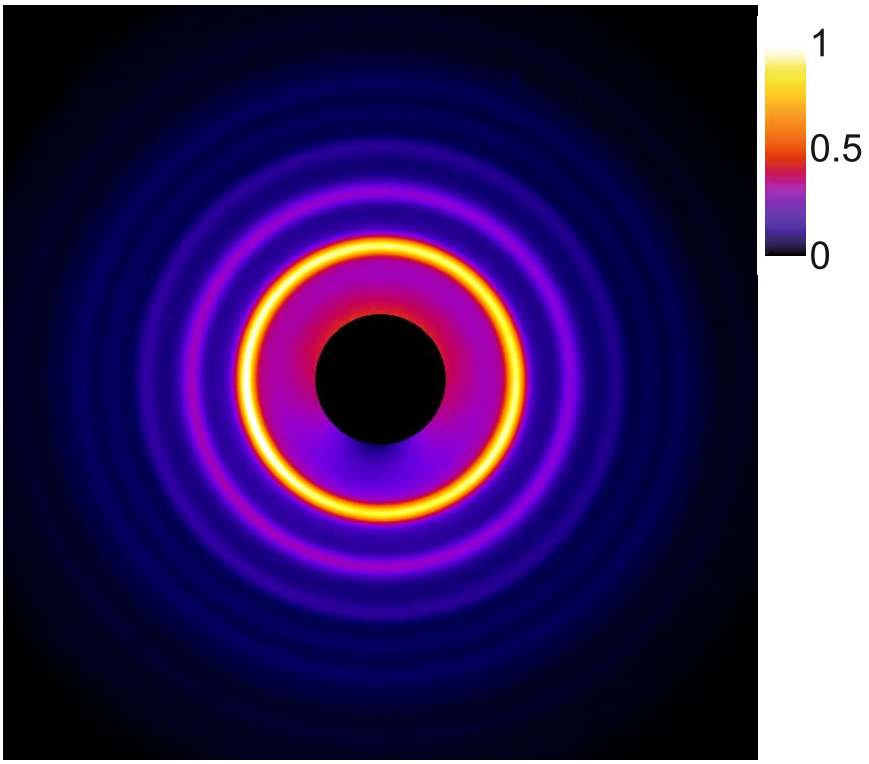

Fig. 4.10.: Static, unpumped electron diffraction pattern of a $[2\,\text{nm Fe}/5\,\text{nm MgO}]_5$ multilayer heterostructure in false color representation [42].

To complement the time-resolved soft X-ray absorption spectroscopy experiments discussed in chap. 4.2.2, time-resolved ultrafast electron diffraction (UED) experiments using the MeV-UED facility at SLAC National Accelerator Laboratory [151] have been performed. The ultrafast electron diffraction measurements directly and exclusively probe the lattice response of the Fe/MgO heterostructures after fs laser excitation. The UED experiments reported here were carried out in normal incidence transmission geometry at a repetition rate of $120\,\text{Hz}$ with pulses of approximately $2 \cdot 10^5$ electrons per pulse, a bunch duration of $\tau_{bunch} \approx 200\,\text{fs}$ (FWHM), and kinetic energy of $E_{kin} = 3.7\,\text{MeV}$. I want to emphasize that due to the normal incidence diffraction geometry and the MeV electron energies, essentially the in-plane lattice dynamics of the heterostructures is probed. In other words, in the shown UED experiments, only the in-plane relative mean squared (r.m.s.) displacement is measured. The UED measurements have been performed and evaluated by K. Sokolowski-Tinten of the University of Duisburg-Essen, with the help of the respective beamline scientists at SLAC, for more details to the acknowledgement see [152].
For the UED experiments I have prepared slightly different $[\text{Fe/MgO}]_n$ heterostructures as for the XAS experiments. The substrate consists of a thinner, $20\,\text{nm}$ thick Si_3N_4 membrane without the $100\,\text{nm}$ Cu heat sink, to minimize additional back-

ground contributions and to optimize the overall scattering signal due to the lower repetition rate of the UED experiment. Furthermore, while for the XAS experiments, the relative amount of Fe and MgO in the heterostructures was equal, in most samples used for UED, the relative amount of MgO in the samples has been increased to enhance the relatively weak scattering signal of MgO. To systematically address the role of interface effects two different sample configurations have been investigated. Namely, the response of a multilayer heterostructure, with enhanced interface mediated effects, is compared to a bilayer sample with only one Fe-MgO interface. Using pump laser photon energies of $4.66\,\text{eV}$ and $3.10\,\text{eV}$ allows again to exploit the two different local pump scenarios, discussed above (see chap. 4.2.1, Fig. 4.4).

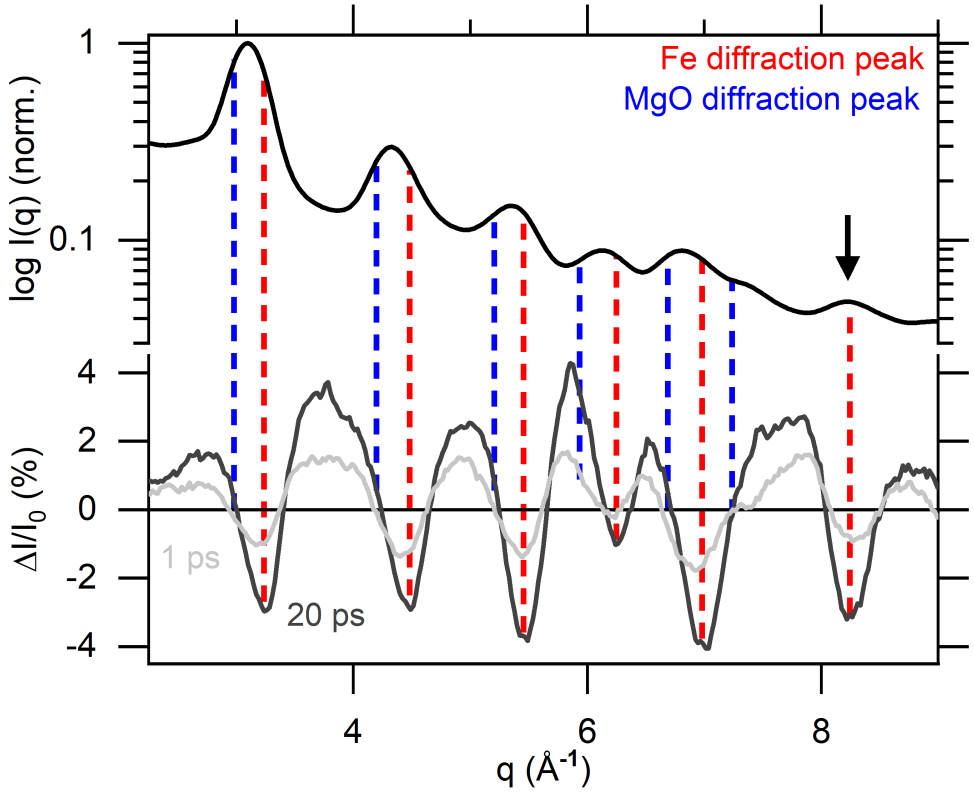

Fig. 4.11.: Top panel: Scattering intensity $I(q)$ of the respective electron diffraction pattern of the $[2\,\text{nm Fe}/5\,\text{nm MgO}]_5$ heterostructure (Fig. 4.10) as a function of momentum transfer q. Bottom panel: Difference scattering pattern $\Delta I\,(q,t) = I\,(q,t) - I_0\,(q)$, with $I_0\,(q)$ representing the unpumped case, for delay times t=1 ps (light grey) and t=20 ps (dark grey) after $4.66\,\text{eV}$ pump excitation at an incident fluence of $9\,\text{mJ/cm}^2$. Red and blue dashed vertical lines mark the positions of diffraction peaks of Fe and MgO, respectively. The arrow at $q = 8.19\,\text{Å}^{-1}$ indicates the only Fe diffraction peak, which is not influenced by diffraction from MgO.

Fig. 4.10 depicts an exemplary static unpumped diffraction image of a multilayer heterostructure, i.e., $[2\,\text{nm Fe}/5\,\text{nm MgO}]_5$ without laser pumping. Fig. 4.11 displays in the top half the resulting unpumped diffraction signal $I(q)$, which is obtained by azimuthal integration along the lines of constant momentum transfer $q \approx 2\pi/\lambda \cdot \theta$,

with de Broglie wavelength $\lambda = 0.003\,\text{Å}$ and scattering angle θ. Upon laser pumping, the corresponding diffraction intensity shows a transient difference to the unpumped signal. By displaying the transient differences in the scattering intensity, namely the pumped minus unpumped signal, for specific time delays, the effect of the laser pumping on the diffraction image becomes clear. Fig. 4.11 shows in the bottom half the transient difference in the scattering intensity for a time delay of $1\,\text{ps}$ (light grey) and $20\,\text{ps}$ (dark grey) after $4.66\,\text{eV}$, UV laser excitation at an incident fluence of $9\,\text{mJ/cm}^2$. A clear decrease of the Bragg peak intensities as well as an increase of the diffuse background in between the Bragg peaks is observed. This can be attributed to the incoherent excitation of the lattice and the increase of the r.m.s. atomic displacement after sample excitation, which is known as the transient Debye-Waller effect.

Unfortunately, at the given momentum resolution of the experiment of $0.14\,\text{Å}^{-1}$, the diffraction peaks of Fe (Fig. 4.11, red vertical lines) and MgO (Fig. 4.11, blue vertical lines) overlap in most cases. Furthermore, the observed transient changes are dominated by the response in Fe. This is especially the case for earlier delay times when the changes in MgO are relatively weak compared to the changes in Fe. The transient diffraction data can be quantitatively analyzed by determining the integrated signal of each individual Bragg-peak, by fitting them separately with a Gaussian function superimposed on a linear background for each delay time. However, due to the overlap of diffraction peaks and the generally weak changes in MgO at earlier delay times, I focus here solely on the results obtained for the diffraction peaks of Fe. More precisely, solely the isolated (321)-diffraction peak at $q = 8.19\,\text{Å}^{-1}$ was used, since this peak is not influenced by diffraction from MgO (see Fig. 4.11, indicated by the arrow).

With this, I can describe the incoherent vibrational excitation of the Fe lattice due to energy transfer from the optically excited electrons to phonons by the transient changes of the r.m.s. atomic displacement of the ion cores $\Delta\langle u^2\rangle\,(t)$:

$$-\ln\left(\frac{I_{hkl}\,(t)}{I^0_{hkl}}\right) = \frac{1}{3}\Delta\langle u^2\rangle(t)\cdot G^2_{hkl},$$

with I^0_{hkl} the scattering signal of the unpumped sample and G_{hkl} the length of the reciprocal lattice vector corresponding to reflection (hkl).

I want to note that the dependence on diffraction order predicted by the given equation was verified for a representative subset of the data (not presented within this thesis). This shows that within the experimental accuracy, the lattice response in Fe is indeed incoherent, see also [42].

Fig. 4.12 compares the obtained $\Delta\langle u^2_{\text{Fe}}\rangle(t)$ as a function of pump-probe time delay for two different sample configurations and two different excitation conditions. In more detail, the figure shows the two different local pump scenarios (cf. Fig. 4.4)

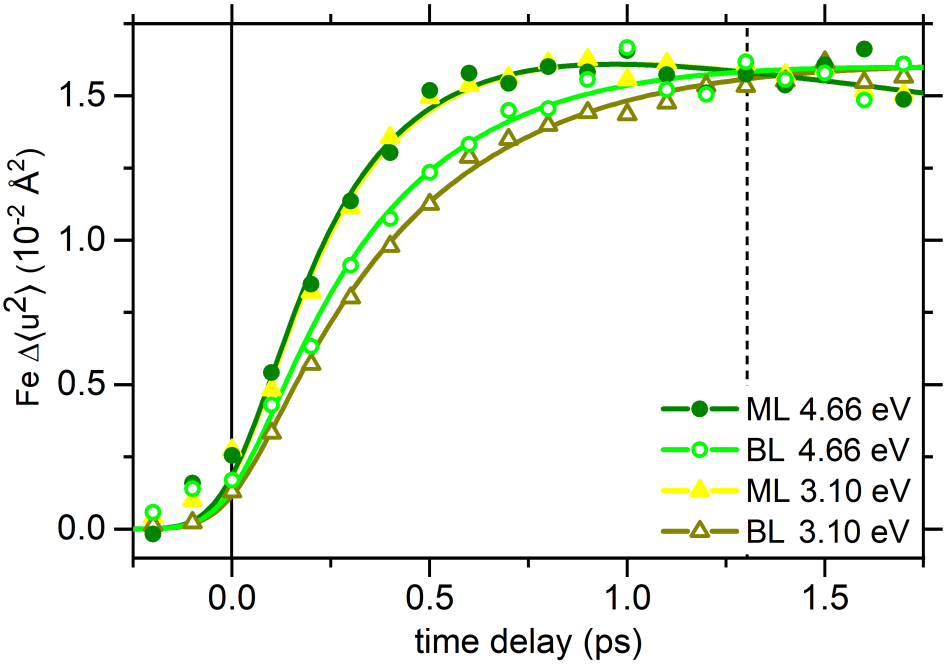

Fig. 4.12.: Change of the r.m.s. displacement $\Delta\langle u^2_{\mathrm{Fe}}\rangle(t)$ as a function of pump-probe time delay for the different sample configurations, namely a $[2\,\mathrm{nm\,Fe}/5\,\mathrm{nm\,MgO}]_5$ multilayer heterostructure (filled symbols) and a $[10\,\mathrm{nm\,Fe}/25\,\mathrm{nm\,MgO}]_1$ bilayer sample (open symbols). Both samples are measured for two excitation conditions, namely a laser pump photon energy of $4.66\,\mathrm{eV}$ (circles) and $3.10\,\mathrm{eV}$ (triangles). The incident laser fluence was set to $9\,\mathrm{mJ/cm^2}$. The solid curves represent fits to the measured data as explained in the text.

using laser photon energies of $4.66\,\mathrm{eV}$ (circles) and $3.10\,\mathrm{eV}$ (triangles). Additionally, the response of a $[2\,\mathrm{nm\,Fe}/5\,\mathrm{nm\,MgO}]_5$ multilayer heterostructure (filled symbols), with enhanced interface mediated effects to a $[10\,\mathrm{nm\,Fe}/25\,\mathrm{nm\,MgO}]_1$ bilayer sample (open symbols) is analyzed. The change of the r.m.s. displacement exhibit for all four configurations the same maximum $\Delta\langle u^2\rangle_{max}$ of $\approx 0.016\,\mathrm{Å}^2$, but at different delay times, which will be addressed further below. The excitation of the Fe lattice starts in all measurements at time zero. Furthermore, the data show that the response is independent of the pump photon energy, but exhibits clear differences for the two sample configurations.

To analyze the time evolution of the Fe atomic mean square displacement quantitatively, the data have been fitted by an exponential rise (with amplitude A_{r} and time constant τ_{r}) followed by an exponential decay (with amplitude A_{d} and time constant τ_{d}) convoluted with a Gaussian function of $200\,\mathrm{fs}$ FWHM to account for the finite electron pulse duration of the UED experiment:

$$\begin{aligned}\Delta\left\langle u^2_{\mathrm{Fe}}\right\rangle(t) \propto \int_{-\infty}^{\infty} d\tau \;\; e^{-\frac{(t-\tau)^2}{2\sigma^2}} \times \\ \times \left[\Theta(\tau)A_{\mathrm{r}}\left(1-e^{-\frac{\tau}{\tau_{\mathrm{r}}}}\right) - \Theta(\tau-\tau_{\mathrm{r}})A_{\mathrm{d}}\left(1-e^{-\frac{\tau-\tau_{\mathrm{r}}}{\tau_{\mathrm{d}}}}\right)\right].\end{aligned} \tag{4.3}$$

I want to note that while the electron pulse duration has not been explicitly measured in this experiment, the fitting parameters showed only minor changes when varying the electron pulse duration over a range from 150 fs to 300 fs. However, the best fits (judged from the onset of $\Delta\langle u^2\rangle$ at early delay times) have been obtained for a finite electron pulse duration of 200 fs. The resulting fits are shown in Fig. 4.12 by the solid curves together with the experimental data.
The heterostructure multilayer sample (filled symbols) exhibits a faster rise of the time dependence of $\Delta\langle u^2_{\mathrm{Fe}}\rangle(t)$ compared to the bilayer sample (open symbols). This faster rise time is independent of the initial laser pump photon energy. Hence, the differences in the rise times can be explained solely by interface effects, which contribute to an accelerated lattice response in Fe.

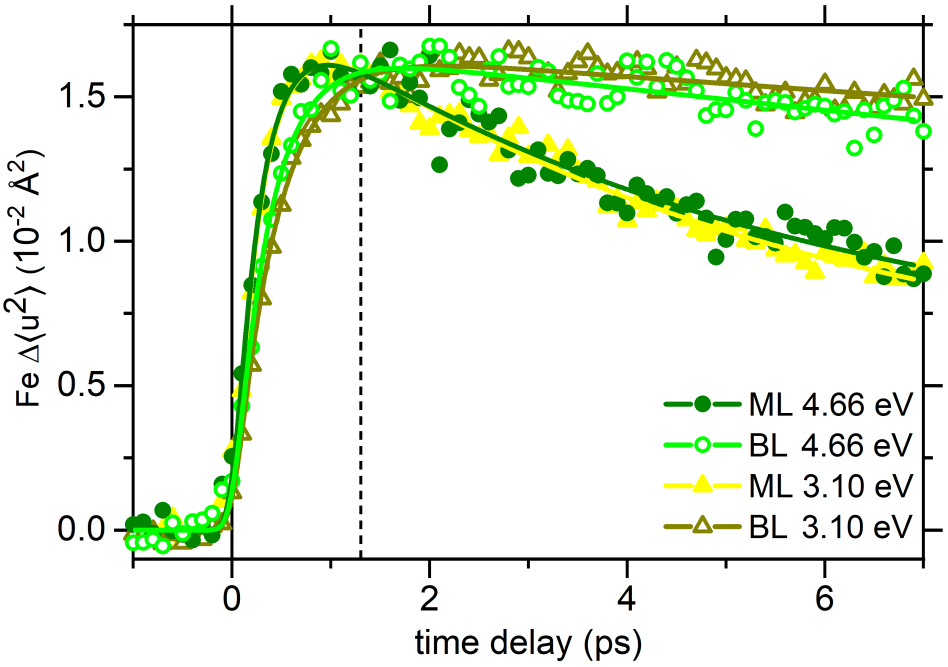

Fig. 4.13.: Same change of the r.m.s. displacement $\Delta\langle u^2_{\mathrm{Fe}}\rangle(t)$ as a function of pump-probe time delay for the two different sample configurations and excitation conditions as shown in Fig. 4.12 but over an extended pump-probe delay range.

Moreover, also the subsequent relaxation process exhibits clear differences between the multilayer and the bilayer sample, independent of the pump photon energy. Fig. 4.13 shows the same measurements as shown in Fig. 4.12 but over an extended pump-probe delay range, to point out the relaxation process more clearly. The decay occurs within 5 ps in the multilayer sample, whereas the corresponding decay time is almost an order of magnitude larger for the bilayer sample.

The measurements shown in Fig. 4.12 and Fig. 4.13 correspond to a maximum increase of the Fe r.m.s. displacement of $\Delta\langle u^2_{\mathrm{Fe}}\rangle_{max} \approx 0.016\,\text{Å}^2$. Additionally, the time dependence of $\Delta\langle u^2_{\mathrm{Fe}}\rangle(t)$ over an extended range of excitation fluences, corresponding to a $\Delta\langle u^2_{\mathrm{Fe}}\rangle_{max}$ ranging from $0.008\,\text{Å}^2$ to $0.042\,\text{Å}^2$ was measured. From

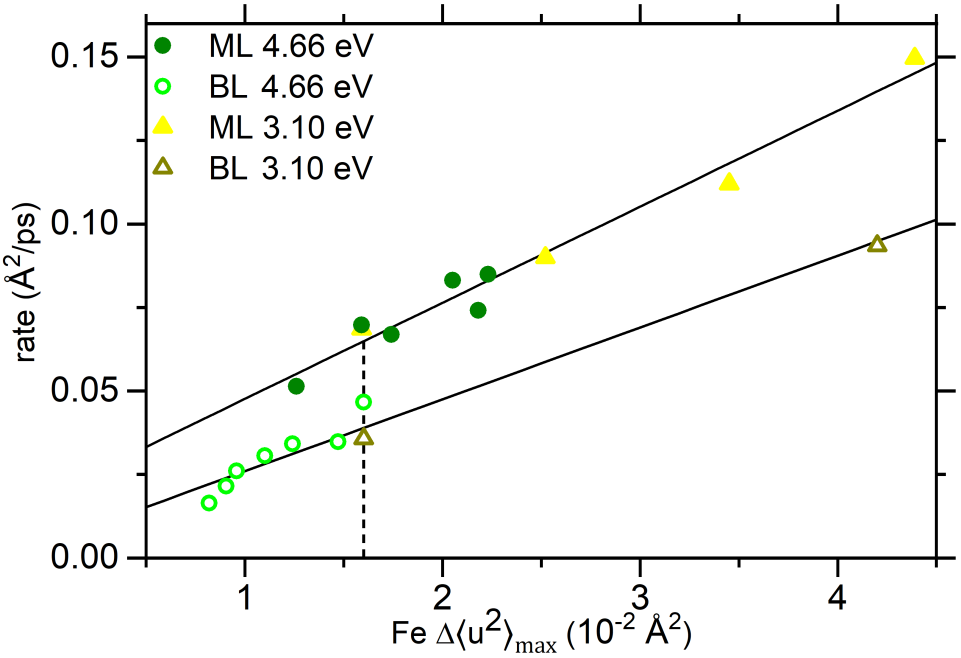

Fig. 4.14.: Maximum rate of the increase of $\Delta\langle u^2_{\mathrm{Fe}}\rangle(t)$ obtained from the fits as shown in Fig. 4.12 for a range of pump fluences. The different values of maximum $\Delta\langle u^2_{\mathrm{Fe}}\rangle_{max}$ were obtained from pump fluences ranging from 6 to 15 mJ/cm^2. Sample configurations and excitation conditions are the same as in Fig. 4.12, indicated by the symbols.

the amplitudes A_{r} and the time-constants τ_{r} of the initial exponential rise of resulting fits the maximum rate of the increase of $\Delta\langle u^2_{\mathrm{Fe}}\rangle(t)$ as a function of the maximum increase of the Fe r.m.s. displacement $\Delta\langle u^2_{\mathrm{Fe}}\rangle_{max}$ can be derived. Fig. 4.14 demonstrates the findings. Consistently with Fig. 4.12 and Fig. 4.13, all the time dependencies are independent of the two used pump photon energies, corresponding to the two different local pump scenarios (cf. chap. 4.2.1, Fig. 4.4), which is in agreement, and independently supports the results observed in XAS for the two different laser excitations (cf. chap. 4.2.2). All the measurements show clear differences between the two different sample configurations. Thus, the Fe-MgO interface mediated coupling clearly accelerates the electron-lattice equilibration in Fe. As will be discussed in the following chap. 4.2.4, I can conclude that *combined hot electron- and phonon-mediated processes at the interface are essential for the observed pump-induced dynamics of the Fe/MgO heterostructure*.

4.2.4 Combining XAS with UED, and *ab initio* theory

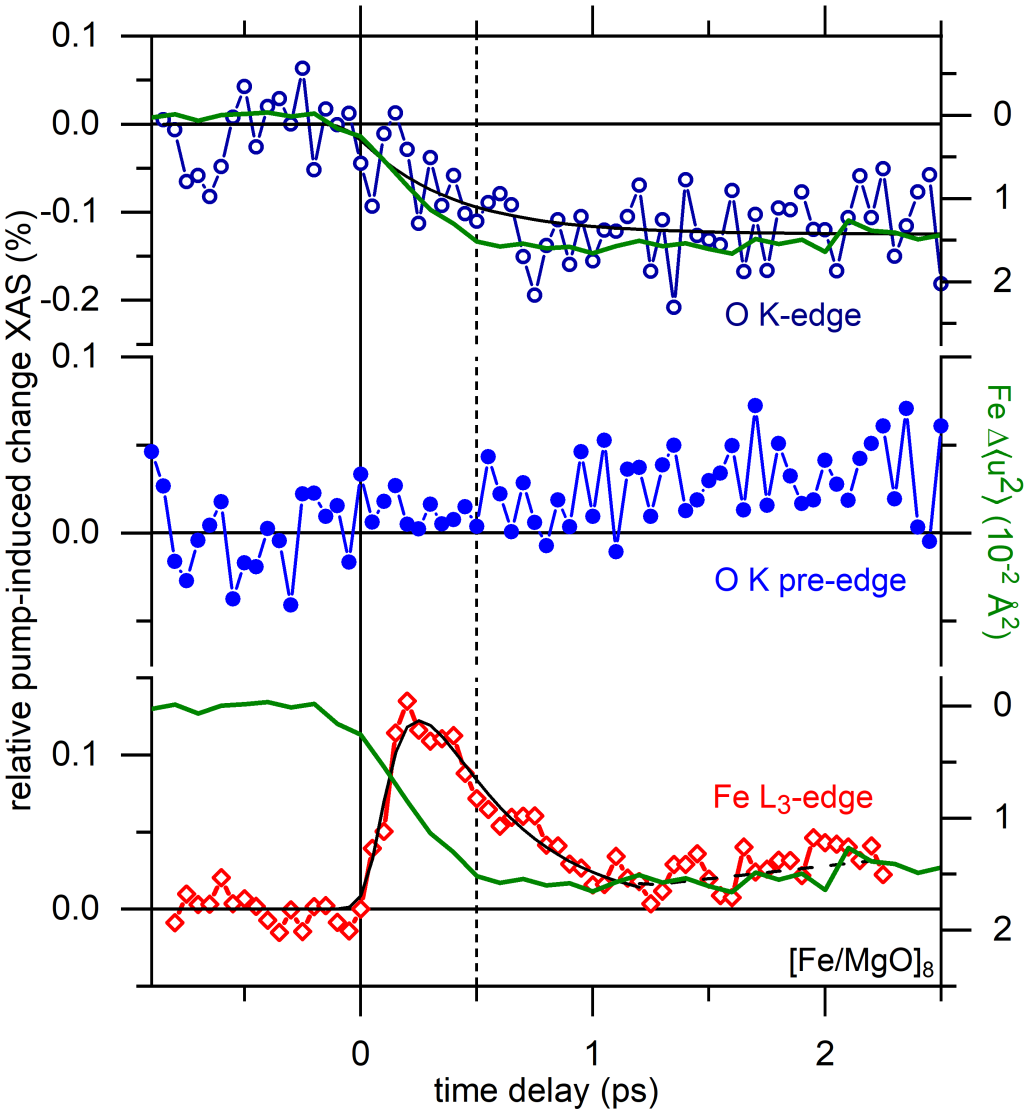

Fig. 4.15.: Pump-induced changes for the $[Fe/MgO]_8$ heterostructure sample after 4.66 eV laser pumping. Left axis: Changes in X-ray absorption spectroscopy from Fig. 4.6 at a fixed X-ray photon energy at the O K-edge (top panel), O K pre-edge region (middle panel) and Fe L_3-edge (bottom panel). Right axis: Transient of the Fe atomic mean square displacement $\Delta\langle u^2_{\mathrm{Fe}}\rangle(t)$ from Fig. 4.12, displayed in the top and bottom panel. The incident laser fluence was set to 20 mJ/cm^2 (XAS) and 9 mJ/cm^2 (UED).

The combination of the findings of the ultrafast soft X-ray spectroscopy measurements (chap. 4.2.2) and the results from the ultrafast electron diffraction measurements (chap. 4.2.3) yield a comprehensive insight into the microscopic processes in the metal-insulator heterostructure $[Fe/MgO]_n$ after localized optical excitation. Both ultrafast methods are complementary measurement techniques to analyze on ultrafast timescales the electronic and phononic contributions to the microscopic non-equilibrium energy transfer dynamics in these kinds of heterostructures. Fig. 4.15 shows the selected transient changes of both methods jointly: The pump-

induced changes in X-ray absorption spectroscopy at a fixed X-ray photon energy (cf. Fig. 4.6) are combined with the transient of the Fe atomic mean square displacement $\Delta\langle u^2_{\mathrm{Fe}}\rangle(t)$ (cf. Fig. 4.12) for the heterostructure multilayer sample after UV laser pumping with 4.66 eV. The pump-induced changes in XAS, measured as a function of pump-probe delay, are depicted on the left y-axes for a fixed X-ray photon energy at the Fe L_3-edge, O K-edge and O K pre-edge. The dynamic of the Fe atomic mean square displacement measured with UED is depicted in green on the right y-axes twice, once on top of the O K-edge transient, once on top of the Fe L_3-edge transient. Matching of time zero of the independent XAS and UED experiments is determined as the time delay at which the pump-induced changes begin, with a precision of ± 50 fs given the finite probe pulse durations. In the following, I will gradually break down Fig. 4.15, and discuss separately the dynamics happening in the Fe constituent, and the oxide constituent.

Dynamics of the Fe constituent

I start with the discussion of the dynamics of the Fe constituent and compare the time-dependent results of X-ray absorption and electron diffraction experiments: The time-dependent X-ray absorption signal of the Fe L_3-edge is characterized by an absorption increase, which reaches its maximum at 240 fs, see Fig. 4.15, bottom panel. This pump-induced dynamic results from a red-shift of the absorption edge and is in qualitative agreement with literature results for other transition metal films [60, 101, 149] and will be discussed in detail in chap. 4.3. The absorption of the laser pump pulse occurs in the Fe constituent within the pump pulse duration of 70 fs. However, the maximum X-ray absorption increase is reached well after the pump pulse. This can be explained by inelastic electron-electron (e-e) and hole-hole scattering of the primarily excited, non-equilibrium electron distribution, which leads to the relaxation and redistribution of electrons and holes towards E_F [11, 22]. Finally, the electrons thermalize at an electron temperature T_e higher than the initial static temperature T_0. The observed timescale of the initial rise corresponds to typical electron thermalization times in transition metals [15]. The subsequent relaxation of the absorption increase can be assigned to the dissipation of the excess energy out of the electronic system, which is mediated by the coupling to bosons [18]. The ultrafast electron diffraction measurements analyze the resulting lattice dynamics of the Fe constituent exclusively by measuring the transient of the mean square displacement $\Delta\langle u^2_{\mathrm{Fe}}\rangle(t)$ of the Fe ion cores, see Fig. 4.15, green curve. This probes the underlying electron-phonon (e-ph) coupling and, consequently, the dissipation of the excess energy out of the Fe electronic system.

Fig. 4.16 further compares the transients in X-ray absorption and $\Delta\langle u^2_{\mathrm{Fe}}\rangle(t)$ for the $[\mathrm{Fe/MgO}]_8$ multilayer sample with the dynamics measured in thicker Fe films,

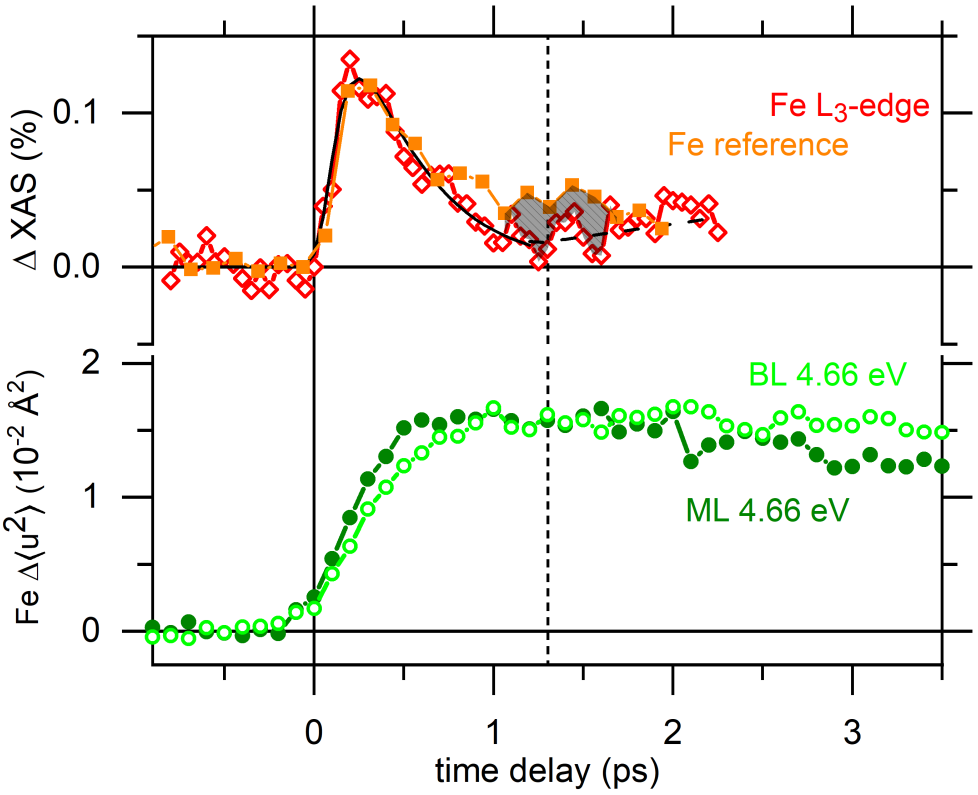

Fig. 4.16.: Comparison of the pump-induced changes after 4.66 eV laser pumping for the $[\mathrm{Fe/MgO}]_8$ multilayer sample with the dynamics measured in thicker Fe films, namely the 20 nm thick Fe reference sample and the $[10\,\mathrm{nm\,Fe/25\,nm\,MgO}]_1$ bilayer sample. Top panel: Changes in X-ray absorption. Bottom panel: Changes in $\Delta\langle u^2_{\mathrm{Fe}}\rangle(t)$. The incident laser fluence was set to $20\,\mathrm{mJ/cm^2}$ (top) and $9\,\mathrm{mJ/cm^2}$ (bottom).

namely the 20 nm thick Fe reference sample (XAS), and the $[10\,\mathrm{nm\,Fe/25\,nm\,MgO}]_1$ bilayer sample (UED). The UED measurements report that the heterostructure reaches the maximum of $\Delta\langle u^2_{\mathrm{Fe}}\rangle(t)$ already at 0.5 ps, while the bilayer sample reaches it not until 1.5 ps, and both transients cross at 1.2 ps (vertical line, see also Fig. 4.13). This crossing point matches with the minimum in the time-dependent X-ray absorption, which is reached for the heterostructure also at 1.2 ps. While the minimum in X-ray absorption indicates the dissipation of the electronic excess energy by the coupling to phonons, the maximum in $\Delta\langle u^2_{\mathrm{Fe}}\rangle(t)$ probes the phonon excitation of the Fe ion cores. Consequently, the energy transfer from the optically excited electrons to the lattice can be verified by the combination of the presented absorption and diffraction measurements. I want to stress that both experimental methods identify faster dynamics in the heterostructure compared to the dynamics measured in the thicker Fe films. Hence, both methods are able to probe the interface mediated coupling at identical time scales.

I further want to note that while the heterostructure exhibits in $\Delta\langle u^2_{\mathrm{Fe}}\rangle(t)$ a comparatively simple dynamic with only two time scales for the increase and subsequent decrease, the time-dependent Fe L_3-edge absorption shows in addition to the initial

increase and subsequent decrease a third time scale. This indicates a second, delayed process with increasing absorption for $t > 1.2$ ps. However, at these time delays, $\Delta\langle u_{\mathrm{Fe}}^2\rangle(t)$ is already decreasing, which represents energy dissipation out of the Fe lattice. Hence, for delay times $t > 1.2$ ps the heterostructure is thermalizing as a whole. Since this second increase in absorption is not observed for the Fe reference sample, it has to be related to the presence of the Fe-MgO interfaces. I will discuss the origin of this second, delayed process further below.

Dynamics of the oxide constituent

Now, I want to turn the attention to the discussion of the dynamics of the oxide constituent, which is probed by the time-dependent X-ray absorption measurements at the O K-edge, see Fig. 4.15, top panel. The measurements show an absorption decrease that saturates within 500 fs. Interestingly, the transient behavior of the O K-edge matches well with the transient increase in $\Delta\langle u_{\mathrm{Fe}}^2\rangle(t)$, see Fig. 4.15, green line. This implies that the Fe lattice, as well as the MgO constituent, have to be excited in parallel.

Since the laser pump pulse primarily excites the Fe constituent, the pump-induced change in XAS at the O K-edge represents a transfer of excitations from Fe to MgO. The maximum change in absorption is reached at a significantly later delay time for the O K-edge compared to the Fe L_3-edge. However, a direct charge transfer should occur on a significantly shorter time scale, namely with the change observed for the Fe constituent, as shown in [150]. In agreement with this, and independently of the laser photon energy, an equal transient behavior in XAS was observed (cf. Fig. 4.9). Consequently, this proves that *the change in the oxide is not related to the transfer of hot electrons from Fe to MgO*.

Furthermore, this conclusion agrees with the observation in time-resolved UED. I reported that the lattice dynamics in the heterostructure is also independent of the pump photon energy (cf. Fig. 4.12). The dynamics of the O K-edge can be understood as follows: An excited electron in Fe with excess energy of $E - E_{\mathrm{F}} > 3.8$ eV, which could potentially transfer elastically from Fe into the conduction band of MgO (cf. Fig. 4.4, process 1) has a lifetime of only several fs [153]. The ultrafast relaxation of the excited electron is mediated by inelastic e-e scattering in Fe. Since the formation of a hot electron temperature occurs within 200 fs [15], the local e-e scattering in Fe competes with the hot electron transfer to MgO. Moreover, and even if an excited electron exhibits a direct charge transfer to MgO, it would gain the energy of Δ=3.8 eV by transferring back to the Fe constituent and subsequent relaxation to E_{F}. Consequently, all of the experimental results indicate, consistently, that the localized relaxation process due to e-e scattering in Fe dominates this competition, whether or not a hot electron charge transfer would take place.

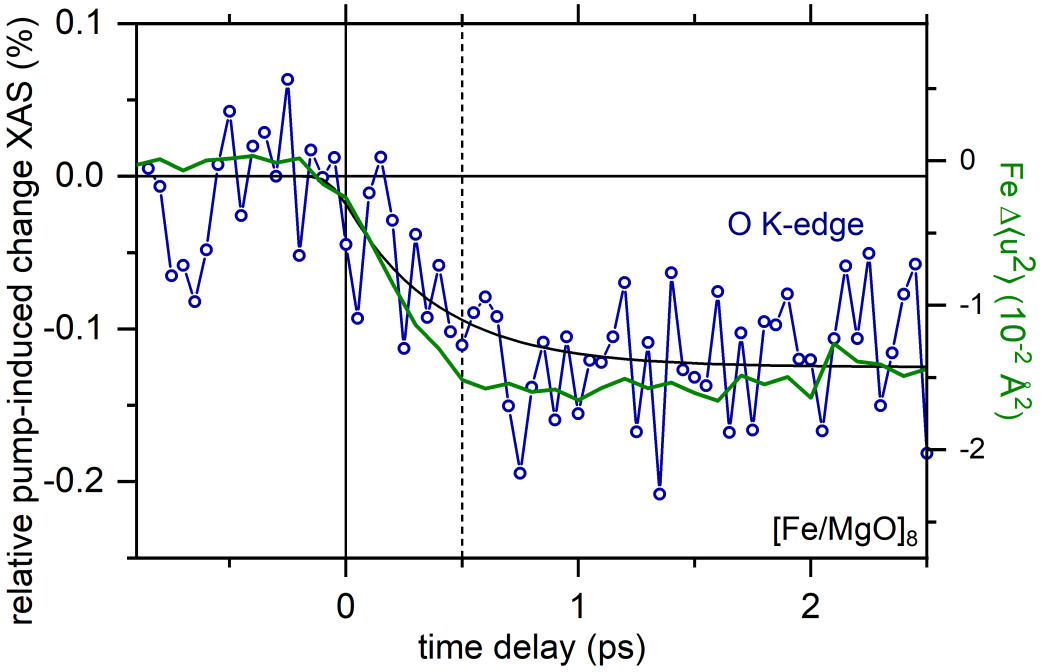

Fig. 4.17.: Pump-induced changes for the $[Fe/MgO]_8$ heterostructure sample after $4.66\,eV$ laser pumping. Left axis: Changes in X-ray absorption spectroscopy at a fixed X-ray photon energy at the O K-edge. Right axis: Transient of the Fe atomic mean square displacement $\Delta\langle u^2_{Fe}\rangle(t)$. The incident laser fluence was set to $20\,mJ/cm^2$ (XAS) and $9\,mJ/cm^2$ (UED). The figure is equal to Fig. 4.15, top panel, and shown here again to highlight the respective transients.

I found that the initial hot electron population remains localized in Fe and derived that the transfer of the excitation from the metal to the insulator is mediated by phonons. Fig. 4.17 shows that the lattice excitation in Fe and MgO builds up simultaneously and starts at time zero. Hence, the energy flow from Fe to MgO requires either, on the one hand, a coupling of hot, thermalized electrons in Fe to hybrid phonon modes at the Fe-MgO interface. Or it requires the coupling of these hot electrons to bulk phonons in Fe, which then couple to phonons in MgO. As I described in chap. 2.1, the second possible mechanism is widely considered in the diffuse mismatch model [49]. Here a temperature gradient drives the energy transfer across the interface, which is described by a thermal boundary conductance. I stress that the reported timescale related to this mechanism is in the range of about $10\,ps$, or longer [54]. Furthermore, it requires the thermalization of the lattice excitations by phonon-phonon coupling on similar timescales [20]. However, the measurements showed that the increase of the O K-edge signal starts instantly before the e-ph equilibration in Fe occurs. Hence, I exclude this thermal mechanism as the explanation for the ultrafast excitation of the MgO constituent.

The other possible mechanism for the energy transfer is similar to a process that determines, in a thermal picture, an electronic Kapitza conductance. It was reported [43] that at a metal-insulator interface electrons on the metallic side can couple to hybrid phonon modes which are localized directly at the interface, and decay into

both constituents. For other heterostructures [56, 154], such a coupling was found to be essential for the observed dynamics. Here it was reported that thinner samples with two instead of only one interface show a faster relaxation, which has been attributed to a coupling of hot electrons in the metal to interface vibrational modes [43, 44]. Following these findings, I derive for the dynamics of the investigated [Fe/MgO] heterostructure system, that an *energy transfer to hybrid phonon modes which are localized at the Fe-MgO interface represents an additional channel for the hot electrons in Fe to relax into, as long as the electron and lattice systems in Fe have not yet equilibrated*. Furthermore, this explanation is supported by the findings of the comparison of the pump-induced response at the Fe L_3-edge of the $[Fe/MgO]_8$ heterostructure to the Fe reference sample (cf. Fig. 4.6). I showed that the presence of the Fe/MgO interfaces accelerates the dissipation of the excess energy out of the Fe electronic subsystem.

Layer-resolved *ab initio* DFT calculations

To support and deepen the findings I achieved by combining both ultrafast, complementary measurement methods, layer-resolved *ab initio* DFT calculations have been conducted. All in the following presented *ab initio* DFT calculations have been carried out by M. E. Gruner from the University of Duisburg-Essen. In the calculations, the $[Fe/MgO]_n$ heterostructure is represented by a reduced, periodically repeated heterostructure $[Fe_8/(MgO)_8](001)$ consisting of eight monolayers Fe and eight monolayers of MgO stacked along the (001) direction. In more technical detail (see also [42]): The calculations were carried out in the framework of density functional theory (DFT) using the generalized gradient approximation (GGA) in the formulation of Perdew, Burke, and Ernzerhof (PBE) [155]. It was started with the structural optimization of the 24 atom primitive cell with respect to atomic positions and lattice parameters using the VASP code [156, 157]. PAW potentials with the electron configurations $3p^6 3d^7 4s^1$ for Fe, $2p^6 3s^2$ for Mg and $2s^2 2p^4$ for O and an energy-cutoff of 580 eV have been used. The calculations of the structural optimization were considered converged when the energy fell below 10^{-8} eV between two consecutive electronic optimization steps and 10^{-6} eV between two geometric optimization steps. Subsequently, Brillouin zone integration on 90 k-points in the irreducible Brillouin-zone in combination with a Gaussian-type Fermi-surface smearing with a width of $\sigma = 0.1$ eV has been carried out. Using this optimized structure, allowed finally to calculate either the electronic or vibrational density of states (DOS), or the resulting X-ray absorption spectra of the $[Fe/MgO]_n$ heterostructure. In the following, I shortly outline the details for all the different approaches used by M. E. Gruner for the *ab initio* DFT calculations shown in this chap. 4.2.
The layer- and spin-resolved electronic DOS of the Fe and MgO constituent of the [Fe/MgO] multilayer results by applying the so-called tetrahedron method with

Blöchl-corrections [158], using $408\,k$-points for the Brillouin-zone integration.
To calculate the phonon dispersion and the corresponding vibrational density of states (vDOS), the so-called direct approach, based on the restoring forces obtained from central differences between 2×24 displacements of inequivalent atoms in a 768 atom supercell, was used. The supercell itself was constructed as a $4 \times 4 \times 2$ replication of the initial 24 atom primitive cell. Implementing a k-mesh of $5 \times 5 \times 1$ points in the full Brillouin-zone in combination with Gaussian smearing of $\sigma = 0.05$ eV width guarantees the required accuracy. With this, the dynamical matrix and the resulting vDOS can be obtained by employing the PHON code by Dario Alfè [159].
Furthermore, the X-ray absorption spectra for the O K-edge and the Fe $L_{3,2}$-edges have been calculated in an atomic layer resolved manner by employing the spin-polarized relativistic Korringa-Kohn-Rostoker (SPRKKR) multiple scattering approach [160, 161]. A contour integration on an arc with 48 energy points was carried out, which corresponds to $1134\,k$-points in the irreducible Brillouin-zone, and an angular momentum expansion included d-states until the convergence criterion of 10^{-6} Ry was achieved. The X-ray absorption spectra are obtained within the independent particle approximation. The calculated spectra are broadened with a Lorentzian with a width of 0.2 eV, and subsequently shifted on the energy scale by a constant offset to match the experimental peak at the O K-edge and the Fe L_3-edge, respectively.

Fig. 4.18 shows the calculated spin-polarized layer-resolved electronic DOS for the majority and minority spin directions of the MgO (left) and Fe constituent (right) of the $[Fe_8/(MgO)_8](001)$ heterostructure. I restrict the comparison to the central and interface layers of each constituent. However, full layer-resolved calculations of the electronic DOS can be found in Fig. A.1 of the attachment. The contribution of Fe is represented by the red lines, Mg by the dotted pink lines, and O by the dashed cyan lines. The sum of the Mg and O contributions is indicated by the dark blue area. Both central layers report, as expected, an electronic DOS similar to the respective bulk materials. For the Fe central layer, the Fermi-level crosses the upper edge of the majority d-band and passes through a wide valley in the minority channel. For the MgO central layer, the electronic DOS shows a clear insulating state with a valence band maximum located 3.3 eV below the Fermi energy E_F. In contrast to the central layers, strong modifications in the partial DOS of the Fe and MgO interface layers can be identified. Due to the strong hybridization of Fe d- and O p-orbitals, a considerable amount of interface states arises throughout the gap region. Especially two distinct, pronounced features in the minority channel of Fe stand out: On the one hand, a large peak, located approximately 0.2 eV above the Fermi level appears. This feature has predominantly d_{xz} and d_{yz} character and hybridizes with the p_x- and p_y-orbitals of the O contribution of the MgO constituent. On the other hand, features in Fe around 2 eV above E_F can be found. These consist of $d_{3z^2-r^2}$ orbitals,

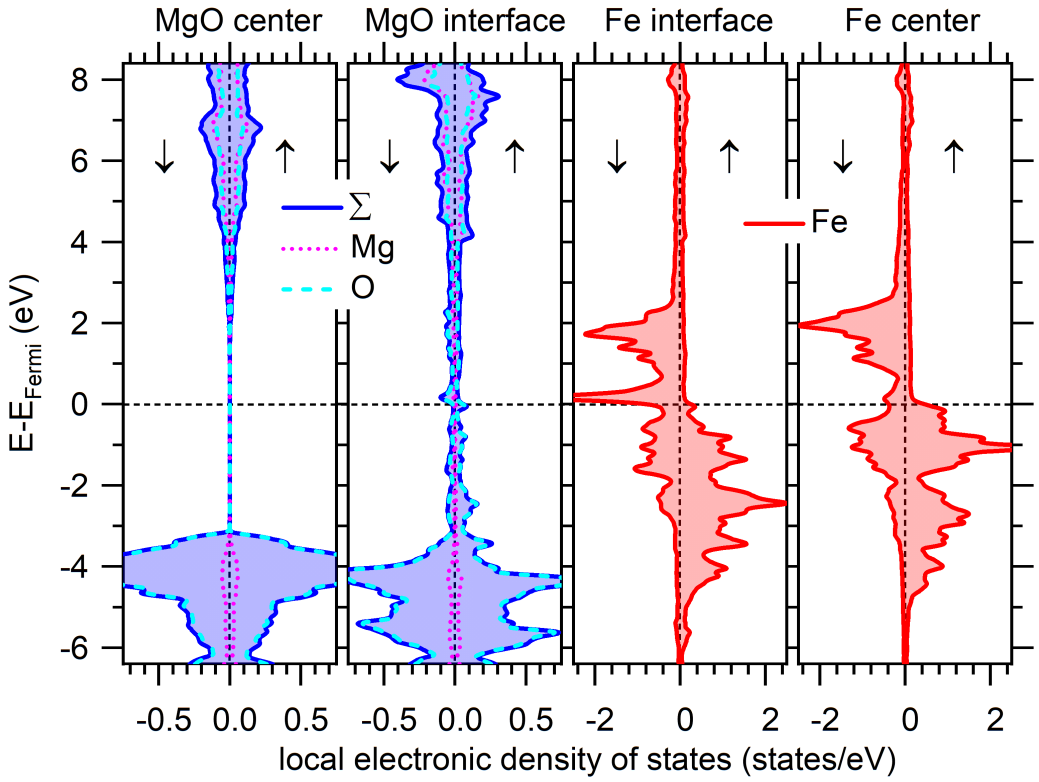

Fig. 4.18.: Spin-polarized element- and layer-resolved electronic density of states of $[Fe_8/(MgO)_8](001)$ obtained from DFT calculations. Only the interface layers (middle) and the central layers of the slabs (leftmost panel for MgO and rightmost for Fe) are shown. The contribution of Fe is represented by the red lines, Mg by pink dotted lines and O by the cyan dashed lines. The sum of Mg and O contributions is indicated by the blue area. Upward and downward arrows denote the respective spin channels. While the central layers are similar to the respective bulk materials, pronounced features close to the Fermi energy appear in both interface layers arising from the strong hybridization between the Fe d-states and the p-states of the apical O. The entire electronic DOS including the four intermediate layers is provided in the attachment.

which leads to an increased p_z character of the states at the O interface contribution. Overall it can be concluded from the calculations that the electronic structure of the investigated [Fe/MgO] heterostructure is in its central layers, mostly unaffected. However, when discussing in fine detail the microscopic non-equilibrium energy transfer dynamics from one constituent to the other, a relevant contribution to the dynamics can be expected, due to pronounced electronic interface states of Fe-MgO hybrid character.

Fig. 4.19 shows the calculated layer-resolved vibrational density of states (vDOS) of the $[Fe_8/(MgO)_8](001)$ heterostructure. Again I restrict the comparison to the central and interface layers of each constituent. However, full layer-resolved calculations of the vDOS can be found in Fig. A.2 of the attachment. The calculated

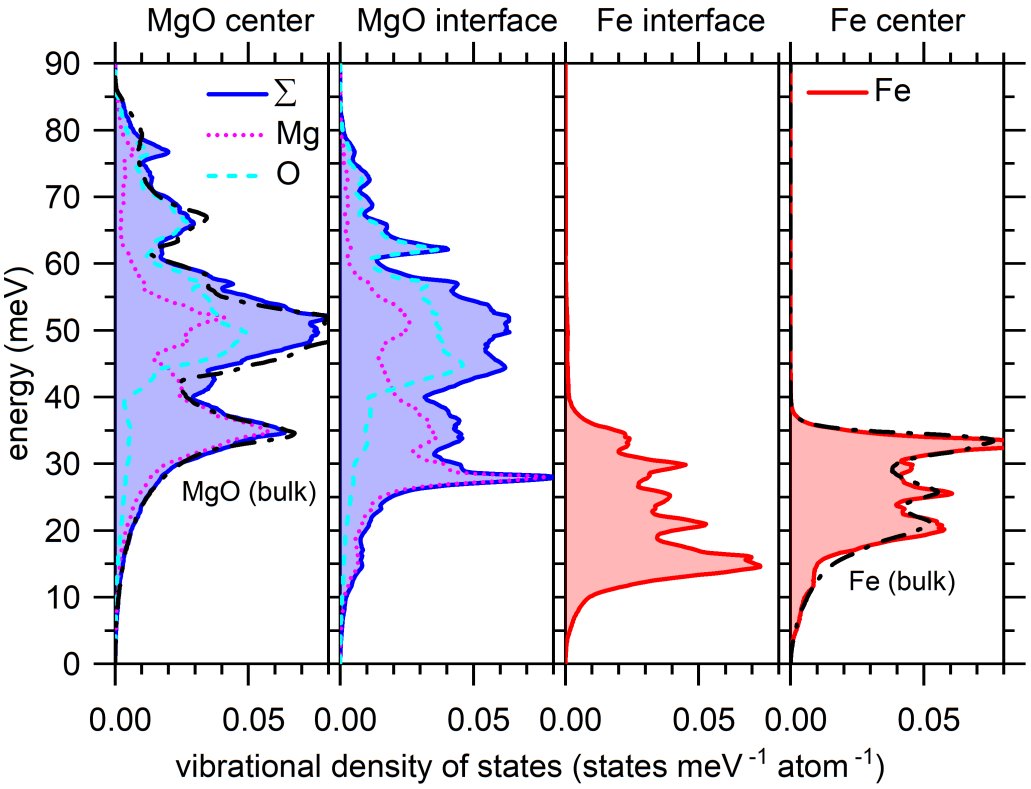

Fig. 4.19.: Layer-resolved vibrational density of states of $Fe_8/(MgO)_8(001)$ obtained from DFT calculations. The contribution of Fe is represented by the red lines, Mg by pink dotted lines and O by the cyan dashed lines. The sum of Mg and O contributions is indicated by the blue area. The respective vDOS of the bulk materials is shown by the black dashed lines. Again, I show only the central layers of the slabs (leftmost panel for MgO and rightmost for Fe) and the interface layers (middle). The entire vDOS including the four intermediate layers is provided in the attachment.

vDOS agrees well with experimental findings from ^{57}Fe nuclear resonant inelastic X-ray scattering (NRIXS) measurements on comparable samples [162]. In the discussion of the dynamics of the oxide constituent, I showed that the transfer of the excitation from the metal to the insulator constituent is mediated by phonons. The layer-resolved vDOS can now provide insight on which phonon modes are contributing to this process. Fig. 4.19 indicates that at energies above the acoustic phonons, which have a rather small vDOS, the [Fe/MgO] heterostructure exhibits a sizeable vDOS for both, the center and the interface layers. While the MgO center layer shows a peak in the vDOS at 35 meV, this peak is found at the MgO interface layer already at 27 meV. Furthermore, also the Fe constituent exhibits for the center layer as well as for the interface layer a sizable vDOS at these energies. In the Fe interface layer, a clear interface mode at 15 meV is reported, which couples to the MgO constituent as indicated by the bump in the vDOS of the MgO interface layer at the same energy. More precisely, it is the contribution of Mg to the MgO vDOS, which forms the coupling to Fe.

The layer-resolved calculation in Fig. 4.19 show that both constituents of the heterostructure exhibit a high vDOS at the interface layers which corroborates the following scenario: (i) *The energy transfer across the Fe/MgO interface on the sub-ps timescale* (cf. Fig. 4.17) *is predominantly mediated by the coupling of hot electrons in Fe to combined high-frequency interface phonon modes in Fe and MgO* at phonon energies at 15 meV and above. I want to note that due to the small film thickness of the single constituents of the multilayer of only 2 nm, the vibrational amplitude of the interface phonons is not localized at the interface but reaches well into the individual layer.
(ii) *Subsequently, these excited high-frequency interface vibrational modes couple to bulk phonon modes in MgO in a mode-selective, non-thermal manner. This leads to an initially highly non-thermal, hot phonon population in MgO.*
(iii) Finally, *on the timescale of* $t > 1$ *ps* both ultrafast, complementary measurement methods identify a second, slower timescale, which can be attributed to the *thermalization of the heterostructure as a whole and an energy transfer across the interface, which involves a different subset of phonons, namely lower energy phonons*.

Furthermore, I want to recall that the presented MeV UED experiment measures, due to the experimental geometry, only the incoherent lattice excitation in the heterostructure, but is not sensitive to any possible coherent strain wave propagation normal to the layer stack. Even though it was reported in literature that an ultrafast optical excitation can also generates coherent acoustic phonons [163–168], which occur concurrently to the incoherent lattice excitation [164]. The temporal evolution of the coherent acoustic phonons is typically reflected, for a uniform ultrafast heating, by a periodic breathing motion along the surface normal, with an oscillation period given by the sound velocity of the material and the film thickness. Given the MgO single layer thickness of $L = 2$ nm and a longitudinal sound velocity of $v_S \approx 9.2$ nm/ps for MgO at room temperature [169], the resulting periodicity $T = 2L/v_S$ of the coherent acoustic wave [164] generated in MgO would be with $T \approx 0.43$ ps indeed in the order of the observed transients. However, I stress that the time-dependent XAS at the O K-edge (cf. Fig. 4.17) does not show any characteristic oscillatory behavior, which should occur in case the dynamics in MgO would be caused by coherent acoustic phonon modes. Therefore, I am confident to exclude any significant influence of coherent acoustic waves to the observed dynamics. Consequently, the agreement of the timescale of the incoherent lattice excitation of Fe observed in the UED experiment with the timescale of the excitation of the MgO constituent observed in XAS is governed by the coupling of hot electrons in Fe to high-frequency interface phonon modes above 15 meV phonon energy between Fe and MgO.

O K pre-edge dynamics

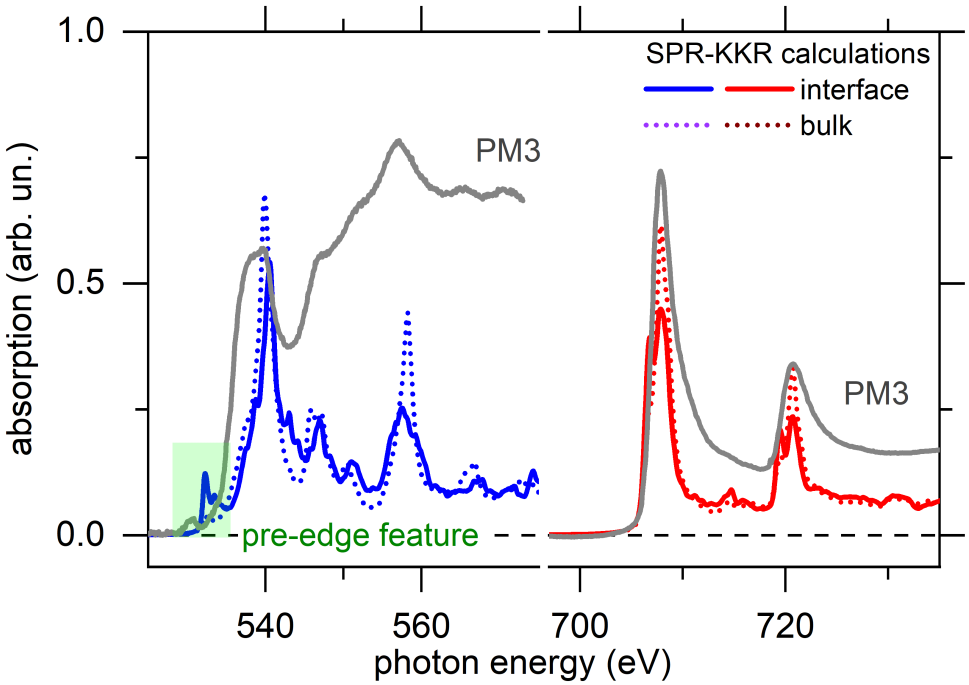

Fig. 4.20.: High-resolution X-ray absorption spectra of $[Fe/MgO]_4$ with 2 nm individual layer thickness measured in transmission geometry (grey lines), normalized to the incident X-ray intensity. The Fe spectrum (right) is composed of the L_3- and L_2-edges. The spectrum at the O K edge (left) contains several features in agreement with literature [170–172] and the green area highlights the pre-edge feature assigned to an interface state, see text. Calculated atomic layer-resolved spectra of $Fe_8/(MgO)_8$ are shown by the red (Fe) and blue (MgO) lines. Spectra at the interface are shown by a solid, those from the center of the respective layers by a dashed line.

As I indicated throughout this chapter (e.g., in Fig. 4.6 or Fig. 4.15) the pump-induced changes in XAS as a function of pump-probe delay have been measured not only at the energetic position of the absorption edge where also the maximum pump-induced change is observed, but also at the O K pre-edge region. The change observed in the O K pre-edge region has an even slower increase than the corresponding edge itself and is continuously increasing within the investigated time delay. Furthermore, this slow change can be described by the same linear increase as the second increase at later time delays at the Fe L_3-edge XAS. Hence, understanding the origin and behavior of the O K pre-edge and its pump-induced change seems to be crucial for the understanding of the energy flow dynamics of the Fe/MgO heterostructure at longer time delays.

Fig. 4.20 shows the calculated layer-resolved X-ray absorption spectra for the O K-edge (left) and the Fe $L_{3,2}$-edges (right) together with high-resolution experimental spectra ("PM3", grey). The high-resolution X-ray absorption spectra were also measured at the synchrotron BESSY II, but at the beamline PM3 using a plane grating monochromator and the ALICE endstation. The high-resolution spectra

have been measured by A. Eschenlohr, and C. Schmitz-Antoniak before the work of this Ph.D. thesis started. The comparison of the experimental spectra with the calculations shows an overall agreement of the relative positions of all the main features. The measured O K-edge spectrum clearly shows a small pre-edge feature at ~ 532 eV. In the calculated layer-resolved spectra, this O K pre-edge feature can be clearly identified in the spectrum of the interface layer. In contrast, the spectrum of the center layer lacks this feature. Therefore, the O K pre-edge feature can be assigned to an Fe-MgO interface state. This is also in agreement with literature [170, 172], where it was shown that such a pre-edge feature can occur at a MgO-metal interface but not in bulk MgO. I want to note that the small interface-induced changes obtained in the calculations at the Fe $L_{3,2}$-edges were not resolved in the experiment.

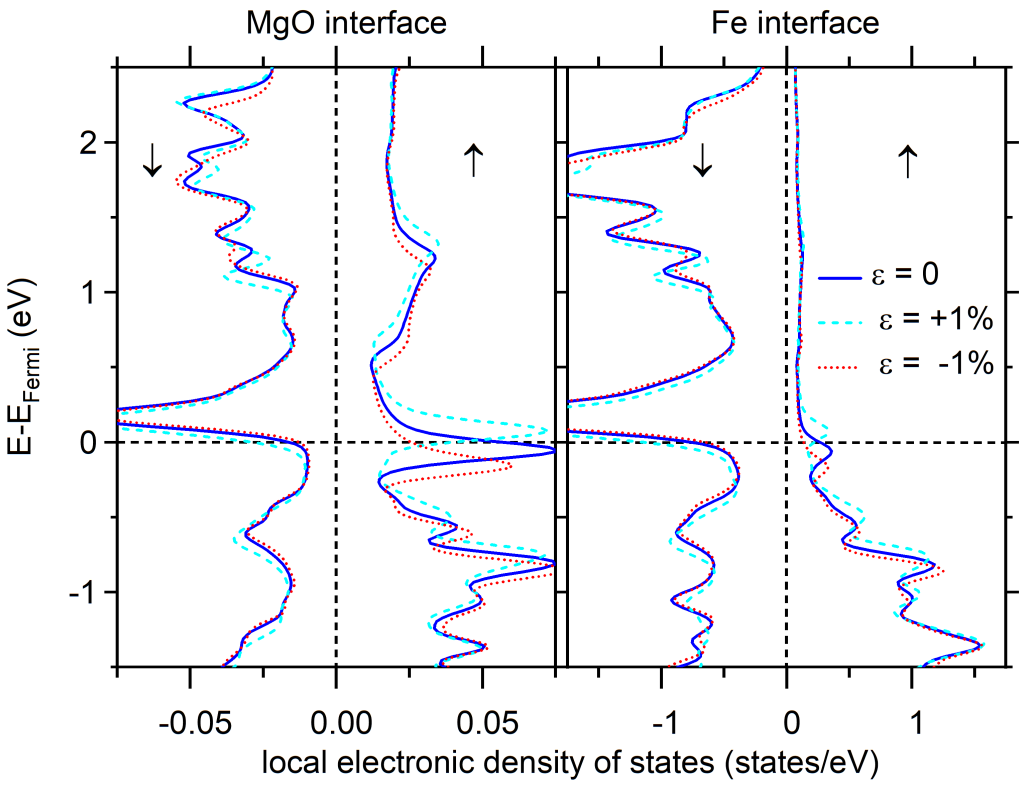

Fig. 4.21.: Layer-resolved electronic density of states under 1 % compression (cyan, dashed line) and expansion (red, dashed line) of $Fe_8/(MgO)_8(001)$ at the Fe-MgO interface obtained from DFT calculations. 1 % compression and expansion maintain the hybrid character of the interface states. The strongest response to lattice compression/expansion is found for majority electronic states (↑) of the interface at O sites, second panel from the left, witch shifts of up to 0.1 eV. Similar shifts are observed for the Fe majority interface states, while the minority states in both Fe and O shift by about 0.03 eV per 1 % compression (or expansion).

Fig. 4.18 showed that the O K pre-edge feature originates from hybridized states of Fe d- and O p-orbitals at the interface, which are located close to the Fermi level. This energetic position of the hybridized states makes them very sensitive to local

lattice distortions. Fig. 4.21 shows the same calculated spin-polarized layer-resolved electronic DOS of Fig. 4.18 (blue solid line) under $1\,\%$ compression (cyan, dashed line) and expansion (red, dashed line). I restrict the response of the electronic density of states to uniaxial lattice compression and expansion to the interface layers of each constituent. However, the full layer-resolved calculations can be found in Fig. A.3 of the attachment. The results show that both the modeled $1\,\%$ compression, or $1\,\%$ expansion maintain the hybrid character of the interface states. Furthermore, these interface states respond significantly due to the applied lattice compression (or expansion), while the center layers barely show any changes. In more detail, the strongest response to lattice compression (or expansion) is reported for the majority electronic states (indicated by the up-arrow $\uparrow$) of the interface at the O sites as well as for the Fe majority interface states. Both these states exhibit shifts of up to $0.1\,\text{eV}$. The minority states for the Fe and O site shift by about $0.03\,\text{eV}$ per $1\,\%$ compression (or expansion).

Consequently, the observed pump-induced changes in XAS at the O K pre-edge suggest the following: Due to the different static thermal expansion coefficients of MgO and Fe [173], a local lattice distortion at the interface starts to build up on a timescale of $1\,\text{ps}$ and longer. As shown in Fig. 4.21, such a lattice distortion shifts the position of the interface states. Since the O K pre-edge feature can be unambiguously assigned to the Fe-MgO interface state (cf. Fig. 4.20), such a shift will directly affect the resonant absorption at the O K pre-edge. Thus, the observed second change in XAS at the Fe L_3-edge at delay times of $t > 1\,\text{ps}$ (cf. Fig. 4.15) can finally be understood. I already related this second increase in absorption to the presence of the Fe-MgO interfaces since it is only visible for the transient of the heterostructure and not for the Fe reference sample. Due to the hybridization of O and Fe at the interface and the significant response of the electronic states of both sites to lattice distortion, a similar origin for the pump-induced changes observed at the O K pre-edge and the Fe L_3-edge for delay times of $1\,\text{ps}$ and longer can, therefore, be anticipated.

4.2.5 Summary: Non-equilibrium energy transfer dynamics

In this chap. 4.2, I reported on the microscopic non-equilibrium energy transfer dynamics in a photo-excited metal/insulator heterostructure, using $[Fe/MgO]_n$ as a model system. Since this chapter represents the focal point of this thesis, and the presented results will be revisited throughout the upcoming chapters, I will present already here a small summary of the findings. I showed complementary time-resolved X-ray absorption spectroscopy and ultrafast electron diffraction experiments to analyze and disentangle the electronic and phononic contributions to the dynamical processes induced on ultrafast timescales after the localized optical excitation of the metal constituent. Together with *ab initio* calculations, both pump-probe methods yield a comprehensive insight into the microscopic processes leading to local relaxation within a single constituent and non-local relaxation between the two constituents. I concluded on two different phonon-mediated energy transfer mechanisms acting in the $[Fe/MgO]_n$ heterostructure. Therefore, I divide the findings on the dynamics on the $t < 1$ ps timescale, and on the $t > 1$ ps timescale.

Dynamic on the $t < 1$ ps timescale

The 50 fs, UV or IR laser pump pulse excites the electronic system of the Fe constituent of the $[Fe/MgO]_n$ heterostructure exclusively. The highly non-equilibrium Fe electronic subsystem then thermalizes within the first hundreds of femtoseconds by electron-electron scattering. As a consequence, the pump-induced change in the soft X-ray absorption at the Fe L_3-edge peaks at a pump-probe delay of 240 fs, which indicates this localized electronic excitation in Fe. However, the experiments did not show any indications of a direct hot electron charge transfer from Fe to MgO across the interface. The direct charge transfer competes with the localized relaxation processes due to electron-electron scattering in the Fe constituent itself. Hence, it can be concluded that the latter process dominates this competition, which is essential for the understanding of the subsequent dynamics of the heterostructure. Both, the change in X-ray absorption at the O K-edge, which probes the MgO constituent and saturates at 500 fs, and the increased mean square displacement of the Fe ion cores probed in ultrafast electron diffraction, build up simultaneously. This indicates that the Fe hot electronic subsystem redistributes its initial input energy via phononic processes among the heterostructure due to the coupling to an interfacial Fe-MgO phonon mode. The layer-resolved *ab initio* calculations of the vibrational density of states find a pronounced overlap of high-frequency phonons above 15 meV phonon energy between Fe and MgO at the interface. Therefore I can conclude that the ultrafast energy transfer across the Fe-MgO interface is *mediated*

by high-frequency interface vibrational modes. These interface vibrational modes then couple to vibrations in MgO in a mode-selective, non-thermal manner leading to an *initially highly non-thermal, hot phonon population in MgO*. Consequently, as frequently questioned in literature [20, 21, 31], the assumption of a thermal distribution function of the lattice in the description of the ultrafast dynamics as it is done, i.e., in the 2TM (cf. chap. 2.1), indeed cannot be applied to truly describe the sub-ps dynamics after laser excitation. In agreement with the ongoing debate, I reported here that a non-thermal phonon system plays a crucial role for the initial step of the energy redistribution.

Dynamic on the $t > 1$ ps timescale

For time delays of $t > 1$ ps both of the ultrafast pump-probe experiments identify a second, slower energy transfer process. In the UED experiment, a receding of $\Delta\langle u^2_{\mathrm{Fe}}\rangle(t)$ was reported, indicating the coupling of Fe vibrations in the heterostructure to the MgO constituents, which act as sinks for the vibrational excess energy. In XAS, at these later delay times after UV laser excitation, increasing signals at the Fe L_3-edge as well as at the O K pre-edge have been observed. Consequently, I attribute this second, slower process to an energy transfer across the interface mediated by acoustic, lower energy phonons, which contributes to the thermalization of the entire heterostructure. I thus showed that the interfacial energy transfer is associated with non-equilibrium behavior in the phonon system. Finally, on a timescale of some 10 ps phonon thermalization occurs [20], and all the different phonon sub-systems are equilibrated. Hence, the complete heterostructure will be close to its fully thermalized state. Due to the considerably larger specific heat of the lattice relative to the one of the electrons, the major part of the excess energy is then hosted by the phonon sub-systems of the Fe- and MgO-constituent of the heterostructure.

4.3 Spectroscopic fine structures of pump-induced changes in soft X-ray absorption spectroscopy of a Fe/MgO multilayer

In chap. 4.2, I concentrated mostly on the *time-dependent dynamics* in the Fe/MgO heterostructure at a fixed photon energy. In the course of this, I focused in the conducted X-ray absorption measurements exclusively on the *femtosecond* timescale. However, I noted already here, that the two different absorption edges exhibit two fundamentally different spectral signatures. Therefore, the focal point of this chap. 4.3 is the analysis of the time-resolved modification of the fine structures of the X-ray absorption spectra. I start with the understanding of the *spectral changes* in *picosecond* time resolution, since I conducted here a systematic study of the changes with the pump fluence (cf. chap. 4.3.3).

4.3.1 Pump-induced spectroscopic changes with picosecond time resolution

Fig. 4.22 shows in the top half, similar to chap. 4.2, Fig. 4.5, the measured X-ray absorption spectra of the $[Fe/MgO]_8$ heterostructure at the O K-edge (left) and the Fe L_3-edge (right). Again, the spectra are measured before excitation with a laser pump pulse (so-called unpumped spectrum) and after excitation (so-called pumped spectrum) with 50 fs UV laser pulses with 266 nm wavelength ($h\nu = 4.66$ eV). However, in contrast to chap. 4.2, Fig. 4.5 these measurements have been done at a fixed pump-probe delay of 90 ps, measured with 70 ps time resolution. The incident laser fluence was set to $25\,\mathrm{mJ/cm^2}$, which is slightly higher than for the fs data with $20\,\mathrm{mJ/cm^2}$ (cf. Fig. 4.5). A detailed comparison of the differences and similarities of the ps measurements with the fs measurements will be done in chap. 4.3.4. First, I concentrate on the understanding of the spectroscopic fine structures of the pump-induced changes with picosecond time resolution. The energy resolution of all shown time-resolved XAS measurements is due to the use of a zone plate monochromator $E/\Delta E = 500$, resulting in $\Delta E \approx 1.4$ eV and ≈ 1.1 eV at the Fe L_3-edge (≈ 710 eV) and O K-edge (≈ 540 eV), respectively. The temporal overlap of the fs UV laser pump pulse and the ps X-ray probe pulse has again been determined by an independent transmission experiment through a 20 nm thick Fe reference film.

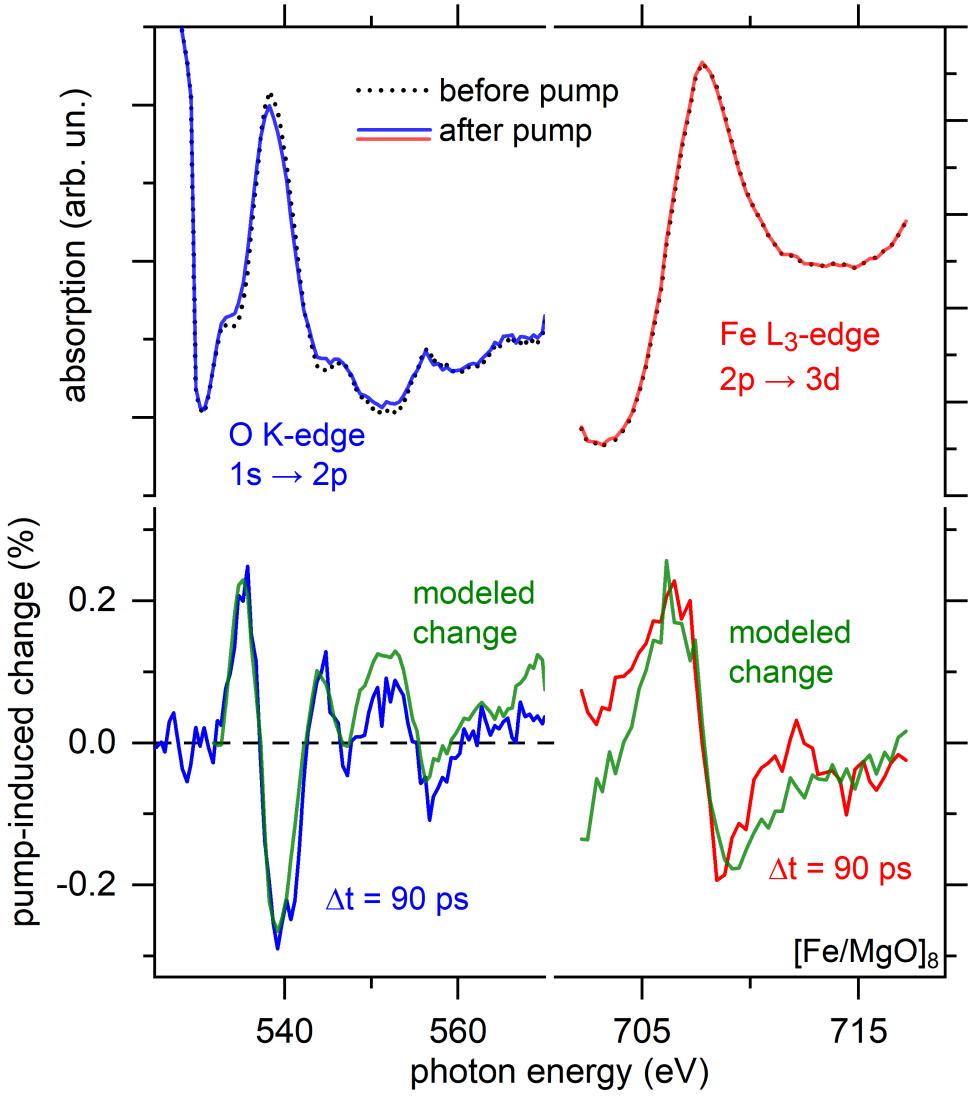

Fig. 4.22.: Top half: Soft X-ray absorption spectra as a function of photon energy for the O K-edge (left) and the Fe L_3-edge (right) before and after optical excitation, measured with 70 ps time-resolution. The incident laser fluence was 25 mJ/cm^2. Bottom half: Measured relative pump-induced change in absorption as a function of soft X-ray photon energy at a fixed pump-probe delay of 90 ps. The green solid lines depict modeled signals generated out of simple modeling and fitting procedure from the measured unpumped spectra, for more detail see text.

At first glance, the laser excitation does not influence the general shape of the unpumped spectra. The bottom half of Fig. 4.22 shows the differences between pumped and unpumped spectra at the two absorption edges, revealing that also for a delay time of 90 ps both the two absorption edges show a clear pump-induced change. The maximum pump-induced changes at the two absorption edges have a similar strength of up to 0.25 %. However, both pump-induced changes exhibit a different spectral shape: At the Fe L_3-edge, a first derivative-like spectral signature is observed, which corresponds to a red-shift of the pumped spectrum with respect to the unpumped one. In contrast, the pump-induced change at the O K-edge exhibits

a different spectral signature, which originates from a constant intensity change of the fine structures of the X-ray absorption signal.
To quantify these particular spectroscopic fine structures of the pump-induced changes, namely the size of the red-shift at the Fe L_3-edge and the intensity decrease at the O K-edge, I simulate in the following the pump-induced signal by the unpumped signal in the following way: I generate an artificial pumped spectrum (*pumped* spectrum*) by manually shifting the unpumped spectrum to smaller energies for the case of the Fe L_3-edge, or by manually decreasing the intensity of the fine structures for the O K-edge, respectively. The resulting simulated pump-induced changes (cf. Fig. 4.22 below) describe the shape and strength of the measured changes over the whole energy range well. In the following, I will describe and discuss the two used methods to model the different absorption edges in more detail.

Red-shift of the Fe L_3 absorption spectrum

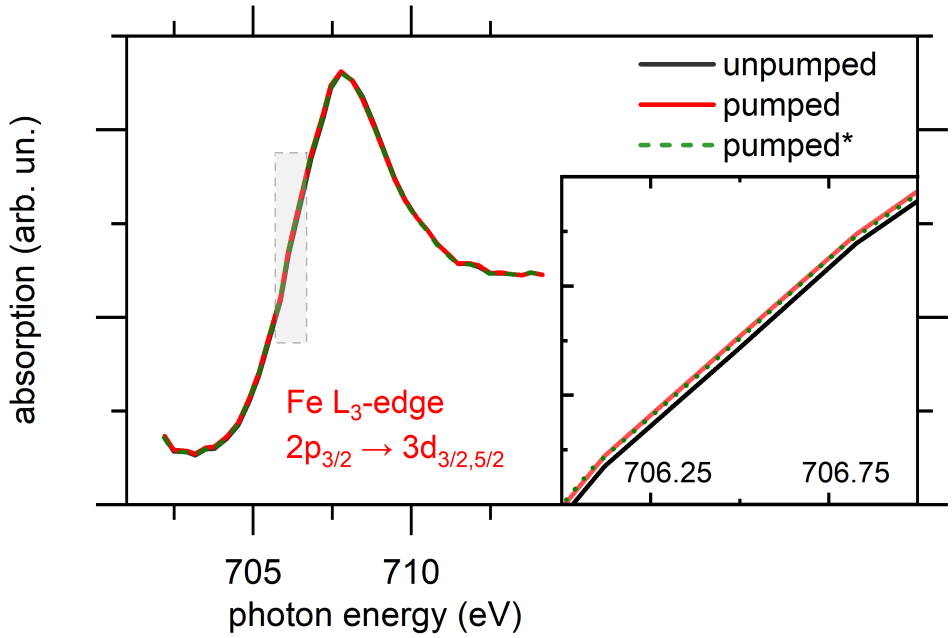

Fig. 4.23.: Depiction of the modeling and fitting procedure of the energy shift for the case of the Fe L_3-edge. Measured unpumped and pumped Fe L_3-edge spectra from Fig. 4.22 together with an artificially generated pumped spectrum (green dashed line). The gray dashed box indicates the area of the closeup, shown in the inset. The pumped spectrum exhibits for the complete energy range of the Fe L_3-edge a uniform energy shift with respect to the unpumped spectrum.

Fig. 4.23 shows explicitly the procedure to simulate the pumped spectrum by energy shifting for the Fe L_3-edge. Therefore I display again the measured unpumped and pumped Fe L_3-edge spectra as in Fig. 4.22, together with a closeup of the spectra in the vicinity of the rising edge (see inset of Fig. 4.23). The measurements show that the optical excitation induces a uniform energy red-shift of the unpumped

spectrum. Thus, the pumped* spectrum can be generated by solely shifting the measured unpumped spectrum without changing its shape or intensity:

$$\text{pumped}^*\,(E) = \text{unpumped}\,(E - x)\,.$$

Then, the simulated pump-induced change can be deduced by dividing the pumped* spectrum by the unpumped spectrum and subtracting 1:

$$\text{pump-induced change}_{\,\text{simulated}} = \left(\frac{\text{pumped}^*}{\text{unpumped}}\right) - 1.$$

To match this simulated pump-induced change for the complete energy range of the Fe L_3-edge with the measured one (see Fig. 4.22, bottom half, right) the energy shift is the only fitting parameter. For a fluence of $25\,\text{mJ/cm}^2$, I identified an energy shift of the Fe L_3-edge of 31 meV.

Intensity change of the O K absorption spectrum

In contrast to the procedure to simulate the pumped spectra at the Fe L_3-edge by energy shifting (cf. Fig. 4.23), fitting the intensity decrease at the O K-edge requires an entirely different approach. In the top half of Fig. 4.24, I display the measured unpumped and pumped O K-edge spectra as in Fig. 4.22. Both two measured spectra exhibit definite crossing points, which are marked by vertical lines. These crossing points define the limits of distinct energy windows where the pumped spectrum has either lower or higher intensity than the unpumped spectrum in this region, as indicated by the arrows. I want to note that the existence of these distinct energy windows is not only an experimental observation but also supported by DFT calculations, and will be discussed further below (cf. Fig. 4.27). Hence, I will use the following mathematical method to model and simulate the intensity decrease at the O K-edge: Firstly, subtracting a linear base line, which originates simply from linear interpolation of the crossing points, from the measured unpumped spectrum, results in the variation of purely the fine structure around the base line, which is shown in the bottom half of Fig. 4.24. Subsequently multiplying this base line subtracted unpumped spectrum with a constant factor decreases only the intensity of the fine structure variation, leaving any possible background signal (which is present in both, the measured unpumped and pumped signal) unaffected. Lastly, adding the same base line results in the simulated pumped* spectrum:

$$\text{pumped}^* = ((\text{unpumped} - \text{base line}) \cdot x) + \text{base line}.$$

Similar to the procedure for the Fe L_3-edge, the one single factor to induce the intensity decrease is the only fitting parameter to match the corresponding pump-induced

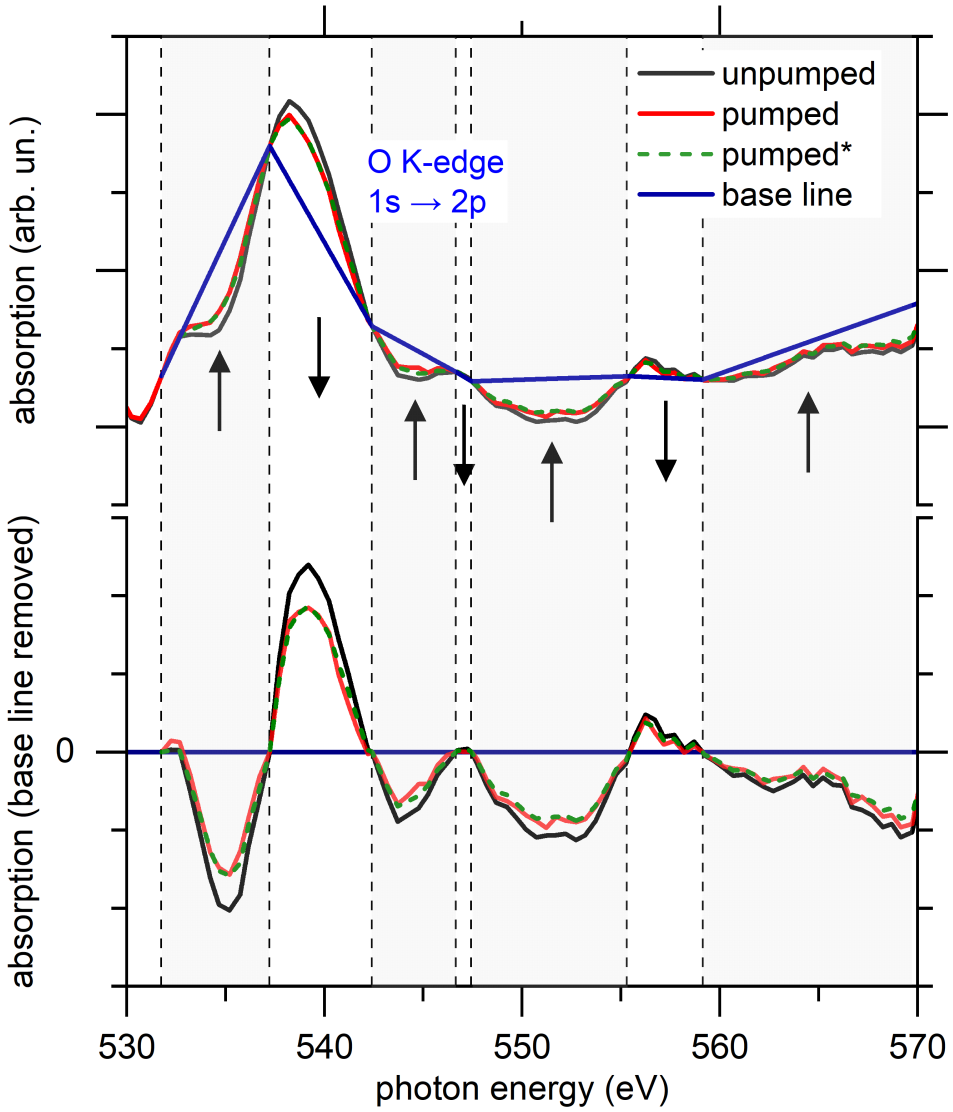

Fig. 4.24.: Depiction of the modeling and fitting procedure of the intensity decrease for the case of the O K-edge. Top half: Measured unpumped and pumped O K-edge spectra from Fig. 4.22 together with a linear base line (blue solid line) and an artificially generated pumped spectrum (green dashed line). Bottom half: Spectra of the top half after subtracting the base line. The vertical lines indicate the crossing points of the unpumped and pumped spectra. The crossing points define distinct energy windows where the pumped spectrum has either lower or higher intensity than the unpumped spectrum in this region, indicated by the arrows.

change for the complete energy range of the O K-edge with the measured one (see Fig. 4.22, bottom half, left). For a fluence of $25\,\mathrm{mJ/cm^2}$, I identified an intensity decrease of the O K-edge with respect to the base line of $23\,\%$ to fit the intensity in the entire energy range to the measured data.

I emphasize that this, within this thesis, newly introduced, basic mathematical procedure offers the simplest way to describe the pump-induced spectral changes of

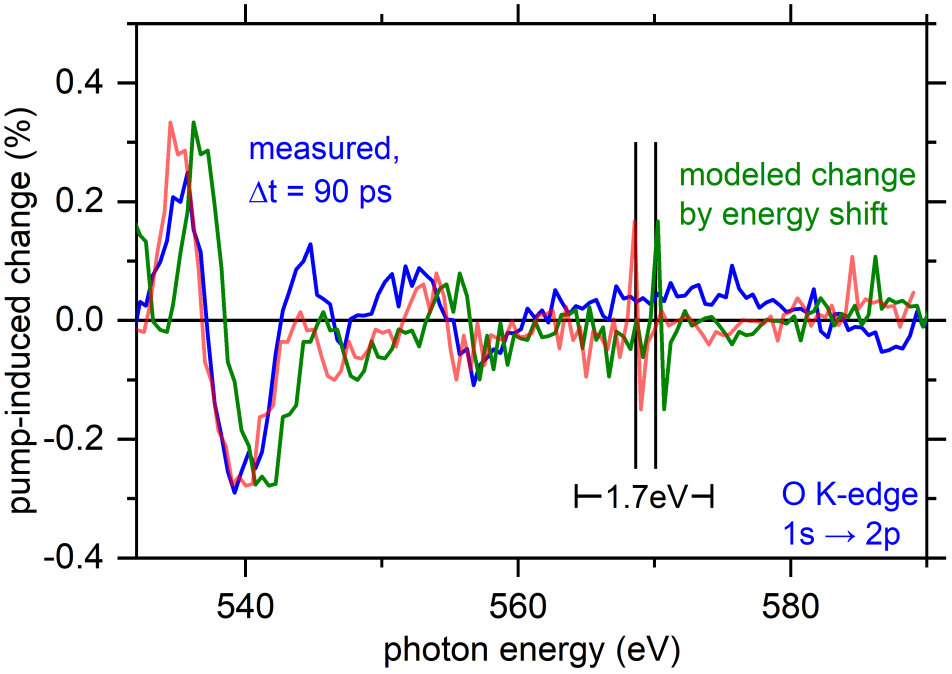

Fig. 4.25.: Attempt of generating the O K-edge pump-induced change by the red-shifting procedure, similar to the Fe L_3-edge. The simulated signal (green solid line) reproduces the spectral shape and intensity but does not agree with the energetic position of the measured spectrum (blue solid line). An additional energy shift of $1.7\,\mathrm{eV}$ is required to match both signals (red solid line).

the insulating constituent of the heterostructure. As indicated by the non-derivative like spectral signature of the pump-induced change, the procedure of generating the O K-edge signal by solely applying a red-shift is not sufficient to describe the observed pump-induced changes in the spectra: Fig. 4.25 shows exemplarily the attempt of generating the O K-edge signal by the red-shifting procedure, similar to the Fe L_3-edge. Even though an energy shift of $300\,\mathrm{meV}$ (10 times higher than what was found for the transition metal edge for the same fluence of $25\,\mathrm{mJ/cm^2}$) can reproduce the spectral shape and intensity of the measured pump-induced change over the whole energy range, the modeled signal does not coincide with the energetic position of the measured spectrum. Hence, an additional energy shift of $1.7\,\mathrm{eV}$ is required to match both simulated and measured pump-induced changes. However, this additional energy shift cannot, to my current understanding, be explained by any physical means. Whereas the experimental finding of the intensity decrease of the fine structure is not only supported by literature [174–176] but the corresponding modeling procedure can furthermore be understood by theoretical calculations of a bulk MgO spectrum with elevated lattice temperature. The latter will be discussed further below in Fig. 4.27. Moreover, if one simply compares the energetic position of the maximum pump-induced change with the unpumped absorption spectrum for the transition metal edge and the insulator, it becomes clear that both changes have to have a different origin. While the maximum pump-

induced change for the Fe L_3-edge is measured at the edge itself, the O K-edge signal shows its maximum pump-induced signal near to the peak of the spectrum. Consequently, it is not surprising that two unambiguously different simulating and fitting procedures are needed to describe the different edges. Hence, the procedure of generating the O K-edge signal by red-shifting is clearly not sufficient to describe the laser-induced changes on the spectrum. However, upon closer inspection, it appears that the maximum pump-induced signal of the O K-edge spectrum is not exactly at the peak of the spectrum but slightly displaced. Therefore the O K-edge exhibits presumably not only a pure intensity decrease but also a slight energy shift of the spectrum. However, within the current state of the analysis and the signal-to-noise ratio of the existing measurement data, I attribute, within the framework of this thesis, the pump-induced change of the spectroscopic fine structure of the O K-edge spectrum exclusively to an intensity decrease. Future, systematic studies are necessary to disentangle the influence of the laser pump pulse to the spectroscopic changes entirely. Nevertheless, I want to emphasize that both presented modeling and fitting procedures describe the shape as well as the strength of the respective measured changes over the whole energy range surprisingly well. Fig. 4.26 reports once more the bottom half of Fig. 4.22, to summarize and highlight the results of the two methods to model the different absorption edges. Furthermore, I want to recapitulate from Fig. 4.5 that the spectroscopic signatures reported for the *femtosecond* timescale showed a similar fingerprint of an energy red-shift for the Fe L_3-edge measured after 240 fs, and an intensity decrease for the O K-edge measured after 870 fs. A detailed comparison of the differences and similarities of the ps measurements with the fs measurements will be done in chap. 4.3.4.

Both of the findings of the pump-induced changes of the spectroscopic fine structures in soft X-ray absorption spectroscopy are in qualitative agreement with literature results, which I outline briefly in the following: The observation of an energy red-shift upon laser excitation is in qualitative agreement with results reported for other transition metal absorption edges in transition metal thin films [60, 101, 149] or ferromagnetic insulating thin films [174]. In agreement with the literature [149, 177], the observed spectral change of an energy shift at the Fe L_3-edge can be correlated to temperature effects. Similar transient spectral changes have been reported for a wide range of different excitation conditions, on the two different investigated timescales: For the femtosecond timescale, it has been observed that an optical excitation, leading to an elevated electronic temperature, which can range from several hundred [60] to several thousand Kelvin [177] induces that kind of changes. But also on the longer, picosecond timescales a phononic excitation or even static heating [149] manifests itself in an energy shift of the spectrum. I want to note that the experimental finding for the transient red-shift at the Fe L_3-edge of

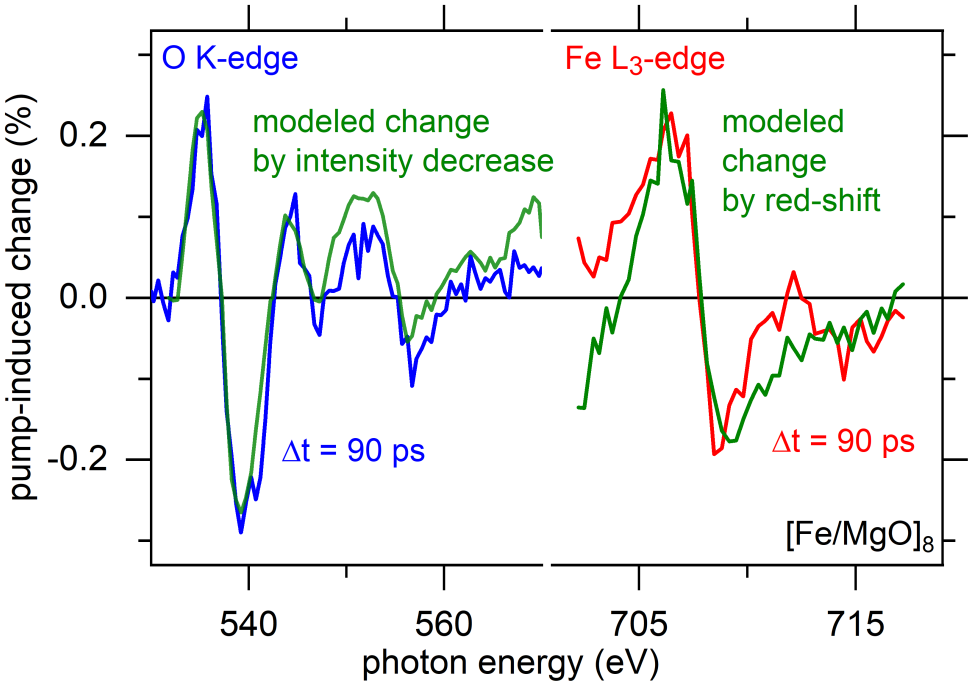

Fig. 4.26.: Measured relative pump-induced change at the O K-edge (blue, left) and Fe L_3-edge (red, right) as a function of soft X-ray photon energy at a fixed pump-probe delay of 90 ps. The green solid lines depict the modeled signals generated out of the modeling and fitting procedures shown in Fig. 4.24 (O), and Fig. 4.23 (Fe), respectively. The figure is equal to Fig. 4.22, bottom half, and shown here again to highlight the result of the two modeling procedures.

31 meV, is of similar magnitude than for elevated lattice temperatures in Ni [149], indicating a successful modeling and fitting procedure for the transition metal edge. In summary, the occurrence of the transient spectral shift can be explained as following: Since the Fermi-level E_F in metallic Fe is located within the valence band, both optically (cf. femtosecond timescale) or thermally excited electrons can redistribute their energy during the carrier thermalization. As a consequence, different final states will be available in the X-ray absorption process, which leads to an energy shift of the spectra due to the induced shift of the respective chemical potential. In the case of lattice excitation (cf. picosecond timescale), the electronic temperature should be in equilibrium with the lattice temperature, might explain the similarity of the shape of the transient spectral changes caused by electronic and lattice excitation in transition metal samples (cf. Fig. 4.31). It can be assumed that at the measured time delay of 90 ps, the entire $[Fe/MgO]_8$ heterostructure is equilibrated at an elevated lattice temperature (cf. chap. 4.2.5). This leads to a corresponding elevated electronic temperature, corresponding to a broadened Fermi-Dirac distribution, which in turn manifests itself again in a red-shift of the absorption edge.

Moreover, the observation of the spectral change of an intensity decrease at the O K-edge upon laser excitation is also in qualitative agreement with spectral changes reported in the literature for the oxide absorption edge of various materials [174–

176]. However, I have to note that especially time-resolved spectroscopic changes of the oxide absorption edge are not as much reported in the literature as for the transition metal absorption edge. For the latter, I can related the measured changes of the spectral signatures to be induced by an elevated electronic (femtosecond timescale) or lattice (picosecond timescale) temperature. Similarly, it has been observed in $LaCoO_3$ [175] that also the O K-edge can exhibit an intensity decrease of the fine structure due to a pump-induced elevated temperature. Moreover, e.g., in MgO [176], this kind of spectral change of the absorption spectrum has been reported to be induced by static heating. In summary, I can therefore assume that, while an elevated lattice temperature results for the Fe L_3-edge in a red-shift of the absorption edge, the same elevated lattice temperature leads to the measured spectral changes of an intensity decrease at the O K-edge.

4.3.2 Temperature-induced spectroscopic changes of the O K absorption edge

To better understand the presented experimental findings and support the reported modeling and fitting procedure, DFT calculations of the O K-edge XAS of bulk MgO have been carried out, using the KKR-CPA approach. As stated above, all presented DFT calculations have been carried out by M. E. Gruner from the University of Duisburg-Essen. In more detail [140]: The first-principles X-ray absorption spectra were calculated within the Korringa-Kohn-Rostoker multiple scattering approach using the SPR-KKR package [160, 161]. The ground state was obtained within the atomic sphere approximation using the generalized gradient approximation [155] for the exchange-correlation functional and an angular momentum expansion up to f-states ($l_{max} = 3$). Both a dense energy-mesh, with 800 energy points along the contour line, and k-mesh, with 11368 points in the irreducible Brillouin zone, which corresponds to a 55 x 55 x 55 mesh in the full zone was used. Furthermore, states up to 47 eV above the Fermi-level E_F have been taken into account. The finite temperature modification of O K-edge X-ray absorption spectra arising from lattice dynamics was modeled in the framework of the alloy analogy model [178, 179] using the coherent potential approximation to describe the average scattering problem for a set of thermally displaced ions with 14 independent displacements. Their magnitude was obtained according to the average square displacements within the Debye model with an appropriate value for the Debye temperature of MgO, $\Theta_D = 743$ K. To concentrate on the impact of the lattice vibrations on the calculated spectra, the volume of the two atom primitive cell was kept constant at $a = 4.214$ Å, which neglects the effect of thermally induced lattice expansion on the spectra. To all spectra a Lorentzian broadening with an arbitrary width of 0.2 eV was applied, to better mimic the experimental data, but still resolve most of the rich spectroscopic

fine structures. However, the measured spectra show a greater broadening and, therefore, less pronounced fine structure, which should be taken into account when comparing theory and experiment. Moreover, it should be noted that for an accurate description of the O K-edge also core-hole corrections are necessary [180, 181], which go beyond the approach described above, and are not presented within this thesis.

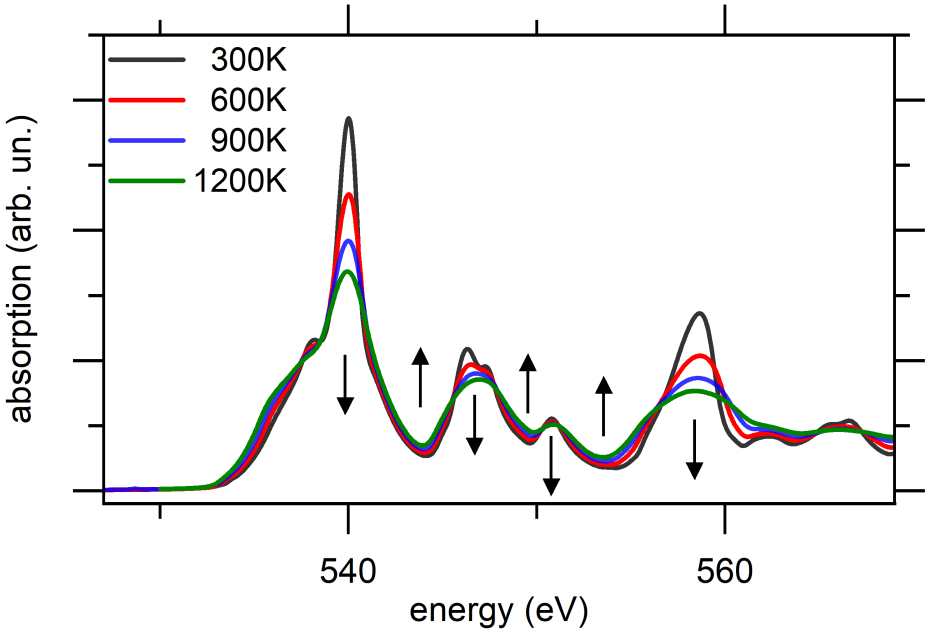

Fig. 4.27.: *Ab initio* DFT calculations of the O K-edge XAS of bulk MgO at four different temperatures modeled with a finite set of thermal displacements in the framework of the alloy analogy model [178, 179]. With increasing temperature, the calculation shows an overall intensity decrease of the fine structures, with well defined energy regions where the XAS at elevated temperature has lower or higher energy than the spectrum at lower temperature, indicated by the arrows.

Fig. 4.27 shows the respective results of the calculations, carried out with the alloy analogy model [178, 179] for different, selected lattice temperatures, ranging from 300 K to 1200 K. Matching with the experimental results for the O K-edge (cf. Fig. 4.24), the *ab initio* calculations show that with increasing temperature, there is indeed no shifting of the spectra. However, they report that the overall fine structures decrease in their intensity. Moreover, the calculation demonstrates that there are, in fact, defined alternating regions where the XAS at elevated temperature has a lower or higher intensity than the spectra at a lower temperature, indicated by the arrows in Fig. 4.27. Consequently, the calculations support the simple attempt to extract the variation of purely the fine structure by subtracting a base line given by the defined alternating regions and therefore verify the general idea of the modeling and fitting procedure of the O K-edge by an intensity decrease.
I want to note that the approach to describe the measured spectral changes observed

at 90 ps, with the static *ab initio* DFT calculations, is indeed justified: As I reported in chap. 4.2, for the *picosecond* timescale, the phonon systems of the individual Fe and MgO layers and the entire heterostructure itself can be assumed to be in thermal equilibrium with each other, thus making a description of the ps spectra by a common lattice temperature feasible. Moreover, I described above (cf. Fig. 4.19) that the differences in the vibrational density of states of bulk MgO compared to the MgO constituent in the heterostructure occur due to hybridization with Fe phonon modes at the interface. However, those are mostly relevant only for high energy phonon modes in the heterostructure. Consequently, the equilibrated state of the heterostructure at 90 ps presumably allows a valid comparison of the spectra of the O K-edge for bulk MgO and the heterostructure.

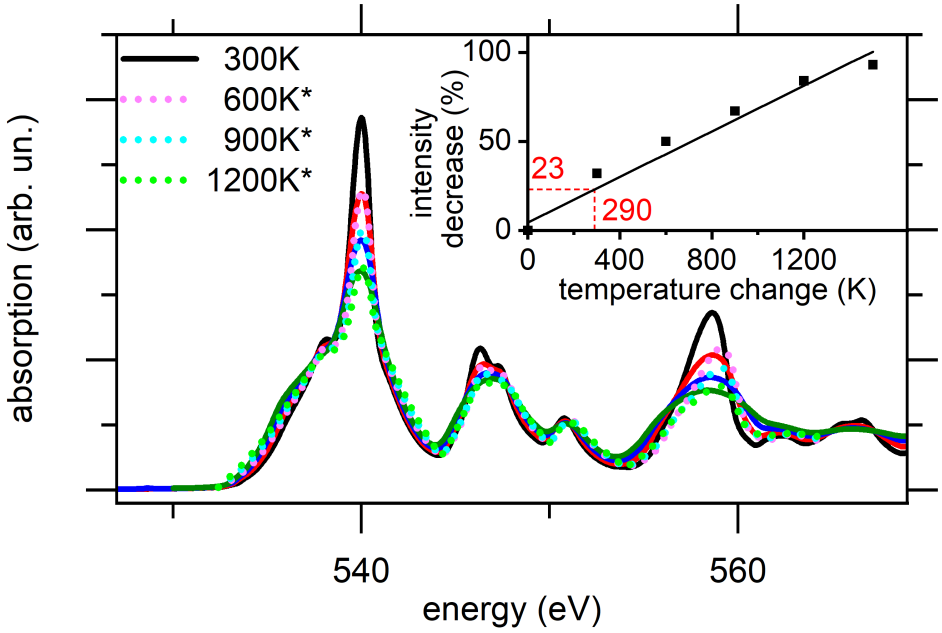

Fig. 4.28.: *Ab initio* DFT calculations of the O K-edge XAS of bulk MgO at four different temperatures from Fig. 4.27. Additionally, artificial spectra generated from the 300 K spectrum according to the previously described (cf. Fig. 4.24) modeling and fitting procedure (dotted lines), which match the corresponding finite temperature KKR-CPA spectra. The inset shows the observed linear relation between temperature change and intensity decrease according to the modeling procedure.

Taking advantage of the well-defined energy regions identified in the calculated X-ray absorption spectra, I can utilize the modeling and fitting procedure to relate the magnitude of intensity decrease derived from the modeling to an induced lattice temperature change: Using the spectrum at 300 K, I generated by intensity decreasing of the fine structures an artificial spectrum at elevated temperatures. Fig. 4.28 shows that the simulated spectra (dotted lines) match the calculated ones (solid lines) in intensity and shape reasonably well. The inset of Fig. 4.28 summarizes the observed relation between the derived intensity decrease to the respective temperature change for all calculated temperatures from 300 K up to

1800 K in 300 K steps, which has been fitted by a linear function. With this linear relation, I attempt to quantify the measured pump-induced effects by correlating the observed intensity decrease derived from the modeling and fitting procedure of the pump-induced effects to an effective temperature change. However, I want to note that the calculated spectra show an increased broadening of the fine structures at elevated temperatures, which makes the simulation and fitting procedure less accurate the higher the temperature. Additionally, the calculated temperature steps are all higher than the ones expected for the experimental data. Consequently, the linear fit function derived from the calculations (Fig. 4.28, inset) presumably slightly underestimates the absolute temperature change associated with the experimental measurements. Nonetheless, I am confident that the combination of the presented simulation and fitting procedure and the KKR-CPA calculations offer an easy but powerful possibility to analyze and quantify the measured pump-induced changes in an insulator. For example, the intensity decrease of the O K-edge with respect to the base line of 23 %, measured for a fluence of 25 mJ/cm^2 (cf. Fig. 4.24) resembles a lattice temperature change of 290 K (Fig. 4.28, inset red lines). This temperature change is of the same order of magnitude as findings of an equilibrated temperature of the Fe/MgO heterostructure derived from the UED measurements, which I come back to in more detail in chap. 4.3.3 below.

Lastly, I want to attempt to give one possible approach to understand the pump- and temperature-induced spectroscopic changes observed at the O K absorption edge. The decrease of the O K-edge fine structures in the near-edge region seen in the experiment (cf. Fig. 4.22) and theory (cf. Fig. 4.27) are similar to the reported reduction of the extended X-ray absorption fine structure (EXAFS) oscillations with temperature, i.e., with increasing thermal disorder. In the EXAFS description, one uses a Debye-Waller factor $\exp\left(-2 \cdot \sigma^2(T) \cdot k^2\right)$, with k being the wavenumber of the photo-electron, to describe in the extended energy regime the reduction of the fine structures with increasing temperature T by the increasing mean square relative displacement $\sigma^2(T)$. Generally, the EXAFS description is used to describe the fine structures for photon energies up to several hundred eV above the absorption edge. However, also the immediate near edge structures can be calculated in multiple scattering theory, when conceivably considering larger mean square relative displacements for the multiple scattering paths [182]. Furthermore, it should be noted that due to the limited energy range of about 30 eV investigated in the present work, the usual photon energy dependence of the EXAFS Debye-Waller (k-dependence) factor does not play a role. Consequently, the presented simple modeling approach to reduce the measured and calculated fine structures in the near edge regime by a single factor (cf. Fig. 4.24) appears plausible. Using this EXAFS analogy, to describe the thermal disorder by the EXAFS Debye-Waller factor,

it can be understood that for the absorption edges of the insulator (O K-edge), elevated phononic temperatures do not induce an energy red-shift but an intensity decrease of the near edge fine structures.
The presented EXAFS analogy is a very promising finding, even though I could within this thesis not fully exploit the pump-induced spectroscopic changes observed for the full extended X-ray absorption fine structure oscillations, but only concentrated on the near edge region itself. Because of this, one of the future plans for the subsequent Ph.D. thesis in this project in the CRC 1242 is to continue my work and extend the understanding of the pump-induced changes of the spectroscopic fine structures in soft X-ray absorption spectroscopy by performing time-resolved EXAFS measurements.

4.3.3 Fluence dependence of the pump-induced changes with picosecond time resolution

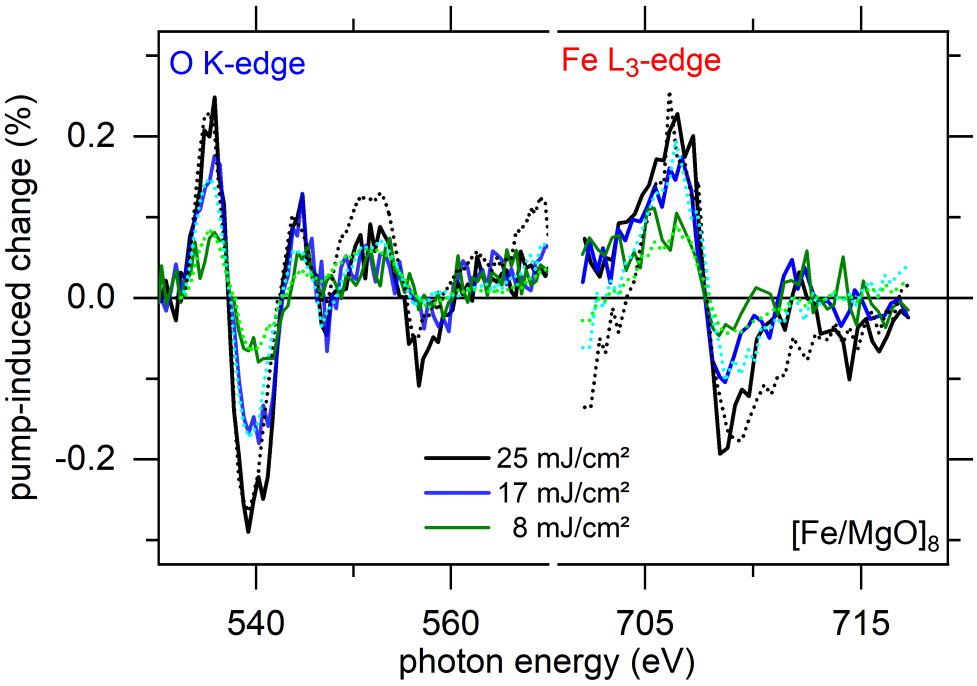

Fig. 4.29.: Pump fluence dependence of the relative pump-induced change as a function of X-ray photon energy for the O K-edge (left) and Fe L_3-edge (right) at a pump-probe delay time of 90 ps with 70 ps time resolution. The dotted lines present the respective modeled changes by intensity decrease (O K-edge), and energy red-shift (Fe edge). The relation between the pump fluence with the fitting parameters, and simultaneously with the pump-induced change, defined as half of the peak-to-peak value, is shown in Fig. 4.30.

Fig. 4.29 shows the measured pump-induced changes of the $[Fe/MgO]_8$ heterostructure at the O K-edge (left) and the Fe L_3-edge (right) at a fixed pump-probe delay of 90 ps with 70 ps time resolution, for a systematic variation of the laser pump

fluences, ranging from 8 to 25 mJ/cm^2. Both changes at 25 mJ/cm^2 correspond to the measurements shown in Fig. 4.22. The pump-induced changes exhibit the same spectral shape for all fluences. The size of the pump-induced change, defined here as half of the peak-to-peak amplitude, shows a linear relation with the pump fluence, see Fig. 4.30. I apply the individual fitting procedure for the different absorption edges for all the fluence-dependent measurements. This shows that I can indeed successfully describe all of the measured spectra with the individual simulation and fitting procedures (Fig. 4.29, dotted lines).

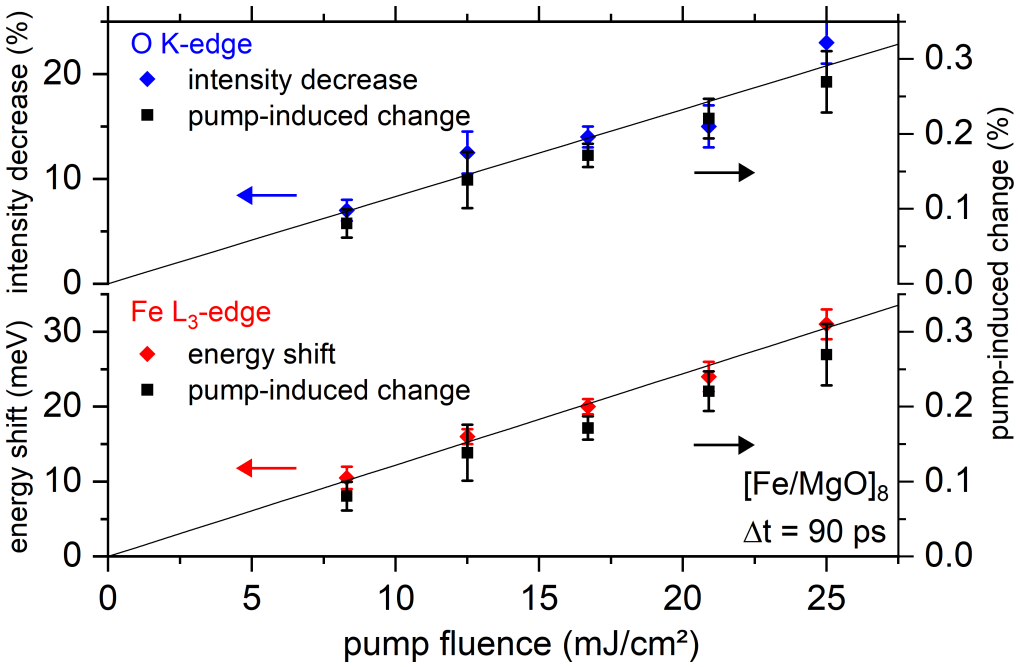

Fig. 4.30.: Linear relation of the pump fluence with the fitting parameters (namely, the intensity decrease for the O K-edge or the energy shift for the Fe L_3-edge), and simultaneously with the pump-induced change, defined as half of the peak-to-peak value, for the O K-edge (top half) and Fe L_3-edge (bottom half) at a pump-probe delay time of 90 ps with 70 ps time resolution.

Fig. 4.30 shows the observed linear relation of the fitting parameters, namely the intensity decrease for the O K-edge (top half) or the energy shift for the Fe L_3-edge (bottom half) with the laser-fluence. Additionally, Fig. 4.30 displays on the right y-axis the linear fluence-dependence of the pump-induced change, defined as half of the peak-to-peak value for the respective absorption edges. Within the measurements, I identify a maximum effect of the intensity decrease with respect to the baseline of 23 % and energy shift of 31 meV for the highest used fluence of 25 mJ/cm^2, both corresponding to a pump-induced change of ~ 0.3 %. For the lowest used fluence of 8 mJ/cm^2 I find a minimum effect of the intensity decrease with respect to the baseline of 7 % and energy shift of 11 meV, corresponding to a pump-induced change of ~ 0.1 %.

I want to highlight the fact that both of the individual modeling and fitting pro-

cedures are not restricted to only one single measurement for each absorption edge, but have been successfully applied to in total ten (5 per edge) individual datasets. Moreover, the observation of the direct relation between the measured pump-induced change and the extracted fitting parameters strengthens the validity of the individual modeling procedure further.

pump fluence	intensity decrease	temperature change
8 mJ/cm^2	7 %	41 K
13 mJ/cm^2	13 %	127 K
17 mJ/cm^2	14 %	150 K
21 mJ/cm^2	15 %	166 K
25 mJ/cm^2	23 %	290 K

Tab. 4.1.: Assignment of the observed intensity decrease (with respect to the baseline) at the O K-edge for the measured pump-fluences, to a calculated absolute temperature change. See text for more detail.

Finally, as I showed in chap. 4.3.2, the measured pump-induced change, and the resulting amount of fitted intensity decrease at the O K-edge can be assigned to an effective temperature change. Therefore I use the linear relation between the amount of intensity decrease and the effective temperature change that was derived from the *ab initio* DFT calculations (cf. Fig. 4.28). In Tab. 4.1, I summarize the resulting relation between the pump-fluence, the intensity decrease with respect to the baseline, and the temperature change for all of the measurements at the O K-edge with ps time resolution. The measurements show, after a time delay of 90 ps, a pump-induced temperature change between ~ 41 K for the lowest used fluence of 8 mJ/cm^2 and ~ 290 K for the highest used fluence of 25 mJ/cm^2. As I stated above, the derived temperature changes presumably slightly underestimate the absolute temperature change associated with the experimental measurements. Nonetheless, the temperature changes are of the same order of magnitude as previous findings of an equilibrated temperature of the Fe/MgO heterostructure at pump-probe delays of > 5 ps, which can be estimated from the ultrafast electron diffraction measurements, presented in chap. 4.2.3. It is possible to derive from a two-temperature model calculation (cf. chap. 2.1, not done in this thesis but in [42]) that a laser fluences of only 9 mJ/cm^2 yields to a temperature change of $\Delta T_{\mathrm{MgO},>5\,\mathrm{ps}} = (130 \pm 10)$ K, which is slightly higher than the temperature change extracted from the XAS measurement with comparable fluence. I attribute those differences mostly to the longer time delay at which the XAS measurements have been conducted. Especially due to the absence of the Cu heatsink for the UED samples (cf. chap. 4.1), which is used to transport the excess energy out of the heterostructure, the respective smaller cooling time could explain the differences. Furthermore, different laser spot profiles, varying experimental conditions, the

mentioned underestimation for the XAS temperature change, and other reasons might also play a minor role. Nonetheless, and in summary, within this chap. 4.3, I clearly showed and introduced a powerful possibility to analyze measured pump-induced changes in soft X-ray absorption spectroscopy. Moreover, I demonstrated the sensitivity of transient X-ray absorption spectroscopy to phonons and reported that XAS can be a powerful tool to quantify temperature changes in complex materials.

4.3.4 Comparison of the spectral changes with femtosecond and picosecond time resolution

Throughout this chap. 4, I reported on the pump-induced spectroscopic changes of the $[Fe/MgO]_8$ heterostructure on two fundamentally different timescales. In the following, I compare and identify the differences and similarities of the spectroscopic fine structures reported in the fs measurements (cf. Fig. 4.5) with the ps measurements (cf. Fig. 4.22).

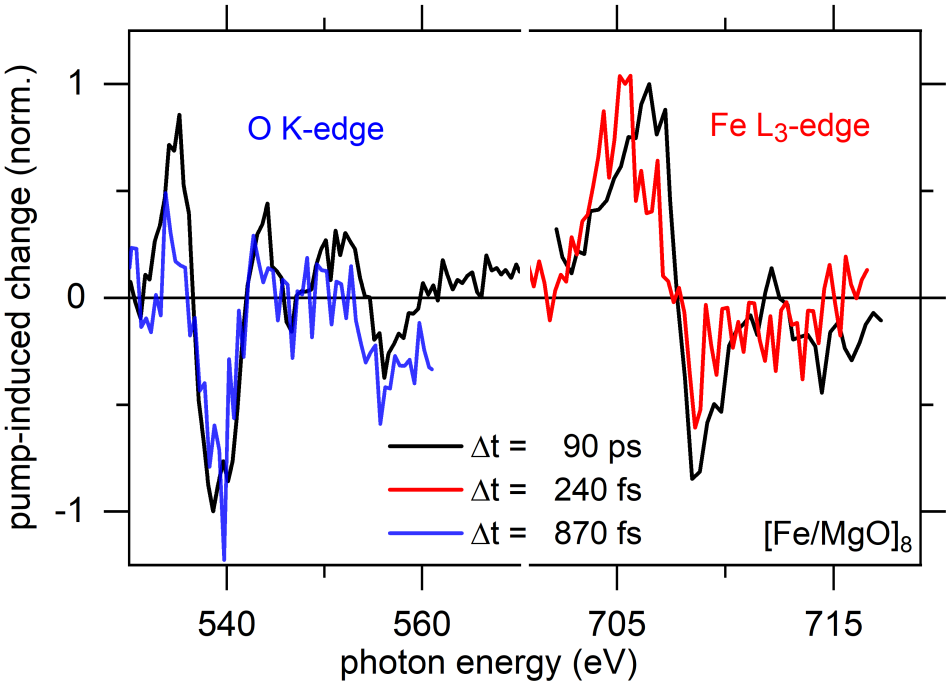

Fig. 4.31.: Comparison of the relative pump-induced change as a function of X-ray photon energy for the O K-edge (left) and Fe L_3-edge (right) at a pump-probe delay time of 90 ps with 70 ps time resolution with the spectra measured at a pump-probe delay time of 240 fs (Fe) and 870 fs (O) with 150 fs time resolution. Spectra are normalized to the respective maximum pump-induced changes.

Fig. 4.31 shows the pump-induced changes at the O K-edge (left) and Fe L_3-edge (right) measured at a pump-probe delay of 90 ps with 70 ps together time resolution with the spectra measured at a pump-probe delay of 240 fs (Fe) and 870 fs (O) with 150 fs time resolution. Since the spectra at the two timescales have been measured

in two different beamtimes, with presumably slightly different laser parameters, e.g., spot profiles, I forgo a quantitative analysis and restrict myself to a qualitative comparison. Therefore, I normalize the spectra to their respective absolute maximum pump-induced change. Interestingly, the picosecond and femtosecond pump-induced changes show a very similar spectroscopic structure over the entire energy range. Astonishingly, the spectra for the two different timescales show at first glance the same spectral shape. However, looking in more detail, actual differences between the spectra can be identified.

For the O K-edge (Fig. 4.31, left), there are indications that the spectrum with fs time resolution exhibits a slightly smaller positive pump-induced change compared to the respective ps spectrum. The Fe L_3-edge (Fig. 4.31, right), shows the trend that the spectral weight at the rising edge is bigger for the fs spectrum than for the spectrum with ps time resolution. However, due to the lower signal-to-noise ratio (SNR) of the fs spectra, I do not attempt, within this thesis, to quantify these defined spectral differences at the two different pump-probe delay times.

From the similar overall structure of the pump-induced changes at the different timescales, I can conclude on similar pump-induced spectroscopic changes of the corresponding absorption spectra. For this, I compare the measured unpumped and pumped X-ray absorption spectra with fs time resolution (cf. Fig. 4.5) with the ps measurements (cf. Fig. 4.22). The laser-pumped spectra at the O K-edge exhibit in both cases the distinct spectral signature originating from a constant intensity change of the fine structures of the unpumped spectra. In contrast, the Fe L_3-edge reports on both timescales a red-shift of the pumped spectrum with respect to the unpumped one, which is also visible in the first derivative-like spectral signature of the respective pump-induced changes. Therefore, I expect that the same individual fitting procedures, as shown above for the ps spectra, can be applied to describe the spectral changes on the fs timescale. However, the lower SNR of the fs data makes it more difficult, especially for the O K-edge, to evaluate the presented fs spectra with the introduced modeling and fitting procedures. Furthermore, I want to note that for the case of the insulating constituent of the heterostructure, represented by the O K-edge, the lattice excitation is on the sub-ps timescales strongly non-thermal. This is due to the preferential coupling of hot electrons in Fe with hybrid interface vibrational modes, which extend into MgO, as I reported in chap. 4.2.4. Therefore, a comparison of the pump-induced changes to calculations based on an enhanced lattice temperature in bulk MgO, as it was done in Tab. 4.1, is inappropriate on the fs timescales, and will not be attempted here. Nonetheless, I stress that the similarity of the relative pump-induced changes on the sub-ps timescale and after 90 ps indicates that *the transient X-ray absorption fine structures are sensitive to incoherent lattice excitation on all timescales*. Consequently, with a suitable modeling approach, combined with optimized simulations that also take the non-thermal phonon populations into account, I expect a great future possibility to not only

characterize spectroscopic fine structures for a system that is in an equilibrated state but also to quantify the highly non-equilibrated state.

To summarize the spectral changes at the Fe L_3-edge on both timescales, I reported that an elevated electronic temperature, as well as an elevated phononic temperature, have the same effect, namely an energy red-shift, on the absorption spectra (see Fig. 4.31, right). As I stated before, these spectral changes are in agreement with previous results for transition metal thin films [60, 101, 149], where the time-dependent red-shift of the metal absorption edge was correlated to an electron or respectively lattice temperature-induced change on the spectra [149, 177]. This similarity is presumably characteristic for all metal absorption edges, where the chemical potential is positioned within an electron band. However, I stress that special care has to be taken when one tries to compare the absolute size of the red-shift for the different timescales since, for the sub-ps delay times, the electrons and phonons are still in a highly non-equilibrium state.
To conclude the comparison for the O K-edge: Within the experiment I reported on in chap. 4.2, no hot electron mediated charge transfer to the MgO constituent has been observed. Hence, the pump-induced spectral changes measured at the O K-edge on both timescales (see Fig. 4.31, left) are of phononic origin. Therefore, it is not surprising that very similar spectral changes at the O K-edge for both timescales are observed, namely a uniform intensity decrease of the fine structure, but no edge-shifting. As mentioned above, qualitatively, these kinds of spectral changes upon laser excitation have been reported in literature for the oxide system $LaCoO_3$ [175]. Even though the O K-edge shows for both timescales a decrease of the intensity, it should be noted that the changes reported on the sub-ps time delay are driven by a non-thermalized phononic subsystem. In contrast, the change observed at $90\,\mathrm{ps}$ originate from an equilibrated state of the complete heterostructure. Hence, I believe that both of my findings of the fundamentally different spectral changes at the Fe L_3-edge and the O K-edge may serve as an exemplary model for the laser pump-induced changes at transition metal absorption edges and the absorption edges of insulating oxides, and presumably even indicating future possibilities to characterize, quantify and compare measured pump-induced changes for all kinds of different absorption edges and timescales.

4.4 Local ultrafast magnetization dynamics in a Fe/MgO heterostructure after IR laser excitation

4.4.1 Ultrafast magnetization dynamics of the Fe constituent

Up to now all presented time-dependent X-ray absorption spectra have been measured with linearly polarized light in zero magnetic field, exploring the energy flow dynamics between the electron and phonon subsystem (chap. 4.2) or the effect of the laser pump pulse on the spectroscopic fine structures (chap. 4.3) but disregarding any possible magnetization dynamics. However, a system containing of one of the only natural room temperature ferromagnetic materials seems somehow predestined for an additional investigation of its ultrafast demagnetization behavior, especially since those materials have been the first reported on since the first discovery of the sub-ps demagnetization dynamics 1996 [8]. In particular, as outlined in chap. 2.1.3, using the Fe/MgO heterostructure system, consisting of thin ferromagnetic Fe constituents embedded between the insulating MgO constituents is suppressing any contributions to the ultrafast demagnetization due to spin currents. Thus, revealing the microscopic origin of the demagnetization process, i.e., if one can achieve a significant degree of demagnetization on the electronic timescale, and therefore identifying the role of phonon excitation to it. Consequently, I will focus in the following on time-dependent X-ray absorption measurements, conducted with circularly polarized light in an applied magnetic field after IR laser excitation to investigate the ultrafast magnetization dynamics of the Fe constituent in the heterostructure.

Starting, I report on element-specific hysteresis curves of the $[Fe/MgO]_8$ heterostructure and the Fe reference sample at the fixed photon energy of the Fe L_3-edge maximum, see Fig. 4.32. Both magnetization curves are measured, without laser pumping with the 70 ps X-ray pulses. The measurements are conducted in 42 degree grazing incident with respect to the surface normal, reporting an in-plane easy axis of the magnetization for both samples, which is expected for the respective Fe thicknesses [162, 183, 184], even though it should be noted that for even thinner Fe thicknesses an out-of-plane component becomes more and more dominant [162, 185–187]. I want to note that the experimental setup did not allow to measure at a greater incident angle. Consequently, all time-dependent magnetization measurements presented in the following have been conducted in 42 degree grazing incident

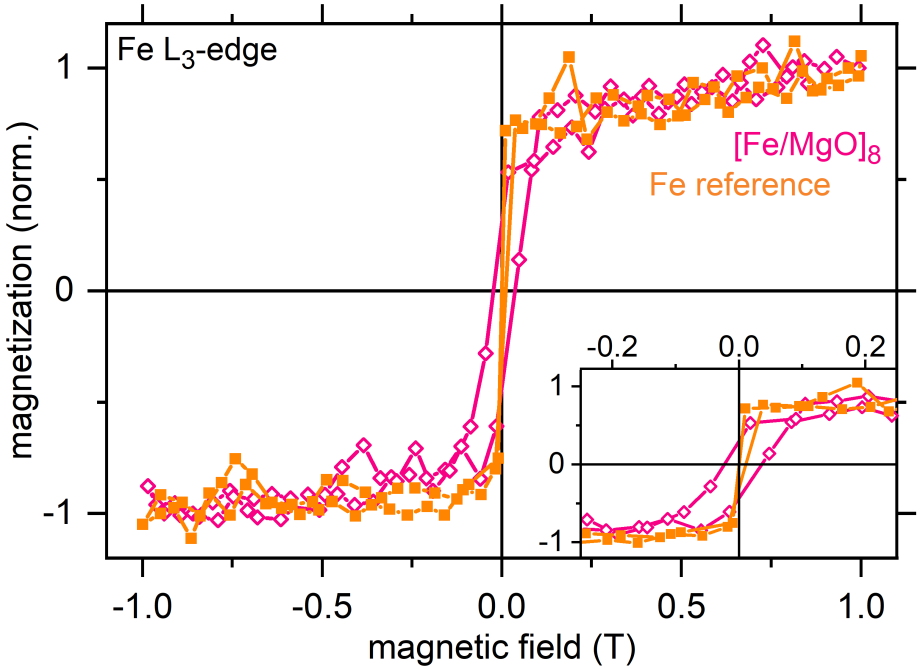

Fig. 4.32.: Element-specific hysteresis curves of the $[Fe/MgO]_8$ heterostructure (pink) and the Fe reference sample (orange) at the fixed photon energy of the Fe L_3-edge maximum, measured without laser pumping with 70 ps long X-ray pulses, in 42 degree grazing incident with respect to the surface normal. Both magnetization curves clearly indicate that a magnetic field of ± 0.2 T (used later on) is sufficient to fully switch the magnetization direction.

with respect to the surface normal. Since both hysteresis curves are measured at the maximum of the Fe L_3-edge, but not at the maximum of the respective XMCD-signal, I normalized both curves to the highest field value of 1 T for a solely qualitative comparison. Both magnetization curves clearly show that a magnetic field of ± 0.2 T, which will be used for the time-dependent measurements below, is sufficient to switch the magnetization direction fully. Admittedly, the two shown magnetization curves are not conducted with the best possible parameters, e.g., the step-size of the data points. However, I want to point out that the purpose of the presented data in Fig. 4.32 was simply to pre-characterize the measurement parameters for the subsequent time-resolved magnetization curves, which are presented in the following.

Fig. 4.33 shows in the top half the Fe L_3 X-ray absorption spectra of the Fe/MgO heterostructure, measured with circularly polarized light in an alternating magnetic field of ± 0.2 T, corresponding to μ^+ and μ^-, respectively. For both field directions, the spectra are measured, with a time resolution of 150 fs, before and after IR 1.55 eV laser excitation with an incident laser fluence of 20 mJ/cm^2. The temporal overlap of the fs laser pump and fs X-ray probe pulses was determined by the preceding experiment at the Fe L_3-edge (cf. Fig. 4.9 above) using linear polarized light. Changing the polarization does not influence the temporal overlap of the two pulses. Fig. 4.33

reports in the bottom half the normalized asymmetry $(\mu^+ - \mu^-) / (\mu^+ + \mu^-)$, which is proportional to the magnetic moment, before and after laser excitation at a fixed time delay of 1.8 ps.

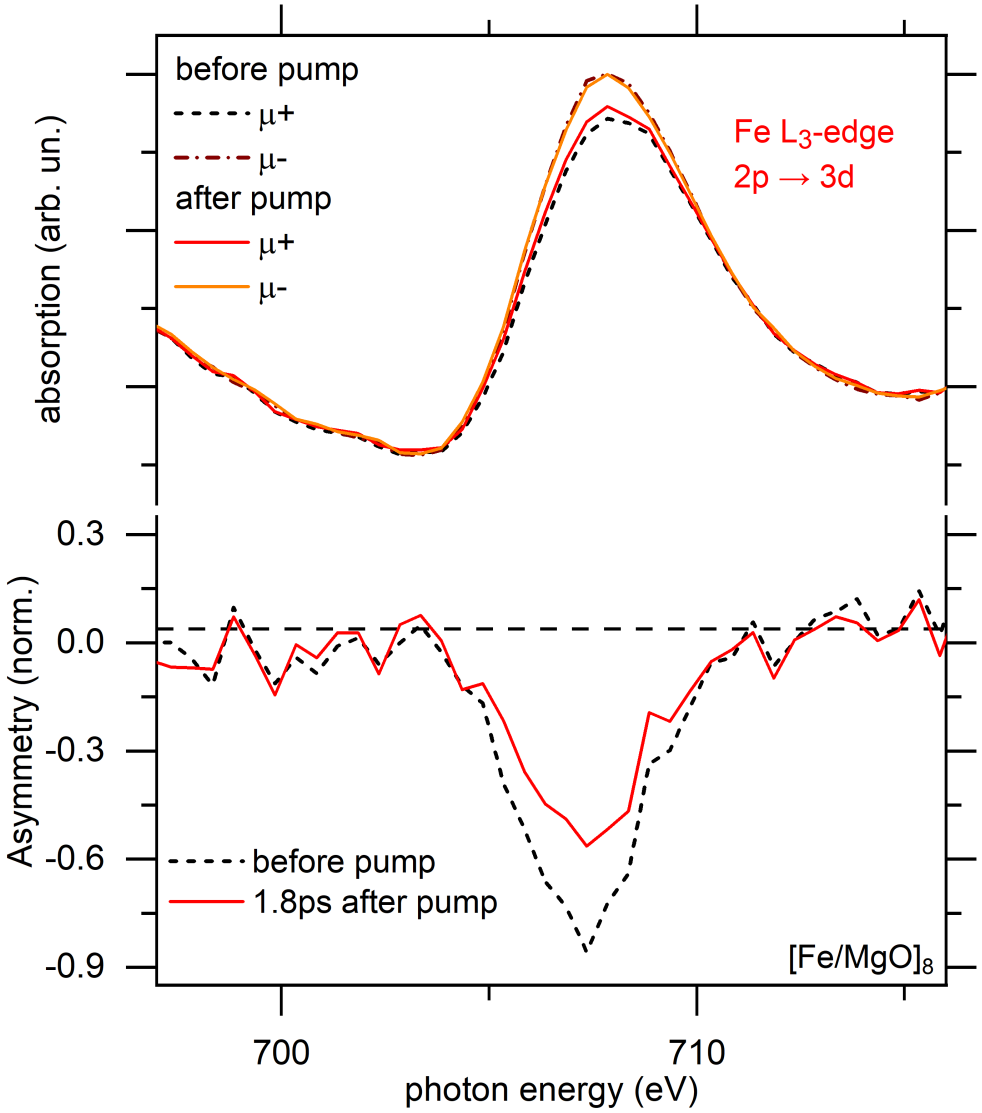

Fig. 4.33.: Top panel: Soft X-ray absorption spectra of the $[Fe/MgO]_8$ heterostructure at the Fe L_3-edge, measured with circularly polarized light in an alternating magnetic field of ± 0.2 T, corresponding to μ^+ and μ^-, respectively. For both field directions, the spectra are measured before and after IR 1.55 eV laser excitation. Bottom panel: Respective normalized asymmetry before and after IR laser pumping at a fixed time delay of 1.8 ps. The incident laser fluence was set to $20\,\mathrm{mJ/cm^2}$.

The absorption spectra before laser excitation exhibit a clear difference at the Fe L_3-edge for the two field directions. This results in a distinct asymmetry signal with its maximum slightly below the maximum of the Fe L_3 absorption edge, i.e., 1 eV below. Upon laser excitation, the spectrum for one field direction (μ^-) stays unaffected, while the spectrum for the opposite field direction changes uniformly. This manifests itself in a uniform decrease of the asymmetry signal, representing

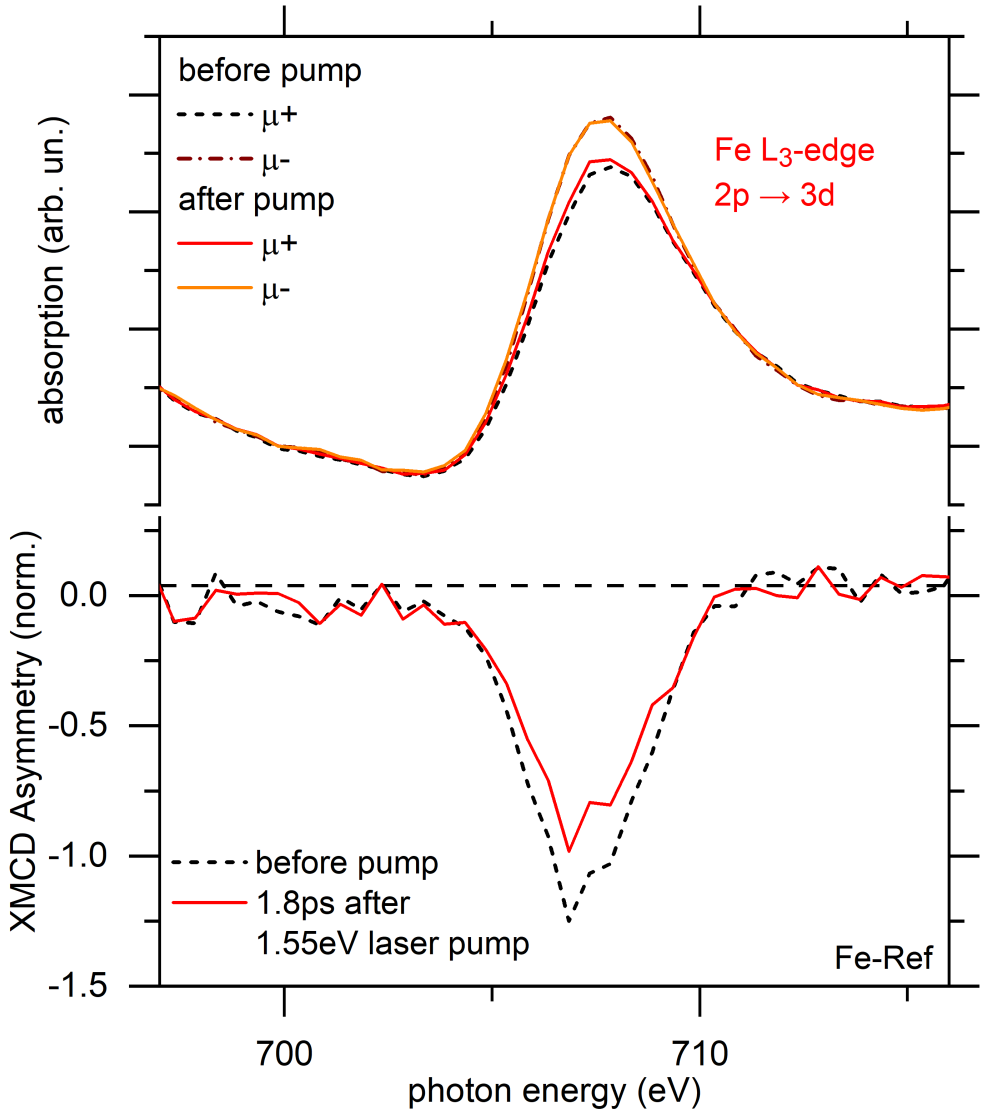

Fig. 4.34.: Similar measurement as in Fig. 4.33 but for the Fe reference sample. Top panel: Soft X-ray absorption spectra of the Fe reference sample at the Fe L_3-edge, measured with circularly polarized light in an alternating magnetic field of $\pm 0.2\,\mathrm{T}$, corresponding to μ^+ and μ^-, respectively. For both field directions, the spectra are measured before and after IR $1.55\,\mathrm{eV}$ laser excitation. Bottom panel: Respective normalized asymmetry before and after IR laser pumping at a fixed time delay of $1.8\,\mathrm{ps}$. The incident laser fluence was set to $20\,\mathrm{mJ/cm^2}$.

the demagnetization of the Fe system due to the laser excitation. A similar measurement of the Fe reference sample (see Fig. 4.34) resulted in the same qualitative spectroscopic behavior of the Fe L_3 absorption spectra for the two field directions and hence also of the asymmetry upon laser excitation. In the following, I focus on the time-dependent dynamics of the pump-induced change of the asymmetry at the fixed photon energy of the maximum asymmetry for both samples.

In Fig. 4.35, I compare the transient behavior of the pump-induced change of the asymmetry for the Fe/MgO heterostructure and the Fe reference sample. Both

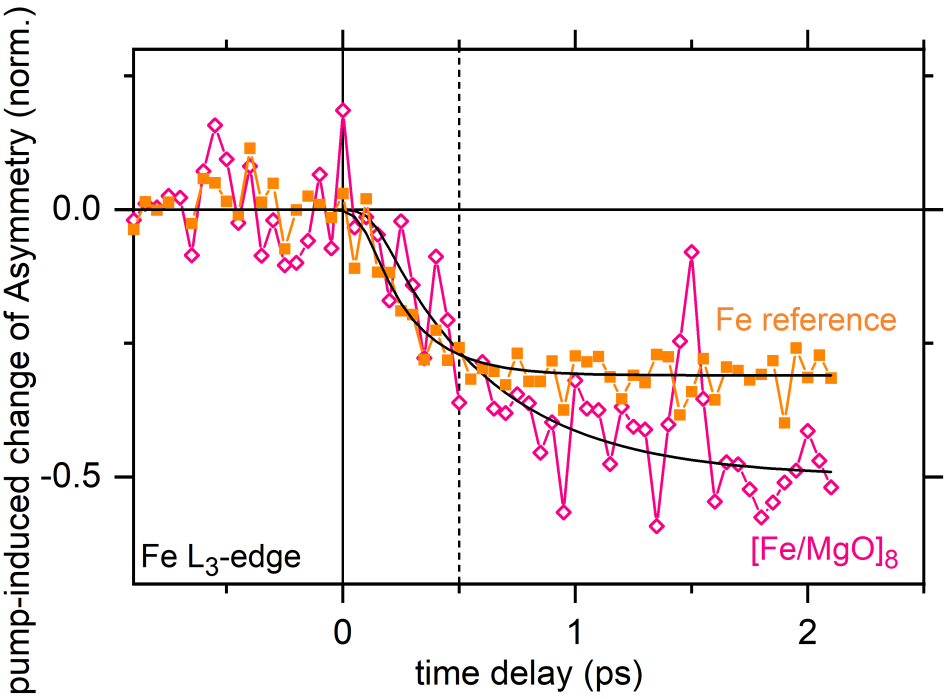

Fig. 4.35.: Pump-induced change of the asymmetry for the $[Fe/MgO]_8$ heterostructure (pink, open symbols) and the Fe reference sample (orange, closed symbols) at a fixed X-ray photon energy of the maximum asymmetry of the Fe L_3-edge as a function of pump-probe delay. Both pump-induced changes are normalized to their respective asymmetry value before laser excitation. The incident laser fluence was set to $20\,mJ/cm^2$. The black lines are fits to the data as specified in the text. The vertical dashed line highlights the 0.5 ps mark.

pump-induced changes are normalized to their respective asymmetry value before laser excitation, allowing a qualitative and quantitative comparison of the induced demagnetization dynamics. Both time-dependent asymmetries show a one-step transient behavior, similar to the overall trend observed for the time-dependent O K-edge X-ray absorption signal. Hence, I describe the time-dependent asymmetries using the same fit function as before (cf. eq. 4.2). The fit to describe the heterostructure yield a time zero shift $t_0 = 0.12 \pm 0.07$ ps and a time constant $\tau_1 = 0.50 \pm 0.10$ ps ($\tau_1 = 1.44 \pm 0.13$ ps for the extended delay range shown in Fig. 4.36, measured with a smaller resolution) representing the demagnetization time. For the reference sample I find $t_0 = 0.08 \pm 0.03$ ps and $\tau_1 = 0.23 \pm 0.05$ ps ($\tau_1 = 0.42 \pm 0.03$ ps), respectively. Comparing the maximum strength of demagnetization for the two sample systems, a nearly twice as strong pump-induced collapse of asymmetry for the heterostructure than for the pure Fe reference sample is reported, which could be attributed to a difference in absorbed laser fluence in the two different samples. However, the relative pump-induced changes measured with linearly polarized light show the same amount of change in absorption for both samples. Therefore it seems that presumably the presence of the additional Fe-MgO interfaces make the total amount of demagnetization more effective. I noted above for the time-resolved XAS measurements (see Fig. 4.9) that the IR 1.55 eV laser excitation seemingly hints to a

less effective coupling to the interface hybrid phonon modes than the UV 4.66 eV laser excitation. But, the existence of the interfaces seems to be explicitly noticeable in the X-ray demagnetization data. This also agrees with the presented ultrafast electron diffraction measurements (cf. Fig. 4.13) conducted with different laser photon energies, showing the importance of the interfaces but the independence of the laser photon energies. Unfortunately, a systematic X-ray absorption study of various sample systems with a varying number of interfaces could not be performed yet. However, to systematically address the importance and influence of the interfaces to the time-resolved X-ray absorption measurements appears to be crucial for a profound understanding.

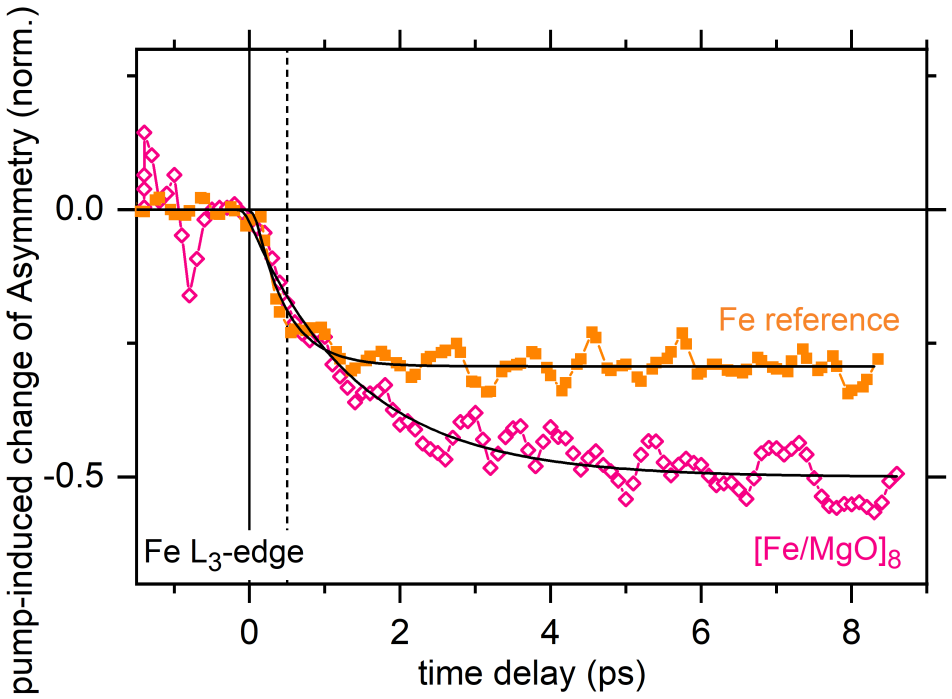

Fig. 4.36.: Same pump-induced change of the asymmetry for the $[Fe/MgO]_8$ heterostructure (pink, open symbols) and the Fe reference sample (orange, closed symbols) as a function of pump-probe delay as shown in Fig. 4.35 but over an extended pump-probe delay range with reduced point density. Both samples do not exhibit any recovery of the asymmetry within the maximum measured time delay of 9 ps.

Comparing the time constants of the pump-induced changes of the asymmetry for the two samples, the reference sample exhibits a faster (but less pronounced) demagnetization than the heterostructure. However, neither of the two sample systems shows within the experimental resolution an ultrafast dynamic but a surprisingly slow behavior. The reference sample reaches the maximum amount of demagnetization only after 1.0 ps, and then stays constant up to the maximum measured time delay of 9 ps. In contrast, the heterostructure continues to demagnetize until the maximum measured time delay of 9 ps (cf. Fig. 4.36). Hence, both samples do not report any recovery of the asymmetry within the presented measurements.

To shortly recapitulate the previous sub-ps findings of chap. 4.2 above: I reported on the microscopic non-equilibrium energy transfer dynamics in the photo-excited Fe/MgO heterostructure. The complementary time-resolved X-ray absorption spectroscopy and ultrafast electron diffraction experiments allowed to analyze and disentangle the electronic and phononic contributions to the dynamical processes induced on ultrafast timescales after the localized UV 4.66 eV optical laser excitation of the Fe constituent. Both pump-probe methods yielded together with the presented *ab initio* calculations to a comprehensive insight into the microscopic processes leading to a local relaxation process within the Fe constituent and a non-local relaxation process between the Fe and MgO constituents of the heterostructure. I concluded on two different *phonon*-mediated energy transfer mechanisms acting in the Fe/MgO heterostructure system. In the following, I compare the various measured transients of the heterostructure to get an insight into whether or not the observed demagnetization dynamic also exhibits a *phonon*-mediated characteristic or if it is following the *electronic* time behavior.

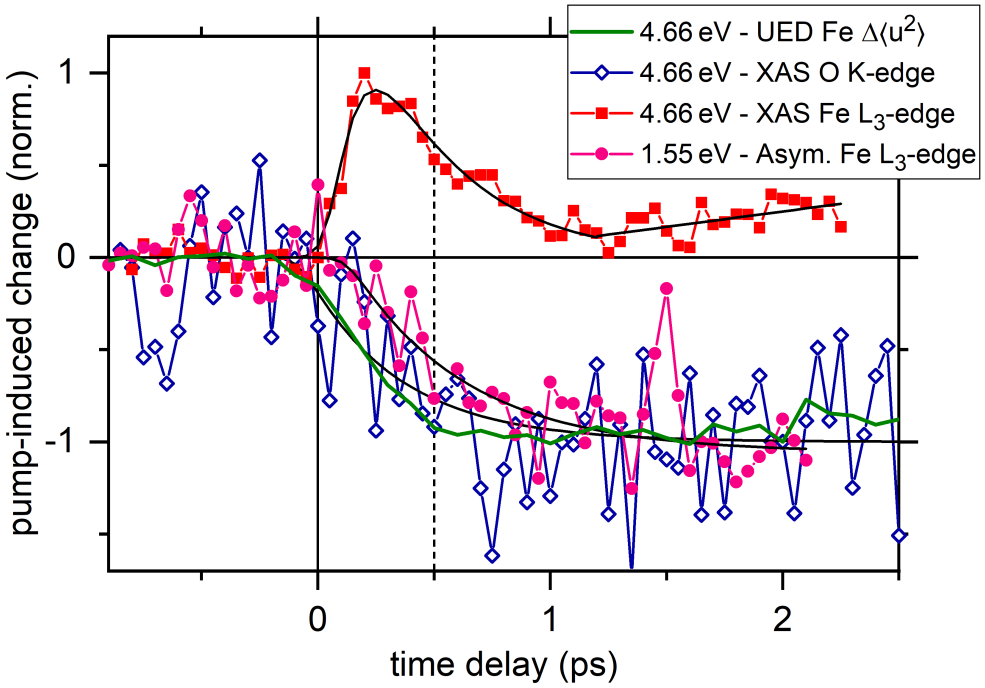

Fig. 4.37.: Comparison of the normalized transients of the three different kind of pump-induced measurements in the $[Fe/MgO]_8$ heterostructure: First, the change in X-ray absorption at the Fe L_3-edge and O K-edge after UV 4.66 eV laser excitation (cf. Fig. 4.15). Second, the transient of the Fe atomic mean square displacement $\Delta\langle u^2_{Fe}\rangle(t)$ after UV 4.66 eV laser excitation (cf. Fig. 4.15). Third, normalized change of the asymmetry at the Fe L_3-edge after IR 1.55 eV laser excitation (cf. Fig. 4.35). For better comparison, all transients are normalized to their respective maximum pump-induced change.

Fig. 4.37 shows a comparison of the normalized transients of the three different kinds of pump-induced measurements in the heterostructure multilayer sample. I compare the change in X-ray absorption at the Fe L_3-edge and O K-edge after UV

4.66 eV laser excitation together with the transient of the Fe atomic mean square displacement $\Delta\langle u^2_{\mathrm{Fe}}\rangle(t)$ after UV 4.66 eV laser excitation (cf. Fig. 4.15), with the normalized change of the asymmetry at the Fe L_3-edge after IR 1.55 eV laser excitation (cf. Fig. 4.35). Unfortunately, no UED measurements after IR laser excitation have been conducted, but only after excitation with either 4.66 eV or 3.10 eV (cf. Fig. 4.12) laser energy. Hence, I can not compare all four different transients of the heterostructure with the same excitation condition. In the comparison, I forego on the 1.55 eV XAS measurements and only compare the 4.66 eV changes in XAS and UED with the 1.55 eV demagnetization data due to two reasons: First, as I noted in the discussion of Fig. 4.9 the data quality of especially the IR O K-edge data is (due to time reasons on the corresponding beamtime) noticeably worse than for the UV data. Therefore I could not quantify with certainty any true differences in the respective pump-induced changes. Moreover, I want to recall that the ultrafast electron diffraction measurements (cf. Fig. 4.13) conducted with different laser excitation showed no dependency of the laser photon energies. Consequently, I have to assume within the current measurement data that the transient of the 4.66 eV XAS measurements represents, due to its improved SNR, better the change in X-ray absorption after laser excitation. Second, I established in chap. 4.2 already a profound understanding of the microscopic non-equilibrium energy transfer dynamics by comparing among other things the 4.66 eV changes in XAS and UED.
Comparing, in Fig. 4.37, the four different time-dependent behaviors shows that the magnetization dynamic at the Fe L_3-edge is clearly slower than the Fe L_3 XAS dynamic. This is in agreement with the dynamics reported for a thin Ni film [60], even though here the laser induced demagnetization was mainly governed by superdiffusive spin transport due to the conductive substrate (Al) [36], which is, however, suppressed in the Fe/MgO heterostructure for the Fe constituent embedded between insulating MgO. Moreover, Fig. 4.37 shows that the the Fe L_3-edge demagnetization is slower than the two other transients in XAS. In more detail: I attributed the initial rise time of the change in XAS of the Fe L_3-edge to the thermalization of the Fe electronic subsystem of the heterostructure. In contrast, I concluded that the change in XAS at the O K-edge is governed by a phonon-mediated process, hence following the dynamic behavior of the Fe atomic mean square displacement (cf. chap. 4.2.5). Since the Fe L_3 demagnetization process does not exhibit any ultrafast change like the corresponding initial change in XAS, I can infer that the observed loss of demagnetization is not directly driven by the excited electronic subsystem. In a closer look, a slightly slower response of the change in demagnetization (if the data quality allows it) than for both the change in X-ray absorption at the O K-edge and for the increased mean square displacement of the Fe ion cores can presumably be identified. I attributed the latter two dynamics to be mediated by high-frequency interface vibrational modes. Consequently, the local demagnetization process of the Fe constituent in the Fe/MgO heterostructure also exhibits

a *phonon*-mediated characteristic. However, the measurements indicate that the demagnetization presumably might not be governed by the same high-frequency interface vibrational modes, which are responsible for the observed transients of the O K-edge XAS and the Fe UED. As I noted above, due to limited measurement time at the femtoslicing setup at the synchrotron, a systematic study of various sample systems with a varying number of interfaces could not be performed yet. A systematic study and building on that, a more comprehensive insight with the help of *ab initio* calculations appears to be crucial to deepen the understanding further.

As I pointed out in chap. 2.1.3, this phonon-mediated characteristic is a crucial finding in the ongoing debate of achieving a profound understanding of the ultrafast magnetization dynamics: In particular, the actual role of the phonon-mediated contribution to the ultrafast demagnetization process is hereby controversially discussed. The most prominent microscopic mechanisms considered in the debate are phonon-mediated Elliot-Yafet-like spin-flip scattering events [62, 78, 79], spin-dependent charge transport [36, 60, 80–82], or spin-flip events mediated by spin-orbit coupling, which do not require the excitation of phonons [83–85]. It was reported that spin-flip scattering events as well as spin transport phenomena are both clearly contributing to the ultrafast demagnetization process, whereby the quantity of the contributions for both mechanisms depend on the details of the material system and the excitation condition [77]. Unfortunately, most studies dedicated to resolve the microscopic origin of the ultrafast demagnetization process still missed to disentangle the actual magnetization dynamics and the dynamics of the lattice, especially while contributions of transport processes to the ultrafast demagnetization are suppressed. That is why, the presented comparison of all the different transients is highly relevant for building a more profound understanding. The observed phonon-mediated origin of the demagnetization process of the Fe constituent in the Fe/MgO heterostructure shows that, in the absence of spin transport processes, a significant degree of demagnetization requires the excitation of phonons, and does not occur on the electronic timescale. Eventually, a heating of the sample as a consequence of the incoherent lattice excitations is therefore an unavoidable side-effect accompanying the ultrafast laser-induced demagnetization.

4.5 Conclusion: Time-resolved pump-induced dynamics in a Fe/MgO heterostructure

The focal point of this thesis is the investigation of the pump-induced dynamics in a metal-insulator heterostructures, namely an $[Fe/MgO]_n$ multilayer system. Among other things, I made use of the element-specificity of soft X-ray absorption spectroscopy as a tool to analyze constituent-specific the ultrafast dynamics in the heterostructure system induced by a localized optical excitation of one constituent. In more detail, measuring the transient changes in XAS at the O K-edge and the Fe L_3-edge allowed me to specifically analyze the non-equilibrium *dynamics* and the distinct time-dependent *spectroscopic* signatures of the two constituents of the heterostructure, Fe and MgO.

Fig. 4.38 depicts a short but illustrative summary of the complementary investigation techniques used in chap. 4 to analyze the pump-induced processes in the Fe/MgO heterostructure. In the following, I highlight the most important findings of the individual sub-chapters.

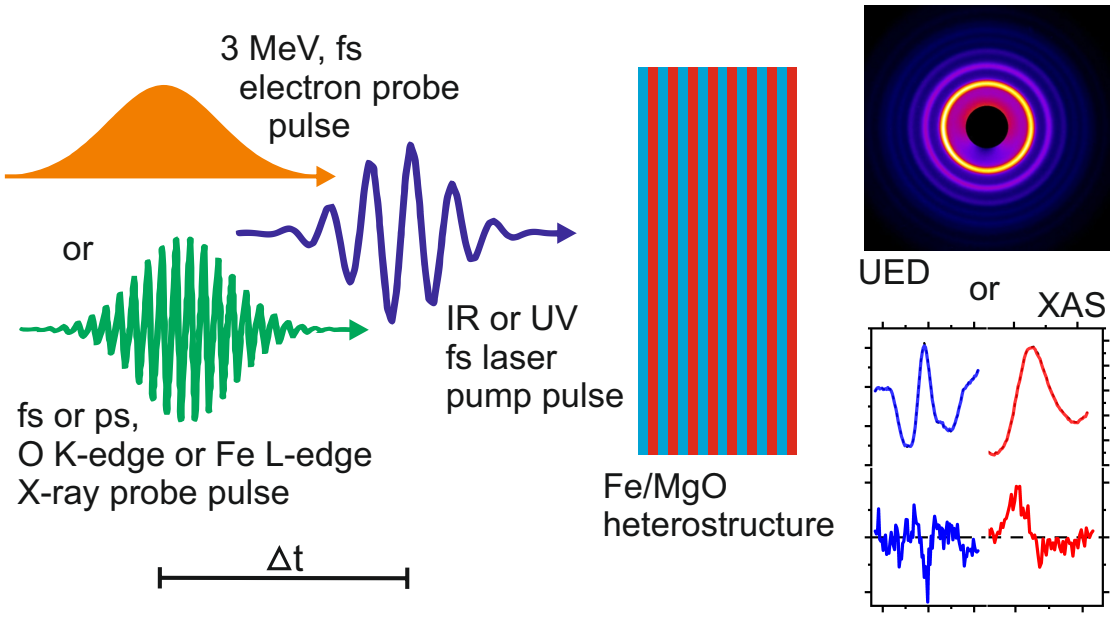

Fig. 4.38.: Illustrative summary of the complementary investigation techniques used in chap. 4 to analyze the pump-induced processes in the Fe/MgO heterostructure induced by a localized IR, or UV femtosecond laser excitation. I made use of femtosecond time-resolved ultrafast electron diffraction (UED) experiments and femtosecond, as well as picosecond time-resolved soft X-ray absorption spectroscopy (XAS) at the O K and Fe L absorption edge. Both experimental measurement techniques are supported by *ab initio* DFT calculations.

In chap. 4.1 I introduced and pre-characterized the Fe/MgO sample system. Making use of conversion electron Mössbauer spectroscopy (CEMS) measurements, I concluded that the Fe-MgO interfaces in the heterostructure can be considered to be

atomically sharp since a potential intermixing of the constituents was found to be limited to a maximum of one monolayer at the interfaces.

Chap. 4.2 can be considered the centerpiece of chap. 4 and therefore of this thesis. I focused explicitly on the understanding of the pump-induced ultrafast microscopic *energy transfer dynamics*, taking place in the heterostructure after the localized laser excitation. Hereby, I reported on *femtosecond* time-resolved X-ray absorption experiments, probing constituent-specific the electronic as well as the lattice excitation in the heterostructure. I complemented the XAS measurements by ultrafast electron diffraction (UED) experiments, analyzing the lattice dynamics of the Fe constituent independently. This yielded, together with layer-resolved *ab initio* DFT calculations, a comprehensive insight into the microscopic local and non-local relaxation processes of the two constituents. I reported a localized electronic excitation in the Fe constituent, with a peak in the pump-induced change of the Fe L_3-edge at $240\,\mathrm{fs}$, which subsequently relaxes within $\sim 1\,\mathrm{ps}$ by electron-phonon coupling. In the experiments, no indications of a hot electron mediated charge transfer to the MgO constituent was observed, independently of the pump photon energy. In contrast to the Fe dynamic, the change in absorption at the O K-edge showed a slow change, which builds up within $0.5\,\mathrm{ps}$. This change in XAS exhibits nearly the same transient behavior than the increased mean square displacement of Fe ion cores probed in ultrafast electron diffraction. Consequently, I concluded that the ultrafast energy transfer across the Fe-MgO interface is mediated by high-frequency (above $15\,\mathrm{meV}$ phonon energy) interface vibrational modes, which are excited by the hot electrons in Fe and subsequently couple to vibrations in MgO in a mode-selective, non-thermal manner. Thus, demonstrating the importance of a hot phonon population for the ultrafast interfacial non-equilibrium energy transfer dynamics. Furthermore, both time-resolved pump-probe experiments identified for time delays $t > 1\,\mathrm{ps}$ a second, slower process, which I attributed to the thermalization of the heterostructure as a whole and energy transfer across the interface involving lower energy acoustic phonons.

In chap. 4.3, I specifically focused on the understanding of the *spectroscopic* differences of the pump-induced spectral changes of the two different absorption edges in the Fe/MgO system, on the *picosecond* timescale. I reported that the transition metal absorption edge exhibits a red-shift of the spectra. In contrast, the oxygen absorption edge of the insulator features a uniform intensity decrease of the fine structures. I introduced two distinct modeling and fitting procedures to analyze this specific pump-induced changes in soft X-ray absorption spectroscopy. Doing a systematic fluence-dependent study up to $25\,\mathrm{mJ/cm^2}$, I found that the pump-induced changes of both edges, as well as the corresponding fitting parameters, show a linear dependency on the pump fluence. Combining the time-resolved XAS experiment

with *ab initio* DFT calculations, I explicitly demonstrated in chap. 4.3 the sensitivity of transient XAS to phonons, even under conditions of a phonon non-equilibrium, where a description by a common lattice temperature is not applicable. Further, I showed the possibility to use time-resolved XAS as a tool to quantify temperature changes in complex materials.

At last, chap. 4.4 was dedicated to the investigation of the ultrafast local *demagnetization* behavior of the Fe constituent in the heterostructure. Thereby, I compared the transient behavior of the demagnetization process, specifically with the energy transfer dynamics described in chap. 4.2, which allow to integrate the dynamics of the Fe spin-system to the understanding of the overall dynamics. I identified that the local demagnetization process of the Fe constituent is not directly governed by the electronic subsystem but mediated by a phononic process. Consequently, in the absence of contributions to the demagnetization by spin transport processes, which are suppressed for the Fe constituent embedded between the insulating MgO, a significant degree of demagnetization requires the excitation of phonons. Thus showing that the heating of the sample as a consequence of the incoherent lattice excitations is an unavoidable side-effect accompanying the ultrafast laser-induced demagnetization.

5 First results: X-ray absorption study of Ni and NiO at the European XFEL

During the time of this Ph.D. thesis, I participated in the very-first user experiment at the Spectroscopy and Coherent Scattering instrument of the European XFEL, which took place in December 2018, and was followed by a second beamtime in November 2019. Both experiments have been open community proposals with an experimental team of over 50 participants each time, whose names can be found in the proposals with number 2170 and 2161, respectively. The corresponding principal investigators have been M. Beye of the Deutsches Elektronen-Synchrotron DESY, for the very-first community proposal, and A. Eschenlohr of the University of Duisburg-Essen, for the second experiment. Both experiments have been dedicated to an entirely different sample system than in chap. 4, namely nickel and nickel oxide films. Thereby, I prepared personally a part of the samples for the first measurement, in particular two test samples which have been used for a control experiment conducted at the synchrotron SOLEIL, and all samples used for the second experiment. Moreover, I was strongly involved in both on-site measurements, and the subsequent data evaluation, especially for the second experiment. I will not present a profound analysis of those Ni and NiO data here. Nonetheless, I want to show selected first results, to report on the conducted measurements, as well as to highlight the possibilities of the European XFEL facility. A more detailed and quantitative evaluation of both experiments will be done elsewhere. In particular, the analysis of the very-first experiment will be part of the Ph.D. thesis of R. Engel from the Deutsches Elektronen-Synchrotron DESY, and the analysis of the second experiment will be part of the master thesis of T. Lojewski from the University of Duisburg-Essen. Even though, both community proposals have been a team effort and would not be possible without the help of all participants, I want to especially emphasize the following contributions of various researchers: The two principal investigators of both community proposals, M. Beye from the Deutsches Elektronen-Synchrotron DESY, and A. Eschenlohr from the University of Duisburg-Essen. B. Rösner, F. Döring, and C. David from the Paul Scherrer Institut (PSI), who fabricated and pre-characterized the special transmission zone plate setup, which was necessary to ensure a shot-to-shot-reproducibility of the experiments, and was implemented and tested during the very-first user experiment. L. Le Guyader from the European XFEL , and R. Engel from the Deutsches Elektronen-Synchrotron DESY who put a tremendous effort into the calibration and readout of the detectors and the python scripts used for the data evaluation. The control experiment for the characterization of the static properties of the Ni and NiO samples have been conducted at the synchrotron SOLEIL through the proposal with the ID 20160880 and has been carried out by E. Jal, K. Légaré, and V. Chardonnet from the Sorbonne Université with help of the beamline scientist N. Jaouen of the synchrotron SOLEIL.

As the very-first external users at the Spectroscopy and Coherent Scattering (SCS) instrument of the European XFEL we aimed to demonstrate and establish the possibility to conduct at high repetition rates, high-quality and reproducible static

X-ray absorption spectroscopy (XAS) measurements, which are in its data quality (more than) comparable to ones measured at synchrotron facilities. Moreover, we aim to extend those measurements to the femtosecond timescale to combine, similarly to the femtoslicing setup at a storage ring, the element-specific character of XAS with information in the time domain, using a laser pump X-ray probe setup. However, in contrast to the femtoslicing scheme, a X-ray free electron laser provides fs X-ray pulses with orders of magnitudes higher number of photons, and a shorter time resolution (cf. chap. 3.2), which theoretically enables the possibility to conduct in a significant shorter measurement time, time-resolved data with even better quality. Even though, XAS is today at a storage ring one of the most developed elementary key spectroscopy techniques, the adaptation to a X-ray free electron laser is not straightforward and requires considerable effort and preparation. In this chap. 5, I will therefore show that we successfully implemented a specially designed transmission zone plate setup at the SCS instrument of the European XFEL, which was necessary to ensure a shot-to-shot-reproducibility. I will show in the following that we successfully established with this the possibility to conduct static and fs time-resolved spectroscopy measurements, using a suitable reference systems, i.e., thin films of nickel and nickel oxide.

In more detail, in chap. 5.1 I will first described the working principle of the specially designed transmission zone plate setup. Second, I will report on the preparation of the nickel and nickel oxide samples in chap. 5.2. Thereafter, I will compare in chap. 5.3 the static X-ray absorption spectra measured during the two community proposals, and at the synchrotron SOLEIL. I will hereby demonstrate that the implementation of the specially designed transmission zone plate setup at the SCS instrument allowed to successful measure high-quality static X-ray absorption spectra, which are comparable to the ones measured at the synchrotron.
In chap. 5.4, I will then focus on the fs time-resolved XAS measurements, which have been part of the second proposal, to highlight the high data quality of the time-resolved X-ray spectroscopy data. Therefore I compare the data acquisition time of the fs time-resolved XFEL data with reasonable signal to noise to the one needed at a synchrotron using the femtoslicing scheme.
Moreover, a free electron laser allows to conduct measurements at very high X-ray fluences. During the first community proposal, we performed measurements in the high fluence regime to study the influence of non-linear X-ray processes in the X-ray absorption. Finally, I will report briefly in chap. 5.5 on the successful demonstration to measure non-linear absorption spectra at the SCS instrument of the European XFEL.

5.1 TZPG measurement scheme

The generation and coherent emission of X-ray photons at the European XFEL facility originate from the self-amplified spontaneous emission (SASE) process, described in chap. 3.2. Since the SASE process is initiated by an arbitrary noise fluctuation in the electron bunch, the subsequent generation of coherent light emission has also an intrinsic random character. Consequently, successive X-ray pulses are not identical, and the conducted pump-probe experiments are not necessarily reproducible as long as one can not ensure the possibility to monitor within each pulse its properties to reference the measured data.

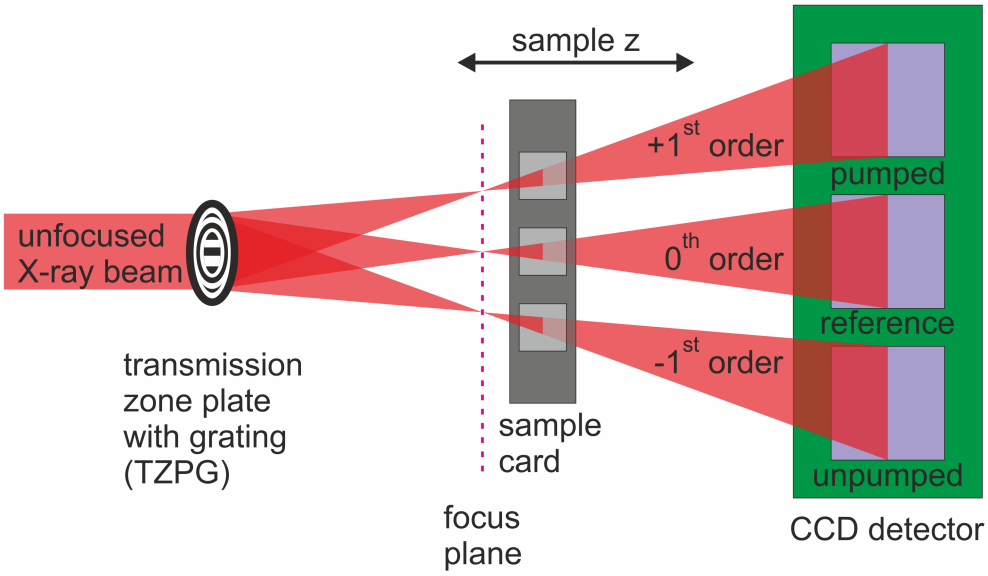

Fig. 5.1.: Transmission zone plate with a specially designed grating pattern (TZPG). Successfully introduced and tested at the Spectroscopy and Coherent Scattering (SCS) instrument of the European XFEL during our first user experiment in December 2018 for a two beam geometry (using only the -1^{st} and $+1^{st}$ orders for reference and unpumped signal), and in November 2019 for the three beam geometry as shown. The special TZPG setup solves the problem of the shot-to-shot-reproducibility of the European XFEL by splitting the incident X-ray beam in two diffraction orders and measuring which each X-ray pulse reference, unpumped and laser pumped sample simultaneously on the CCD detector. By moving the sample card perpendicular to the focus plane of the TZPG, it is possible, due to the high photon flux of the European XFEL, to explore different X-ray fluence regimes. The TZPG was fabricated and pre-characterized by B. Rösner, F. Döring, and C. David from the Paul Scherrer Institut (PSI).

As the first external users of the European XFEL Spectroscopy and Coherent Scattering (SCS) instrument, we successfully introduced and tested in December 2018 a special zone plate setup at this beamline for a two beam geometry (using only the -1^{st} and $+1^{st}$ orders for reference and unpumped signal), and in November 2019 for the three beam geometry as shown in Fig. 5.1. We measured with this setup on

the Ni and NiO sample the first-ever recorded spectroscopy data as external users at this beamline of the European XFEL facility and proved that our special zone plate setup solves the shot-to-shot-reproducibility issue. Fig. 5.1 shows schematically the scheme of the transmission zone plate setup, which was fabricated and pre-characterized by B. Rösner, F. Döring, and C. David from the Paul Scherrer Institut (PSI). The basic idea of this setup can be summarized as the following: The monochromatic, unfocused X-ray beam, originating from the SASE process, is not directly transmitted through the sample to be measured. Instead, the X-ray beam is directed onto a transmission zone plate with a specially designed grating pattern. The transmission zone plate with grating (TZPG) on the one hand focuses but, on the other hand, splits the incident X-ray beam in various diffraction orders. Since the split beams all originate from the same arbitrary noise fluctuation in the electron bunch, they can be used to monitor within each pulse its intrinsic properties. As depicted in Fig. 5.1 for the three beam geometry, the 0^{th} order is transmitted through a bare substrate, serving as the reference measurement, while the -1^{st} and $+1^{\text{st}}$ orders are used to measure an unpumped and a laser pumped sample, respectively. Hence, the TZPG scheme allows us to measure on a subsequent detector separated in space all three respective signals at the same time. However, the TZPG setup makes it necessary to utilize a special sample card, consisting of a well-defined array of samples and references, as shown in Fig. 5.2b below.

In addition to the main advantage of intrinsically monitoring the reference with the same pulse, the TZPG scheme offers another essential possibility: The TZPG focuses the incident monochromatic, unfocused X-ray beam onto a fixed focus plane. By moving the sample card with a step motor perpendicular through this focus point of the TZPG, it is possible, due to the high photon flux of the European XFEL, to explore different fluence regimes even beyond the linear X-ray spectroscopy up to non-linear multi-photon X-ray interactions. I address this aspect shortly in chap. 5.5. Since one single TZPG can fulfil the diffraction conditions only for a small photon energy range, e.g., for the Ni $L_{3,2}$-edges, one TZPG is not sufficient for the entire range of soft X-ray photon energies accessibly at the SCS instrument. Therefore, several interchangeable TZPGs, optimized for different photon energy windows, had been manufactured. In both our user experiment, we successfully implemented and tested the TZPGs for a wide range of incident X-ray intensities and photon energies ranging from the O K-edge ($\sim 530\,\text{eV}$) to the Ni $L_{3,2}$-edges ($\sim 860\,\text{eV}$), by applying them to suitable reference systems, i.e., the presented Ni and NiO samples.

5.2 Sample preparation and characterization

Just like the $[Fe/MgO]_n$ heterostructure samples discussed throughout chap. 4, the Ni and NiO samples used for the time-resolved X-ray absorption studies at the European XFEL facility were grown ex situ by molecular beam epitaxy in our laboratory. The same MBE-chamber as described in chap. 4.1 was used for the sample preparation. However, due to the different requirements for the new material system, some changes to the Fe/MgO sample preparation have been applied. As indicated in Fig. 5.2a, an O_2-supply line has been mounted to the MBE-chamber, allowing the evaporation in an O_2-background pressure, which is necessary for the NiO preparation.

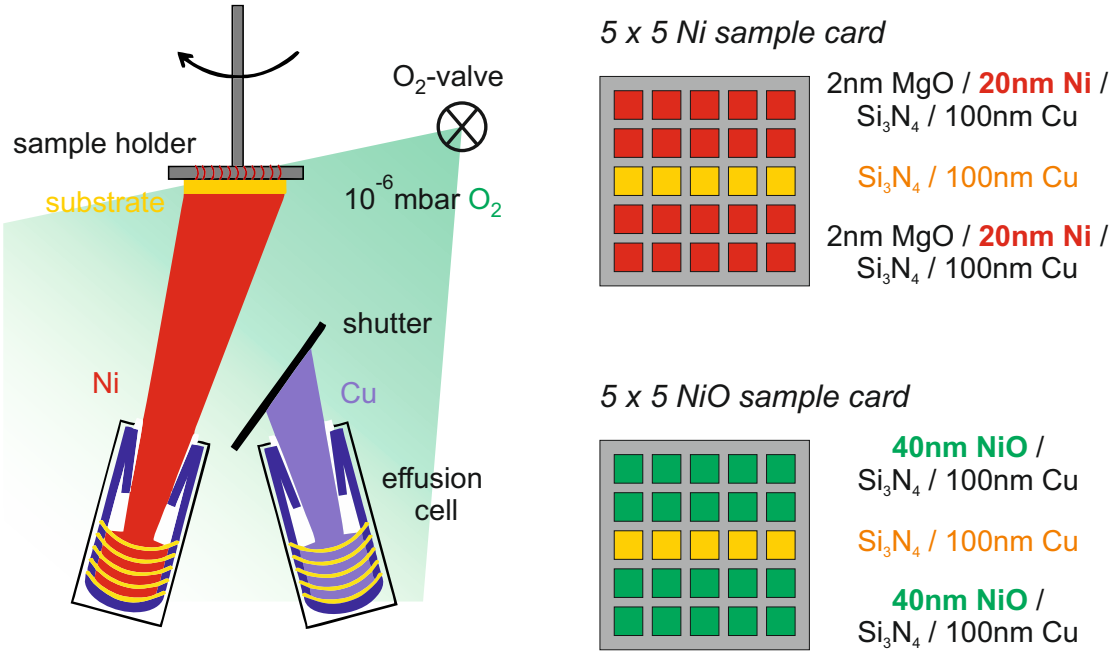

Fig. 5.2.: Left side: Schematic of the MBE-chamber (cf. Fig. 4.1) used to grow the Ni and NiO samples. Due to the special requirements an O_2-supply line has been mounted to the MBE-chamber, allowing the evaporation in an O_2-background pressure. Right side: Schematic of a 5×5 Ni sample card (top) and a 5×5 NiO sample card (bottom). For both sample cards the middle row provides in the experiment the blank reference samples. All $200\,\text{nm}$ thick Si_3N_4 windows carry a $100\,\text{nm}$ thick Cu heat sink on the backside. The nominal thickness of the samples are $20\,\text{nm}$ Ni with a $2\,\text{nm}$ MgO capping layer for the Ni sample (top) and $40\,\text{nm}$ NiO for the NiO sample (bottom).

Furthermore, due to the special measurement scheme (cf. chap. 5.1) used for the time-resolved X-ray absorption studies at the European XFEL a special substrate layout consisting of an 5×5 sample-array of $200\,\text{nm}$ thick Si_3N_4-windows had to be used. As shown in Fig. 5.2b (and described in chap. 5.1), the middle row of

the 5×5 Si_3N_4-windows serves in the experiment as the reference sample. Hence, before the sample preparation in the MBE-chamber this middle row had to be covered by a mask preventing the material growth on these Si_3N_4-windows.
In order to eliminate any possible pre-existing water on the Si_3N_4-windows, the substrates were heated before growth in situ for 20 min to 500 K. This temperature was chosen smaller compared to the Fe/MgO-preparation, to ensure no destruction of the respective mask used for the Ni- and NiO-preparation. The preparation of the Ni-samples was carried out at a sample temperature of 400 K in a background pressure of 10^{-10} mbar. Using a growth rate of 0.05 Å/s, 20 nm thick Ni samples with a 2 nm thick MgO capping layer, to prevent subsequent oxidation, were prepared on the remaining uncovered windows. For the preparation of the NiO-samples nominally 23.5 nm of Ni was evaporated in a O_2-background pressure of 10^{-6} mbar (with respect to a base pressure of 10^{-10} mbar), resulting in ~ 40 nm thick NiO on the uncovered windows. To ensure the growth of pure NiO on the substrate and not a coexisting phase of Ni and NiO, the growth rate was reduced to only 0.003-0.005 Å/s. As determined subsequently by X-ray diffraction measurements (see Fig. 5.3 below) a bigger growth rate favors the formation of Ni over the formation of NiO. For the same reason also the sample temperature during growth was lowered by 100 K to only 300 K [188]. Before the actual sample preparation a 100 nm thick Cu heat sink was deposited on the backside of all 5 rows of Si_3N_4-windows, without using the mask, in order to dissipate the excess energy deposited by the laser pump beam in the experiment.

Fig. 5.3 shows small-angle X-ray diffraction measurements of three test samples. For simplicity, the three test samples have been prepared on the single window Si_3N_4 membranes used for the Fe/MgO measurements. The sample thickness of these test samples is slightly thinner than the actual samples used in the experiment, due to time reasons in the preparation of the test samples. The first test sample (Fig. 5.3, top red curve) represents a Ni sample without any capping layer, prepared by evaporating nominally 18.0 nm of Ni with 0.05 Å/s in an O_2 free background pressure of 10^{-10} mbar. As reported by the small-angle X-ray diffraction measurements, the corresponding fit of the Kiessing fringes [145] using the *pi.exe* program package by U. von Hörsten [146] indeed results in a sample thickness of 18.6 nm. The second and third test samples (Fig. 5.3, middle pink and bottom green curve) depict two NiO samples that have been prepared by evaporating nominally 18 nm of Ni in a 10^{-6} mbar O_2-background pressure using two different growth rates of 0.05 Å/s and 0.005 Å/s, respectively. However, the small angular X-ray diffraction measurements show that the test sample prepared with 0.05 Å/s lead to a slightly increased sample thickness of only 19.3 nm, which is very similar to the one of the first test sample. In contrast, the test sample prepared with 0.005 Å/s results in a

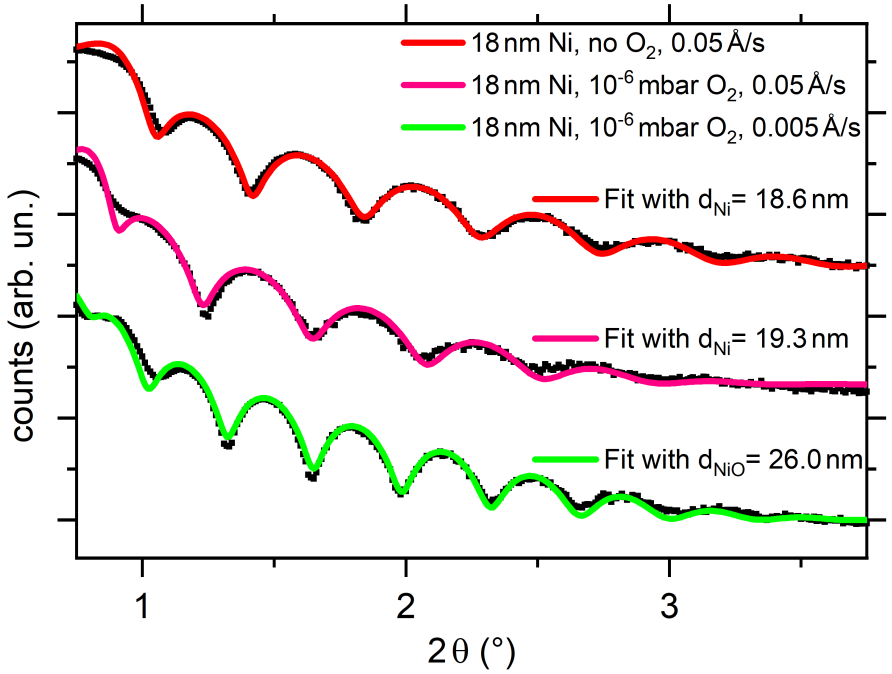

Fig. 5.3.: Small-angle X-ray diffraction measurements of three test samples prepared by evaporating nominally 18.0 nm of Ni under different preparation conditions. Top (red): 18.0 nm Ni test sample evaporated with 0.05 Å/s in a O_2 free background pressure. Middle (pink): Failed 26.0 nm NiO test sample evaporated with 0.05 Å/s in a 10^{-6} mbar O_2-background pressure. Bottom (green): Successful 26.0 nm NiO test sample evaporated with 0.005 Å/s in a 10^{-6} mbar O_2-background pressure. For more details see text.

sample thickness of 26.0 nm, indicating the successful growth of NiO, due to the bigger lattice parameter of NiO compared to Ni. Hence, the bigger growth rate seems to favor the formation of Ni over the formation of NiO. Consequently, to ensure the growth of NiO for the actual samples used in the experiment, I limited the growth rate to 0.003-0.005 Å/s.

For further characterization, Fig. 5.4 shows small and wide-angle X-ray diffraction measurements of two additional test samples of Ni and NiO, which then have been used for the actual X-ray absorption experiments at the synchrotron SOLEIL. The Ni sample was prepared by evaporating nominally 25.0 nm of Ni with 0.05 Å/s in an O_2 free background pressure of 10^{-10} mbar, while the NiO sample was evaporated with a growth rate of 0.003 Å/s in a 10^{-6} mbar O_2 background pressure. The fits of the small angular diffraction measurements (Fig. 5.4, left side) result in sample thickness of 25.5 nm for the Ni sample, matching the nominal thickness, and a thickness of 35.7 nm for the NiO sample, indicating again the successful growth of NiO due to the smaller growth rate. The amorphous Si_3N_4 membranes do not support a crystalline growth of either Ni or NiO, resulting in polycrystalline samples. Hence, the wide-angle X-ray diffraction data of both samples (Fig. 5.4, right side) have a bad signal-to-noise ratio. Nonetheless, comparing the expected diffraction

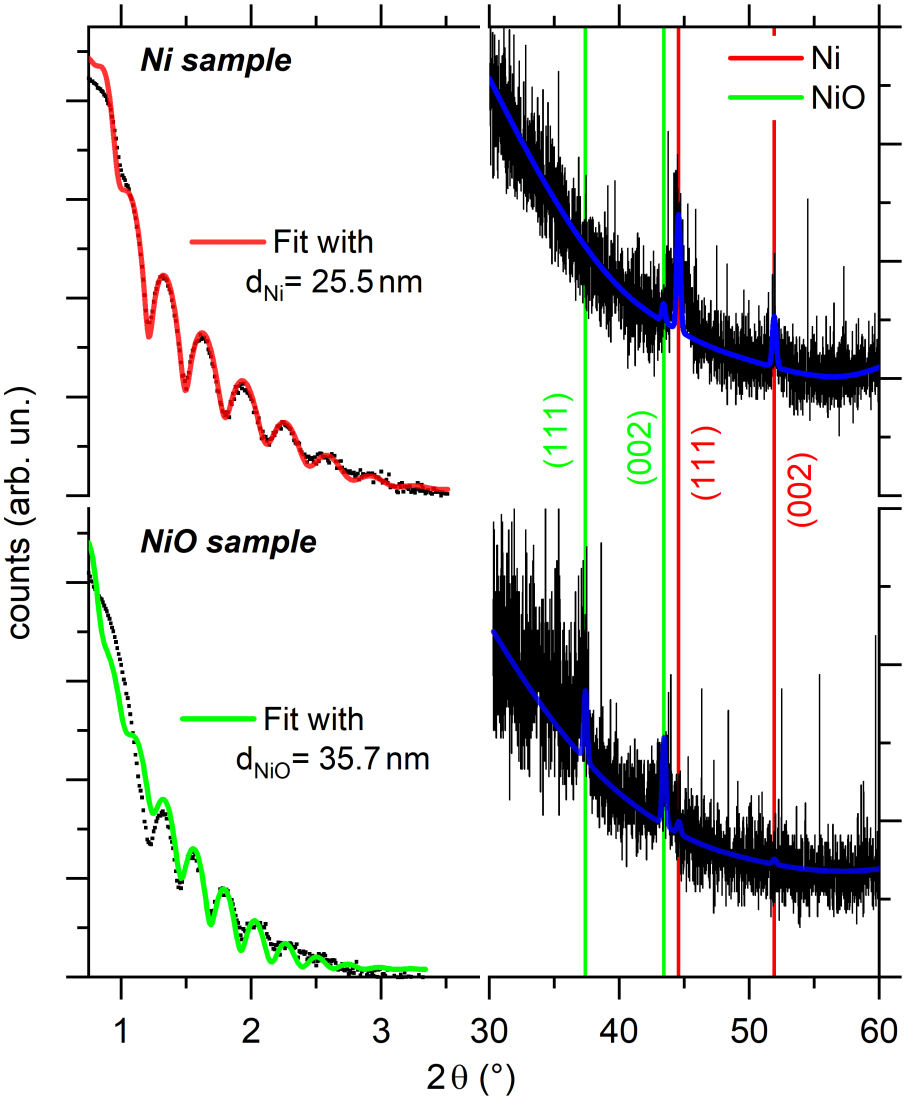

Fig. 5.4.: Small- (left) and wide- (right) angle X-ray diffraction measurements of one 25.0 nm Ni sample (top) and one 36 nm NiO sample (bottom). The expected diffraction peaks of Ni (red vertical lines) and NiO (green vertical lines) from the AMCSD database [189] coincide with the measurement data (or for better visibility with the blue fitting curves), confirming the successful growth of both samples, Ni and NiO. The amorphous Si_3N_4 membrane do not support a single crystalline growth of either sample resulting in the bad signal-to-noise ratio.

peaks of Ni (red vertical lines) and NiO (green vertical lines) using the AMCSD database [189], with the measurement data (or for better visibility with the blue fitting curves using *pi.exe* [146]) results again in the confirmation of the successful growth of both samples, Ni and NiO. I want to note that the thickness of the Ni samples had been reduced to 20.0 nm for the experiments at the European XFEL, because of time reasons during the preparation. Furthermore, the thickness of the NiO samples are slightly ($\sim$ 11%) smaller than the nominal thickness. I attribute this small deviation to the quartz crystal: Even though the growth rate had been adjusted before opening the O_2-valve to the chamber, the subsequent regulation of the growth

rate presumably was influenced by the O_2 background pressure. Nonetheless, the preparation of all NiO samples appeared to be successful; That is why I will address the NiO samples solely by their nominal thicknesses.

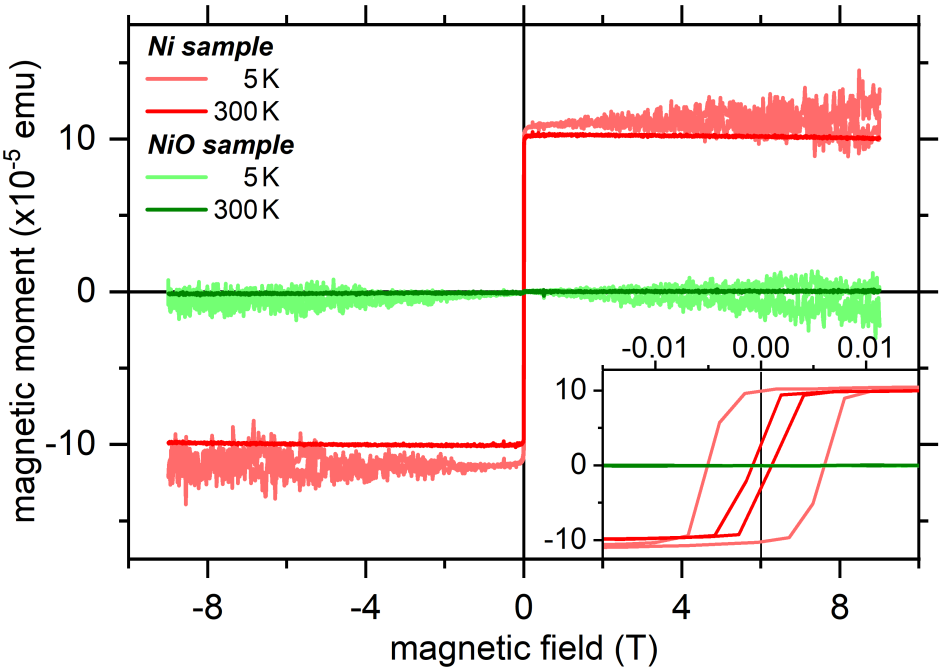

Fig. 5.5.: Vibrating-sample magnetometer measurements for magnetic fields of up to 9 T for 5 K (light color) and 300 K (dark color) for the Ni (red) and NiO (green) sample. The inset shows a magnification around zero field. The Ni sample exhibits a clear hysteretic behavior while the NiO sample does not show any macroscopic magnetization.

For these two samples, I furthermore measured their respective magnetization curves for 5 K and 300 K. Fig. 5.5 shows the corresponding vibrating-sample magnetometer measurements for magnetic fields of up to 9 T. The Ni sample exhibits a clear hysteretic behavior with a saturation magnetization of $10 \cdot 10^{-5}$ emu, and a coercive field of 5.5 mT for the low temperature and 1.0 mT for the room temperature measurement. The magnetization curves are typical for a ferromagnetic material, hence confirming the existence of Ni metal in the sample, as expected. In contrast, the NiO sample does not show any hysteretic behavior or macroscopic magnetic signal, as expected for an antiferromagnetic sample.
In summary, both the pre-characterization measurement methods, namely the X-ray diffraction (Fig. 5.4) and vibrating-sample magnetometer measurements (Fig. 5.5), indicate the successful preparation of the Ni metal sample as well as the NiO sample. However, to certainly ensure the expected composition of both types of samples before the time-resolved X-ray absorption studies at the European XFEL facility, additionally static X-ray absorption measurements at the Ni $L_{3,2}$-edge at the synchrotron SOLEIL have been carried out (see below Fig. 5.6, grey curves), which have been measured by E. Jal and co-workers, see [190]. The

spectral shape of the transition metal absorption edge exhibits precise characteristics of a nickel metal film for the Ni sample and pure nickel oxide for the NiO sample. Hence, also those measurements confirm the successful preparation of both samples, as expected.

5.3 Static X-ray absorption spectra of Ni and NiO at the European XFEL

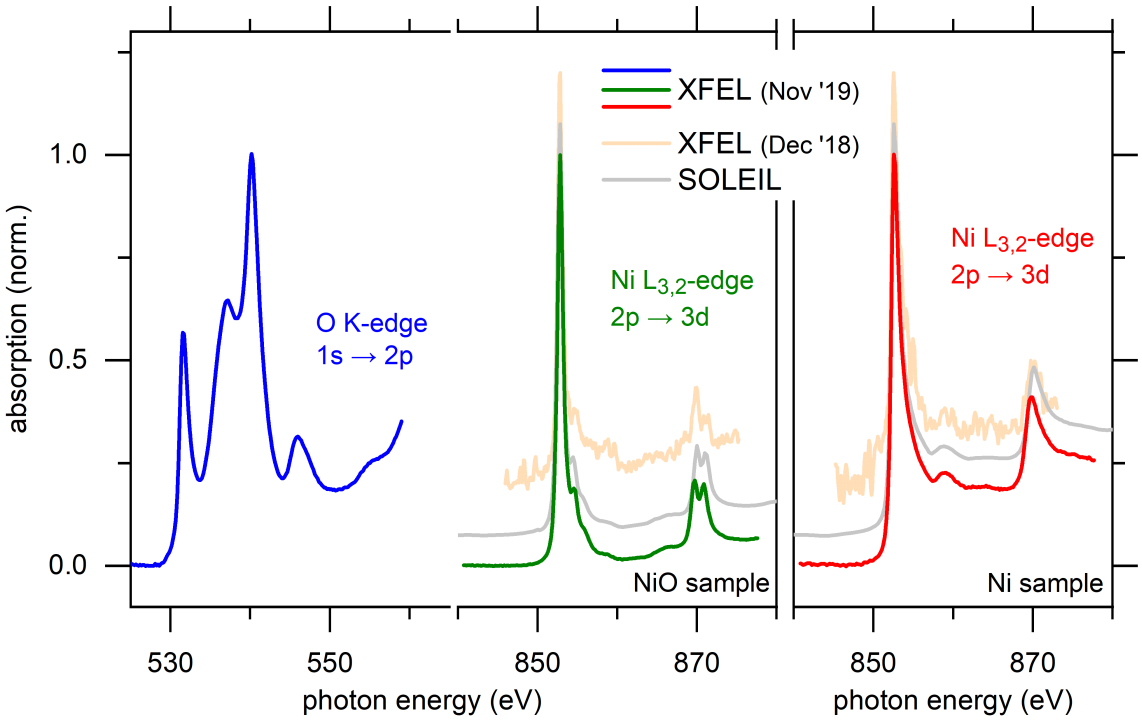

Fig. 5.6.: Static X-ray absorption spectra at the O K-edge (blue, left) and Ni $L_{3,2}$-edges (green, middle) of the NiO sample (left panel) and the Ni $L_{3,2}$-edges (red, right) of the Ni sample (right panel). For comparison, the Ni $L_{3,2}$ spectra are measured at the synchrotron SOLEIL (light grey lines), during the very-first user experiment at the European XFEL in Dec '18 (light yellow lines), measured with a repetition rate of only 10 Hz, and at our second experiment at the European XFEL in Nov '19, measured with a repetition rate of 70000 Hz. The Ni spectra are vertically offset for better visibility. For more details see text.

Fig. 5.6 shows the unpumped X-ray absorption spectra at the O K-edge (blue line) and Ni $L_{3,2}$-edges (green line) of the NiO sample (left panel) and the Ni $L_{3,2}$-edges (red line) of the Ni sample (right panel), measured at the European XFEL facility during our second experiment in Nov '19. Furthermore, I show the very-first recorded spectra, at the Ni $L_{3,2}$-edge, of external users at the SCS instrument, measured during the very-first community experiment in Dec '18 (light yellow). I compare both X-ray absorption spectra of the Ni $L_{3,2}$-edges, of both beamtimes, with static X-ray absorption spectra of the Ni and NiO test samples measured at

the synchrotron SOLEIL (grey lines) by E. Jal and co-workers, see [190]. In the following, I will concentrate mostly on the measurement data from the second experiment (Nov '19). This is because in the first experiment (Dec '18) slightly different samples have been used (where some of them have not been prepared within the framework of this thesis), and furthermore because the instrument itself experienced during this first test run still some performance issues with the undulator and the detector resulting in the given non-optimized data quality compared to the second experiment. The repetition rate used to measure the Dec '18 spectra (light yellow lines) was set to only 10 Hz, while the presented data of our second experiment in Nov '19 have been measured with a repetition rate of 70000 Hz.
First of all, I want to highlight the astonishing data quality of the spectroscopy data measured at the European XFEL facility with the zone plate setup introduced above. The Ni $L_{3,2}$-edge spectra of both samples exhibit, for both the small repetition rate and especially for the 70 kHz data, clear and defined fine structures, which allows to unambiguously distinguish between nickel and nickel oxide, and therefore assign them clearly to either the transition metal sample or the oxide sample, respectively. As reported in literature [191–193], the $L_{3,2}$ absorption spectrum of the nickel sample exhibits two main peaks, corresponding to the transitions from the spin-orbit-split $2p_{3/2}$ initial state (L_3-edge), and $2p_{1/2}$ initial state (L_2-edge) to the $3d$ final states. Furthermore, the Ni absorption spectrum shows a distinct satellite peak ~ 6 eV above the L_3-edge at 852.6 eV, which can be clearly identified in all three different measurements (Fig. 5.6, right), and are assigned to transitions of $2p_{3/2}$ to empty states of sp character in the bulk nickel band structure [191]. In contrast, all three measured absorption spectra of the nickel oxide sample (Fig. 5.6, middle) show not three, but four distinct features, which are also all in agreement with literature [194–197]. The NiO spectrum displays with its four features clearly the well-reported shape of a Ni^{2+} compound, which results from the effect of the crystal field with octahedral symmetry on the Ni^{2+} ion [197]. In detail, the NiO spectrum shows, compared to Ni, an unambiguously distinguishable L_3-edge peak at 852.8 eV with a satellite only ~ 2 eV above the L_3-edge, and a clear two-peak like L_2-edge structure at 869.9 eV and 871.1 eV instead of a single peak [195]. The clear identification and classification of the spectra to the respective transition metal sample or the oxide sample presents one of the key features of static X-ray absorption spectroscopy. However, while a synchrotron facility, e.g., SOLEIL, is predestined for those kinds of static spectroscopy measurements, the emphasis of a X-ray free electron laser facility like the European XFEL laid firstly on measurements with a fixed X-ray energy and the aspect of spectroscopy had still to be optimized. Therefore, as the first external users of the European XFEL SCS instrument, we introduced in Dec '18 the presented zone plate setup (cf. Fig. 5.1), to enable reproducible spectroscopic measurement at the respective instrument. The direct comparison of the absorption spectra conducted at the synchrotron and the European XFEL (Nov '19) does not show any

visible differences with respect to data quality or energy resolution, demonstrating the ability to successfully classify the measured Ni $L_{3,2}$ absorption spectra to the respective transition metal sample or the oxide sample at both facilities.
Moreover, Fig. 5.6 also presents measurements at the O K absorption edge (left, blue line) ~ 300 eV below the Ni $L_{3,2}$ absorption edges, which therefore had to be recorded with a different zone plate. Also the O K-edge spectrum of nickel oxide shows an excellent data quality, allowing to identify a defined fine structure with in total five main features, all in agreement with literature [198–200]. In NiO, the O K absorption edge probes transitions from O $1s$ initial states to empty O $2p$ final states, which are hybridized with various Ni states [200], resulting in the feature-rich absorption spectrum. In particular, the first feature in the pre-edge region of the NiO O K-edge spectrum at 531.7 eV corresponds to transitions of $1s$ initial state to O $2p$ final states, which are hybridized with the Ni $3d$ states [199]. The main O K-edge feature of maximum absorption at 540.1 eV, and the corresponding feature ~ 3 eV below resembles transitions to O $2p$ final states hybridized with Ni $2s$ and $4p$ states [200]. Consequently, also the O K-edge spectrum successfully demonstrates the ability to unambiguously classify the nickel oxide sample from its defined fine structures, and moreover represents the great possibility to measure at the SCS instrument X-ray absorption spectra in a wide range of X-ray photon energies. In summary, all measurements (high and low repetition rate) presented in Fig. 5.6 do not only serve as a proof of concept of the zone plate setup for successful spectroscopy measurements at the SCS instrument at the European XFEL facility, but also highlight its possibilities and the respective astonishing data quality of the corresponding X-ray absorption spectra.

5.4 Ultrafast soft X-ray spectroscopy of Ni and NiO at the European XFEL

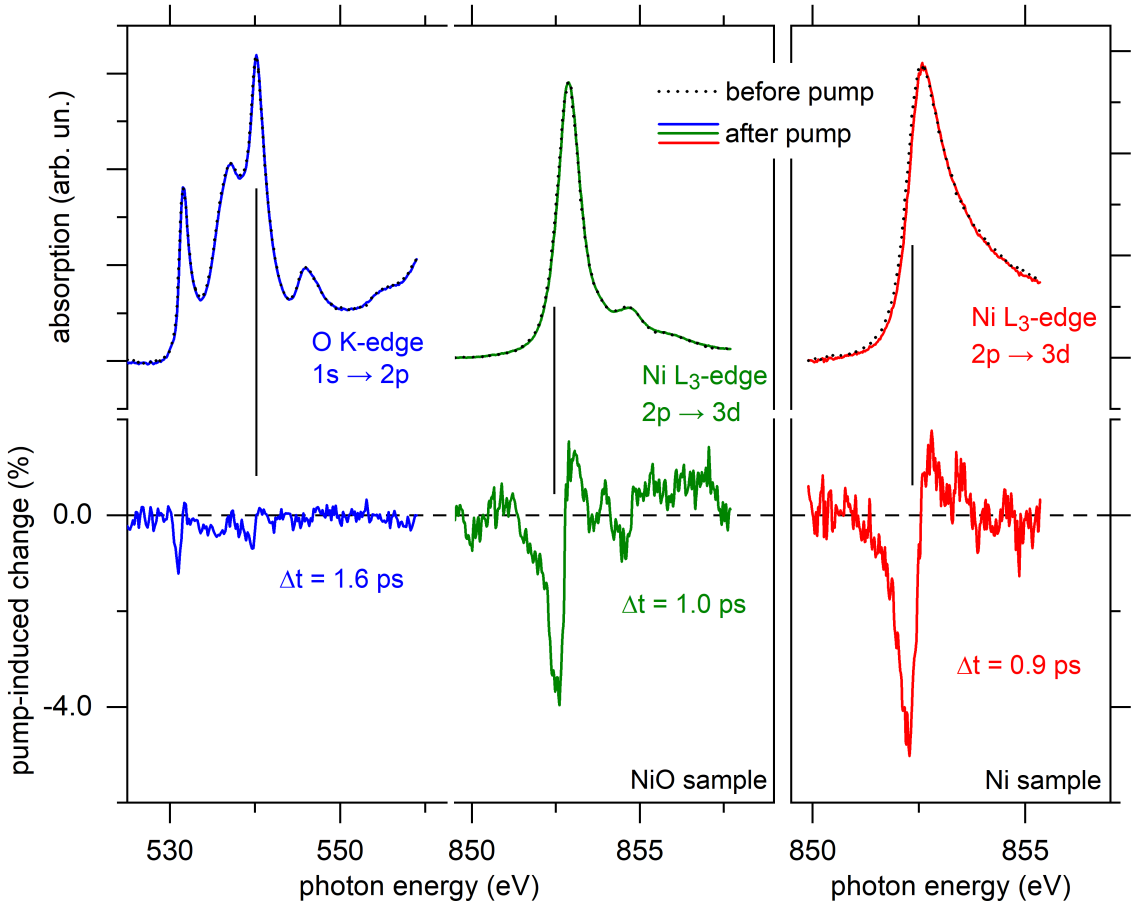

Fig. 5.7.: Top panel: Soft X-ray absorption spectra at the O K-edge (left, blue) and Ni L_3-edge (middle, green) of the NiO sample (left panel) and the Ni L_3-edge (right, red) of the Ni sample (right panel) measured before and after IR laser pumping. Bottom panel: Pump-induced changes of the corresponding absorption spectra as a function of soft X-ray photon energy at the indicated fixed pump-probe delays t. The incident laser fluence was set to $15\,\mathrm{mJ/cm^2}$. The vertical lines indicate photon energies at which the time-dependent measurements (cf. Fig. 5.8) were conducted.

Fig. 5.7 shows in the top half the X-ray absorption spectra of the NiO sample (left panel) and the Ni sample (right panel) at the respective O K absorption edge and Ni L_3 absorption edge before and after laser pumping, measured with $< 25\,\mathrm{fs}$ short X-ray pulses at the European XFEL facility. This results in an effective time resolution of $110\,\mathrm{fs}$ for the single measurements as determined during the experiments, taking possible drifts and the jitter between laser and X-ray pulse into account. The incident laser fluence was set to $15\,\mathrm{mJ/cm^2}$ for a laser photon energy of $h\nu = 1.55\,\mathrm{eV}$ ($800\,\mathrm{nm}$ wavelength).

The bottom half of Fig. 5.7 presents the pump-induced changes of the corresponding absorption spectra measured at selected fixed pump-probe delays t. A clear pump-

induced change at all measured absorption edges, for both the transition metal sample or the oxide sample can be seen. Both samples thereby present model systems to investigate and compare the influence of the metallic and oxide character, as well as of the ferromagnetic and antiferromagnetic order, on the time-dependent behavior [201]. The maximum pump-induced changes at the Ni L_3 absorption edges for the two different samples are similar in strength of up to 5.0 and $4.0\,\%$, at a similar time delay of 0.9 and $1.0\,$ps, respectively. The pump-induced change at the O K-edge is with a strength of only $1.0\,\%$ noticeably smaller than at the corresponding transition metal edge. I start with the spectral changes of the two Ni L_3-edges: Similar to the spectral signature observed for the Fe L_3-edge (cf. chap. 4.2.2, Fig. 4.5), the maximum pump-induced changes at the Ni L_3 absorption edges for both samples occur at the rising edge of the absorption spectra, i.e., $0.4\,$eV (NiO) and $0.25\,$eV (Ni) below the maximum absorption. Consequently, similar to the Fe L_3-edge, the pump-induced change shows a first derivative-like spectral signature, corresponding to a red-shift of the absorption edge due to the laser pump pulse. The measurements at the NiO sample presented in Fig. 5.7 show that not only the Ni L_3-edge itself but also the following satellite $\sim 2\,$eV above the L_3-edge exhibits a pump-induced change with a first derivative-like spectral signature. In contrast, the satellite of the nickel sample $\sim 6\,$eV above the L_3-edge (not shown in Fig. 5.7, but showcased in Fig. 5.9 below) does not follow the change of the main edge and displays a different transient behavior, which I will discuss further below.

Starting, I want to highlight again the high data quality of the now *time-resolved* XAS data measured at the European XFEL. Due to the substantially higher photon flux of the free electron laser, especially compared to the femtoslicing scheme used at a synchrotron, the acquisition of fs time-resolved X-ray spectroscopy data with a reasonable signal to noise ratio is much faster. While the measurement time for the pump-induced change of the Fe L_3-edge shown in chap. 4.2.2, Fig. 4.5 was of the order of at least $\sim 2\,$hours, the pump-induced change of the Ni L_3-edge shown in Fig. 5.7 was only $10\,$minutes. Consequently, the fast acquisition time for high-quality data offers *great possibilities of systematic measurements*, e.g., identifying time-resolved, pump-induced dynamics of not only various absorption edges (i.e., the transition metal L-edges and the oxygen K-edge, which turned out to be crucial for the Fe/MgO system), but also investigating the dynamics of several spectral signatures, or analyzing the pump-induced spectral changes at various time delays (cf. Fig. 5.10). However, the focus point of this thesis is mainly dedicated to chap. 4, the dynamics in the Fe/MgO heterostructure. Therefore, I will only outline a selected quantity of first results of the recorded time-resolved Ni and NiO data within the framework of this chapter, while a complete and profound analysis of these measurements is done elsewhere.
Following the example of the analysis of the Fe/MgO heterostructure, I focus next

on the investigation of the pump-induced dynamics as a function of the pump-probe delay at a fixed soft X-ray photon energy, indicated by vertical lines in Fig. 5.7. The selected fixed energy values I chosed to discuss here are: (i) for the Ni sample at the Ni L_3-edge, as well as (ii) for the NiO sample at the Ni L_3-edge both at the energy of maximum change, and (iii) for the NiO sample at the O K-edge at the maximum of the absorption spectra.

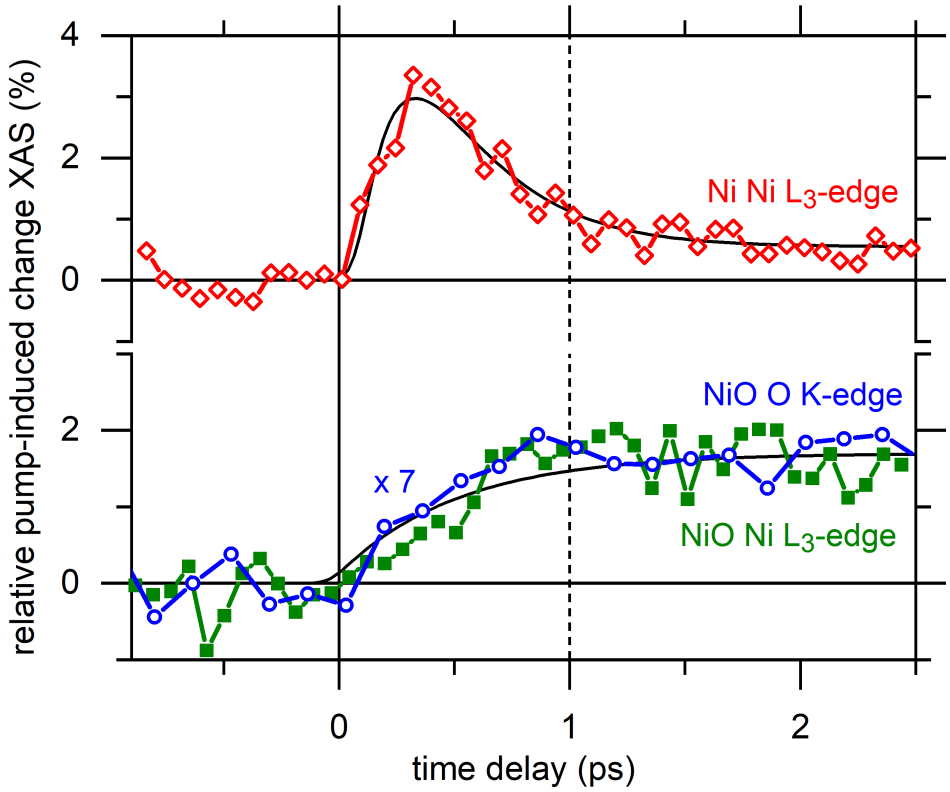

Fig. 5.8.: Relative pump-induced changes with 1.55 eV pump photon energy observed at two selected fixed soft X-ray photon energies as a function of pump-probe delay. Top panel: Rising edge of the Ni L_3-edge (red) for the Ni sample. Bottom panel: Rising edge of the Ni L_3-edge (green) and maximum absorption of the O K-edge (blue, multiplied by a factor of 7) for the NiO sample. The incident laser fluence was set to 15 mJ/cm^2. The black lines are fits to the data as specified in the text. The vertical dashed line at 1.0 ps highlights the different transient behavior.

Fig. 5.8 shows the transient of the pump-induced changes at the three selected photon energies measured as a function of pump-probe delay. The transient of the Ni L_3-edge for the transition metal sample and the nickel oxide sample exhibit a completely different behavior. The transient of the O K-edge follows the dynamic of the pump-induced change of the corresponding Ni L_3-edge, presumably due to the hybridization of the O $2p$ final states with the Ni states. The different transient behavior of the transition metal sample (Fig. 5.8, top panel) and the oxide sample (Fig. 5.8, bottom panel) is highlighted at the 1.0 ps mark, indicated by the vertical dashed line. While the pump-induced change of the Ni L_3-edge of the Ni sample (red line) has already gone through its maximum and has started to recover, both

the Ni L_3-edge (green line) and the O K-edge (blue line) of the NiO sample just reached their maximum change.
In more detail, the Ni L_3-edge of the Ni sample shows a fast increase of the change in absorption with its maximum at $320\,\text{fs}$ and a subsequent recovery almost but not entirely back to zero change until $1.5\,\text{ps}$ from where it then stays on this finite value until the end of the measured time delay. The dynamic behavior of the Ni L_3-edge for the transition metal sample is known from literature [61, 149], and very similar to the transient observed for the Fe L_3-edge of the Fe/MgO heterostructure until $1.2\,\text{ps}$ (cf. Fig. 4.6) or of the Fe reference sample (cf. Fig. 4.7). Hence, I fitted the time-dependent intensity of the Ni L_3-edge of the Ni sample with the same fit function as for the Fe L_3-edge (cf. eq. 4.1). The fit to describe the measured transient takes into account the following three distinct time constants: The time zero shift $t_0 = 0.07 \pm 0.01\,\text{ps}$, the time constant $\tau_1 = 0.18 \pm 0.06\,\text{ps}$ representing the fast increase of the change, and the exponential relaxation with the time constant $\tau_2 = 0.30 \pm 0.09\,\text{ps}$. In contrast, both the Ni L_3-edge and the O K-edge of the NiO sample exhibit a single, slower change in absorption, which builds up within $1.0\,\text{ps}$, and then stays constant until the end of the measured time delay. This one step dynamic behavior of both absorption of the NiO sample edges can be fitted, taking only two time constants for time zero shift and build up into account (cf. eq. 4.2). The fit to describe the data yield $t_0 = 0.01 \pm 0.02\,\text{ps}$ and $\tau_1 = 0.55 \pm 0.03\,\text{ps}$.

The observations made from the pump-induced dynamics happening in the different constituents of the Fe/MgO heterostructure (cf. chap. 4.2), and the understanding of the effect of the pump-induced changes to the spectroscopic fine structures of the respective absorption edges (cf. chap. 4.3) can be transfered directly to the transient and spectroscopic changes of the Ni and NiO sample: The time-dependent X-ray absorption signal at the rising flank of the Ni L_3-edge of the metallic Ni sample (Fig. 5.8, top panel) is characterized by an absorption increase, which reaches its maximum at $320\,\text{fs}$, well after the laser pump pulse duration of $35\,\text{fs}$. In qualitative agreement with literature [60, 61, 149], and the observations for the absorption edge of the Fe metallic constituent, this transient behavior is resulting from a red-shift of the Ni L_3-edge. Therefore, the origin of this time-dependent change can be explained in the same manner as it was done before, namely by the relaxation of the primarily excited, non-equilibrium electron distribution and the subsequent redistribution of electrons and holes towards E_F in the metallic system. Similarly, I can quantify the size of the red-shift with the simple modeling procedure introduced in chap. 4.3 above. For a fixed delay time of $0.9\,\text{ps}$, and laser fluence of $15\,\text{mJ/cm}^2$, I find a red-shift of the Ni L_3-edge of the Ni sample of $60\,\text{meV}$.
The transients of the Ni L_3-edge and the O K-edge of the insulating NiO sample (Fig. 5.8, bottom panel) are characterized by a significantly slower response than for the metallic Ni sample. The response is in its time-dependent behavior comparable

with the observations for the O K absorption edge of the insulating MgO constituent. However, in contrast to the Fe/MgO heterostructure, where initially the Fe electronic system was excited and subsequently a phononic transfer of the excitation from the metallic constituent to the insulating constituent was observed, the NiO sample only consists of the insulating constituent itself. For the Fe/MgO system, I reported that the dynamics at the O K-edge occur exclusively in the heterostructure. At the same time, a MgO reference sample showed no transient changes at the respective absorption edge (cf. Fig. 4.7). However, for the NiO sample, the measurements show a pump-induced change even though the $h\nu = 1.55$ eV pump laser excites within the bandgap of the insulator. Consequently, the absorption of the laser pump pulse in NiO is most likely mediated by possible defect sites in the sample. I note that in contrast to the preparation of the Fe/MgO multilayer system, the preparation of the NiO samples was indeed more prone to errors. Thus the existence of possible defect sites in this sample, e.g., metallic Ni atoms or oxygen vacancies, seems likely. However, I can ensure that those possible defects are not a dominant contribution to the overall sample system, since an essential quantity of Ni defects would significantly change the fine structure of the presented (static) NiO X-ray absorption spectra. Furthermore, a successful preparation of the insulating NiO sample has been concluded within the accuracy of all presented pre-characterization measurements (cf. chap. 5.2). Consequently, with the current state of the analysis of the time-resolved X-ray absorption measurements of the Ni and NiO samples at the European XFEL, I do attribute the observed pump-induced changes for the insulating NiO sample to be mediated by the excitation of defect sites in the sample system. Again, I can quantify the size of the observed red-shift of the NiO L_3-edge spectrum with the modeling procedure. For a fixed delay time of 1.0 ps, and laser fluence of 15 mJ/cm^2, I find a red-shift of the Ni L_3-edge of the NiO sample of 30 meV.
I stress that the more detailed analysis and the profound interpretation of the measurement data shown in chap. 5.4 is still ongoing and not part of this thesis. Within the current discussion, a systematic study of possible additional heating effects on the spectra due to the high repetition rates used for the measurements at the European XFEL may also be of importance. I want to note that the here presented analysis of the first results tries to exclude, in the currently best possible way, those effects by only including the measurement data, where heating or accumulation effects are minimized.

The fast acquisition time for high-quality data allows us to conduct systematic measurements, e.g., identifying time-resolved, pump-induced dynamics of several spectral signatures or investigating pump-induced spectral changes at various time delays. To emphasize this point, I report in Fig. 5.9 exemplarily on the X-ray absorption spectrum of solely the Ni sample; however, at the extended energy range of the Ni $L_{3,2}$ absorption edges: The spectra are measured with 110 fs

effective time resolution before and after laser pumping with a laser photon energy of $h\nu = 1.55\,\text{eV}$ (800 nm wavelength) and an incident laser fluence of $15\,\text{mJ/cm}^2$. As expected, the pumped spectrum shows an energy red-shift compared to the unpumped spectrum, but additionally, a small reduction of the peak intensities. It should be noted that such an intensity decrease, due to a broadening of the peak, can also be attributed to state-blocking effects [101]. However, in context with all previously presented transition metal spectra in this thesis, in particular Fig. 5.7, it is unlikely that this peak reduction results directly from a pump-induced effect rather than being a result of remaining heating or accumulation effects.

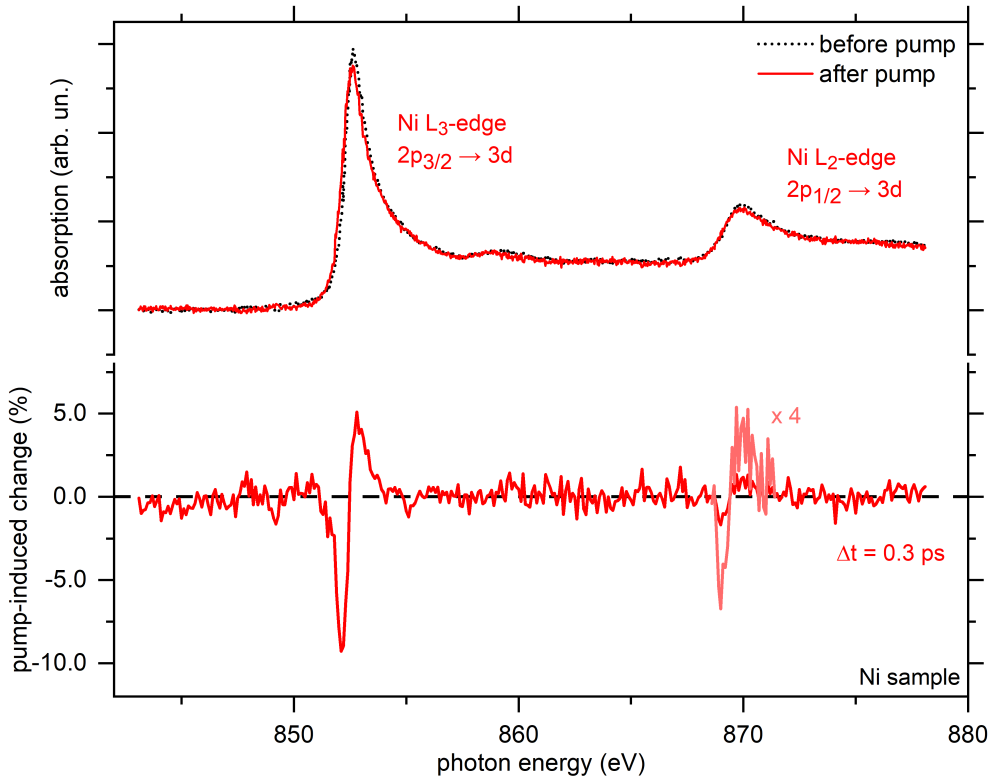

Fig. 5.9.: Top panel: Soft X-ray absorption spectrum at the extended energy range of the Ni $L_{3,2}$ absorption edges measured before and after IR laser pumping. Bottom panel: Pump-induced change of the corresponding absorption spectrum as a function of soft X-ray photon energy at the indicated fixed pump-probe delays t. The pump-induced change of the L_2-edge is additionally magnified by a factor of four (light red). The incident laser fluence was set to $15\,\text{mJ/cm}^2$.

The bottom half of Fig. 5.9 presents the corresponding pump-induced change at the selected fixed pump-probe delays of $0.3\,\text{ps}$. For better representation, the pump-induced change at the L_2-edge is magnified by a factor of four. In agreement with literature [61], not only the Ni L_3-edge but also the L_2-edge exhibit a pump-induced change with a first derivative-like spectral signature, resulting from an energy red-shift of the pumped spectrum. Using the modeling procedure I find a red-shift of the Ni L_3-edge of $130\,\text{meV}$, while the L_2-edge shows only a shift of $80\,\text{meV}$. I reported above that in NiO (cf. Fig. 5.7 above, green curve) both the Ni L_3-edge

itself but also the following satellite ~ 2 eV above the L_3-edge exhibit a qualitatively similar pump-induced change. In contrast Fig. 5.9 shows that the satellite of the nickel sample, ~ 6 eV above the L_3-edge, does not follow the transient of the main absorption edge. We observed during the experiments (not shown here in this first results) that the nickel satellite exhibits a pump-induced change only after a time delay of ~ 2 ps, which can not be described by an energy red-shift.

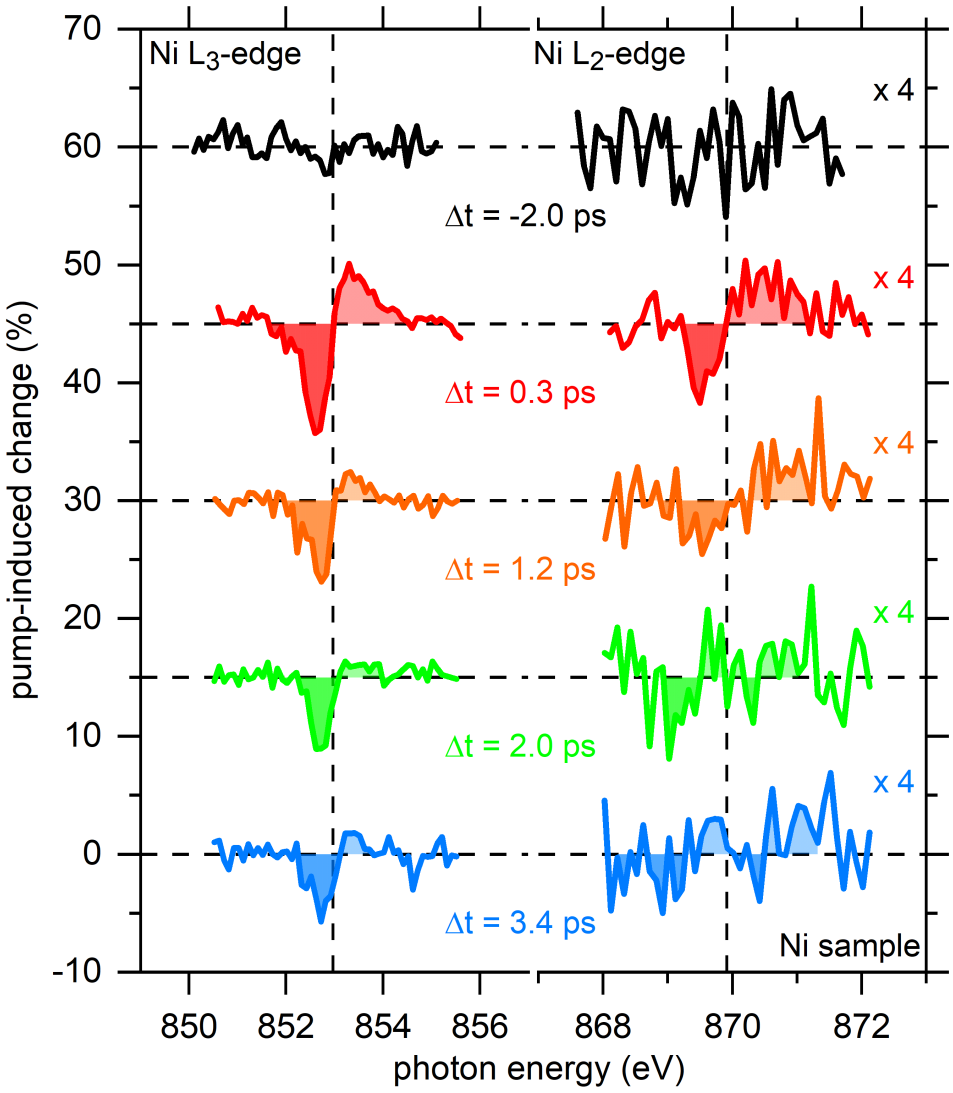

Fig. 5.10.: Evolution of the pump-induced spectral changes of the Ni L_3- (left) and L_2-edge (right) of the nickel sample with progressing (up to down) pump-probe delay t. The pump-induced changes of the L_2-edge are magnified by a factor of four for better visualization. The area ΔA under the derivative-like changes is indicated by the colored area. The incident laser fluence was set to $15\,\mathrm{mJ/cm^2}$.

It was reported in literature [61] that the investigation of the pump-induced change of the L_3 and L_2-edge of a 35 nm Ni metal film revealed that both the two absorption edges exhibit a energy shift upon laser excitation. In agreement with the presented measurements, both absorption edges have been found to shift in the same direction, with the size of the red-shift being different for the Ni L_3

and L_2-edge. Furthermore, Stamm et al. [61] reported that the integrated signal over the respective absorption edges are of opposite sign, which allowed them to conclude on the importance of spin-orbit interaction during ultrafast magnetization dynamics. This highlights that a systematic study and a profound comparison of pump-induced dynamics at a variety of spectral signatures is highly welcomed and can be of great importance to achieve a full understanding of time-resolved studies of selected material systems. However, detailed systematic time-resolved X-ray spectroscopy measurements require a fast acquisition time for high-quality data. Hence, due to the significantly higher photon flux of the free electron laser, compared to the femtoslicing scheme used at a synchrotron, such a study is only truly possible at the former. Finally, I show in Fig. 5.10 exemplarily first results of such a systematic study for the Ni L_3 (left) and L_2-edge (right) of the nickel sample. Fig. 5.10 reports on the evolution of the pump-induced spectral changes of both absorption edges with progressing (up to down) pump-probe delay t. The pump-induced changes of the L_2-edge have been magnified by a factor of four for better visualization. Starting with the first time delay after laser excitation, namely 0.3 ps, which is also reported in Fig. 5.9: The pump-induced change of the different absorption edges exhibit both a derivative-like spectral signature originating from an energy red-shift of the pumped spectrum. The size of the shift is differently strong for both edges. Furthermore, the integrated areas ΔA (indicated by the colored area) under the derivative-like changes shows an opposite sign for the 0.3 ps data, all in agreement with previous findings [61]. Fig. 5.10 shows that while the pump-induced change at the L_3-edge is clearly visible up to delay times of 3.4 ps, the change at the L_2-edge is vanished after 2.0 ps. The integrated area ΔA of the change of both absorption edges is non-zero for a time delay of 0.3 ps, corresponding to the stronger negative change than positive change. The integrated area for the L_3-edge decreases around $\sim 36\%$ for the time step from 0.3 ps to 1.2 ps, and then stays constant until 3.4 ps. The integrated area for the L_2-edge becomes, within the signal-to-noise ratio already zero for time delays of 1.2 ps and longer.

In summary, even though a profound analysis the time-resolved X-ray absorption measurements of the Ni and NiO sample will be done elsewhere, the presented first results provided a comprehensive overview of the time-resolved measurements, conducted during the experiment in November 2019 at the SCS instrument of the European XFEL. Throughout this chapter I highlighted various possibilities, and their importance, to measure with a fast acquisition time high-quality ultrafast soft X-ray spectroscopy measurements: In particular, starting with measuring pump-induced spectral changes (Fig. 5.7), and dynamics (Fig. 5.8) of different absorption edges, to conducting systematic measurements, i.e., identifying time-resolved, pump-induced dynamics of several spectral signatures (Fig. 5.9) or investigating pump-induced spectral changes at various time delays (Fig. 5.10).

5.5 Non-linear X-ray absorption study at the European XFEL

A free-electron laser provides highly intense, ultrashort X-ray pulses. This enables for the first time the opportunity to reach with X-ray photons a situation where one needs to consider the interaction with more than one photon as "concurrent". Here "concurrent" refers to the interaction of several photons within the core-hole lifetime or the coherence time, which are both in the regime of a few femtoseconds [202]. This multi-photon interaction opens the possibility to combine established highly informative spectroscopic methods from the field of non-linear optics with the advantages of photons, namely their sensitivity and selectivity. However, currently, no free-electron laser can provide all experimental requirements to employ most of the rather complex non-linear techniques [203], i.e., multiple coherent X-ray pulses with tunable photon energies directed on the sample from different directions to obey phase-matching conditions for a four-wave mixing geometry [204, 205]. Regardless of the difficult experimental requirements, before the realization of complex non-linear X-ray techniques becomes possible, some elementary demonstrations are still required. Most importantly, while most observations of X-ray pulse stimulated emission so far have been made either indirectly [206] or stimulated by spontaneous emission [207–209] a direct demonstration is up to now still missing. Furthermore, concurrent processes, which might occur during the pulse [210], have to be understood as well. absorption spectroscopy measurements of intense X-ray pulses transmitting through thin film samples offer one of the most simple and informative approach to, on the one hand, demonstrate direct stimulated emission and, on the other hand, to understand possible concurrent processes [203].

Using the TZPG measurement scheme (cf. Fig. 5.1) introduces not only the great possibility of a shot-to-shot reference detection method but also to explore distinct X-ray fluence regimes, ranging from low fluences ($\mu J/cm^2$ to mJ/cm^2) up to highest fluences (beyond J/cm^2), by moving the samples through the focus plane of the TZPG. Since linear X-ray absorption effects, corresponding to low X-ray fluences, are already available at synchrotron facilities and well understood, they served at the first external user spectroscopy experiment at the European XFEL mainly as a tool to explore and test the different conditions of the instrument. However, approaching more and more intermediate or even high fluences, the initiated electron dynamics start to occur during a single femtosecond pulse, which can lead to strong distortions in the spectra [211, 212], representing first non-linear X-ray absorption effects [203].

Throughout chap. 5, I concentrated mainly on time-resolved data measured during our second user experiment in November 2019. I only once actually displayed the recorded spectroscopy data from our first user experiment in December 2018 (cf.

Fig. 5.6). The latter was, among other things, focused on quantitatively studying non-linear X-ray processes in the high fluence regime on solids whose data analysis is up to now part of the Ph.D. thesis of R. Engel from the group of M. Beye. Nevertheless, I want to present here shortly one non-linear X-ray absorption spectrum measured at the Ni $L_{3,2}$-edge of a Ni sample to highlight once more the possibilities and perspective for future measurements at the European XFEL facility.

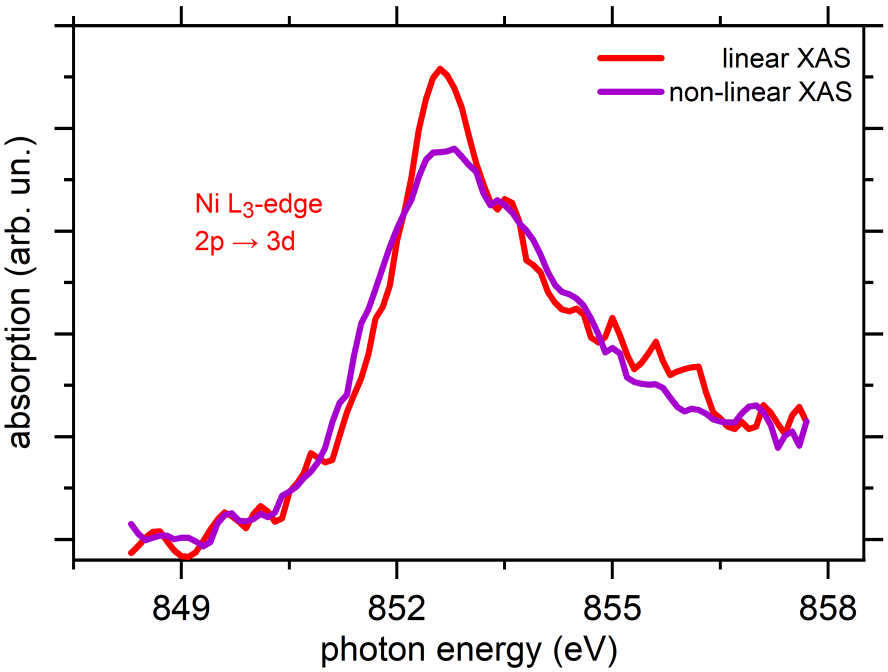

Fig. 5.11.: Comparison of the Ni L_3-edge absorption spectra of a Ni sample measured in the linear (red) and non-linear X-ray regime (purple). The non-linear absorption spectrum exhibits a decrease of peak intensity and a nonuniform broadening compared to the linear one. Shown exemplary spectra are in a preliminary status of analysis. A more detailed and quantitatively evaluation will be part of the Ph.D. thesis of R. Engel from the group of M. Beye.

Fig. 5.11 shows exemplarily a preliminary comparison of the Ni L_3-edge absorption spectra of a Ni sample measured in the linear (red curve) and non-linear X-ray regime (purple curve). Clear difference between the two spectra can be identified. Most noticeably, the non-linear absorption spectrum exhibits a decrease in peak intensity compared to the linear one. Furthermore, the non-linear spectrum shows a nonuniform broadening with a slightly stronger effect on the lower energy side of the absorption peak. However, within the framework of this thesis, I have to forego on a more detailed and quantitative evaluation and interpretation of the non-linear X-ray absorption data, since it will be part of another thesis. In summary, Fig. 5.11 clearly reports a successful first direct demonstration of non-linear X-ray pulse stimulated emission.

Conclusions and perspectives

6

Pump-induced dynamics in a Fe/MgO heterostructure

This thesis was dedicated to femtosecond (fs) time-resolved soft X-ray absorption spectroscopy (XAS) studies on complex materials. The focal point was thereby the element-specific investigation of the pump-induced dynamics induced in an Fe/MgO multilayer sample, which acts as a model system for a metal-insulator heterostructure. The element-specific character of XAS made it the ideal tool to analyze, constituent-specifically, the ultrafast dynamics induced in both constituents of the heterostructures, after a localized optical excitation of only the metal constituent with a femtosecond laser pulse. Hereby I firstly focused on achieving a comprehensive insight into the microscopic origin of the induced dynamics, i.e., local relaxation processes within a single constituent and non-local energy transfer processes between the two constituents. To accomplish a profound understanding of the ultrafast dynamics, I complemented the time-resolved XAS measurements, which are sensitive to both the electronic and the lattice excitations, with ultrafast electron diffraction (UED) experiments, which are independently analyzing the lattice dynamics of the Fe constituent. Both measurements have been supported by *ab initio* density functional theory (DFT) calculations. In detail, the experiments showed a localized electronic excitation in the Fe constituent, with a peak in the pump-induced change in absorption of the Fe L_3-edge at 240 fs, which subsequently relaxes within ~ 1 ps by electron-phonon coupling. In contrast, the change in XAS observed at the O K-edge exhibits nearly the same transient behavior as compared to the increased mean square displacement of Fe ion cores probed in ultrafast electron diffraction, both building up significantly slower, within 0.5 ps. Consequently, the investigation of the pump-induced ultrafast dynamics in the heterostructure revealed that the ultrafast energy transfer across the Fe-MgO interface is, independently of the laser pump photon energy not mediated by a direct electronic charge transfer. Instead, the ultrafast energy transfer is mediated by high-frequency (above 15 meV phonon energy) interface vibrational modes, which become excited by the hot electrons in Fe and then couple to vibrations in MgO in a mode-selective, non-thermal manner. Consequently, demonstrating the importance of a hot phonon population for the initial step in the ultrafast interfacial non-equilibrium energy transfer dynamics of the heterostructure. Subsequently, for time delays $t > 1$ ps, both time-resolved pump-probe experiments showed a second, slower process, which can be attributed to the thermalization of the heterostructure as a whole and energy transfer across the interface involving lower energy acoustic phonons. The access to

energy-selective phonon excitation across the interface illustrates emerging possibilities to tailor transient material properties by addressing specific vibrational phonon modes. In particular, the localized optical excitation of the heterostructure allowed to spatially separate the excitation and the resulting material response, which might open up new ways to design and optimize the respective constituents of selected heterostructure systems towards the desired properties for future applications, e.g., new electronic devices, potentially even with the ability to control their material properties in response to an external excitation. [42]

After examining the ultrafast dynamics, I concentrated explicitly on the understanding of the time-dependent spectroscopic signatures of the pump-induced spectral changes of the two distinct absorption edges. Hereby, I reported, in a systematic fluence-dependent study, that the transition metal Fe L_3 absorption edge exhibited a clear red-shift of the spectra upon laser excitation. In contrast, the O K absorption edge of the insulator featured a uniform intensity decrease of its fine structures. Introducing two distinct modeling and fitting procedures to analyze this specific pump-induced changes in soft X-ray absorption spectroscopy, I showed that the corresponding fitting parameters, as well as the respective pump-induced changes of both edges, exhibit a linear dependency on the laser pump fluence. By combining the time-resolved XAS experiments with *ab initio* DFT calculations, I subsequently demonstrated the sensitivity of transient XAS to phonons, showing the great possibility to use time-resolved XAS to quantify temperature changes in complex materials, presumably even under conditions of a phonon non-equilibrium, where a description by a common lattice temperature is not applicable. The fundamental differences of the spectroscopic signatures of the pump-induced spectral changes of the two distinct absorption edges suggest the possibility to catalog in the future the pump-induced changes for all sort of different absorption edges, and eventually predict specific spectral changes on the femtosecond and picosecond timescale, and the amount of induced temperature changes upon laser excitation. [140]

Lastly, the study of the Fe/MgO heterostructure was dedicated to the investigation of the ultrafast local *demagnetization* behavior of the Fe constituent. In particular, the fact that the thin ferromagnetic layers are embedded between the insulating MgO constituents, was hereby crucial for the investigation, since all contributions of spin transport processes to the ultrafast demagnetization dynamics are suppressed. I combined the transient behavior of the Fe magnetization dynamic with the energy transfer dynamics to achieve a comprehensive understanding of the overall dynamics. By comparing the individual transients, I identified that the local demagnetization process of the Fe constituent is not directly governed by the electronic subsystem, but determined by a phonon-mediated process. However, the demagnetization measurements indicate a slightly slower response than for the energy transfer

dynamics, implying that the change in demagnetization might not be governed by the same high-frequency interface vibrational phonon modes, which are responsible for the energy transfer dynamics. The demagnetization did not show any recovery of the magnetization up to the maximum measured time delay of 9 ps. The phonon-mediated character of the demagnetization is a crucial finding in the ongoing debate of achieving a profound understanding of the ultrafast magnetization dynamics. I demonstrated that in the absence of spin transport processes, a significant degree of demagnetization requires the excitation of phonons. Eventually, a heating of the sample as a consequence of the incoherent lattice excitations is an unavoidable side-effect accompanying the ultrafast laser-induced demagnetization.

First results: X-ray absorption study of Ni and NiO at the European XFEL

Additionally to the study of the Fe/MgO system, I presented in this thesis first results of two open community proposals, including the very-first user experiment, conducted at the Spectroscopy and Coherent Scattering (SCS) instrument of the European XFEL, focused on a X-ray absorption study of Ni and NiO. A specially designed transmission zone plate setup with a grating (TZPG), which was successfully introduced during our experiment, was crucial to be able to conduct reproducible pump-probe experiments at the instrument. Using this setup, I demonstrated the possibility of performing high-quality static XAS measurements. The measured spectra conducted at the SCS instrument showed excellent data quality, comparable to that measured at the synchrotron facility SOLEIL, allowing to identify all fine structures in the respective Ni $L_{3,2}$ and O K absorption spectra. Subsequently, I highlighted as well the possibility to conduct femtosecond time-resolved XAS measurements at the XFEL facility, in particular, identifying time-resolved, pump-induced dynamics of several spectral signatures, and investigating a series of pump-induced spectral changes at various time delays. Finally, I ended the first results of the Ni and NiO study by outlining the opportunity to conduct X-ray absorption spectroscopy measurements in the non-linear X-ray regime at the XFEL. Thereby, I identified a clear specific difference between the non-linear and linear spectrum, i.e., a decrease in the peak intensity and a nonuniform broadening of the absorption peak. In conclusion, all these different first results demonstrate and emphasize the great perspectives for all kind of X-ray absorption spectroscopy measurements at the free-electron laser. In particular, the fast acquisition time for high-quality femtosecond time-resolved XAS measurements present a promising addition to synchrotron-based femtoslicing sources, allowing a variety of systematic measurements, which would not be possible at the latter.

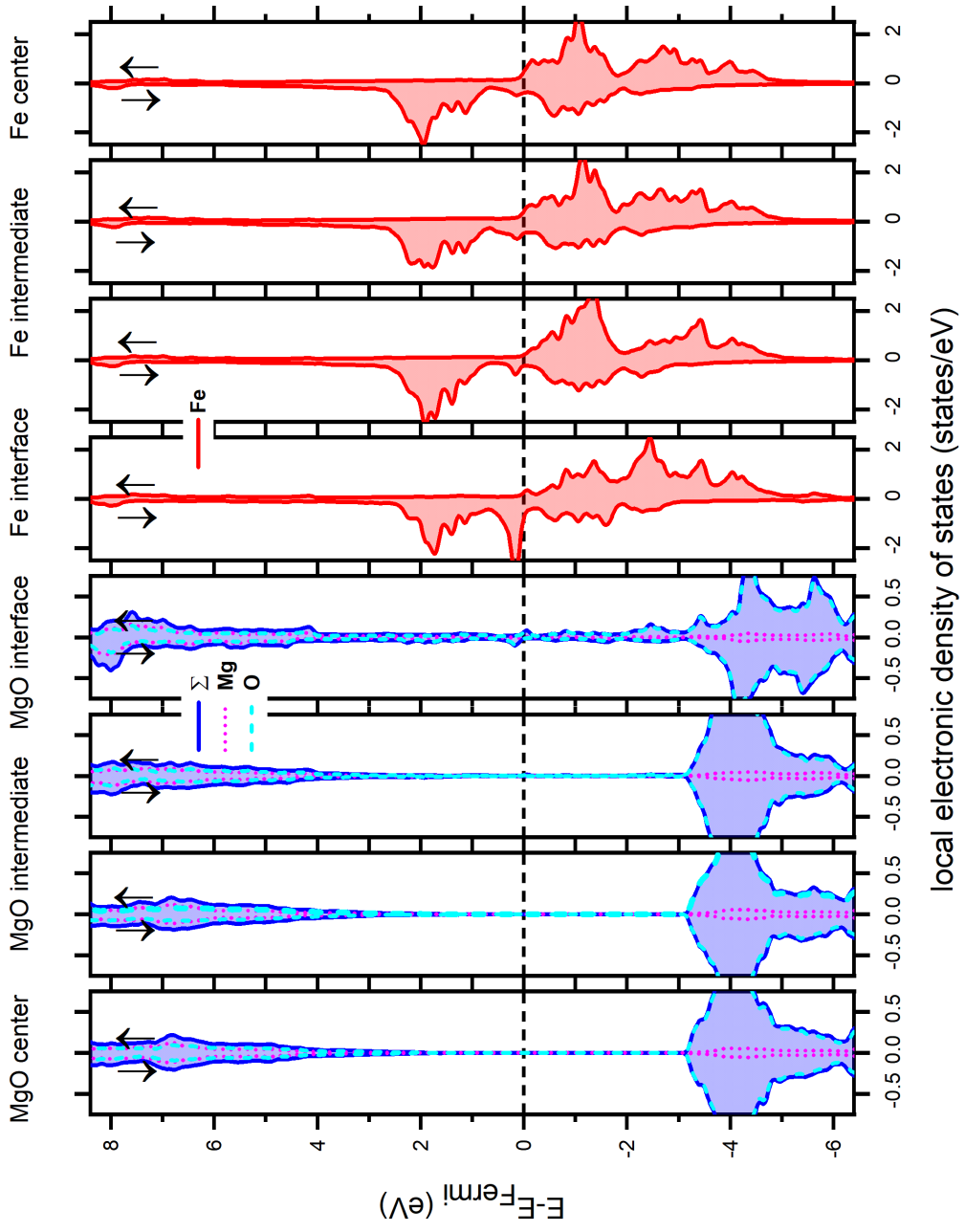

Fig. A.1.: Full spin-polarized element- and layer-resolved electronic density of states of $[Fe_8/(MgO)_8](001)$ obtained from DFT calculations. For more detail see Fig. 4.18 of chap. 4.2.4.

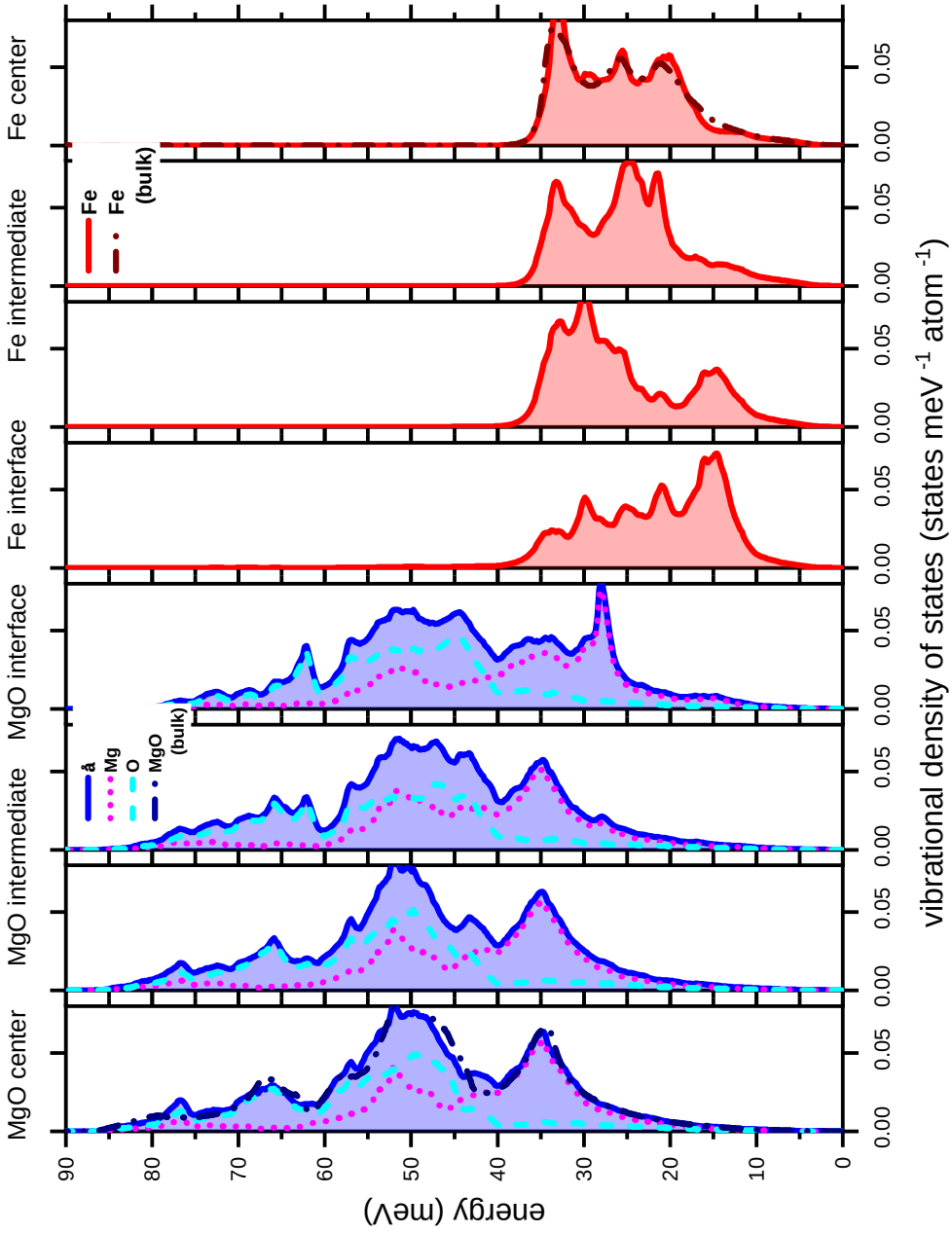

Fig. A.2.: Full layer-resolved vibrational density of states of $Fe_8/(MgO)_8(001)$ obtained from DFT calculations. For more detail see Fig. 4.19 of chap. 4.2.4.

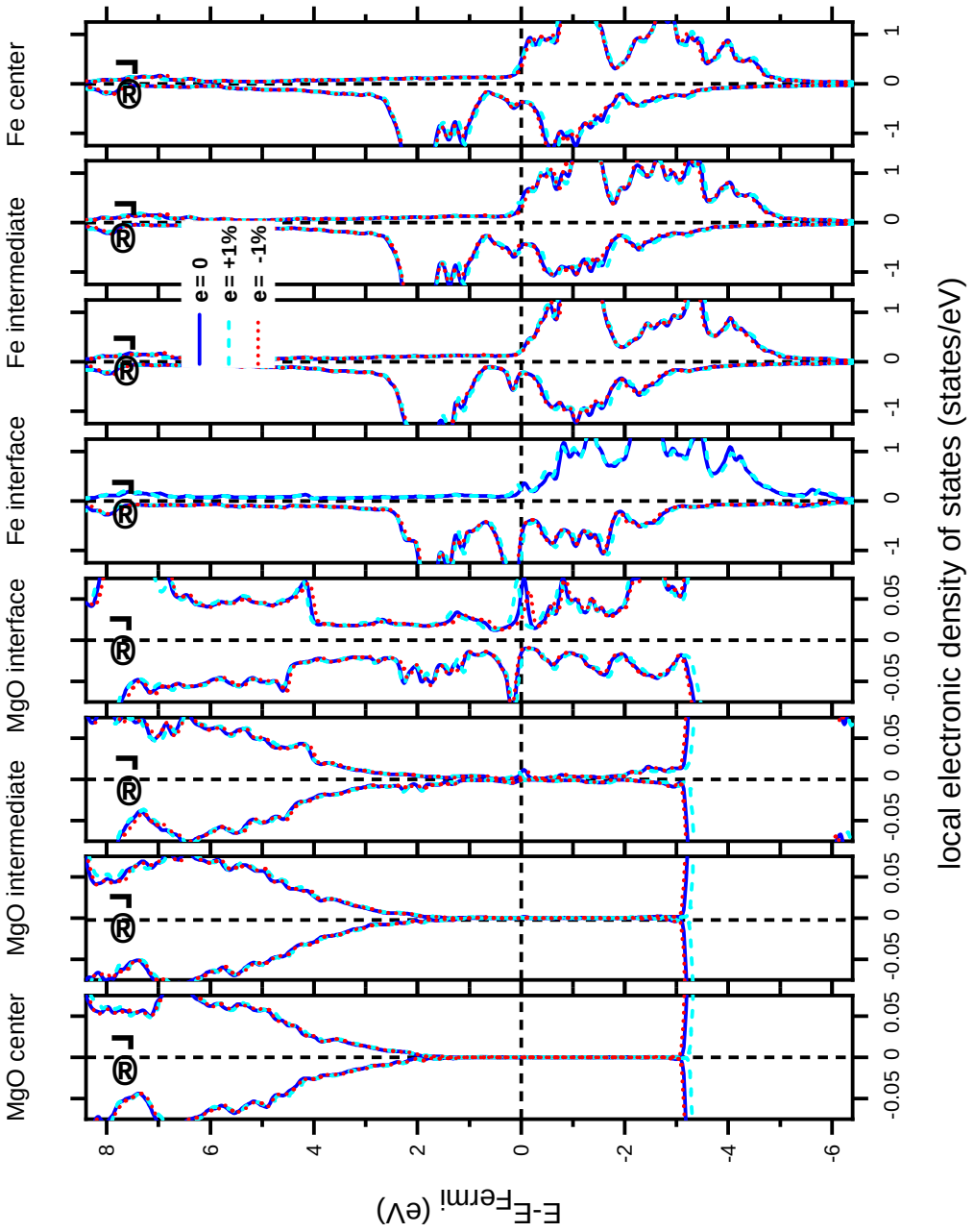

Fig. A.3.: Full layer-resolved electronic density of states under 1 % compression (red line) and expansion (blue, dashed line) of $Fe_8/(MgO)_8(001)$ obtained from DFT calculations. For more detail see Fig. 4.21 of chap. 4.2.4.

Bibliography

[1] J. M. Hopkins and W. Sibbett, „Ultrashort-pulse lasers: big payoffs in a flash," *Scientific American*, vol. 283, no. 3, pp. 72–79, 2000 (cit. on p. 1).

[2] A. Fognini and Y. Acremann, „Free electron lasers," in *Magnetism and Synchrotron Radiation: Towards the Fourth Generation Light Sources*, E. Beaurepaire, H. Bulou, L. Joly, and F. Scheurer, Eds., Springer International Publishing, 2013, pp. 139–153 (cit. on p. 1).

[3] H. W. Roberts, A. C. Day, and D. P. S. O'Brart, „Femtosecond laser–assisted cataract surgery: A review," *European Journal of Ophthalmology*, vol. 30, no. 3, pp. 417–429, 2020 (cit. on p. 1).

[4] X. Chen, W. Xiao, S. Ye, W. Chen, and Y. Liu, „Efficacy and safety of femtosecond laser-assisted cataract surgery versus conventional phacoemulsification for cataract: a meta-analysis of randomized controlled trials," *Scientific Reports*, vol. 5, no. 1, p. 13 123, 2015 (cit. on p. 1).

[5] Y.-C. Liu, A. J. S. Ji, T.-E. Tan, M. Fuest, and J. S. Mehta, „Femtosecond Laser-assisted Preparation of Conjunctival Autograft for Pterygium Surgery," *Scientific Reports*, vol. 10, no. 2674, 2020 (cit. on p. 1).

[6] W. Sibbett, A. A. Lagatsky, and C. T. A. Brown, „The development and application of femtosecond laser systems," *Opt. Express*, vol. 20, no. 7, pp. 6989–7001, 2012 (cit. on p. 1).

[7] „1999 Nobel Prize in Chemistry," *Journal of Chemical Education*, vol. 77, no. 1, p. 14, 2000 (cit. on p. 2).

[8] E. Beaurepaire, J.-C. Merle, A. Daunois, and J.-Y. Bigot, „Ultrafast Spin Dynamics in Ferromagnetic Nickel," *Phys. Rev. Lett.*, vol. 76, pp. 4250–4253, 22 1996 (cit. on pp. 2, 6, 9, 13, 102).

[9] A. Kirilyuk, A. V. Kimel, and T. Rasing, „Ultrafast optical manipulation of magnetic order," *Rev. Mod. Phys.*, vol. 82, pp. 2731–2784, 3 2010 (cit. on pp. 2, 8, 10, 13, 14).

[10] U. Bovensiepen, „Coherent and incoherent excitations of the Gd(0001) surface on ultrafast timescales," *Journal of Physics: Condensed Matter*, vol. 19, no. 8, p. 083 201, 2007 (cit. on pp. 2, 7–10).

[11] S. Anisimov, B. Kapeliovich, and T. Perelman, „Electron emission from metal surfaces exposed to ultrashort laser pulses," *JETP*, vol. 39, pp. 375–377, 1974 (cit. on pp. 5, 56, 70).

[12] P. B. Allen, „Theory of thermal relaxation of electrons in metals," *Phys. Rev. Lett.*, vol. 59, pp. 1460–1463, 13 1987 (cit. on p. 5).

[13] A. Vaterlaus, T. Beutler, and F. Meier, „Spin-lattice relaxation time of ferromagnetic gadolinium determined with time-resolved spin-polarized photoemission," *Phys. Rev. Lett.*, vol. 67, pp. 3314–3317, 23 1991 (cit. on p. 6).

[14] A. Vaterlaus, T. Beutler, D. Guarisco, M. Lutz, and F. Meier, „Spin-lattice relaxation in ferromagnets studied by time-resolved spin-polarized photoemission," *Phys. Rev. B*, vol. 46, pp. 5280–5286, 9 1992 (cit. on p. 6).

[15] H.-S. Rhie, H. A. Dürr, and W. Eberhardt, „Femtosecond electron and spin dynamics in $\mathrm{Ni/W(110)}$ films," *Phys. Rev. Lett.*, vol. 90, p. 247 201, 24 2003 (cit. on pp. 6, 8, 70, 72).

[16] V. V. Baranov and V. V. Kabanov, „Theory of electronic relaxation in a metal excited by an ultrashort optical pump," *Phys. Rev. B*, vol. 89, p. 125 102, 12 2014 (cit. on p. 6).

[17] S. T. Weber and B. Rethfeld, „Phonon-induced long-lasting nonequilibrium in the electron system of a laser-excited solid," *Phys. Rev. B*, vol. 99, p. 174 314, 17 2019 (cit. on p. 6).

[18] J. D. Rameau *et al.*, „Energy dissipation from a correlated system driven out of equilibrium," *Nature Communications*, vol. 7, no. 1, p. 13 761, 2016 (cit. on pp. 7, 57, 70).

[19] T. Konstantinova *et al.*, „Nonequilibrium electron and lattice dynamics of strongly correlated $Bi_2Sr_2CaCu_2O_{8+\delta}$ single crystals," *Science Advances*, vol. 4, no. 4, 2018 (cit. on p. 7).

[20] P. Maldonado, K. Carva, M. Flammer, and P. M. Oppeneer, „Theory of out-of-equilibrium ultrafast relaxation dynamics in metals," *Phys. Rev. B*, vol. 96, p. 174 439, 17 2017 (cit. on pp. 7, 8, 12, 73, 83).

[21] T. Chase *et al.*, „Ultrafast electron diffraction from non-equilibrium phonons in femtosecond laser heated Au films," *Applied Physics Letters*, vol. 108, no. 4, p. 041 909, 2016 (cit. on pp. 7, 12, 83).

[22] J. Hohlfeld *et al.*, „Electron and lattice dynamics following optical excitation of metals," *Chemical Physics*, vol. 251, no. 1, pp. 237–258, 2000 (cit. on pp. 8–10, 56, 70).

[23] H. Petek and S. Ogawa, „Femtosecond time-resolved two-photon photoemission studies of electron dynamics in metals," *Progress in Surface Science*, vol. 56, no. 4, pp. 239–310, 1997 (cit. on p. 7).

[24] M. Lisowski *et al.*, „Ultra-fast dynamics of electron thermalization, cooling and transport effects in Ru(001)," *Applied Physics A*, vol. 78, no. 2, pp. 165–176, 2004 (cit. on pp. 8, 10).

[25] F. Dalla Longa, J. T. Kohlhepp, W. J. M. de Jonge, and B. Koopmans, „Influence of photon angular momentum on ultrafast demagnetization in nickel," *Phys. Rev. B*, vol. 75, p. 224 431, 22 2007 (cit. on pp. 8, 9, 13).

[26] N. Del Fatti *et al.*, „Nonequilibrium electron dynamics in noble metals," *Phys. Rev. B*, vol. 61, pp. 16 956–16 966, 24 2000 (cit. on p. 9).

[27] W. Hübner and G. P. Zhang, „Ultrafast spin dynamics in nickel," *Phys. Rev. B*, vol. 58, R5920–R5923, 10 1998 (cit. on p. 9).

[28] A. Eschenlohr, „Charge, spin and energy transfer at interfaces on femtosecond timescales," presentation, unpublished, 2019 (cit. on p. 9).

[29] J. Walowski *et al.*, „Energy equilibration processes of electrons, magnons, and phonons at the femtosecond time scale," *Phys. Rev. Lett.*, vol. 101, p. 237 401, 23 2008 (cit. on p. 9).

[30] J. H. Mentink *et al.*, „Ultrafast spin dynamics in multisublattice magnets," *Phys. Rev. Lett.*, vol. 108, p. 057 202, 5 2012 (cit. on p. 9).

[31] L. Waldecker, R. Bertoni, R. Ernstorfer, and J. Vorberger, „Electron-Phonon Coupling and Energy Flow in a Simple Metal beyond the Two-Temperature Approximation," *Phys. Rev. X*, vol. 6, p. 021 003, 2 2016 (cit. on pp. 9, 10, 12, 83).

[32] X. Wang *et al.*, „Temperature dependence of electron-phonon thermalization and its correlation to ultrafast magnetism," *Phys. Rev. B*, vol. 81, p. 220 301, 22 2010 (cit. on p. 9).

[33] P. Tengdin *et al.*, „Critical behavior within 20 fs drives the out-of-equilibrium laser-induced magnetic phase transition in nickel," *Science Advances*, vol. 4, no. 3, 2018 (cit. on p. 9).

[34] P. E. Dolgirev, M. H. Michael, A. Zong, N. Gedik, and E. Demler, „Self-similar dynamics of order parameter fluctuations in pump-probe experiments," *Phys. Rev. B*, vol. 101, p. 174 306, 17 2020 (cit. on p. 9).

[35] M. Merschdorf, C. Kennerknecht, K. Willig, and W. Pfeiffer, „Transient electron energy distribution in supported Ag nanoparticles," *New Journal of Physics*, vol. 4, pp. 95–95, 2002 (cit. on p. 10).

[36] M. Battiato, K. Carva, and P. M. Oppeneer, „Superdiffusive spin transport as a mechanism of ultrafast demagnetization," *Phys. Rev. Lett.*, vol. 105, p. 027 203, 2 2010 (cit. on pp. 10, 14, 109, 110).

[37] V. P. Zhukov, E. V. Chulkov, and P. M. Echenique, „Lifetimes of excited electrons in fe and ni: First-principles gw and the t-matrix theory," *Phys. Rev. Lett.*, vol. 93, p. 096 401, 9 2004 (cit. on p. 10).

[38] V. P. Zhukov, E. V. Chulkov, and P. M. Echenique, „$GW{+}t$ theory of excited electron lifetimes in metals," *Phys. Rev. B*, vol. 72, p. 155 109, 15 2005 (cit. on p. 10).

[39] V. P. Zhukov, E. V. Chulkov, and P. M. Echenique, „Lifetimes and inelastic mean free path of low-energy excited electrons in fe, ni, pt, and au: Ab initio $\mathrm{GW{+}T}$ calculations," *Phys. Rev. B*, vol. 73, p. 125 105, 12 2006 (cit. on p. 10).

[40] G. Malinowski, N. Bergeard, M. Hehn, and S. Mangin, „Hot-electron transport and ultrafast magnetization dynamics in magnetic multilayers and nanostructures following femtosecond laser pulse excitation," *European Physical Journal B*, vol. 91, no. 98, pp. 1–20, 2018 (cit. on p. 10).

[41] G. R. Fleming and M. A. Ratner, „Grand challenges in basic energy sciences," *Physics Today*, vol. 61, no. 7, p. 28, 2008 (cit. on p. 10).

[42] N. Rothenbach *et al.*, „Microscopic nonequilibrium energy transfer dynamics in a photoexcited metal/insulator heterostructure," *Phys. Rev. B*, vol. 100, p. 174 301, 17 2019 (cit. on pp. 11, 45, 63, 65, 74, 98, 138).

[43] M. L. Huberman and A. W. Overhauser, „Electronic kapitza conductance at a diamond-pb interface," *Phys. Rev. B*, vol. 50, pp. 2865–2873, 5 1994 (cit. on pp. 12, 73, 74).

[44] A. V. Sergeev, „Electronic kapitza conductance due to inelastic electron-boundary scattering," *Phys. Rev. B*, vol. 58, R10199–R10202, 16 1998 (cit. on pp. 12, 74).

[45] P. E. Hopkins and D. A. Stewart, „Contribution of d-band electrons to ballistic transport and scattering during electron-phonon nonequilibrium in nanoscale Au films using an ab initio density of states," *Journal of Applied Physics*, vol. 106, no. 5, p. 053 512, 2009 (cit. on p. 12).

[46] P. E. Hopkins, J. L. Kassebaum, and P. M. Norris, „Effects of electron scattering at metal-nonmetal interfaces on electron-phonon equilibration in gold films," *Journal of Applied Physics*, vol. 105, no. 2, p. 023 710, 2009 (cit. on p. 12).

[47] L. Guo, S. L. Hodson, T. S. Fisher, and X. Xu, „Heat Transfer Across Metal-Dielectric Interfaces During Ultrafast-Laser Heating," *Journal of Heat Transfer*, vol. 134, no. 4, 2012 (cit. on p. 12).

[48] S. Ono, „Thermalization in simple metals: Role of electron-phonon and phonon-phonon scattering," *Phys. Rev. B*, vol. 97, p. 054 310, 5 2018 (cit. on p. 12).

[49] C. Monachon, L. Weber, and C. Dames, „Thermal Boundary Conductance: A Materials Science Perspective," *Annual Review of Materials Research*, vol. 46, no. 1, pp. 433–463, 2016 (cit. on pp. 12, 73).

[50] E. T. Swartz and R. O. Pohl, „Thermal boundary resistance," *Rev. Mod. Phys.*, vol. 61, pp. 605–668, 3 1989 (cit. on p. 12).

[51] J. C. Duda, T. E. Beechem, J. L. Smoyer, P. M. Norris, and P. E. Hopkins, „Role of dispersion on phononic thermal boundary conductance," *Journal of Applied Physics*, vol. 108, no. 7, p. 073 515, 2010 (cit. on p. 12).

[52] P. E. Hopkins, „Multiple phonon processes contributing to inelastic scattering during thermal boundary conductance at solid interfaces," *Journal of Applied Physics*, vol. 106, no. 1, p. 013 528, 2009 (cit. on p. 12).

[53] T. E. Beechem, S. Graham, P. E. Hopkins, and P. M. Norris, „Role of interface disorder on thermal boundary conductance using a virtual crystal approach," *Applied Physics Letters*, vol. 90, no. 5, p. 054 104, 2007 (cit. on p. 12).

[54] A. Hanisch-Blicharski *et al.*, „Heat transport through interfaces with and without misfit dislocation arrays," *Journal of Materials Research*, vol. 27, no. 21, pp. 2718–2723, 2012 (cit. on pp. 12, 73).

[55] P. Reddy, K. Castelino, and A. Majumdar, „Diffuse mismatch model of thermal boundary conductance using exact phonon dispersion," *Applied Physics Letters*, vol. 87, no. 21, p. 211 908, 2005 (cit. on p. 12).

[56] K. Sokolowski-Tinten *et al.*, „Thickness-dependent electron-lattice equilibration in laser-excited thin bismuth films," *New Journal of Physics*, vol. 17, no. 11, p. 113 047, 2015 (cit. on pp. 12, 74).

[57] J. Hohlfeld, E. Matthias, R. Knorren, and K. H. Bennemann, „Nonequilibrium magnetization dynamics of nickel," *Phys. Rev. Lett.*, vol. 78, pp. 4861–4864, 25 1997 (cit. on p. 13).

[58] A. Scholl, L. Baumgarten, R. Jacquemin, and W. Eberhardt, „Ultrafast spin dynamics of ferromagnetic thin films observed by fs spin-resolved two-photon photoemission," *Phys. Rev. Lett.*, vol. 79, pp. 5146–5149, 25 1997 (cit. on p. 13).

[59] J. Güdde, U. Conrad, V. Jähnke, J. Hohlfeld, and E. Matthias, „Magnetization dynamics of ni and co films on cu(001) and of bulk nickel surfaces," *Phys. Rev. B*, vol. 59, R6608–R6611, 10 1999 (cit. on p. 13).

[60] C. Stamm *et al.*, „Femtosecond modification of electron localization and transfer of angular momentum in nickel," *Nature Materials*, vol. 6, no. 10, pp. 740–743, 2007 (cit. on pp. 13, 14, 21, 56, 70, 90, 101, 109, 110, 130).

[61] C. Stamm, N. Pontius, T. Kachel, M. Wietstruk, and H. A. Dürr, „Femtosecond x-ray absorption spectroscopy of spin and orbital angular momentum in photoexcited Ni films during ultrafast demagnetization," *Phys. Rev. B*, vol. 81, p. 104 425, 10 2010 (cit. on pp. 13, 21, 130, 132–134).

[62] B. Koopmans *et al.*, „Explaining the paradoxical diversity of ultrafast laser-induced demagnetization," *Nature Materials*, vol. 9, no. 3, pp. 259–265, 2010 (cit. on pp. 13, 14, 110).

[63] C. D. Stanciu *et al.*, „All-Optical Magnetic Recording with Circularly Polarized Light," *Phys. Rev. Lett.*, vol. 99, p. 047 601, 4 2007 (cit. on p. 14).

[64] I. Radu *et al.*, „Transient ferromagnetic-like state mediating ultrafast reversal of antiferromagnetically coupled spins," *Nature*, vol. 472, no. 7342, pp. 205–208, 2011 (cit. on p. 14).

[65] C.-H. Lambert *et al.*, „All-optical control of ferromagnetic thin films and nanostructures," *Science*, vol. 345, no. 6202, pp. 1337–1340, 2014 (cit. on p. 14).

[66] S. Mangin *et al.*, „Engineered materials for all-optical helicity-dependent magnetic switching," *Nature Materials*, vol. 13, no. 3, pp. 286–292, 2014 (cit. on p. 14).

[67] T. Ogasawara, N. Iwata, Y. Murakami, H. Okamoto, and Y. Tokura, „Submicron-scale spatial feature of ultrafast photoinduced magnetization reversal in tbfeco thin film," *Applied Physics Letters*, vol. 94, no. 16, p. 162 507, 2009 (cit. on p. 14).

[68] J. Wang *et al.*, „Ultrafast quenching of ferromagnetism in inmnas induced by intense laser irradiation," *Phys. Rev. Lett.*, vol. 95, p. 167 401, 16 2005 (cit. on p. 14).

[69] K. Holldack *et al.*, „Ultrafast dynamics of antiferromagnetic order studied by femtosecond resonant soft x-ray diffraction," *Applied Physics Letters*, vol. 97, no. 6, p. 062 502, 2010 (cit. on p. 14).

[70] M. Matsubara *et al.*, „Ultrafast optical tuning of ferromagnetism via the carrier density," *Nature Communications*, vol. 6, no. 1, p. 6724, 2015 (cit. on p. 14).

[71] G. M. Müller *et al.*, „Spin polarization in half-metals probed by femtosecond spin excitation," *Nature Materials*, vol. 8, no. 1, pp. 56–61, 2009 (cit. on p. 14).

[72] A. Mann *et al.*, „Insights into ultrafast demagnetization in pseudogap half-metals," *Phys. Rev. X*, vol. 2, p. 041 008, 4 2012 (cit. on p. 14).

[73] Q. Zhang, A. V. Nurmikko, G. X. Miao, G. Xiao, and A. Gupta, „Ultrafast spin-dynamics in half-metallic Cro_2 thin films," *Phys. Rev. B*, vol. 74, p. 064 414, 6 2006 (cit. on p. 14).

[74] D. Steil *et al.*, „Band-Structure-Dependent Demagnetization in the Heusler Alloy $\mathrm{Co_2Mn}_{1-x}\mathrm{Fe}_x\mathrm{Si}$," *Phys. Rev. Lett.*, vol. 105, p. 217 202, 21 2010 (cit. on p. 14).

[75] A. V. Kimel *et al.*, „Ultrafast non-thermal control of magnetization by instantaneous photomagnetic pulses," *Nature*, vol. 435, no. 7042, pp. 655–657, 2005 (cit. on p. 14).

[76] S. F. Maehrlein *et al.*, „Dissecting spin-phonon equilibration in ferrimagnetic insulators by ultrafast lattice excitation," *Science Advances*, vol. 4, no. 7, 2018 (cit. on p. 14).

[77] M. Hofherr *et al.*, „Speed and efficiency of femtosecond spin current injection into a nonmagnetic material," *Phys. Rev. B*, vol. 96, p. 100 403, 10 2017 (cit. on pp. 14, 110).

[78] B. Koopmans, H. H. J. E. Kicken, M. van Kampen, and W. J. M. de Jonge, „Microscopic model for femtosecond magnetization dynamics," *Journal of Magnetism and Magnetic Materials*, vol. 286, pp. 271–275, 2005 (cit. on pp. 14, 110).

[79] B. Koopmans, J. J. M. Ruigrok, F. D. Longa, and W. J. M. de Jonge, „Unifying ultrafast magnetization dynamics," *Phys. Rev. Lett.*, vol. 95, p. 267 207, 26 2005 (cit. on pp. 14, 110).

[80] M. Battiato, K. Carva, and P. M. Oppeneer, „Theory of laser-induced ultrafast superdiffusive spin transport in layered heterostructures," *Phys. Rev. B*, vol. 86, p. 024 404, 2 2012 (cit. on pp. 14, 110).

[81] A. Eschenlohr *et al.*, „Ultrafast spin transport as key to femtosecond demagnetization," *Nature Materials*, vol. 12, no. 4, pp. 332–336, 2013 (cit. on pp. 14, 110).

[82] A. J. Schellekens, W. Verhoeven, T. N. Vader, and B. Koopmans, „Investigating the contribution of superdiffusive transport to ultrafast demagnetization of ferromagnetic thin films," *Applied Physics Letters*, vol. 102, no. 25, p. 252 408, 2013 (cit. on pp. 14, 110).

[83] G. P. Zhang and W. Hübner, „Laser-Induced Ultrafast Demagnetization in Ferromagnetic Metals," *Phys. Rev. Lett.*, vol. 85, pp. 3025–3028, 14 2000 (cit. on pp. 14, 110).

[84] W. Töws and G. M. Pastor, „Many-Body Theory of Ultrafast Demagnetization and Angular Momentum Transfer in Ferromagnetic Transition Metals," *Phys. Rev. Lett.*, vol. 115, p. 217 204, 21 2015 (cit. on pp. 14, 110).

[85] J. Chen *et al.*, „Competing spin transfer and dissipation at $\mathrm{Co/Cu}(001)$ interfaces on femtosecond timescales," *Phys. Rev. Lett.*, vol. 122, p. 067 202, 6 2019 (cit. on pp. 14, 110).

[86] C. Dornes *et al.*, „The ultrafast Einstein-de Haas effect," *Nature*, vol. 565, no. 7738, pp. 209–212, 2019 (cit. on p. 14).

[87] J. Stöhr and H. C. Siegmann, *Magnetism, From Fundamentals to Nanoscale Dynamics*. Springer Berlin Heidelberg, 2006 (cit. on pp. 16–18, 20).

[88] A. Beer, „Bestimmung der Absorption des rothen Lichts in farbigen Flüssigkeiten," *Annalen der Physik*, vol. 162, no. 5, pp. 78–88, 1852 (cit. on p. 16).

[89] L. Bergmann, H. Niedrig, H. Eichler, and C. Schaefer, *Lehrbuch der Experimentalphysik Bd.3 Optik: Wellen- und Teilchenoptik*, Bd. 3. de Gruyter-Verlag, 2004 (cit. on p. 16).

[90] J. Orear, E. Fermi, A. Rosenfeld, and R. Schluter, *Nuclear Physics: A Course Given by Enrico Fermi at the University of Chicago*, ser. Midway reprint. University of Chicago Press, 1950 (cit. on p. 17).

[91] P. A. M. Dirac and N. H. D. Bohr, „The quantum theory of the emission and absorption of radiation," *Proceedings of the Royal Society of London. Series A, Containing Papers of a Mathematical and Physical Character*, vol. 114, no. 767, pp. 243–265, 1927 (cit. on p. 17).

[92] J. J. Rehr and R. C. Albers, „Theoretical approaches to x-ray absorption fine structure," *Rev. Mod. Phys.*, vol. 72, pp. 621–654, 3 2000 (cit. on p. 18).

[93] J. L. Erskine and E. A. Stern, „Calculation of the $M23$ magneto-optical absorption spectrum of ferromagnetic nickel," *Phys. Rev. B*, vol. 12, pp. 5016–5024, 11 1975 (cit. on p. 19).

[94] G. Schütz *et al.*, „Absorption of circularly polarized x rays in iron," *Phys. Rev. Lett.*, vol. 58, pp. 737–740, 7 1987 (cit. on p. 19).

[95] P. Carra, B. T. Thole, M. Altarelli, and X. Wang, „X-ray circular dichroism and local magnetic fields," *Phys. Rev. Lett.*, vol. 70, pp. 694–697, 5 1993 (cit. on pp. 19, 21).

[96] B. T. Thole, P. Carra, F. Sette, and G. van der Laan, „X-ray circular dichroism as a probe of orbital magnetization," *Phys. Rev. Lett.*, vol. 68, pp. 1943–1946, 12 1992 (cit. on pp. 19, 21).

[97] C. T. Chen *et al.*, „Experimental Confirmation of the X-Ray Magnetic Circular Dichroism Sum Rules for Iron and Cobalt," *Phys. Rev. Lett.*, vol. 75, pp. 152–155, 1 1995 (cit. on pp. 19, 20).

[98] M. Altarelli, „Orbital-magnetization sum rule for x-ray circular dichroism: A simple proof," *Phys. Rev. B*, vol. 47, pp. 597–598, 2 1993 (cit. on p. 19).

[99] A. Ankudinov and J. J. Rehr, „Sum rules for polarization-dependent x-ray absorption," *Phys. Rev. B*, vol. 51, pp. 1282–1285, 2 1995 (cit. on p. 19).

[100] U. Fano, „Spin orientation of photoelectrons ejected by circularly polarized light," *Phys. Rev.*, vol. 178, pp. 131–136, 1 1969 (cit. on p. 20).

[101] K. Carva, D. Legut, and P. M. Oppeneer, „Influence of laser-excited electron distributions on the X-ray magnetic circular dichroism spectra: Implications for femtosecond demagnetization in Ni," *EPL (Europhysics Letters)*, vol. 86, no. 5, p. 57 002, 2009 (cit. on pp. 21, 56, 70, 90, 101, 132).

[102] C. Boeglin *et al.*, „Distinguishing the ultrafast dynamics of spin and orbital moments in solids," *Nature*, vol. 465, no. 7297, pp. 458–461, 2010 (cit. on p. 21).

[103] A. A. Zholents and M. S. Zolotorev, „Femtosecond X-Ray Pulses of Synchrotron Radiation," *Physical Review Letters*, vol. 76, no. 6, pp. 912–915, 1996 (cit. on pp. 23, 31).

[104] K. Holldack *et al.*, „FemtoSpeX: a versatile optical pump–soft X-ray probe facility with 100fs X-ray pulses of variable polarization," *Journal of Synchrotron Radiation*, vol. 21, no. 5, pp. 1090–1104, 2014 (cit. on pp. 23, 31–33, 35).

[105] K. Holldack, T. Kachel, S. Kahn, R. Mitzner, and T. Quast, „Characterization of laser-electron interaction at the BESSY II femtoslicing source," *Physical Review Special Topics - Accelerators and Beams*, vol. 8, no. 040704, pp. 1–7, 2005 (cit. on pp. 23, 31).

[106] K. Holldack, S. Kahn, R. Mitzner, and T. Quast, „Femtosecond Terahertz Radiation from Femtoslicing BESSY," *Physical Review Letters*, vol. 96, no. 054801, pp. 1–4, 2006 (cit. on pp. 23, 31).

[107] T. Kachel *et al.*, „Soft X-Ray Beamline for fs Pulses from the BESSY fs-Slicing Source," *AIP Conference Proceedings*, vol. 879, pp. 1250–1253, 2007 (cit. on p. 23).

[108] S. Khan, K. Holldack, T. Kachel, R. Mitzner, and T. Quast, „Femtosecond Undulator Radiation from Sliced Electron Bunches," *Physical Review Letters*, vol. 97, no. 074801, pp. 1–4, 2006 (cit. on pp. 23, 31).

[109] N. Pontius, K. Holldack, C. Schüler-Langeheine, T. Kachel, and R. Mitzner, „The FemtoSpeX facility at BESSY II," *Journal of large-scale research facilities*, vol. 2, no. A46, pp. 1–6, 2016 (cit. on pp. 23, 35).

[110] D. Schick *et al.*, „Analysis of the halo background in femtosecond slicing experiments," *Journal of Synchrotron Radiation*, vol. 23, no. 0, pp. 1–12, 2016 (cit. on pp. 23, 34).

[111] R. W. Schönlein *et al.*, „Generation of Femtosecond Pulses of Synchrotron Radiation," *Science*, vol. 287, pp. 2237–2240, 2000 (cit. on pp. 23, 31).

[112] P. Emma *et al.*, „First lasing and operation of an angstrom-wavelength free-electron laser," *Nature Photonics*, vol. 4, pp. 641–647, 2010 (cit. on p. 23).

[113] W. Ackermann *et al.*, „Operation of a free-electron laser from the extreme ultraviolet to the water window," *Nature Photonics*, vol. 1, pp. 336–342, 2007 (cit. on p. 23).

[114] S. V. Milton *et al.*, „Exponential Gain and Saturation of a Self-Amplified Spontaneous Emission Free-Electron Laser," *Science*, vol. 292, no. 5524, pp. 2037–2041, 2001 (cit. on p. 23).

[115] T. Shintake *et al.*, „A compact free-electron laser for generating coherent radiation in the extreme ultraviolet region," *Nature Photonics*, vol. 2, no. 9, pp. 555–559, 2008 (cit. on p. 23).

[116] Z. Huang *et al.*, „Measurements of the linac coherent light source laser heater and its impact on the x-ray free-electron laser performance," *Phys. Rev. ST Accel. Beams*, vol. 13, p. 020 703, 2 2010 (cit. on p. 23).

[117] T. Ishikawa *et al.*, „A compact X-ray free-electron laser emitting in the sub-ångström region," *Nature Photonics*, vol. 6, no. 8, pp. 540–544, 2012 (cit. on p. 23).

[118] W. Decking *et al.*, „A MHz-repetition-rate hard X-ray free-electron laser driven by a superconducting linear accelerator," *Nature Photonics*, 2020, online available (cit. on p. 23).

[119] D. J. Higley *et al.*, „Femtosecond x-ray magnetic circular dichroism absorption spectroscopy at an x-ray free electron laser," *Review of Scientific Instruments*, vol. 87, no. 3, p. 033 110, 2016 (cit. on p. 23).

[120] J. H. Piddington, „Thermal theories of the high-intensity components of solar radio-frequency radiation," *Proceedings of the Physical Society. Section B*, vol. 66, no. 2, pp. 97–104, 1953 (cit. on p. 23).

[121] A. J. Dean *et al.*, „Polarized Gamma-Ray Emission from the Crab," *Science*, vol. 321, no. 5893, pp. 1183–1185, 2008 (cit. on p. 23).

[122] A. Balerna and S. Mobilio, „Introduction to synchrotron radiation," in *Synchrotron Radiation: Basics, Methods and Applications*, S. Mobilio, F. Boscherini, and C. Meneghini, Eds., Springer Berlin Heidelberg, 2015, pp. 3–28 (cit. on pp. 23–26, 28–31).

[123] M.-E. Couprie and M. Valléau, „Synchrotron radiation, polarization, devices and new sources," in *Magnetism and Synchrotron Radiation: Towards the Fourth Generation Light Sources*, E. Beaurepaire, H. Bulou, L. Joly, and F. Scheurer, Eds., Cham: Springer International Publishing, 2013, pp. 51–94 (cit. on pp. 24, 25, 28).

[124] Canadian Light Source, *Inside the Synchrotron*, [Online]. Available from: `https://www.lightsource.ca/inside_the_synchrotron`, (accessed: 08.05.2020) (cit. on p. 25).

[125] D. H. Tomboulian and P. L. Hartman, „Spectral and Angular Distribution of Ultraviolet Radiation from the 300-Mev Cornell Synchrotron," *Phys. Rev.*, vol. 102, pp. 1423–1447, 6 1956 (cit. on p. 25).

[126] D. Cocco and M. Zangrando, „Synchrotron radiation sources and optical devices," in *Magnetism and Synchrotron Radiation*, E. Beaurepaire, H. Bulou, F. Scheurer, and K. Jean-Paul, Eds., Springer Berlin Heidelberg, 2010, pp. 127–144 (cit. on p. 27).

[127] M. Altarelli, „From third- to fourth-generation light sources: Free-electron lasers in the uv and x-ray range,“ in *Magnetism and Synchrotron Radiation*, E. Beaurepaire, H. Bulou, F. Scheurer, and K. Jean-Paul, Eds., Springer Berlin Heidelberg, 2010, pp. 407–419 (cit. on pp. 28, 38–41).

[128] A. Gaupp and E.-E. Koch, „Wiggler und Undulatoren,“ *Physik in unserer Zeit*, vol. 19(2), pp. 48–57, 1988 (cit. on p. 29).

[129] P. Beaud *et al.*, „Spatiotemporal Stability of a Femtosecond Hard-X-Ray Undulator Source Studied by Control of Coherent Optical Phonons,“ *Physical Review Letters*, vol. 99, no. 174801, pp. 1–4, 2007 (cit. on p. 31).

[130] A. Eschenlohr, „Element-resolved Ultrafast Magnetization Dynamics in Ferromagnetic Alloys and Multilayers,“ Ph.D. dissertation, University of Potsdam, 2012 (cit. on pp. 31–33, 35, 37).

[131] M. Eriksson, J. F. van der Veen, and C. Quitmann, „Diffraction-limited storage rings – a window to the science of tomorrow,“ *Journal of Synchrotron Radiation*, vol. 21, no. 5, pp. 837–842, 2014 (cit. on p. 38).

[132] R. Hettel, „DLSR design and plans: an international overview,“ *Journal of Synchrotron Radiation*, vol. 21, no. 5, pp. 843–855, 2014 (cit. on p. 38).

[133] D. Einfeld, M. Plesko, and J. Schaper, „First multi-bend achromat lattice consideration,“ *Journal of Synchrotron Radiation*, vol. 21, no. 5, pp. 856–861, 2014 (cit. on p. 38).

[134] P. Finetti *et al.*, „Pulse duration of seeded free-electron lasers,“ *Phys. Rev. X*, vol. 7, p. 021 043, 2 2017 (cit. on p. 40).

[135] T. Popmintchev *et al.*, „Bright coherent ultrahigh harmonics in the kev x-ray regime from mid-infrared femtosecond lasers,“ *Science*, vol. 336, no. 6086, pp. 1287–1291, 2012 (cit. on p. 40).

[136] T. Popmintchev *et al.*, „Phase matching of high harmonic generation in the soft and hard x-ray regions of the spectrum,“ *Proceedings of the National Academy of Sciences*, vol. 106, no. 26, pp. 10 516–10 521, 2009 (cit. on p. 40).

[137] European XFEL, *The European XFEL in international comparison*, [Online]. Available from: `https://www.xfel.eu/facility/comparison/`, (accessed: 29.03.2020) (cit. on p. 41).

[138] ——, *Beamlines*, [Online]. Available from: `https://www.xfel.eu/facility/beamlines/`, (accessed: 29.03.2020) (cit. on pp. 41, 42).

[139] ——, *Scientific Instrument SCS*, [Online]. Available from: `https://www.xfel.eu/facility/instruments/scs/`, (accessed: 29.03.2020) (cit. on pp. 42, 43).

[140] N. Rothenbach *et al.*, *Modeling the spectroscopic fine structures of pump-induced changes in time-resolved soft x-ray absorption spectroscopy of an fe/mgo multilayer*, 2019. arXiv: `1911.06201` (cit. on pp. 45, 92, 138).

[141] J. F. Lawler, R. Schad, S. Jordan, and H. van Kempen, „Structure of epitaxial Fe films on MgO(100)," *Journal of Magnetism and Magnetic Materials*, vol. 165, no. 1, pp. 224–226, 1997 (cit. on p. 48).

[142] S. M. Jordan, J. F. Lawler, R. Schad, and H. van Kempen, „Growth temperature dependence of the magnetic and structural properties of epitaxial Fe layers on MgO(001)," *Journal of Applied Physics*, vol. 84, no. 3, pp. 1499–1503, 1998 (cit. on p. 48).

[143] E. Mlynczak, K. Freindl, N. Spiridis, and J. Korecki, „Epitaxial MgO/Fe(001) and Fe/MgO(001): Structures of the interfaces," *Journal of Applied Physics*, vol. 113, no. 2, p. 024 320, 2013 (cit. on p. 48).

[144] O. Dugerjav, H. Kim, and J. M. Seo, „Growth of a crystalline and ultrathin MgO film on Fe(001)," *AIP Advances*, vol. 1, no. 3, p. 032 156, 2011 (cit. on p. 48).

[145] H. Kiessig, „Untersuchungen zur Totalreflexion von Röntgenstrahlen," *Annalen der Physik*, vol. 402, no. 6, pp. 715–768, 1931 (cit. on pp. 48, 120).

[146] U. von Hörsten, *Rechen/Fit Programm pi*, [Online]. Available from: `https://www.uni-due.de/~hm236ap/hoersten/home.html`, (accessed: 25.05.2020) (cit. on pp. 48, 120, 122).

[147] P. Gütlich, E. Bill, and A. Trautwein, *Mössbauer Spectroscopy and Transition Metal Chemistry*. Springer Berlin Heidelberg, 2011 (cit. on p. 49).

[148] D. Petti, M. Cantoni, C. Rinaldi, and R. Bertacco, „Chemical and electronic properties of Fe/MgO/Ge heterostructures for spin electronics," *Journal of Physics: Conference Series*, vol. 292, p. 012 010, 2011 (cit. on p. 51).

[149] T. Kachel *et al.*, „Transient electronic and magnetic structures of nickel heated by ultrafast laser pulses," *Phys. Rev. B*, vol. 80, p. 092 404, 9 2009 (cit. on pp. 56, 70, 90, 91, 101, 130).

[150] M. E. Gruner and R. Pentcheva, „Dynamics of optical excitations in a Fe/MgO(001) heterostructure from time-dependent density functional theory," *Phys. Rev. B*, vol. 99, p. 195 104, 19 2019 (cit. on pp. 57, 72).

[151] S. P. Weathersby *et al.*, „Mega-electron-volt ultrafast electron diffraction at SLAC National Accelerator Laboratory," *Review of Scientific Instruments*, vol. 86, no. 7, p. 073 702, 2015 (cit. on p. 63).

[152] Note: While all the various Fe/MgO samples have been prepared by myself, the actual UED measurements and their evaluation have been done by K. Sokolowski-Tinten from the university Duisburg-Essen. The measurements have been conducted at the MeV-UED facility at SLAC National Accelerator Laboratory under supervision from the respective beamline scientists: R. Li, M. Mo, S. Park, X. Shen, S. Weathersby, J. Yang, and X. J. Wang. (cit. on p. 63).

[153] M. Bauer, A. Marienfeld, and M. Aeschlimann, „Hot electron lifetimes in metals probed by time-resolved two-photon photoemission," *Progress in Surface Science*, vol. 90, no. 3, pp. 319–376, 2015 (cit. on p. 72).

[154] K. Sokolowski-Tinten *et al.*, „Electron-lattice energy relaxation in laser-excited thin-film Au-insulator heterostructures studied by ultrafast MeV electron diffraction," *Structural Dynamics*, vol. 4, no. 5, p. 054 501, 2017 (cit. on p. 74).

[155] J. P. Perdew, K. Burke, and M. Ernzerhof, „Generalized Gradient Approximation Made Simple," *Phys. Rev. Lett.*, vol. 77, pp. 3865–3868, 18 1996 (cit. on pp. 74, 92).

[156] G. Kresse and J. Furthmüller, „Efficient iterative schemes for ab initio total-energy calculations using a plane-wave basis set," *Phys. Rev. B*, vol. 54, pp. 11 169–11 186, 16 1996 (cit. on p. 74).

[157] G. Kresse and D. Joubert, „From ultrasoft pseudopotentials to the projector augmented-wave method," *Phys. Rev. B*, vol. 59, pp. 1758–1775, 3 1999 (cit. on p. 74).

[158] P. E. Blöchl, O. Jepsen, and O. K. Andersen, „Improved tetrahedron method for Brillouin-zone integrations," *Phys. Rev. B*, vol. 49, pp. 16 223–16 233, 23 1994 (cit. on p. 75).

[159] D. Alfè, „PHON: A program to calculate phonons using the small displacement method," *Computer Physics Communications*, vol. 180, no. 12, pp. 2622–2633, 2009 (cit. on p. 75).

[160] H. Ebert, D. Ködderitzsch, and J. Minár, „Calculating condensed matter properties using the KKR-green's function method—recent developments and applications," *Reports on Progress in Physics*, vol. 74, no. 9, p. 096 501, 2011 (cit. on pp. 75, 92).

[161] H. Ebert, *SPR-KKR: Munich SPRKKR band structure program package, version 7.7.3*, [Online]. Available from: = http://olymp.cup.uni-muenchen.de/ak/ebert/SPRKKR, (accessed: 04.11.2019) (cit. on pp. 75, 92).

[162] B. Eggert, ... , N. Rothenbach *et al.*, „Interface-related magnetic and vibrational properties in fe/mgo heterostructures from nuclear resonant spectroscopy and first-principles calculations," *Phys. Rev. Materials*, vol. 4, p. 044 402, 4 2020 (cit. on pp. 77, 102).

[163] M. Bargheer *et al.*, „Coherent atomic motions in a nanostructure studied by femtosecond x-ray diffraction," *Science*, vol. 306, no. 5702, pp. 1771–1773, 2004 (cit. on p. 78).

[164] H. Park, X. Wang, S. Nie, R. Clinite, and J. Cao, „Mechanism of coherent acoustic phonon generation under nonequilibrium conditions," *Phys. Rev. B*, vol. 72, p. 100 301, 10 2005 (cit. on p. 78).

[165] C. Rossignol, J. M. Rampnoux, M. Perton, B. Audoin, and S. Dilhaire, „Generation and Detection of Shear Acoustic Waves in Metal Submicrometric Films with Ultrashort Laser Pulses," *Phys. Rev. Lett.*, vol. 94, p. 166 106, 16 2005 (cit. on p. 78).

[166] A. Cavalleri *et al.*, „Anharmonic Lattice Dynamics in Germanium Measured with Ultrafast X-Ray Diffraction," *Phys. Rev. Lett.*, vol. 85, pp. 586–589, 3 2000 (cit. on p. 78).

[167] D. H. Feng, X. Q. Pan, X. Li, T. Q. Jia, and Z. R. Sun, „Coherent acoustic phonon generation and detection by femtosecond laser pulses in ZnTe single crystals," *Journal of Applied Physics*, vol. 114, no. 9, p. 093 513, 2013 (cit. on p. 78).

[168] T. Henighan *et al.*, „Generation mechanism of terahertz coherent acoustic phonons in Fe," *Phys. Rev. B*, vol. 93, p. 220 301, 22 2016 (cit. on p. 78).

[169] S. V. Sinogeikin, D. L. Lakshtanov, J. D. Nicholas, and J. D. Bass, „Sound velocity measurements on laser-heated MgO and Al2O3," *Physics of the Earth and Planetary Interiors*, vol. 143-144, pp. 575–586, 2004 (cit. on p. 78).

[170] P. Luches *et al.*, „X-ray absorption study at the Mg and O K edges of ultrathin MgO epilayers on Ag(001)," *Phys. Rev. B*, vol. 69, p. 045 412, 4 2004 (cit. on pp. 79, 80).

[171] J. P. Singh *et al.*, „Electronic structure of magnetic Fe/MgO/Fe/Co multilayer structure by NEXAFS spectroscopy," *Vacuum*, vol. 138, pp. 48–54, 2017 (cit. on p. 79).

[172] C. R. Seabourne *et al.*, „Analysis of computational EELS modelling results for MgO-based systems," *Ultramicroscopy*, vol. 110, no. 8, pp. 1059–1069, 2010 (cit. on pp. 79, 80).

[173] A. Dewaele, G. Fiquet, D. Andrault, and D. Hausermann, „P-v-t equation of state of periclase from synchrotron radiation measurements," *Journal of Geophysical Research: Solid Earth*, vol. 105, no. B2, pp. 2869–2877, 2000 (cit. on p. 81).

[174] T. Tsuyama *et al.*, „Photoinduced Demagnetization and Insulator-to-Metal Transition in Ferromagnetic Insulating $\mathrm{BaFeO_3}$ Thin Films," *Phys. Rev. Lett.*, vol. 116, p. 256 402, 25 2016 (cit. on pp. 89–91).

[175] M. Izquierdo *et al.*, „Laser-induced charge-disproportionated metallic state in $\mathrm{LaCoO_3}$," *Phys. Rev. B*, vol. 90, p. 235 128, 23 2014 (cit. on pp. 89, 91, 92, 101).

[176] R. Nemausat *et al.*, „Temperature dependence of X-ray absorption and nuclear magnetic resonance spectra: probing quantum vibrations of light elements in oxides," *Phys. Chem. Chem. Phys.*, vol. 19, pp. 6246–6256, 8 2017 (cit. on pp. 89, 91, 92).

[177] B. I. Cho *et al.*, „Electronic Structure of Warm Dense Copper Studied by Ultrafast X-Ray Absorption Spectroscopy," *Phys. Rev. Lett.*, vol. 106, p. 167 601, 16 2011 (cit. on pp. 90, 101).

[178] H. Ebert *et al.*, „Calculating linear-response functions for finite temperatures on the basis of the alloy analogy model," *Phys. Rev. B*, vol. 91, p. 165 132, 16 2015 (cit. on pp. 92, 93).

[179] H. Ebert, J. Braun, J. Minár, and S. Mankovsky, „Treatment of thermal effects by means of the alloy analogy model," in *Multiple Scattering Theory for Spectroscopies*, D. Sébilleau, K. Hatada, and H. Ebert, Eds., Cham: Springer International Publishing, 2018, pp. 339–344 (cit. on pp. 92, 93).

[180] J. J. Rehr, J. A. Soininen, and E. L. Shirley, „FinalState rule vs the BetheSalpeter equation for DeepCore xray absorption spectra," *Physica Scripta*, vol. T115, pp. 207–211, 2005 (cit. on p. 93).

[181] H. Ikeno and T. Mizoguchi, „Basics and applications of ELNES calculations," *Microscopy*, vol. 66, no. 5, pp. 305–327, 2017 (cit. on p. 93).

[182] A. L. Ankudinov, B. Ravel, J. J. Rehr, and S. D. Conradson, „Real-space multiple-scattering calculation and interpretation of x-ray-absorption near-edge structure," *Phys. Rev. B*, vol. 58, pp. 7565–7576, 12 1998 (cit. on p. 95).

[183] Y. Cao *et al.*, „Hysteresis in single and polycrystalline iron thin films: Major and minor loops, first order reversal curves, and preisach modeling," *Journal of Magnetism and Magnetic Materials*, vol. 395, pp. 361–375, 2015 (cit. on p. 102).

[184] T. Kato *et al.*, „Perpendicular Magnetic Anisotropy in Fe/MgO Multilayer Film Measured by Magnetic Compton Scattering," in *Applied Materials and Technologies for Modern Manufacturing*, ser. Applied Mechanics and Materials, vol. 423, Trans Tech Publications Ltd, 2013, pp. 271–275 (cit. on p. 102).

[185] A. Koziol-Rachwal *et al.*, „Magnetism of ultrathin Fe films in MgO/Fe/MgO in epitaxial structures probed by nuclear resonant scattering of synchrotron radiation," *Journal of Applied Physics*, vol. 113, no. 21, p. 214 309, 2013 (cit. on p. 102).

[186] J. W. Koo *et al.*, „Large perpendicular magnetic anisotropy at Fe/MgO interface," *Applied Physics Letters*, vol. 103, no. 19, p. 192 401, 2013 (cit. on p. 102).

[187] J. Okabayashi *et al.*, „Perpendicular magnetic anisotropy at the interface between ultrathin Fe film and MgO studied by angular-dependent x-ray magnetic circular dichroism," *Applied Physics Letters*, vol. 105, no. 12, p. 122 408, 2014 (cit. on p. 102).

[188] S. D. Peacor and T. Hibma, „Reflection high-energy electron diffraction study of the growth of NiO and CoO thin films by molecular beam epitaxy," *Surface Science*, vol. 301, no. 1, pp. 11–18, 1994 (cit. on p. 120).

[189] R. Downs and M. Hall-Wallace, „The American Mineralogist Crystal Structure Database," *American Mineralogist*, vol. 88, pp. 247–250, 2003 (cit. on p. 122).

[190] Note: The control experiment at the synchrotron SOLEIL for the characterization of the static spectral properties of the Ni and NiO samples have been conducted by E. Jal, K. Légaré, and V. Chardonnet from the Sorbonne Université with help of the beamline scientist N. Jaouen of the synchrotron SOLEIL. Access to Synchrotron SOLEIL the proposal with the ID 20160880 is acknowledged. (cit. on pp. 123, 125).

[191] Y. Ufuktepe, G. Akgül, F. Aksoy, and D. Nordlund, „Thickness and angular dependence of the l-edge x-ray absorption of nickel thin films," *X-Ray Spectrometry*, vol. 40, no. 6, pp. 427–431, 2011 (cit. on p. 125).

[192] Y. K. Chang *et al.*, „Charge transfer and hybridization effects in Ni3Al and Ni3Ga studies by x-ray-absorption spectroscopy and theoretical calculations," *Journal of Applied Physics*, vol. 87, no. 3, pp. 1312–1317, 2000 (cit. on p. 125).

[193] C. T. Chen, N. V. Smith, and F. Sette, „Exchange, spin-orbit, and correlation effects in the soft-x-ray magnetic-circular-dichroism spectrum of nickel," *Phys. Rev. B*, vol. 43, pp. 6785–6787, 8 1991 (cit. on p. 125).

[194] M. W. Haverkort *et al.*, „Magnetic versus crystal-field linear dichroism in NiO thin films," *Phys. Rev. B*, vol. 69, p. 020 408, 2 2004 (cit. on p. 125).

[195] M. Al Samarai *et al.*, „Elucidation of structure–activity correlations in a nickel manganese oxide oxygen evolution reaction catalyst by operando ni l-edge x-ray absorption spectroscopy and 2p3d resonant inelastic x-ray scattering," *ACS Applied Materials & Interfaces*, vol. 11, no. 42, pp. 38 595–38 605, 2019 (cit. on p. 125).

[196] S. C. Das *et al.*, „Band gap tuning in zno through ni doping via spray pyrolysis," *The Journal of Physical Chemistry C*, vol. 117, no. 24, pp. 12 745–12 753, 2013 (cit. on p. 125).

[197] D. Alders *et al.*, „Temperature and thickness dependence of magnetic moments in nio epitaxial films," *Phys. Rev. B*, vol. 57, pp. 11 623–11 631, 18 1998 (cit. on p. 125).

[198] H. Kurata, E. Lefèvre, C. Colliex, and R. Brydson, „Electron-energy-loss near-edge structures in the oxygen k-edge spectra of transition-metal oxides," *Phys. Rev. B*, vol. 47, pp. 13 763–13 768, 20 1993 (cit. on p. 126).

[199] Z. Y. Wu *et al.*, „Structural characterization of nickel oxide nanowires by x-ray absorption near-edge structure spectroscopy," *The Journal of Physical Chemistry B*, vol. 109, no. 7, pp. 2512–2515, 2005 (cit. on p. 126).

[200] J. Y. Zhang *et al.*, „Electronic and transport properties of li-doped nio epitaxial thin films," *J. Mater. Chem. C*, vol. 6, pp. 2275–2282, 9 2018 (cit. on p. 126).

[201] A. Eschenlohr *et al.*, „Open community proposal on femtosecond time-resolved soft x-ray absorption spectroscopy of magnetically ordered transition metals and oxides," European XFEL: proposal 2161, unpublished, 2019 (cit. on p. 128).

[202] S. Mukamel *et al.*, „Coherent Multidimensional Optical Probes for Electron Correlations and Exciton Dynamics: From NMR to X-rays," *Accounts of Chemical Research*, vol. 42, pp. 553–562, 4 2009 (cit. on p. 135).

[203] M. Beye *et al.*, „Open community proposal on efficient X-ray absorption spectroscopy at FELs: from non-perturbing fluences to non-linear effects," European XFEL: proposal 2170, unpublished, 2018 (cit. on p. 135).

[204] J. D. Biggs, Y. Zhang, D. Healion, and S. Mukamel, „Watching energy transfer in metalloporphyrin heterodimers using stimulated X-ray Raman spectroscopy," *Proceedings of the National Academy of Sciences*, vol. 110, no. 39, pp. 15 597–15 601, 2013 (cit. on p. 135).

[205] K. E. Dorfman, Y. Zhang, and S. Mukamel, „Coherent control of long-range photoinduced electron transfer by stimulated X-ray Raman processes," *Proceedings of the National Academy of Sciences*, vol. 113, no. 36, pp. 10 001–10 006, 2016 (cit. on p. 135).

[206] B. Wu *et al.*, „Elimination of X-Ray Diffraction through Stimulated X-Ray Transmission," *Phys. Rev. Lett.*, vol. 117, p. 027 401, 2 2016 (cit. on p. 135).

[207] N. Rohringer *et al.*, „Atomic inner-shell X-ray laser at 1.46 nanometres pumped by an X-ray free-electron laser," *Nature*, vol. 481, no. 7382, pp. 488–491, 2012 (cit. on p. 135).

[208] M. Beye *et al.*, „Stimulated X-ray emission for materials science," *Nature*, vol. 501, no. 7466, pp. 191–194, 2013 (cit. on p. 135).

[209] T. Kroll *et al.*, „Stimulated X-Ray Emission Spectroscopy in Transition Metal Complexes," *Phys. Rev. Lett.*, vol. 120, p. 133 203, 13 2018 (cit. on p. 135).

[210] S. Schreck *et al.*, „Reabsorption of Soft X-Ray Emission at High X-Ray Free-Electron Laser Fluences," *Phys. Rev. Lett.*, vol. 113, p. 153 002, 15 2014 (cit. on p. 135).

[211] H. Yoneda *et al.*, „Saturable absorption of intense hard X-rays in iron," *Nature Communications*, vol. 5, no. 1, p. 5080, 2014 (cit. on p. 135).

[212] B. Nagler *et al.*, „Turning solid aluminium transparent by intense soft X-ray photoionization," *Nature Physics*, vol. 5, no. 9, pp. 693–696, 2009 (cit. on p. 135).

List of Figures

List of Tables

Acknowledgement

This thesis would not been possible without the support and help of many people. I want to take here the opportunity to express my sincere gratitude and appreciation to all those, who made this Ph.D. thesis possible.

First of all, I would like to thank my thesis advisor **Prof. Dr. Heiko Wende**, for giving me the opportunity to make my Ph.D. thesis in his workgroup. I am thankful for all the support I got during the last years, but also for all the freedom I received, which allowed me to develop to the scientist I am today. You are the friendliest advisor I could have hoped for. I enjoyed every single *Kölsch* we had, the skiing, the hiking, and so much more. Thank you for making the time of my Ph.D. thesis not just being work, but also an unforgettable experience in general.
Further, I would like to thank the second advisor of my project within the CRC 1242 **Prof. Dr. Uwe Bovensiepen**, who guided most of the discussions we had throughout the years and put a big effort to help me publish my first publication within the time-resolved community.

I would like to thank **Dr. Katharina Ollefs** for encouraging me throughout my way, always giving me comfort when work made me despair, and teaching me not to take every stepping stone too serious. Even though I sometimes wished a slightly faster response, I always knew that I could ask for your advice. Thank you for all of your calls to check if all is going forward. Thank you for all the times you took me under your wing and supported me during the various experiments. I value your friendship a lot.
I am very grateful to **Dr. Andrea Eschenlohr**, the driving force behind all the time-resolved X-ray absorption experiments I presented throughout my thesis. I am especially thankful to you for reading through my entire dissertation in such a short time, even though many parts have been still work-in-progress. Thank you for all your comments and help. I still remember that you introduced me to the Korean kitchen, and I will always have a good thought for you whenever I eat another *Bibimbap* in my life.

I am thankful to all the members of the **workgroup AG Wende** for establishing a friendly work environment and offering all the support whenever needed.
I want to specially thank **Christiane Leuchtenberger** the "heart of our workgroup". Thank you so much for always having an open door in your office and time for several coffees per day. I appreciate a lot that you always listened to all my complaints and worries.
I am very grateful to **Samira Webers**, nine years ago, we started this journey together, and we finally made it. We finally overcame the never-ending struggle with whatsoever obstacle either the studying time, the bachelor and master thesis, and now the Ph.D. thesis had to offer. Thank you for all the teamwork, and all the coffee breaks. I am extremely glad to have worked together with such a wonderful person like you for nearly a decade.
I want to thank **Ulrich von Hörsten** for all his support and technical assistance with the sample preparation. I hope you know that none of my experiments at the large scale research facilities would have been possible without your great help in our laboratory. Thank you.
I am thankful to **Dr. Soma Salamon** for reading my thesis, and conducting and analyzing the conversion electron Mössbauer spectroscopy measurements. I want to thank you for every time you provided me help and always being so friendly and supportive.
Further, I want to thank our master student **Tobias Lojewski** for his help during the second XFEL beamtime, and for being so dedicated and motivated to learn more about the research area of the superfast timescales.
I also want to thank **Damian Günzing**. You are such an extremely nice and helpful person in general. It was such a fun time to be with you on beamtime. I understand that *one full beer* at the end of a hard working day was sometimes too much for you, but after all, your Ph.D. thesis just started. I wish you all the best.

I want to thank **PD Dr. Carolin Schmitz-Antoniak**, for all her support during the sometimes frustrating experiments. I am very glad for all your help, especially when you volunteered to work with me through the night-shifts, even though you had your own work to do. I am still not sure if you are sleeping at all. Thank you so much.
I am thankful for all the support I got from my collaborators from theoretical physics: **Prof. Dr. Rossitza Pentcheva** for all the discussion helping to publish my work; **PD Dr. Markus Gruner**, to whom I am especially thankful for carrying out all the presented *ab initio* density functional theory calculations supporting my experimental data. Thank you for all your help.
I thank **PD Dr. Klaus Sokolowski-Tinten** who carried out and analyzed the presented UED measurements on my samples. Further, I want to acknowledge the respective **beamline scientist from the MeV-UED facility** at SLAC National Accel-

erator Laboratory, namely R. Li, M. Mo, S. Park, X. Shen, S. Weathersby, J. Yang, and X. J. Wang, who helped Klaus during the measurements, since I could unfortunately not be there.
I thank all the **beamline scientist from the FEMTOSPEX facility** at the synchrotron BESSY II, especially N. Pontius, R. Mitzner, K. Holldack, and C. Schüßler-Langeheine, for all the support during the various beamtimes.
I want to thank all the **participants of the two open community proposals** at the Spectroscopy and Coherent Scattering instrument of the European XFEL, which are unfortunately too many to be listed here. It was an unforgettable experience to be part of this great team, working and learning together, sharing knowledge, and facing unknown difficulties, which only aluminum foil from a local discounter can solve. In particular, I want to thank with this the two corresponding principal investigators of the community proposals, **Dr. Martin Beye**, and **Dr. Andrea Eschenlohr**, who made both experiments possible. Furthermore, I want to thank **Dr. Loic Le Guyader** and **Robin Engel** for, among other things, all the effort they put into the development of the python scripts used for the data evaluation, and all the help they provided whenever I got lost throughout the thousands of lines of code. I also want to thank **Dr. Emmanuelle Jal** and the team who helped her to conduct the control experiment for the characterization of the static properties of the Ni and NiO samples.

I want to especially thank my parents, **Michaela** and **Thomas Rothenbach**. Thank you for all your support, your unconditional love, and care. Thank you for always encouraging me in all the paths I chose, and always believing in me. I always knew that you only wanted the best for me. I would not have made it this far without you.

Finally, I want to thank with all my heart, **Irene Iglesias**. Thank you for your endless patience, for being understanding whenever I was angry and depressed, for always being kind and having a smile, for always having faith in me, and for making our apartment, especially in this difficult time, a home. You are my best friend, my partner, my moral support, my family, *inevitable*, and so much more. I can not express to you with words how lucky I feel every day that we found each other. You have been by my side during the entire road of this Ph.D. thesis, and you know better than anybody else all the ups and downs of this journey. I could not have finished this thesis without your feedback and your support, the countless scientific discussions, and the staying together awake all night working side-by-side to finish both our theses. Thank you so much, Irene. *Te amo*.

DOI: 10.17185/duepublico/73155
URN: urn:nbn:de:hbz:464-20201109-071311-0